

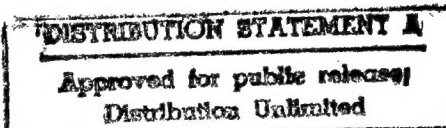
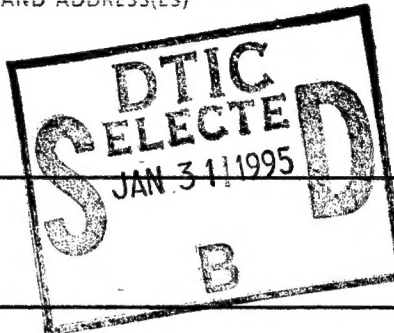
REPORT DOCUMENTATION PAGE

Dist: A

Form Approved
OMB No. 0704-0188

Public reporting burden for this collection of information is estimated to average 1 hour per response, including the time for reviewing instructions, searching existing data sources, gathering and maintaining the data needed, and completing and reviewing the collection of information. Send comments regarding this burden estimate or any other aspect of this collection of information, including suggestions for reducing this burden, to Washington Headquarters Services, Directorate for Information Operations and Reports, 1215 Jefferson Davis Highway, Suite 1204, Arlington, VA 22202-4302, and to the Office of Management and Budget, Paperwork Reduction Project (0704-0188), Washington, DC 20503.

1. AGENCY USE ONLY (Leave blank)	2. REPORT DATE	3. REPORT TYPE AND DATES COVERED FINAL 1 Sep 90 - 30 Nov 94	
4. TITLE AND SUBTITLE PROCESSING, FABRICATION, CHARACTERIZATION, AND DEVICE DEMONSTRATION OF HIGH TEMPERATURE SUPERCONDUCTING CERAMICS		5. FUNDING NUMBERS F49620-90-C-0079 62712E 7476/07.	
6. AUTHOR(S) Dr Luhman			
7. PERFORMING ORGANIZATION NAME(S) AND ADDRESS(ES) Boeing Co. P.O. Box 3999 Seattle WA 98124-2499		8. PERFORMING ORGANIZATION REPORT NUMBER AFOSR-TR- 95 0003	
9. SPONSORING / MONITORING AGENCY NAME(S) AND ADDRESS(ES) AFOSR/NL 110 Duncan Ave Suite B115 Bolling AFB DC 20332-0001 Maj Erstfeld		10. SPONSORING / MONITORING AGENCY REPORT NUMBER	
11. SUPPLEMENTARY NOTES			
12a. DISTRIBUTION / AVAILABILITY STATEMENT Approved for public release; Distribution Unlimited.		12b. DISTRIBUTION CODE A	



13. ABSTRACT (Maximum 200 words)

The goals of our program are to (1) focus on engineering designs and demonstration of flux-trap magnets; (2) develop improved processing and fabrication methods to enhance current densities in strong magnetic fields; (3) optimize processes for grain alignment in bulk and tape samples; and (4) provide a technology base for utilization of flux-trap magnets.

19950127 191

DTIC QUALITY INSPECTED 3

14. SUBJECT TERMS			15. NUMBER OF PAGES
			16. PRICE CODE
17. SECURITY CLASSIFICATION OF REPORT (U)	18. SECURITY CLASSIFICATION OF THIS PAGE (U)	19. SECURITY CLASSIFICATION OF ABSTRACT (U)	20. LIMITATION OF ABSTRACT (U)

The views and conclusions contained in this document are those of the authors and should not be interpreted as necessarily representing the official policies or endorsements, either expressed or implied, of the Advanced Research Projects Agency or the U.S. Government

**PROCESSING, FABRICATION, CHARACTERIZATION
AND DEVICE DEMONSTRATION OF HIGH
TEMPERATURE SUPERCONDUCTING CERAMICS**

Contract No. F49620-90-C-0079

FINAL TECHNICAL REPORT

September 1, 1990 - November 30, 1994

Submitted by:

Boeing Defense & Space Group

Sponsored by:

Advanced Research Projects Agency

ARPA Order No. 7476

Monitored by:

AFOSR Under Contract No. F49620-90-C-0079

PM: Dr. Thomas S. Luhman
(206) 773-1991

PI's: Dr. Michael Strasik
(206) 237-7176

Dr. Ilhan A. Aksay
(609) 258-4393

DTIC QUALITY INSPECTED 3

29 DEC 1994

The views and conclusions contained in this document are those of the authors and should not be interpreted as necessarily representing the official policies or endorsements, either expressed or implied, of the Advanced Research Projects Agency or the U.S. Government

**PROCESSING, FABRICATION, CHARACTERIZATION
AND DEVICE DEMONSTRATION OF HIGH
TEMPERATURE SUPERCONDUCTING CERAMICS**

Contract No. F49620-90-C-0079

ANNUAL TECHNICAL REPORT

September 1, 1993 - November 30, 1994

Submitted by:

Boeing Defense & Space Group

Sponsored by:

Advanced Research Projects Agency

ARPA Order No. 7476

Monitored by:

AFOSR Under Contract No. F49620-90-C-0079

PM: Dr. Thomas S. Luhman
(206) 773-1991

PI's: Dr. Thomas S. Luhman
(206) 773-1991

Dr. Ilhan A. Aksay
(609) 258-4393

Accession For	
RTIS GRA&I	<input checked="checked" type="checkbox"/>
DTIC TAB	<input type="checkbox"/>
Unannounced	<input type="checkbox"/>
Justification	
By	
Distribution/	
Availability Codes	
Dist	Avail and/or Special
A-1	

TABLE OF CONTENTS

PROGRAM OBJECTIVE	2
PROGRAM DESCRIPTION	2
SUMMARY	2
MILESTONE SCHEDULE	4
TECHNICAL RESULTS	5
MATERIALS SYNTHESIS AND CHARACTERIZATION	5
A. Large YBCO Crystal Growth	5
B. Inclined-Field Structure, Morphology, and Pinning of the Vortex Lattice in Microtwinning $\text{YBa}_2\text{Cu}_3\text{O}_{7-x}$	5
SUPERCONDUCTING PROPERTIES	
A. Lower Critical Field Studies of Melt-Textured and Melt-Grown $\text{YBa}_2\text{Cu}_3\text{O}_{7-x}$	18
SUPERCONDUCTIVE DEVICE REQUIREMENTS AND DESIGNS	23
A. Clamping Force Measurements	23
1. Axial Clamping Force	23
2. Lateral Clamping Force	28
B. Prototype High-Temperature Superconductor Clamps in Laser Cutting Operation	32
C. High-Temperature Superconducting Clamp with Joule-Thompson Cryostat	39

PROGRAM OBJECTIVE

To develop material processes and engineering designs for high current applications of $\text{YBa}_2\text{Cu}_3\text{O}_{7-x}$

PROGRAM DESCRIPTION

The goals of our program are to (1) focus on engineering designs and demonstration of flux-trap magnets; (2) develop improved processing and fabrication methods to enhance current densities in strong magnetic fields; (3) optimize processes for grain alignment in bulk and tape samples; and (4) provide a technology base for utilization of flux-trap magnets.

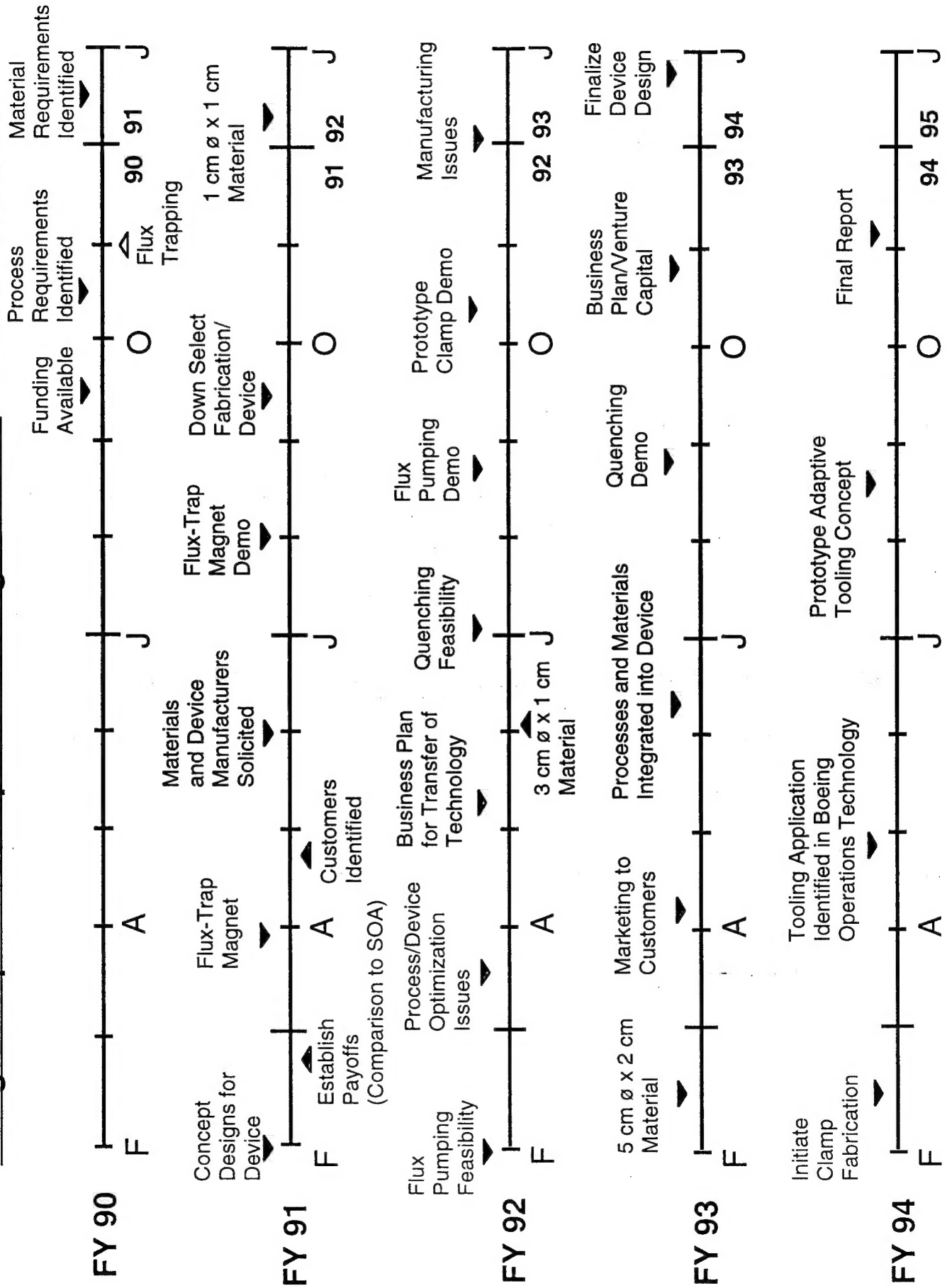
SUMMARY

- a) Improvements in the properties and reproducibility of bulk 123 samples with extremely large grains ($> 5 \text{ cm} \times 5 \text{ cm} \times 2 \text{ cm}$) were accomplished this year. These single crystals were successfully prepared by controlling the number of nucleation sites for the growth of 123 grains from the melt-quenched, 211 + liquid region, and following the Japanese approach of seeding (using $\text{SmBa}_2\text{Cu}_3\text{O}_{7-x}$ single crystal seeds) and growth in a temperature gradient.
- b) Variability reduction (VR) plan was implemented in the processing steps of the YBCO crystal growth. The VR plan examined every step of the precursor powder processing, powder compaction, crystal growth, oxygen annealing, crystal cutting and shaping. As a result of the VR plan, the growth yield of 1" diameter single crystal was increased to $> 80\%$, and yield of 2" diameter single crystal was increased to about 70%.
- c) Studies of the YBCO crystal growth in a-b and c- directions as a function of thermal gradient and growth rate were conducted.
- d) Large crystal growing furnace with a movable sample stage, capable of accommodating samples up to 8" in diameter, was placed in operation during this year.
- e) A detailed small-angle neutron scattering study of the vortex lattice in a single crystal of $\text{YBa}_2\text{Cu}_3\text{O}_{7-x}$ was made for a field of 0.5 tesla inclined at angles between 0 and 80 degrees to the crystalline c axis. The vortex lattice is triangular for all angles. For angles less than or equal to 70 degrees its orientation adjusts itself to maximize the pinning energy to densely and highly regularly spaced twin

planes. These observations have important implications for the microscopic flux-pinning mechanism, and hence for the critical current achievable in $\text{YBa}_2\text{Cu}_3\text{O}_{7-x}$. For large angles (about 80 degrees) the vortex lattice consists of independent chains in the orientation predicted by anisotropic London theory.

- f) Lower critical field measurements have been performed on two samples of melt grown YBCO prepared under different conditions. Measurements using the ΔM approach were made as a function of temperature both with the field parallel to the c-axis as well as perpendicular to it. Relatively large samples (2-4 mm x 7-9 mm) were used, with regular geometries. The demagnetization question was addressed. 4.2 K Lower Critical Field (LCF) of 920 Oe in the H_{\parallel} orientation and 340 Oe in the H_{\perp} orientation was obtained. LCF temperature dependence was related to the presence or absence, respectively, of optical twinning.
- g) Prototype high-temperature superconducting flux-trap magnet clamps were used for clamping of a Boeing 737 aircraft part during a laser (1500 watt carbon dioxide laser) cutting demonstration.
- h) Clamping force measurements of YBCO single crystals were performed using a calibrated linearized load cell. Clamping force was measured as a function of displacement, load, speed and applied field strength and pattern. Clamping force exceeding 110 Newtons (corresponding to a clamping pressure exceeding 37 psi) was achieved on a single element clamp at 77K. Clamping force in the axial as well as radial direction was measured.
- i) A miniature Joule-Thompson cryostat has been assembled with a portable non-magnetic dewar that can house up to a one inch diameter superconductor single crystal. The unit was built to Boeing specifications by R.G.Hansen & Associates of Santa Barbara, California. The clamp will cool a twenty-one-gram crystal from ambient temperature to 77.9K in less than seven minutes. A linear scale-up is possible for superconductors larger than two inches in diameter.

Processing, Fabrication, Characterization and Device Demonstration of High Temperature Superconducting Ceramics: F49620-90-c-0079



TECHNICAL RESULTS

MATERIALS SYNTHESIS AND CHARACTERIZATION

A. Large YBCO Crystal Growth

A Variability Reduction (VR) plan was implemented in the processing steps of the YBCO crystal growth. A typical variability reduction plan flow diagram is shown in Figure 1-2. The VR plan identified key characteristics of the YBCO crystals required for electromagnetic tooling applications. All process parameters in the YBCO crystal growth and testing were investigated during the VR process. The processing parameters investigated were: precursor powder synthesis, powder processing, seed production, formation of pressed pellets, crystal growth, oxygenation, testing and measurements, and post production crystal shaping. The VR process identified three key processing parameters in the growth of large crystals to be the 123 and 211 powder synthesis, powder processing, and furnace crystal growth. As a result of the VR plan, improvements in the properties and reproducibility of bulk 123 samples with extremely large grains ($> 5 \text{ cm} \times 5 \text{ cm} \times 2 \text{ cm}$) were accomplished this year. The growth yield of 1" diameter single crystal was improved to $> 80\%$, and yield of 2" diameter crystal was improved to about 70%. A typical 2" diameter YBCO single crystal with a thickness of 0.5" is shown in Figure 3.

B. Inclined-Field Structure, Morphology, and Pinning of the Vortex Lattice in Microtwinning $\text{YBa}_2\text{Cu}_3\text{O}_{7-x}$

The nature of the vortex state in the cuprate high-temperature superconductors remains an issue of great theoretical and practical interest. A variety of experimental techniques have been used to investigate the static dynamic vortex correlations in these materials. In contrast to surface imaging techniques, such as low-field ($B \leq 0.005 \text{ T}$) Bitter decoration or scanning tunneling microscopy, neutron scattering is sensitive to the entire length of the vortices in the bulk material. Neutron scattering experiments can be performed in a magnetic field range of $\sim 0.05 \text{ T}$ up to several teslas, a theoretically interesting regime in which the vortices interact strongly. This is also the relevant field range for prospective magnet applications of the copper oxide superconductors. In fact, the success of our experiments depended critically on the preparation of a large ($\sim 2.5\text{-cm}$ diameter, 0.9-cm thickness), high-quality single crystal in a program devoted to device applications of bulk $\text{YBa}_2\text{Cu}_3\text{O}_{7-x}$.

VARIABILITY REDUCTION (VR) PLAN

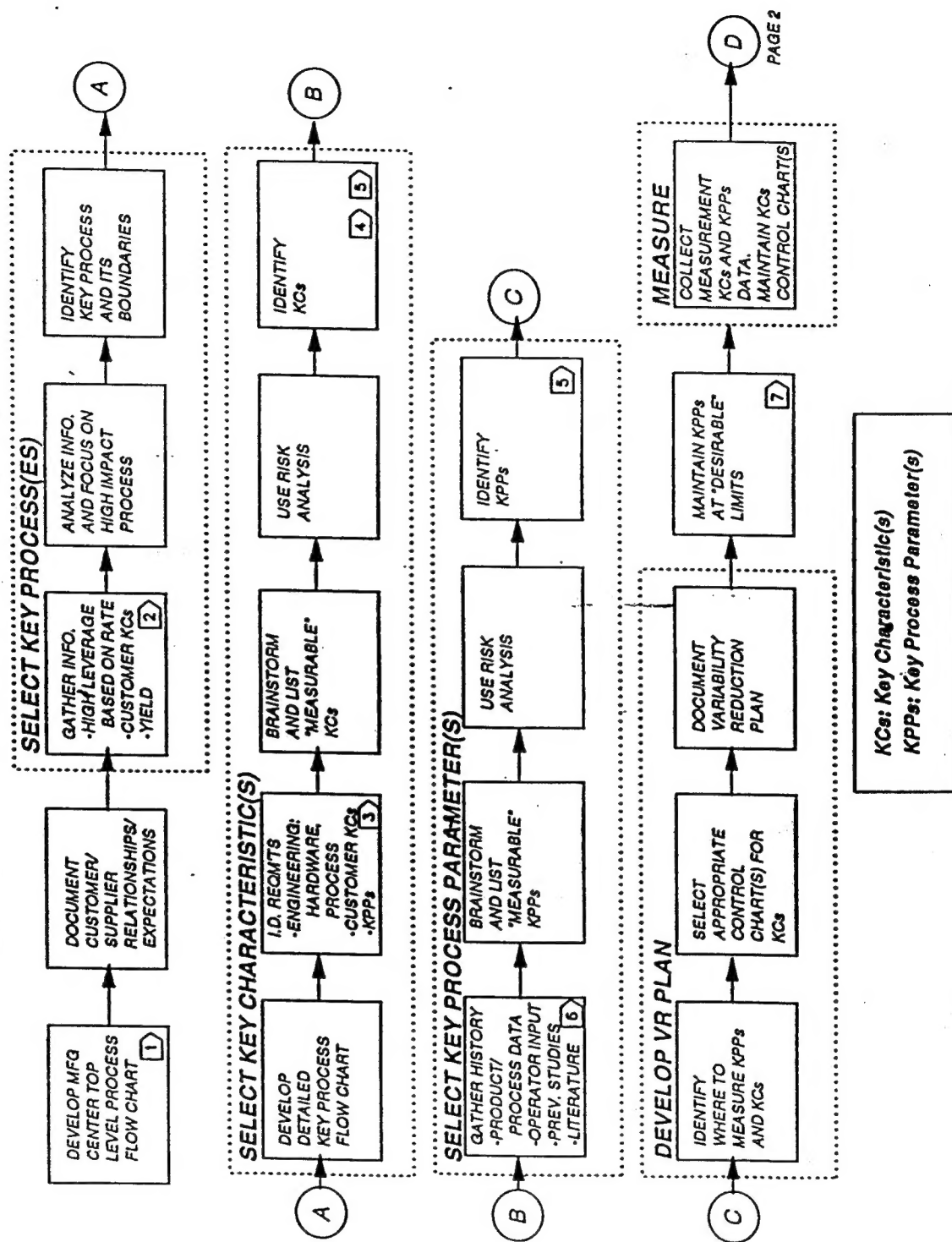


Figure 1. Variability Reduction Plan - Flow Diagram.

```

graph TD
    D((D)) -- FROM PAGE 1 --> D1{IS OUTPUT KCS IN CONTROL?}
    D1 -- YES --> D2{IS MINIMUM CAPABILITY MET?}
    D1 -- NO --> D3{IS THERE SPECIAL CAUSE VARIATION?}
    D2 -- YES --> D4[MAINTAIN PROCESS PARAMETER SETTING]
    D2 -- NO --> D5{HAS GAGE VARIATION BEEN ANALYZED?}
    D3 -- YES --> D6[REMOVE CAUSE]
    D3 -- NO --> D7[UPDATE DATABASE/HISTORICAL RECORD/VR PLAN]
    D6 --> D7
    D7 --> D8[COLLECT NEW MEASUREMENTS AND CHART]
    D8 --> D1
    D5 -- YES --> D9[PERFORM GAGE VARIATION STUDY]
    D5 -- NO --> D10{CHALLENGE ENGINEERING REQMTS?}
    D9 --> D10
    D10 -- YES --> D11[CHANGE ENGINEERING REQMTS]
    D10 -- NO --> D12{PROCESS PARAMETERS BEEN OPTIMIZED?}
    D11 --> D12
    D12 -- YES --> D13[CHALLENGE ENGINEERING REQMTS]
    D12 -- NO --> D14[IDENTIFY POTENTIAL SOURCES OF VARIATION]
    D13 --> D15{NEED NEW KPPs?}
    D14 --> D15
    D15 -- YES --> D16[OPTIMIZE PARAMETER SETTING]
    D15 -- NO --> D17[INVESTIGATE A NEW PROCESS]
    D16 --> D17
    D17 --> D18[UPDATE DATABASE/HISTORICAL RECORD/VR PLAN]
    D18 --> D7
    D13 --> D19[DOCUMENT RESULTS]
    D19 --> D20{CORRECTIVE ACTION TAKEN?}
    D20 -- YES --> D7
    D20 -- NO --> D17
    D4 --> D21[EVALUATE REDUCING MEASUREMENTS]
    D21 --> D22((C))
    D22 --> D23[MAINTAIN PROCESS PARAMETER SETTING]
    D23 --> D4

```

7

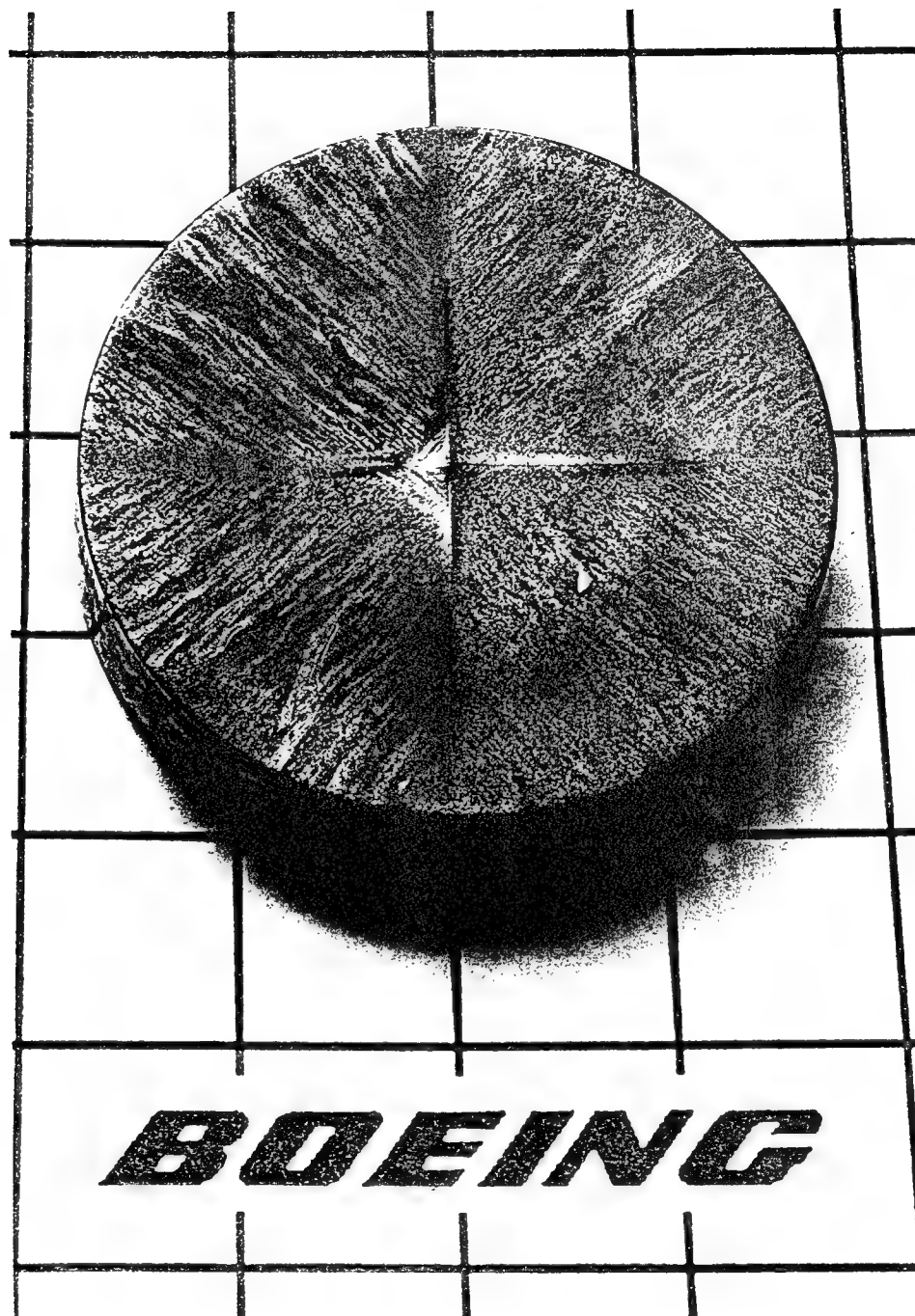


Figure 3. Single crystal YBa₂Cu₃O_{7-x} . Grid size is 0.5".

The experiments address two interrelated issues. First, the layered structure of the copper oxides and the concomitant large anisotropy of the electronic properties gives rise to complex current and field distributions around individual vortices. The resulting unusual interactions between vortices can lead to novel vortex structures as the magnetic field is inclined at an angle θ with respect to the c axis. By performing neutron experiments for $0^\circ \leq \theta \leq 80^\circ$, we tested these theories in fields up to 0.5 T. A second issue of great practical significance is the interaction of the vortex lattice with pinning centers that prevent dissipative vortex motion at high temperatures and cause flux trapping as the external field is removed.

We carried out extensive electron microscopy studies to identify the microstructural features potentially responsible for flux pinning in our samples. Our neutron measurements indicate that among the possible candidates (inclusions of the non-superconducting Y_2BaCuO_5 phase, stacking faults, and twin planes) only the densely spaced twin planes have a substantial effect on the structure of the vortex lattice. Prior evidence for the importance of twin planes as pinning sites derives mainly from Bitter decoration and transport studies conducted for either $\theta = 0^\circ$ or $\theta = 90^\circ$. We show that the vortex lattice orientation locks into the orientation of the twin planes up to a surprisingly large inclination angle $\theta \approx 70^\circ$. We discuss this observation in terms of microscopic models of the vortex structure. For larger inclination angles, we report the observation of a vortex chain state.

The single-crystal sample was synthesized by a seeding technique in a temperature gradient. The characterization of our sample by transmission electron microscopy was carried out by the cutting of several sections perpendicular to the (001) and (110) planes from an identically prepared crystal. A selected-area diffraction pattern with the electron beam in the (001) direction is shown in Figure 4. The orthorhombic strain $\Delta a = (b_o - a_o) / a_t = 1.8\%$ (a_o , b_o , a_t are the basal-plane lattice parameters in the orthorhombic and tetragonal phases) determined from the splitting of the [110] diffraction peak is identical for several sections of the sample. The strain created as the sample is cooled through the tetragonal-orthorhombic transition at 700°C is relieved by the formation of two variants of twin boundaries. As discussed previously, the separation D of the twin boundaries is inversely proportional to Δa , so the highly regular twin-plane spacing again shows a homogenous distribution of oxygen. By measuring 250 twin domains we obtained $D = 900 \pm 30$ Å. We determined the width of the twin boundaries to be 15 ± 5 Å from the width of the weak rod of scattering extending in the direction around the diffraction peak of Figure 4. Because this width is of the order of in-plane superconducting coherence length, the twin planes may be effective core-pinning sites.

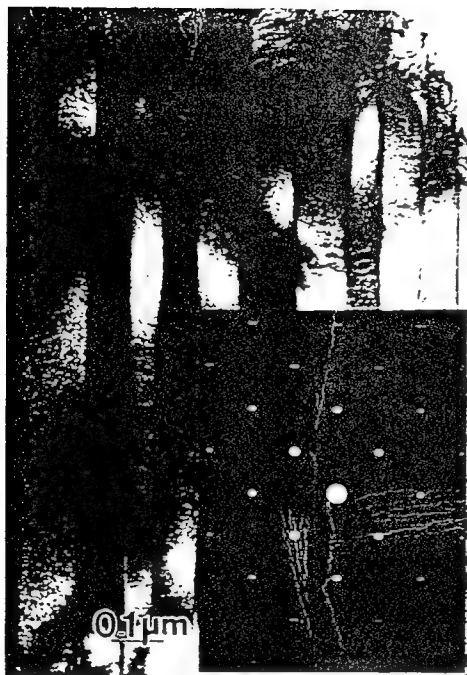


Figure 4. Electron micrograph showing one family of twin boundaries in YBCO crystal. The inset is a selected area diffraction pattern showing the orthorhombic splitting of the $[h00]$ Bragg reflections. From the uniformity of the orthorhombic splitting for different sections of the sample, a highly homogeneous distribution of oxygen throughout the sample can be deduced.

Our coordinate system is defined in Figure 5. The angles χ and ϕ are determined by the orientation of the crystal by x-ray diffraction outside the cryostat. Once the sample is mounted in the cryostat, the angles θ and ϑ can be changed by the rotation of either the cryostat inside the magnet or the entire cryostat-magnet assembly, respectively. The crystalline (100) axis in the (x,y) plane to $\pm 3^\circ$, so that $\phi \approx 45^\circ$. We performed the neutron scattering experiments for two different values of χ : $0^\circ \pm 1^\circ$ and $9^\circ \pm 1^\circ$. It is important to understand the difference between these two configurations: In the first case, the magnetic field bisects the angle between the two sets of twin planes for any value of θ . In the second case, the c axis is slightly offset from the field direction by $\chi = 9^\circ$ at $\theta = 0^\circ$, so that for $\theta \neq 0^\circ$ the angles α_\pm subtended between the magnetic field and the two sets of twin planes. This small difference in angle has profound consequences for the structure of the vortex lattice.

The data for $\chi = 0^\circ$ and $\chi = 9^\circ$ are shown Figure 6, A to F, and Figure 6, G to I, respectively. For $\theta = \chi = 0^\circ$, we observe the diffraction pattern with fourfold symmetry reported for both zero and nonzero θ . This result led others to the conclusion that the vortices for a square lattice, which maximizes the binding energy between vortices and both sets of twin planes, rather than the triangular lattice expected if vortex-vortex interactions dominate. To investigate this point further we oriented the crystal so that $\chi = 9^\circ$ and $\theta = 5^\circ$ (Figure 6G). This small angular offset causes a single-domain triangular lattice to be formed in the entire crystal, as evidenced by the hexagonal diffraction pattern. A fit to the circularly averaged intensity profile gave a peak position (τ) of 0.0092 ± 0.003 , somewhat smaller than the value of $\tau = 2.15\pi\sqrt{B/\Phi_0} = 0.0105$ calculated from the flux quantization rule for an undistorted triangular lattice (Φ_0 is the flux quantum). Within experimental error, no such expansion of the average lattice spacing is observed for a larger θ . The slight expansion of the $\theta \approx 0^\circ$, together with the significant transverse broadening of four of the reflections, indicates the formation of defects that lead to an accumulation of vortices near twin planes.

Because of the poor longitudinal resolution of our instrument, we can only put a lower bound of ~ 3 lattice spacings on the translational correlation length. The instrumental resolution in the ϑ direction is much sharper ($\sim 0.2^\circ$), and rocking curves in the ϑ direction revealed an intrinsic width of $\Delta\vartheta \approx 1^\circ$ for the Bragg reflections, in agreement with previous measurements. The correlation length ξ^* of the vortex displacement field in the magnetic field direction is given approximately by $\xi^* = (\tau\Delta\vartheta)^{-1} \approx 6000$. The vortices are therefore significantly deflected from the field direction as they bend and follow the twin plane over some distance to gain advantage of the twin-plane pinning energy. In this model, the finite-range order in the twin-plane position. The vortex line tension, which opposes this bending, leads to the

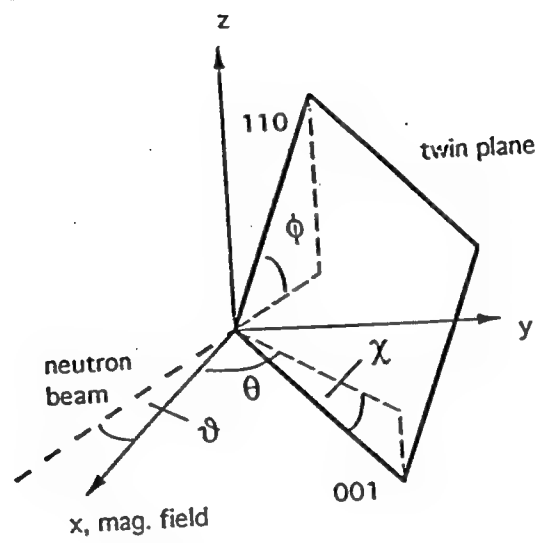


Figure 5. Coordinate system defining angle conventions.

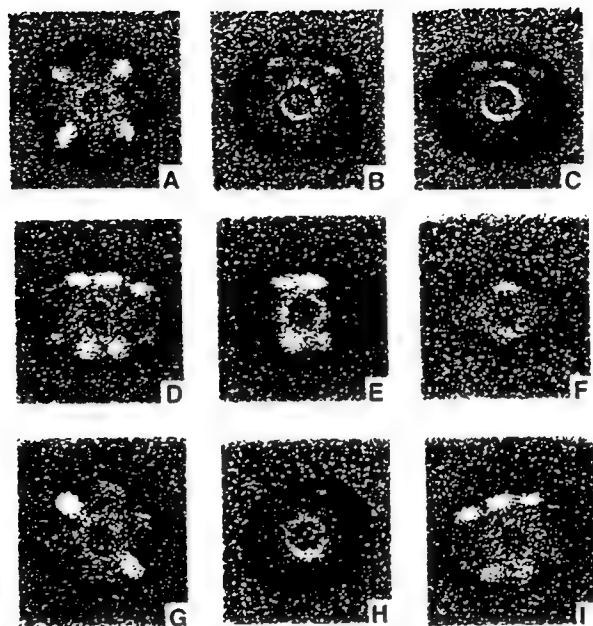


Figure 6. Small angle neutron diffraction patterns obtained from YBCO single crystals at the NIST 30m SANS spectrometer. The angle θ between the crystalline c-axis and the magnetic field direction is varied such that A) $\theta = 0^\circ$, B) $\theta = 50^\circ$, C) $\theta = 60^\circ$, E) $\theta = 70^\circ$, F) $\theta = 80^\circ$, G) $\theta = 5^\circ$, H) $\theta = 30^\circ$, I) $\theta = 60^\circ$. For panels A-F the angles between the magnetic field and both sets of twin planes are equal, while for panels G-I the angles are different.

formation of a single-domain pattern (Figure 6G). The lowest elastic energy and maximum pinning energy of the vortex lattice are achieved if the orientation of one of the principal axes is given by the set of twin planes subtending the smaller angle α with respect to the magnetic field. The square pattern of Figure 6A arises simply as a superposition of two orientations that are degenerate for $\chi = 0^\circ$.

The broadening of the θ rocking curves persists up to $\theta \sim 40^\circ$. However, for $\theta \geq 50^\circ$ the reflections become resolution-limited in all directions. These results are qualitatively consistent with high-temperature transport measurements revealing a drop in the resistivity due to vortex motion when the critical field is applied within a "critical angle" width respect to the twin planes. It has been suggested that vortex bending becomes energetically unfavorable above this critical angle; our neutron scattering data provide microscopic evidence for such behavior.

Inspection of the diffraction patterns of Figure 6, B to E, reveal that although the distortion of the vortex is consistent with equations, the orientation of the lattice does not follow the prediction of the effective mass model because no reflection with a zero y component (Figure 5) is observed.

For a small θ , the orientation of the vortex lattice is determined by pinning interactions between vortices and twin planes. Therefore, we postulate that this relation remains true for a larger θ , which leads to a quandary. The correlation length of the displacement field along the magnetic field direction, for $\theta \geq 50^\circ$, is resolution-limited and therefore at least $\sim 2 \mu\text{m}$. Therefore, any bending of the vortex induced by the twin planes must be allowed to "heal" on a length scale shorter than the twin-plane spacing so that this bending does not cause a long-range displacement field reflecting the imperfect twin-plane periodicity. If, on the other hand, the vortex is assumed to be microscopically homogeneous, the pinning energy should not depend on the location of the intersection point between the vortex and the twin plane.

A length scale much shorter than the twin-plane spacing naturally arises in microscopic models of the vortex structure that also take the discreteness of the crystalline layer structure into account. In such models the vortex consists of "pancake" vortices in the ab plane separated by interplanar Josephson vortices. It has been argued that the pinning forces experienced by the Josephson segments are reduced by a factor of $(\epsilon\xi/d)^3$ with respect to the force experienced by pancake vortices. For $\text{YBa}_2\text{Cu}_3\text{O}_{7-x}$, the in-plane coherence length $\xi \sim 15$ and the interlayer spacing is $d \sim 10$, so that we can neglect the pinning force on the interlayer segments and concentrate on the pinning forces on the pancakes. The pinning energy of the pancake vortices is maximized when one of the principal axes of this lattice is parallel to the "picket fence" pattern of twin boundaries. Viewed along the field direction, the reciprocal lattice vectors of the rotated lattice in the two twin-

plane domains allowed us to carry out a detailed quantitative analysis of the peak positions.

The radial peak positions were obtained from fits to sector averages and were in quantitative agreement for $\theta \leq 60^\circ$. Three-dimensional corrections apply for $\theta \geq 70^\circ$. To obtain the angular peak positions, we averaged the data radially in an elliptical annulus of appropriate eccentricity. Figure 7 shows the typical results of this procedure, together with the predictions from calculated values. Except for the unexplained asymmetry of a few reflections, the observed peak positions are in substantial agreement. This agreement validates our simple model and requires an essentially two-dimensional flux pinning mechanism.

Finally, we focus on the diffraction pattern for $\theta = 80^\circ$ (Figure 6F), which is inconsistent with calculated values. In fact, the anisotropic London model predicts the position of these reflections correctly. A reorientation of the vortex lattice into the unique orientation predicted by anisotropic London theory is expected for a large θ . Fits to high-quality diffraction patterns for B of 0.535 T, θ of 77° , and neutron wavelengths (λ) of 6 and 10 yield a value of 0.0061 ± 0.0003 \AA^{-1} for the radial peak position. The corresponding $\epsilon = 0.23 \pm 0.05$ is within the errors consistent with the values extracted from Bitter decoration patterns.

For a large θ , the triangular vortex lattice is severely stretched in the direction perpendicular to both B and c and can be regarded as a collection of chains whose periodicities are locked. Anisotropic London theory predicts an attractive double well in the intervortex interaction along the chains for small fields, so that the vortices should penetrate as independent chains for small fields, so that the vortices should penetrate as independent chains as the field is increased through the lower critical field H_{c1} . Such a vortex chain state has been observed in low-field Bitter decoration in $\text{YBa}_2\text{Cu}_3\text{O}_{7-x}$. Some workers have used the same theory to predict the persistence of this vortex-lattice shear modulus corresponding to translations of the chains in the chain direction. In $\text{YBa}_2\text{Cu}_3\text{O}_{7-x}$ for B = 0.5 T, the chains are predicted to decouple for $\theta \geq 80^\circ$, thus producing a diffraction pattern consisting of just two reflections. The data represented in Figure 6F confirms this prediction. By translating the detector with respect to the beam to probe a wider momentum range and taking diffraction patterns for different values of θ , we observed only broad and weak diffuse scattering around the remaining four reciprocal lattice vectors for fields of 0.1 and 0.5 T. The broadening of these Bragg peaks reflects the loss of long-range order in the direction perpendicular to the chains.

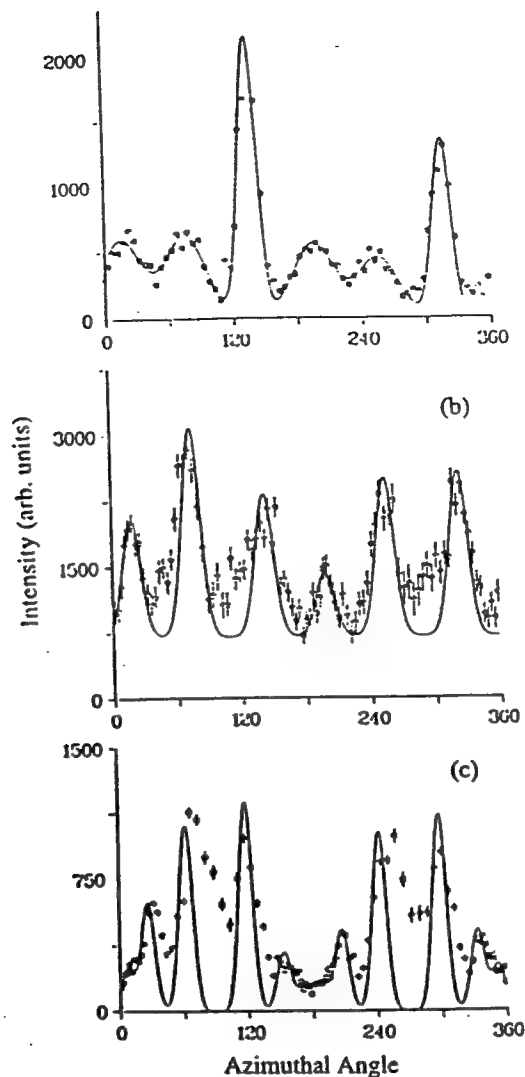


Figure 7. Diffraction patterns for (A) $x = 0^\circ$, $\theta = 5^\circ$, (B) $x = 9^\circ$, $\theta = 30^\circ$ (C) $x = 0^\circ$, $\theta = 5^\circ$, radially averaged over an elliptical annulus of 15 to 20 pixels in width. The azimuthal angle is the angle subtended by a ray from the origin to the center of the annulus and the positive y axis. (A) and (B) show six reflections corresponding to a single-domain vortex lattice. In (C) the Bragg condition is satisfied only for eight of the twelve reflections of the domain lattice. The solid lines show the predicted peak positions. The relative peak heights carry no meaning (the intensity units are arbitrary).

In contrast to observations in other anisotropic superconductors, but in agreement with observations in $\text{YBa}_2\text{Cu}_3\text{O}_{7-x}$ at low fields, we therefore conclude that the mean field anisotropic London theory provides an adequate description of the structure and orientation of the vortex lattice in this material. However, we have also shown that pinning to correlated microstructural defects can obliterate this intrinsic behavior and lead to unexpected changes in morphology and orientation of the vortex lattice as a function of θ . It will be interesting to extend this investigation into a temperature and field range in which the melting of the flux-line lattice is expected to occur. For device applications, the strong response of the vortex lattice to the presence of twin planes, and the absence of any measurable influence of any other microstructural feature, makes the structural design and configuration of twin planes a promising approach to enhance the flux-trapping properties of these materials.

SUPERCONDUCTING PROPERTIES

A. Lower Critical Field Studies of Melt-Textured and Melt-Grown $\text{YBa}_2\text{Cu}_3\text{O}_{7-x}$

Numerous methods for measuring the lower critical field, LCF or H_{c1} , of high- T_c superconductors have been used. The methods used are based on: (i) magnetization measurement, (ii) magnetic screening, (iii) radio frequency techniques, (iv) torque and mechanical oscillation, (v) muon and spin resonance, and (vi) optical visualization of magnetic flux. A Method of LCF determination derived from an extended Bean model, relied on the existence of a trapped magnetization, M_t , that is proportional to an $(H_{hc})^2$. A plot of $\sqrt{M_t}$ versus this H extrapolates to H_{c1} . An advantage of the method is that it is based on a relatively large data set rather than the usual detection of the departure of a single point from the Meissner line. Similarly a "hysteritic method" for superconducting cylinders, also based on the Bean model, enables a H_{c1} to be extracted from an extensive set of hysteritic-loss versus sweep-amplitude data taken above H_{c1} .

The application of this method to two samples (designated "CPS3" and "CPS4"), independently produced by similar techniques, yielded LCF's of 163 and 162 Oe, respectively. Another sample of melt textured YBCO (designated "DC1") yielded 225 Oe.

In melt texturization a molten zone is made to pass along a rod of compacted YBCO. The fast-growing a-b planes tend to lie parallel to the growth direction (the rod axis), causing the c-axes of the resulting crystallites to be randomly directed but always normal to the rod axis.

Further investigation of the LCF was logically chosen to be upon carefully oriented single crystals of YBCO.

Two large crystals of $\text{YBa}_2\text{Cu}_3\text{O}_{7-x}$ were prepared by variants of the melt-growth technique pioneered by Murakami *et al.* Crystal A was grown using a modified Bridgman technique from a $\text{SmBa}_2\text{Cu}_3\text{O}_{7-x}$ seed (oriented with the a-b-plane parallel to the large surface) previously imbedded in a sintered YBCO bar. Sample A, in the form of a square prism $2.26 \times 2.85 \times 9.34 \text{ mm}^3$, was removed from this crystal and oxygenated for 48h/500°C plus 24h/400°C. The c-axis was perpendicular to one of the long faces of the prism. Crystal B was grown at 1050-1080°C in air (from a $\text{SmBa}_2\text{Cu}_3\text{O}_{7-x}$ seed oriented with the a-b plane parallel to the upper surface). The crystal was oxygenated for 168h/450°C after sample B, in the form of a cylinder $4.82 \text{ mm}^\phi \times 7.06 \text{ mm}^l$, was removed from it using a hollow-core diamond drill. The c-axis was parallel to the cylinder axis. Magnetization measurements were carried out in a vibrating-sample magnetometer operating with a 17 kOe iron-core electromagnet.

Sample A was measured with the field in a plane perpendicular to the long axis. With sample B the field was perpendicular to the cylinder axis.

After cooling the sample in zero field, initial magnetization measurements were performed on both samples as function of temperature from 4.2 K to T_c . A straight line was then subtracted from the data and an LCF (uncorrected for demagnetization) was then taken as the field associated with the first nonzero value of magnetization-difference, ΔM ; see Figures 8 and 9. Demagnetization factors, n , were determined from the slope of the initial-magnetization straight line using $\chi = -1/(4\pi(1-n))$; they were seen to agree with the ellipsoidal approximation to better than 10%. The demagnetization-corrected LCF is then given by $H_{c1} = H_e / (1-n)$, where H_e is the applied field for first flux entry (i.e. the uncorrected LCF).

Sample A: Measurements were made on sample A both with the field along the c-axis (H_{\parallel}) and perpendicular to it (H_{\perp}). The results, corrected using a n_{\parallel} of 0.466 and a n_{\perp} of 0.502, respectively, are shown in Figure 8. Taking the H_{\parallel} results first, we note that the 4.2 K value of 920 Oe is close to the literature average. On the other hand, the 4.2 K H_{\perp} value of 430 Oe is rather high, and consequently the resulting $A = H_{\parallel} / H_{\perp}$ is considerably lower than average, Figure 8.

Sample B: With sample B the c-axis was along the cylinder axis, making the geometry amenable to a calculation of the demagnetization factor for the field-traverse case (yielding $n_{\perp} = 0.410$) and therefore for the measurement of H_{\perp} . Here we made the ellipsoidal approximation, which should be valid since the weaker shielding currents are flowing along the length of the cylinder, where the largest fields exist, and the conventional demagnetization correction applies. The data are presented in Figure 9, where we see a 4.2 K H_{\perp} of 340 Oe, which although higher than most of the literature data, is not outside its range.

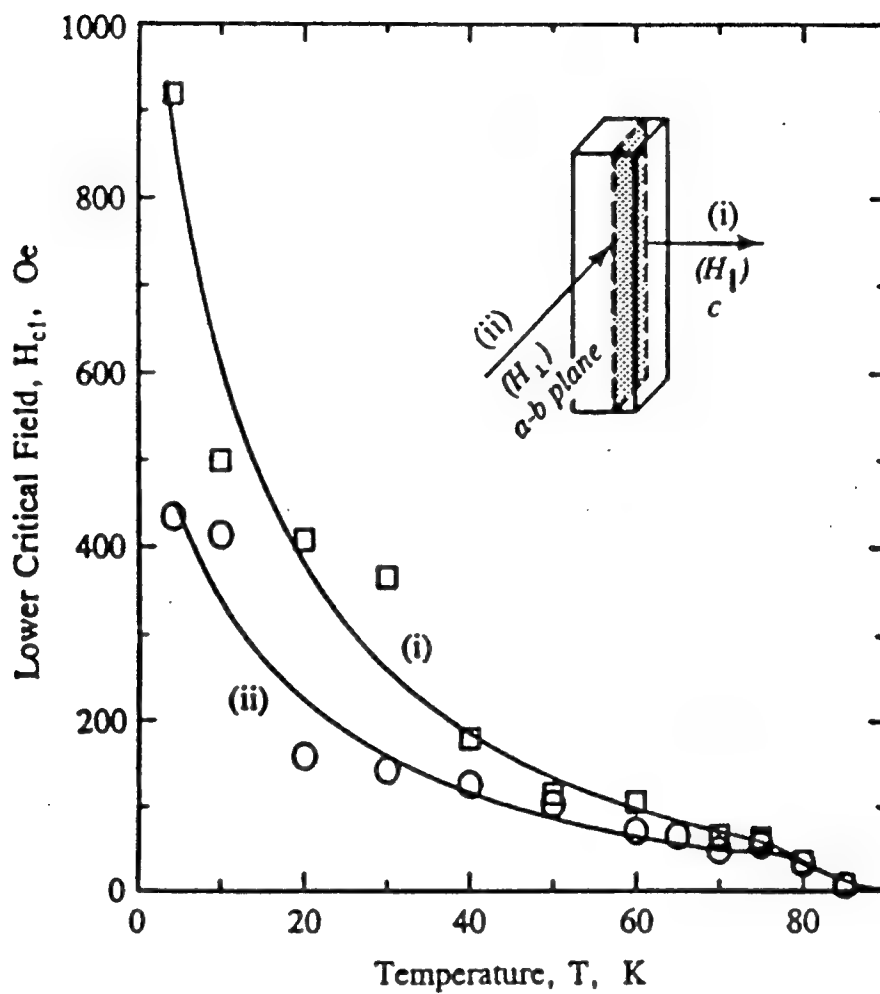


Figure 8. H_{c1} versus T for sample A in the H_{\parallel} (i) and the H_{\perp} (ii) orientations, both corrected for demagnetization.

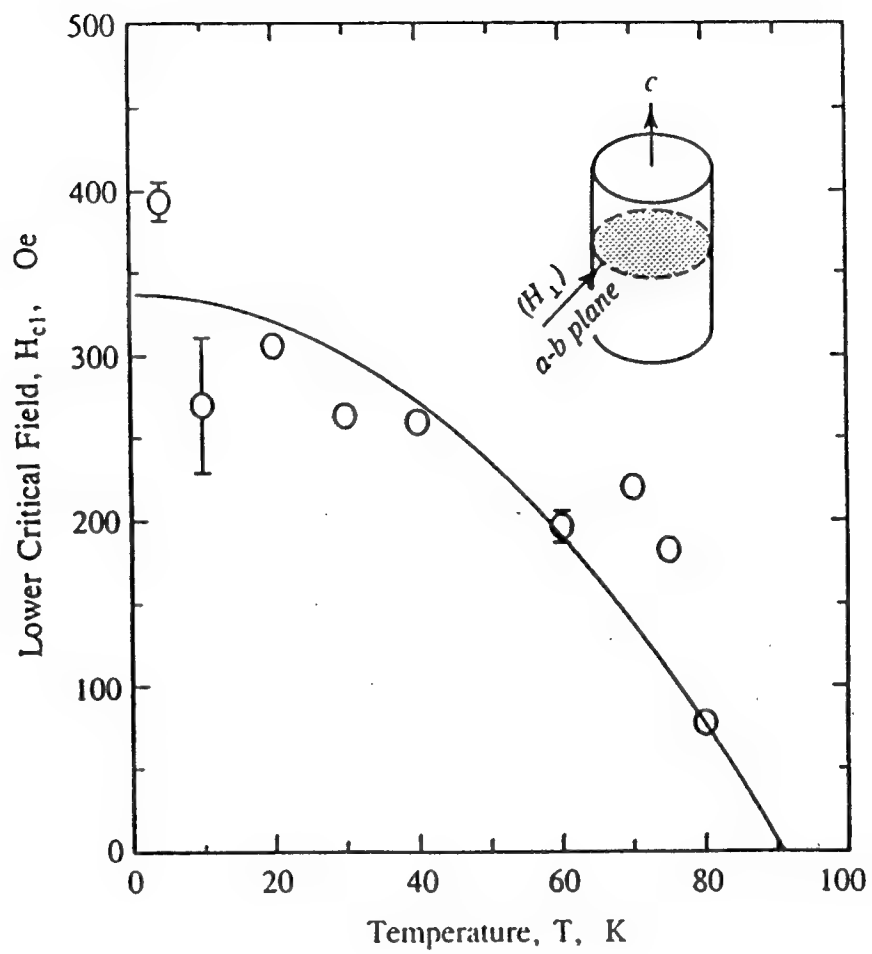


Figure 9. H_{c1} versus T for sample B in the H_{\perp} orientation, corrected for demagnetization.

SUPERCONDUCTIVE DEVICE REQUIREMENTS AND DESIGNS

A. Clamping Force Measurements.

1. Axial Clamping Force

Clamping force measurements of YBCO single crystals were performed using a calibrated linearized load cell. Clamping force was measured as a function of displacement, load, speed and applied field strength and pattern. A schematic diagram of the experimental set-up for the axial clamping force measurements is shown in Figure 10.

The reported clamping force and pressure data is for zero field cooled measurements at 77K. The applied field was provided by a series of cylindrical Nd-Fe-B permanent magnets (0.138-1 inch diameter) with fields at the magnet surface ranging from 3000-5500 Gauss. Force measurements were also performed on multi-grain samples with average grain size of 0.25 inches.

Figure 11 shows the clamping force results for a 1 inch diameter single crystal sample as a function of applied field. These results are for a load displacement rate of 0.5 mm/hour where no significant flux creep was observed. As predicted by theoretical model, the force increased proportionally with increased applied magnetic field. For a large single crystal sample, the clamping force is limited by the availability of permanent magnets with field strengths of only few kilogauss. However, the resulting clamping pressures of about 35 psi (Figure 12) may be adequate for some clamping applications.

Multi-grain samples with average grain size of 0.25 inches were evaluated as potential candidate for magnetic clamps. Figure 13 shows a clamping pressure for a 1.5x1.5 inch multi-grain sample. As expected, the clamping pressure decreased with increased magnetic field strength and field size. The pressure is higher for the small diameter magnets (Magnet #1 with $D=0.138$ " and Magnet #2 with $D=0.25$ ") where the magnets induce screening currents within a single grain of the multi-grain sample. As the magnet size and field increases, the resulting clamping pressure decreases to less than 5 psi due to low intergranular current density. The highest clamping pressure for the multi-grain sample was 7.5 psi. That is five times lower than for a typical single grain YBCO sample, as seen in Figure 14. The clamping pressure of a single grain sample is limited by the availability of stronger permanent magnets, whereas the multi-grain sample is saturated with a medium strength magnet.

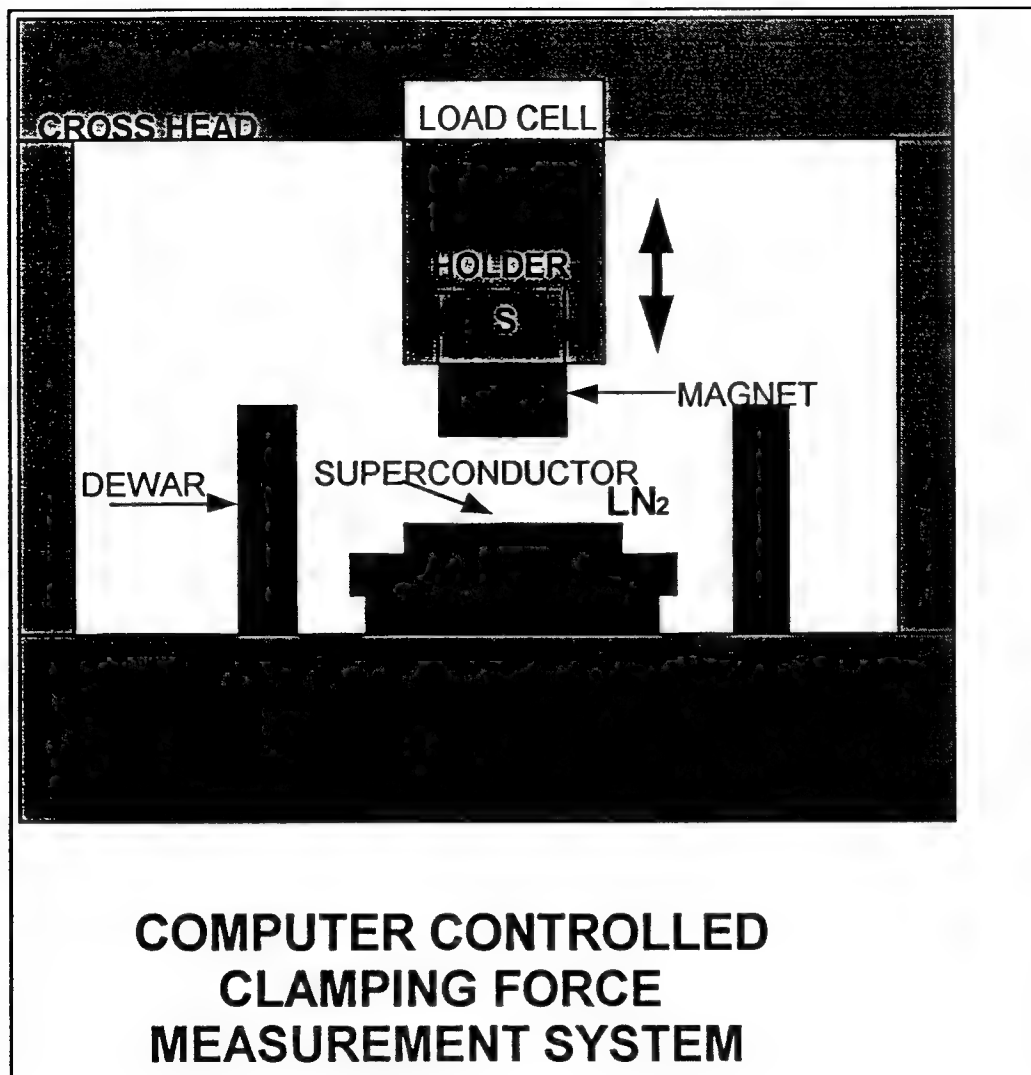


Figure 10. A schematic diagram of a computer controlled axial clamping force measurement system.

- ◆ Magnet #1
B(0)=3000G
- ▲ Magnet #2
B(0)=4200G
- Magnet #3
B(0)=4500G
- Magnet #4
B(0)=4450G
- Magnet #5
B(0)=5000G

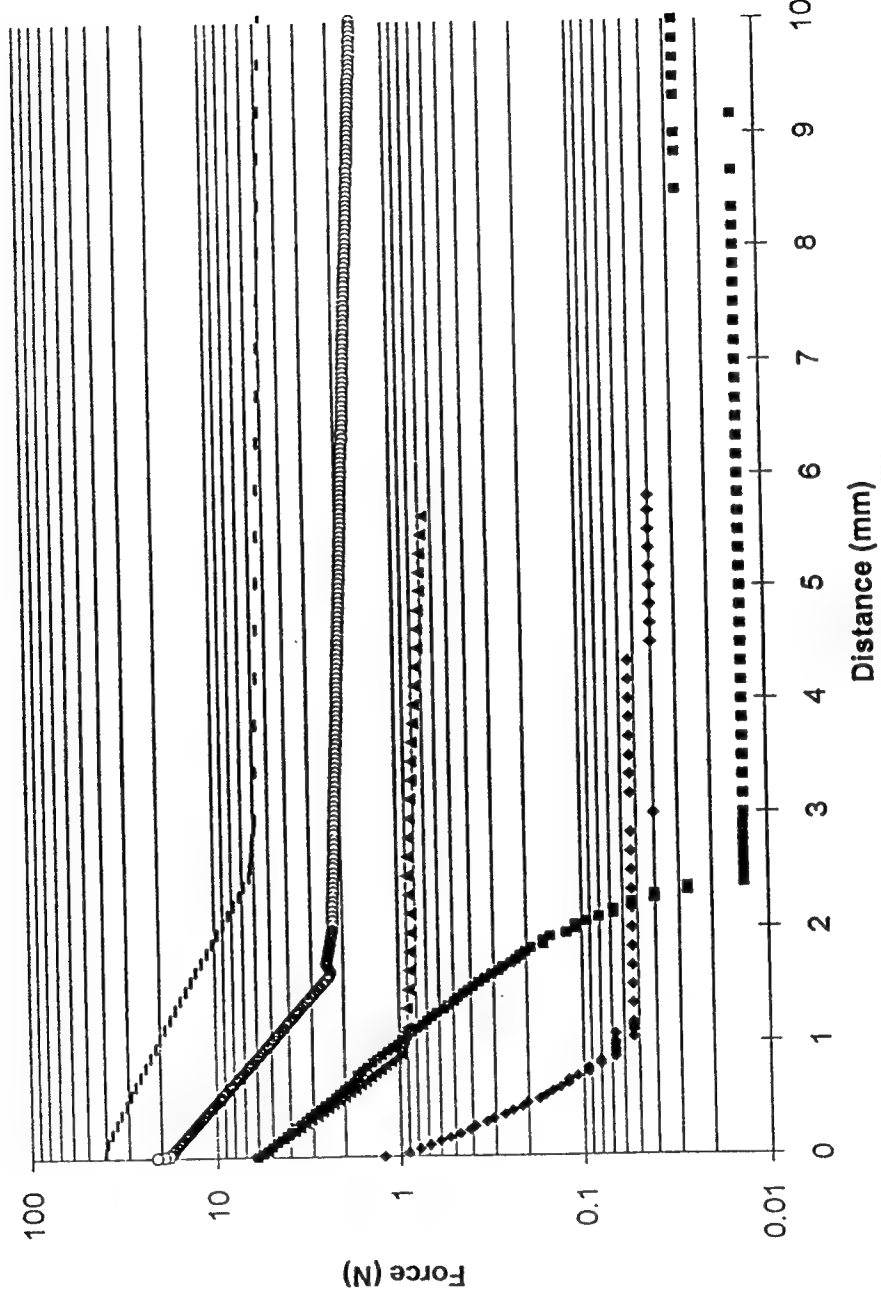


Figure 11. Axial clamping force of a 1 inch diameter single crystal sample as a function of applied field.

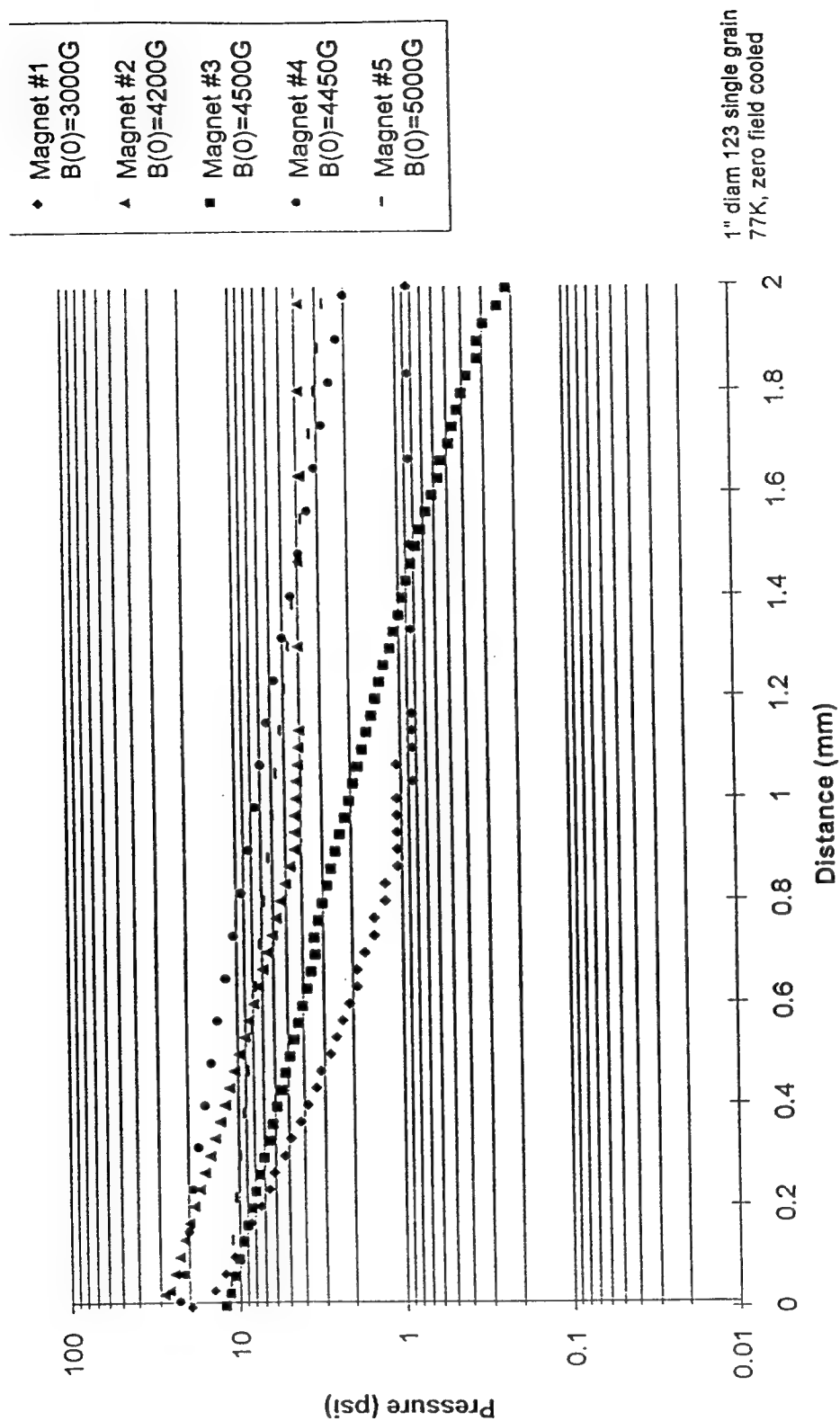


Figure 12. Axial clamping pressure of a 1 inch diameter single crystal sample as a function of applied field.

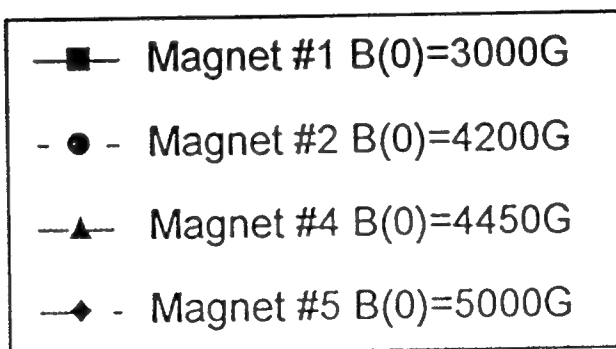
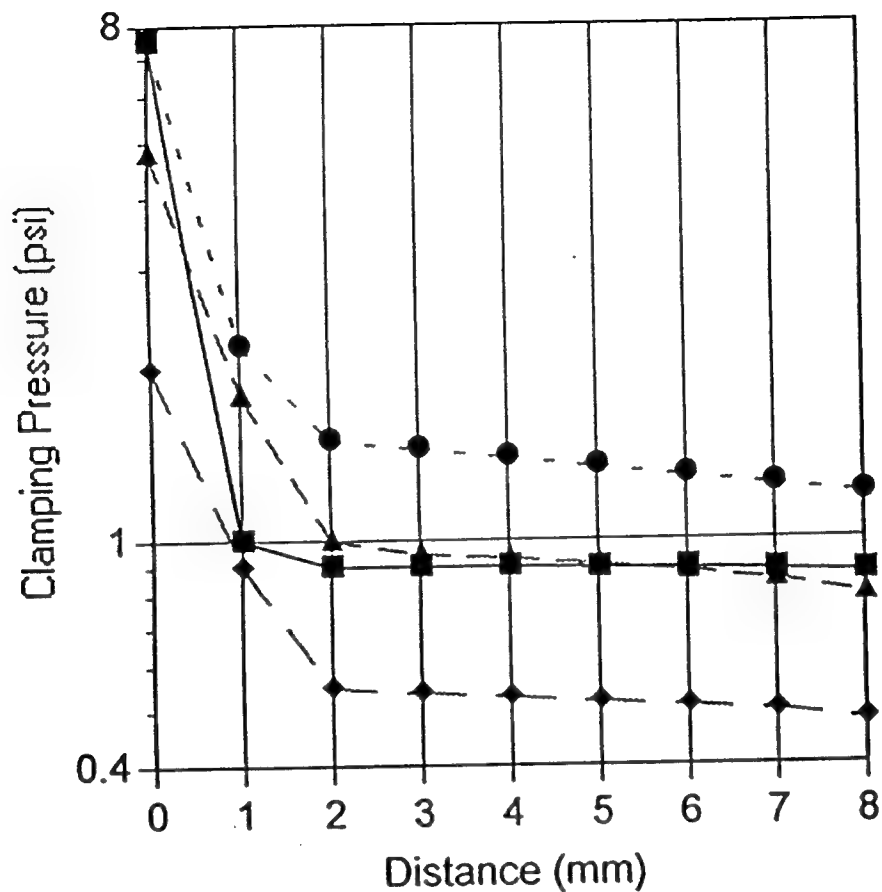


Figure 13. Axial clamping pressure of a 1.5" x 1.5" multi-grain sample as a function of applied field.

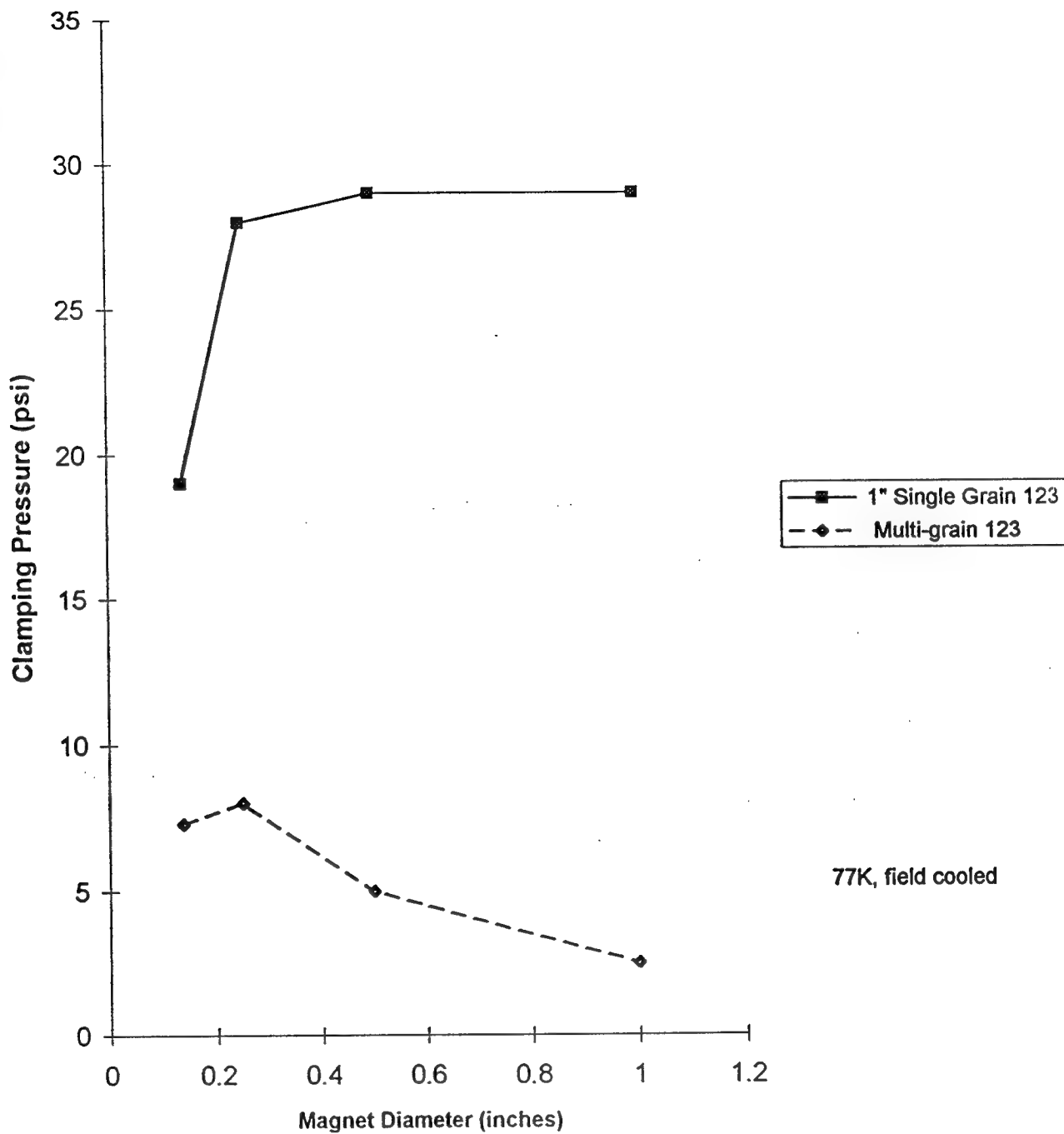


Figure 14. Axial clamping pressure comparison for a single crystal and multi-grain YBCO sample as a function of applied field.

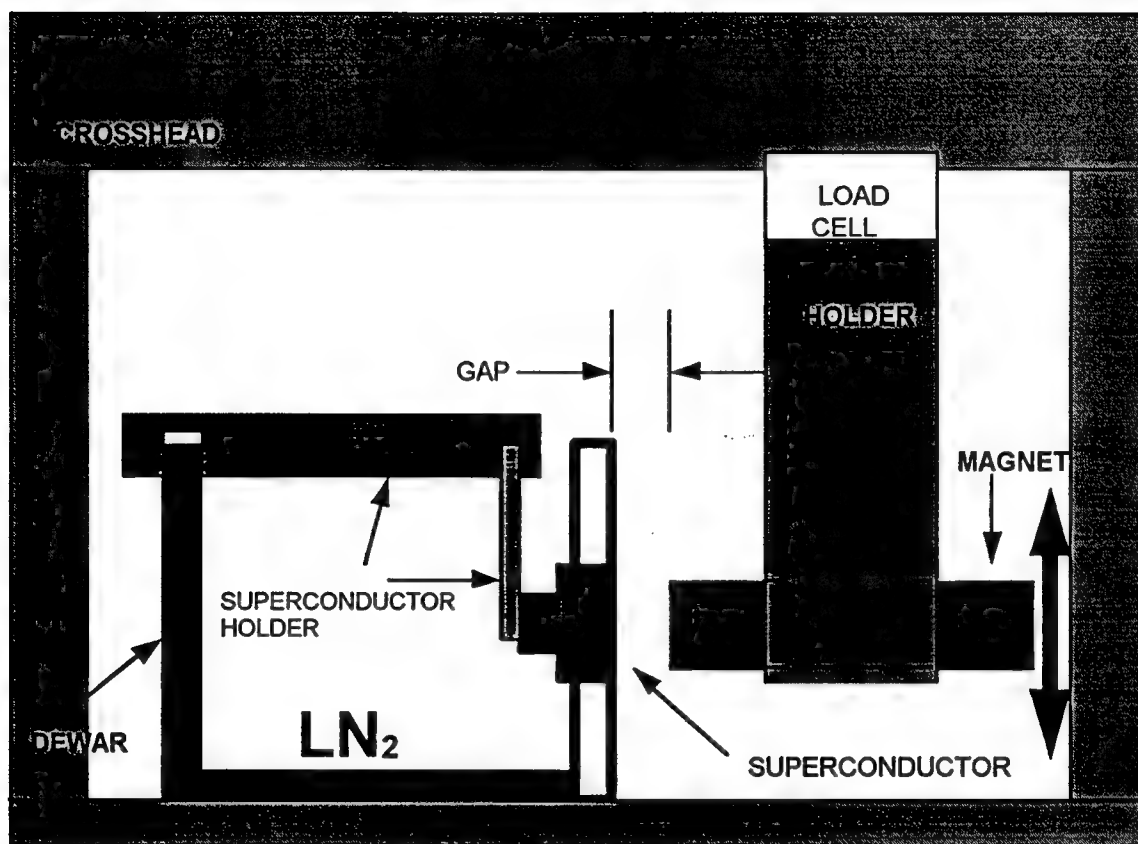
2. Lateral Clamping Force Measurements.

Lateral clamping force measurements were performed on large single-grain and multi-grain samples as a function of horizontal displacement, load speed, and applied field strength and pattern. A schematic diagram of the experimental set-up for the lateral clamping force measurement is shown in Figure 15.

The reported lateral clamping force data are from field cooled measurements at 77K and 4 mm magnet/superconductor gap. The applied field was provided by a series of permanent magnets as in the axial clamping force experiments.

Lateral clamping force for the single-grain and multi-grain sample is shown in Figure 16 as a function of horizontal displacement across the sample. The sample sizes were same as in the axial clamping force measurement. The lateral clamping force achieved in a multi-grain sample was 1.5 N/mm and 20 N/mm in a single crystal sample. The low lateral clamping force in the multi-grain sample is mainly attributed to the significantly lower intergranular current density in an applied magnetic field present at the 4 mm gap during the field cooled experiment. The current density and flux pinning in the single crystal sample is sufficiently high, thus resulting in large uniform, and symmetrical lateral clamping force across the whole grain.

The lateral clamping force of the single crystal sample is limited by the strength and size of the permanent magnet used. Increased thickness of the single grain will not necessarily yield larger restoring force unless the current density or sample diameter is increased. Figure 17 shows the relationship of lateral clamping force as a function of magnet size for both types of bulk superconductors. As evident from the relationship, larger and stronger magnets are necessary to improve the clamping force in the large single crystal YBCO monolith.



COMPUTER CONTROLLED LATERAL CLAMPING FORCE MEASUREMENT SYSTEM

Figure 15. A schematic diagram of a computer controlled lateral clamping force measurement system.

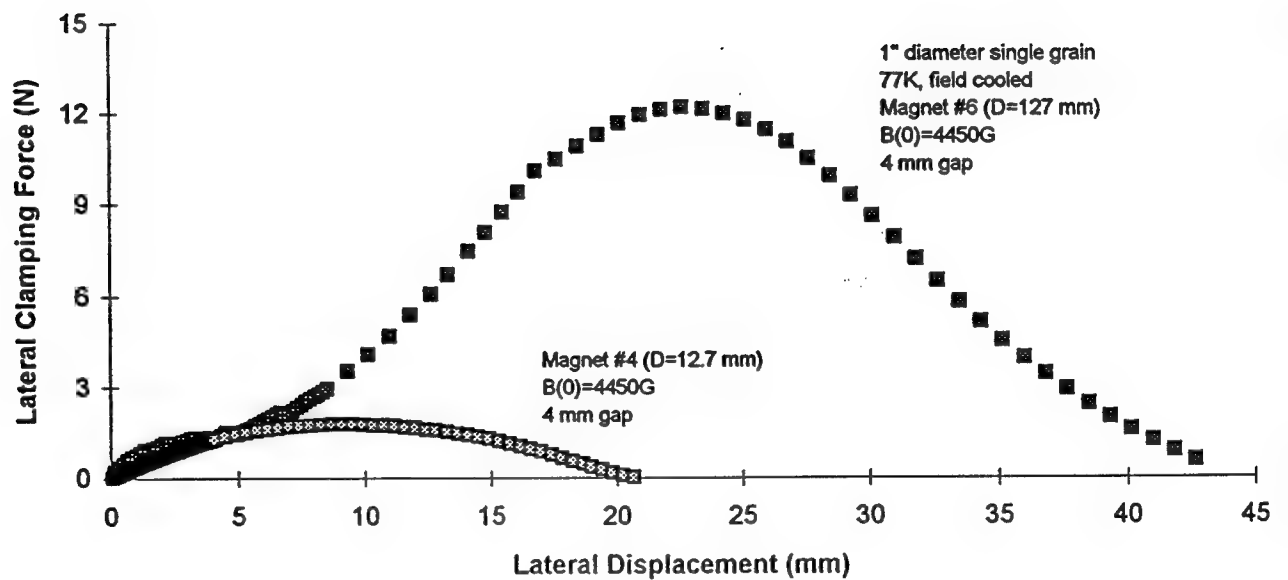


Figure 16. Lateral clamping force of a 1 inch diameter single crystal and 1.5"x1.5" multi-grain sample as a function of horizontal displacement.

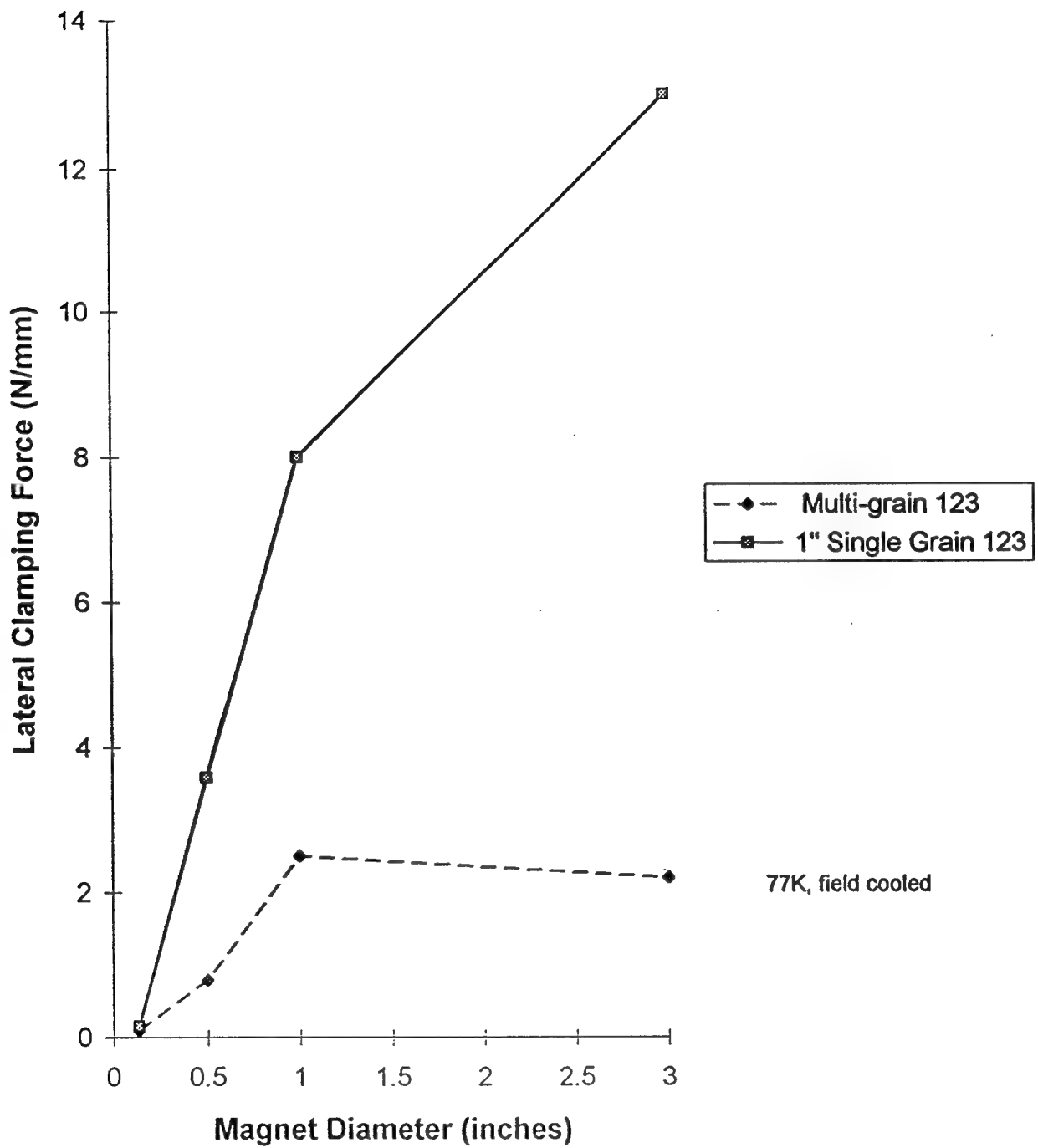


Figure 17. Lateral clamping force of a 1 inch diameter single crystal and 1.5" x 1.5" multi-grain sample as a function of magnet size.

B. Prototype High-Temperature Superconductor Clamps in Laser Cutting Operation

Prototype high-temperature superconducting flux-trap magnet clamps were used for clamping aircraft part during laser cutting demonstration.

Figure 18 shows a 1500 watt carbon dioxide industrial laser with Boeing 737 tool for cutting stainless steel cockpit cabin window reinforcement panel out of a solid sheet of metal. The strengthening part is placed inboard of the outer-skin peripheral to the aircraft cockpit area. The standard manufacturing practice for holding the metal panel to the tool during laser cutting is with either shop-vacuum clamps or with cleco clamps. Shop-vacuum clamps have proven difficult to work with because of low lateral clamping force capability of vacuum. In addition, the part must mate very accurately with the underlying tool for the procedure to work at all. When cleco clamps are used to hold the part to be cut, tabs must be provided around the border of the tool and a part so the cleco clamps can be attached. These tabs have to be removed in a separate operation to finish the cutting operation.

Figures 19-20 show a part that has just been cut after being held in place by two self contained high-temperature superconducting flux-trap magnet clamps. The portable clamps contain a sufficient supply of liquid nitrogen for the duration of most laser cutting operations of small production parts. The handle seen at the top of the superconducting clamp in Figure 19 is a part of a mechanical insertion mechanism of a high permeability metal core into a superconducting cylinder (see Figures 21-22 for a schematic diagram and a disassembled picture of a portable superconducting clamp). This metal core greatly increases the clamping force of the superconducting clamp as well as provide means for clamping strength adjustment. Figure 23 shows a usable trapped magnetic field in a single crystal superconductor with and without using the high permeability metal core.

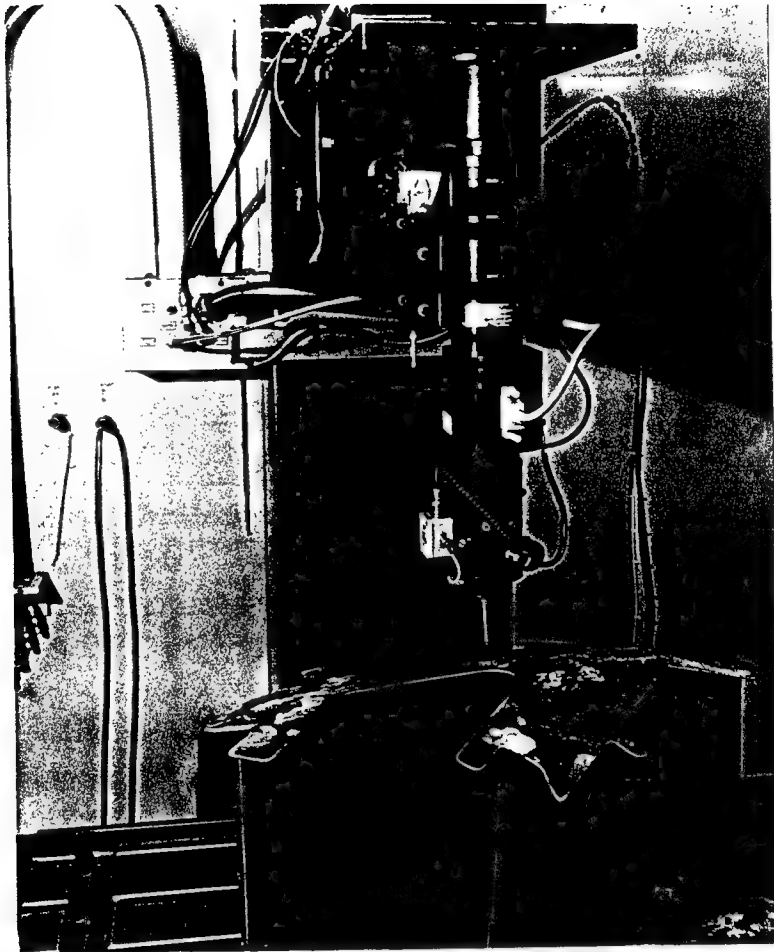


Figure 18. 1500 watt carbon dioxide industrial laser, with a Boeing 737 tool for cutting out stainless steel cockpit cabin window reinforcement panel.

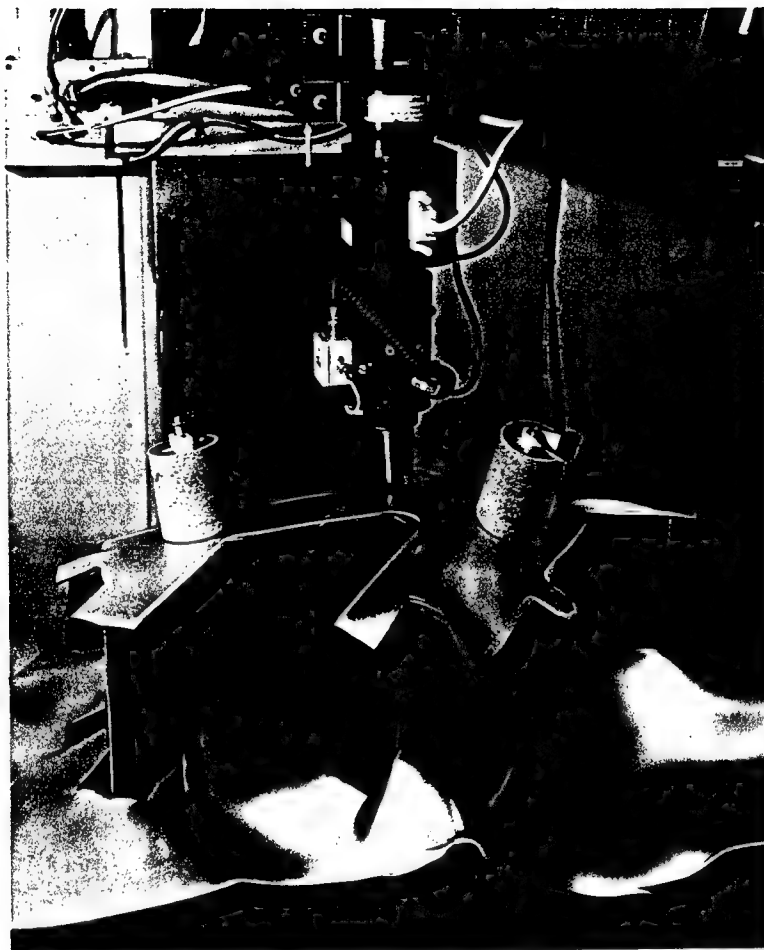


Figure 19. Boeing 737 part being held in place by portable superconducting clamps during a laser cutting operation.



Figure 20. The laser-cut Boeing 737 part after removal of superconducting clamps.

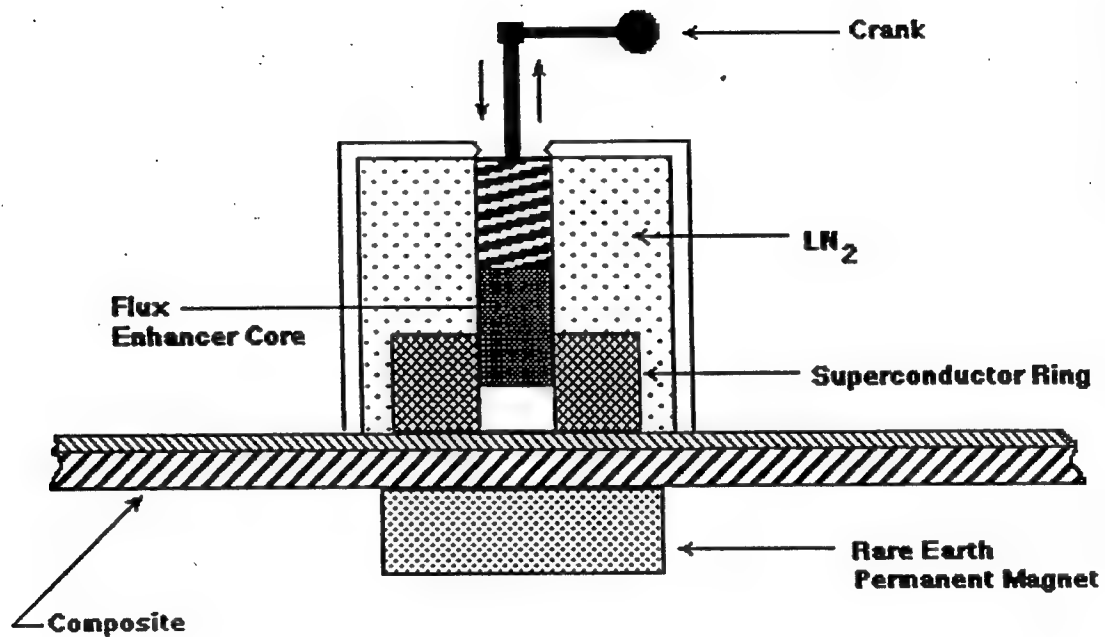


Figure 21. Schematic operational diagram of a portable superconducting flux-trap magnet clamp with a flux-enhancing core.

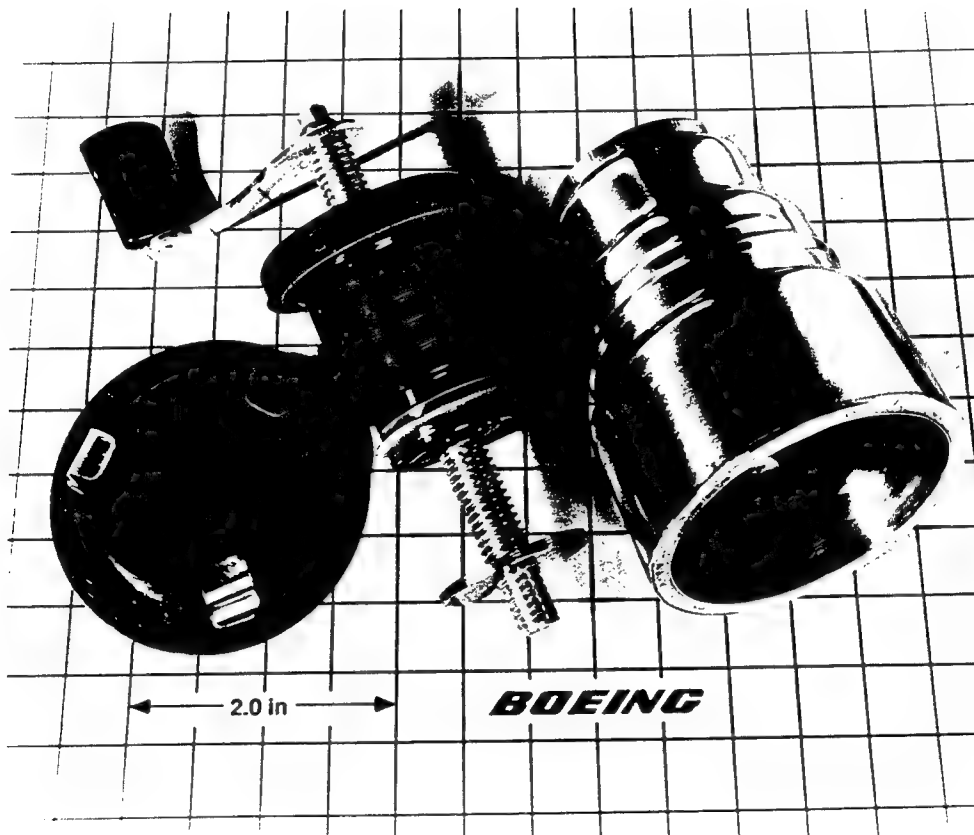


Figure 22. Dismantled portable superconductor clamp.

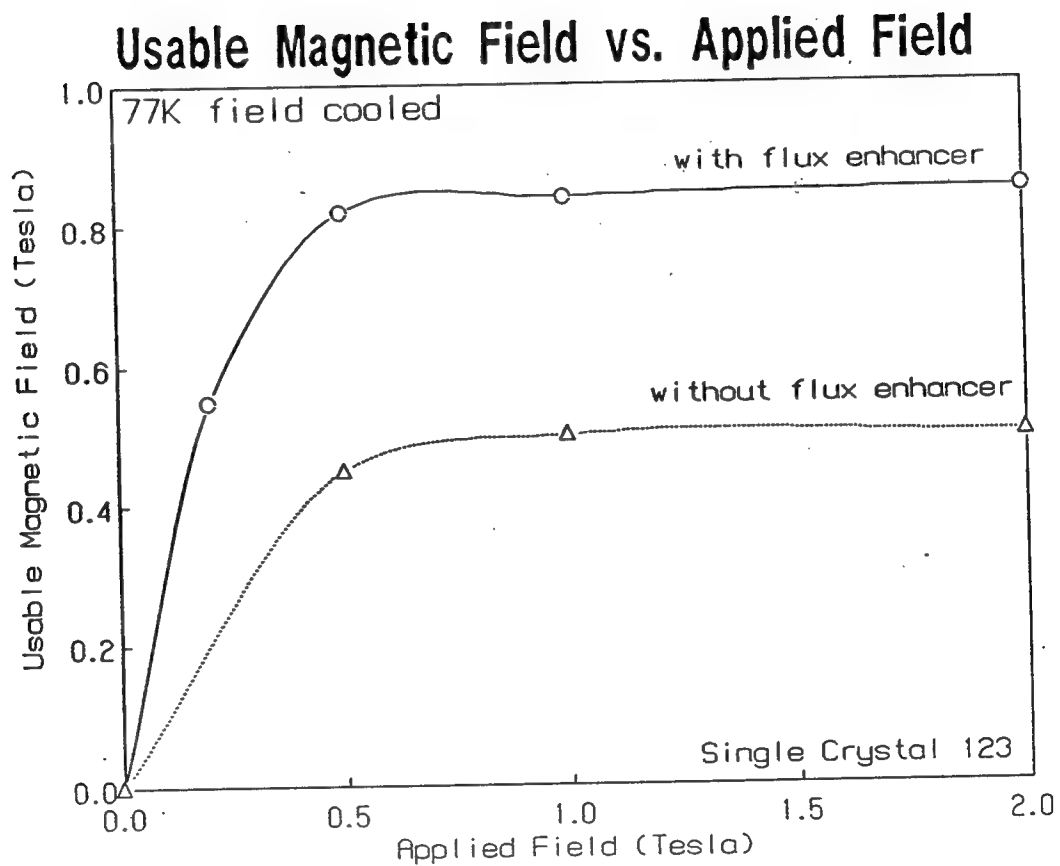


Figure 23. Usable magnetic field as a function of applied field of a superconducting flux-trap magnet clamp with and without the high-permeability metal core.

C. High-Temperature Superconducting Clamp with Joule-Thompson Cryostat.

A miniature Joule-Thompson cryostat was assembled with a portable non-magnetic dewar that can house up to a one inch diameter superconductor single crystal (Figure 24). The unit was built to Boeing specifications by R.G.HANSEN & Associates of Santa Barbara, California. The clamp will cool a twenty-one-gram crystal from ambient temperature to 77.9K in less than seven minutes. Linear scale-up is possible for superconductors larger than two inches in diameter.

The clamp is cooled by a miniature Joule-Thompson cryostat powered by high-pressure high-purity nitrogen gas. The nitrogen gas is supplied via a small diameter stainless steel feed tube visible as a dark line exiting the rear of the device (on the display stand in Figures 25-26). Connected to a reservoir of pressurized gas a whole battery of superconducting clamps could all be powered at once, such as for adaptive tooling applications. For completely portable operation a small gas bottle can be fitted directly to the cryostat clamp assembly (Figure 26). Such clamp systems can be operated in any attitude or position, including upside-down.

To turn the superconducting clamp off, the gas supply is shut-off or suddenly reduced with an expansion valve. With the gas supply turned off the flux-trap superconductor will slowly warm to above its transition temperature of 93 K (~1-4 minutes, depending on the heat-loss characteristics of the specific device), and the magnetic field will collapse as the supercurrents cease. The cryostat can then be pressurized by nitrogen gas to allow the device to remain in the "ready" mode. This procedure will greatly reduce the time required for the next cool-down period, and will minimize the thermal shock to the ceramic superconductor by maintaining a very low ΔT during thermal cycling. An alternate method of warming the superconductor is to rapidly drop the pressure to the cryostat via an expansion valve configured into the device. By using the reverse Joule-Thompson effect, heat is released directly at the cold-finger assembly.

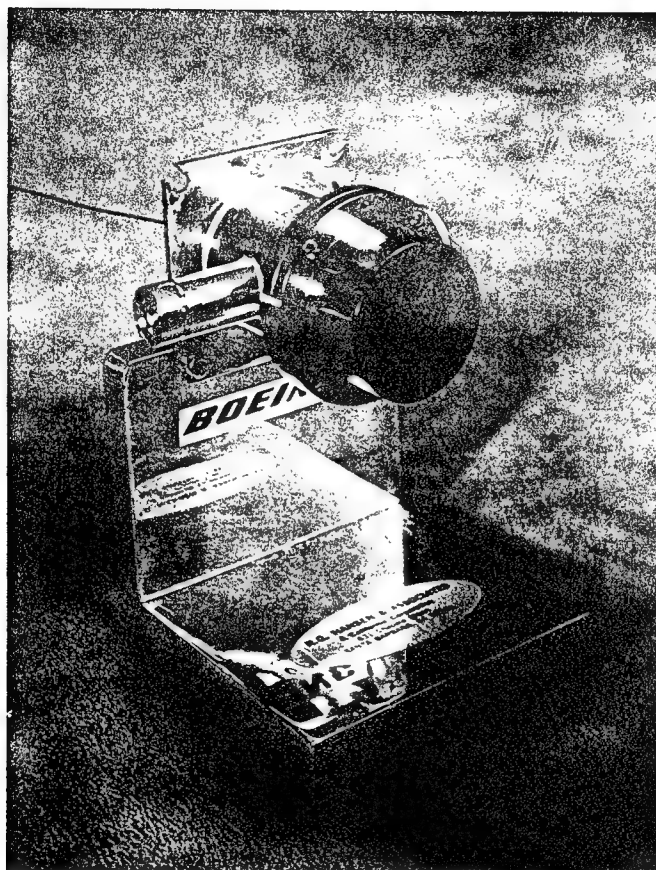


Figure 24. A high-temperature superconducting flux-trap magnet clamp with Joule-Thompson cryostat.

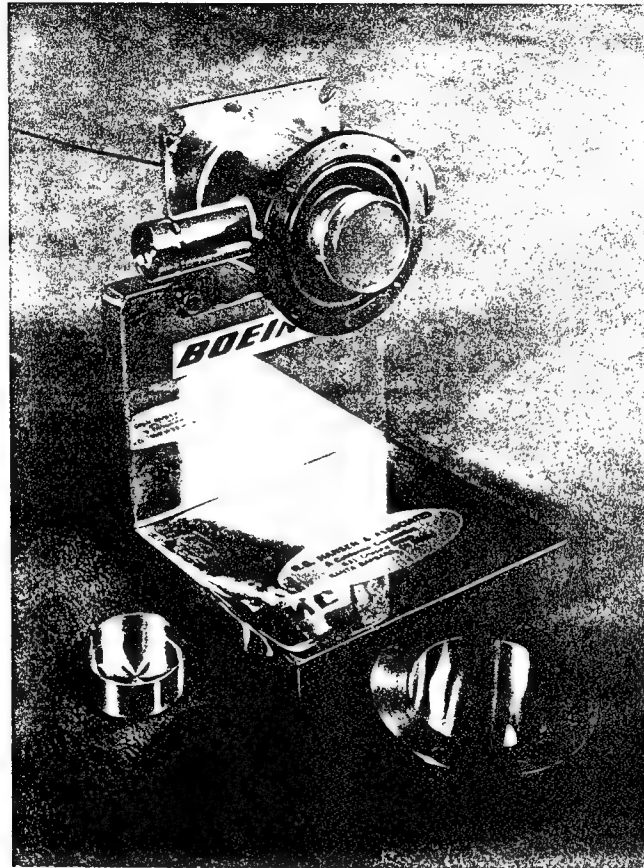


Figure 25. Disassembled superconductor clamp mounted on display stand, showing 1" diameter superconductor disk in left foreground.

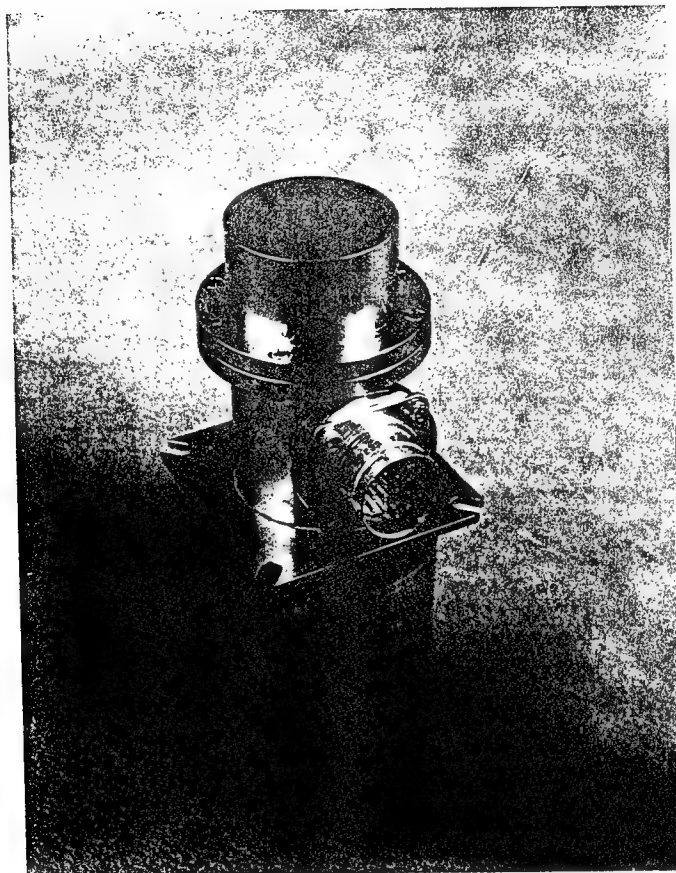


Figure 26. Integral superconducting clamp, Joule-Thompson cryostat, and liquid nitrogen dewar assembly.

The views and conclusions contained in this document are those of the authors and should not be interpreted as necessarily representing the official policies or endorsements, either expressed or implied, of the Advanced Research Projects Agency or the U.S. Government

**PROCESSING, FABRICATION, CHARACTERIZATION
AND DEVICE DEMONSTRATION OF HIGH
TEMPERATURE SUPERCONDUCTING CERAMICS**

Contract No. F49620-90-C-0079

ANNUAL TECHNICAL REPORT

October 1, 1992 - August 14, 1993

Submitted by:

Boeing Defense & Space Group

Sponsored by:

Advanced Research Projects Agency

ARPA Order No. 7476

Monitored by:

AFOSR Under Contract No. F49620-90-C-0079

PM: Dr. Thomas S. Luhman
(206) 773-1991

PI's: Dr. Thomas S. Luhman
(206) 773-1991

Dr. Ilhan A. Aksay
(609) 258-4393

TABLE OF CONTENTS

PROGRAM OBJECTIVE	1
PROGRAM DESCRIPTION	1
SUMMARY	1
MILESTONE SCHEDULE	2
TECHNICAL RESULTS	3
MATERIALS SYNTHESIS AND CHARACTERIZATION	3
SmBa ₂ Cu ₃ O _{7-x} Seeds	3
A. Melt Texturing	3
B. Iso-thermal Seed Growth	3
YBa ₂ Cu ₃ O _{7-x} Monoliths	4
A. Oxygen Anneal Cycle	4
B. Vacuum Assisted Seeding	5
C. Neutron Back-Scattering	7
SUPERCONDUCTIVE DEVICE REQUIREMENTS AND DESIGNS	10
A. Portable Flux-Trap Superconductor Clamp	10
B. Adaptive Tooling	17

PROGRAM OBJECTIVE

To develop material processes and engineering designs for high current applications of $\text{YBa}_2\text{Cu}_3\text{O}_{7-x}$

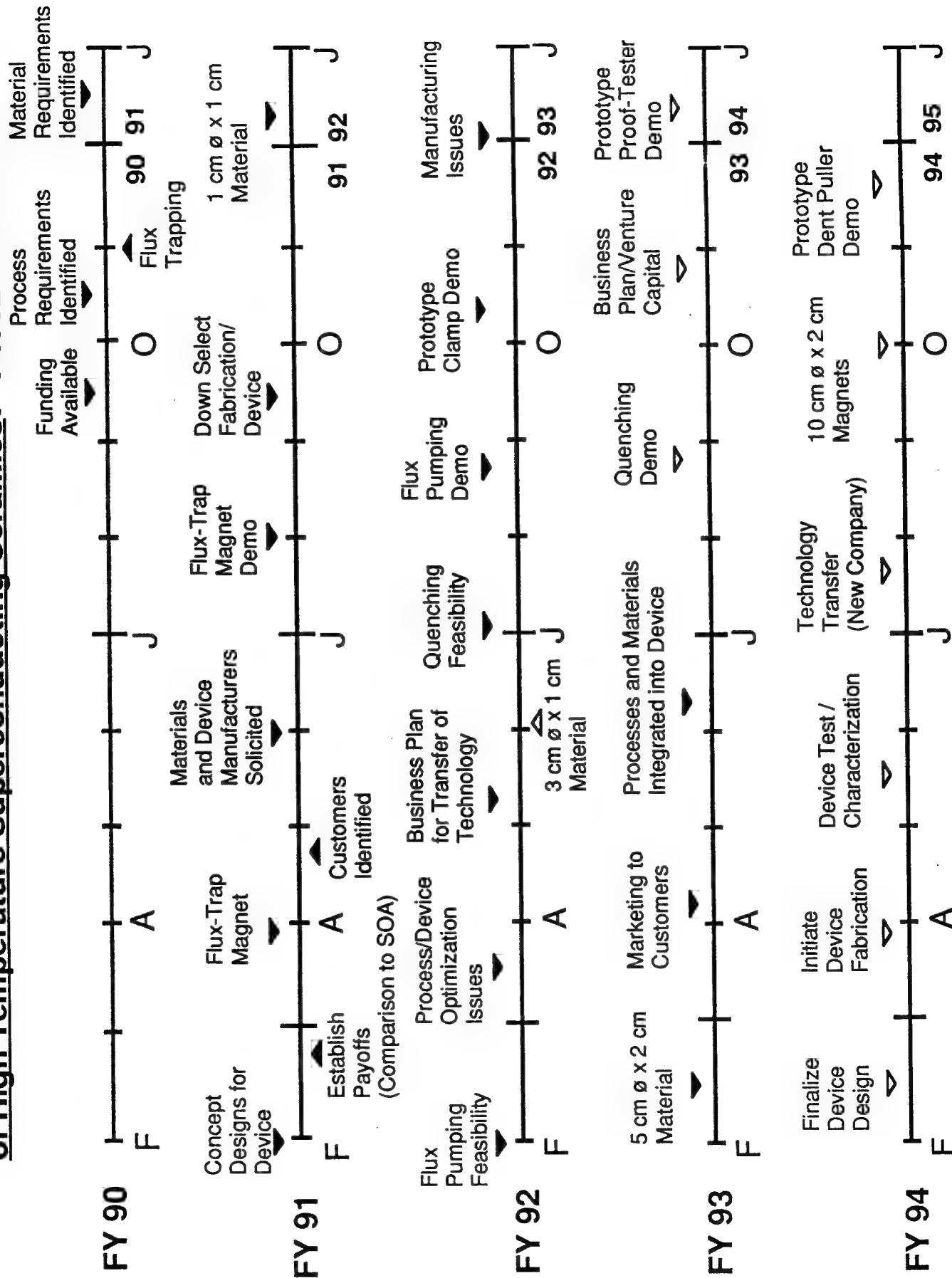
PROGRAM DESCRIPTION

The goals of our program are to (1) focus on engineering designs and demonstration of flux-trap magnets; (2) develop improved processing and fabrication methods to enhance current densities in strong magnetic fields; (3) optimize processes for grain alignment in bulk and tape samples; and (4) provide a technology base for utilization of flux-trap magnets.

SUMMARY

- a) Several prototype high temperature superconductor clamps incorporating magnetic flux enhancement mechanisms have been fabricated for ARPA's annual review in Washington D.C.
- b) Adaptive tooling is one of the latest applications incorporating high temperature superconductor flux-trap magnets. They consist of a number of different possible configurations, the essence of which is that the superconductor flux-trap magnet "device head" conforms or adjusts to the surface being clamped. Such tooling will greatly enhance Boeing products through increased manufacturing flexibility, reduced non-recurring tooling costs, rapid prototyping, and faster introduction of new product lines.
- c) Melt texturing process for producing large samarium barium copper oxide 123 "seed" crystals has been improved. Denser and less porous samples have been grown in a process that saves 130 hours of furnace time.
- d) Improvements in processing 123 bulk material has consisted of "vacuum assisted" placement of samarium 123 seed crystals of the proper crystallographic orientation onto both solid-state and melt-quenched pellets. In addition, multiple seeds have been placed on and within pellets in an attempt to grow thicker grains.
- e) Oxygen-anneal cycle for 123 samples has been improved by lowering the process temperature, while maintaining or increasing the overall soak duration.
- f) Neutron back-scattering experiments confirm orientation of a-b plane and c axis of large single crystal 123 samples.

Processing, Fabrication, Characterization and Device Demonstration of High Temperature Superconducting Ceramics: F49620-90-c-0079



TECHNICAL RESULTS

MATERIALS SYNTHESIS AND CHARACTERIZATION

$\text{SmBa}_2\text{Cu}_3\text{O}_{7-x}$ Seeds

A. Melt Texturing

The seeding of solutions or melts during solidification is a well known process to grow large single crystals. The seeds are usually single crystals of the same material or other materials with the same crystal structure. In our work, we used $\text{SmBa}_2\text{Cu}_3\text{O}_{7-x}$ (SBCO) as seed because it has the same lattice parameters as YBCO. Due to the higher melting temperature of SBCO ($\sim 1060^\circ\text{C}$) in comparison to YBCO ($\sim 1006^\circ\text{C}$), the melt growth of 123 can be carried out in an intermediate temperature range.

Previous large grained SBCO samples were prepared by melt texturing in a temperature gradient. From these bulk samples single crystals were extracted, and then cleaved into thin (less than 1mm thick) coupons anywhere from 1mm square to about 16mm square.

B. Iso-thermal Seed Growth

An easier approach, and one that is sufficient for growing seed quality SBCO crystals is to maintain an iso-thermal condition across the entire diameter of the sample in the $1050\text{--}1100^\circ\text{C}$ range. The most recent preparation schedule consists of crystal growth at 1100°C for shorter times.

The new schedule still uses a five gram pellet that has been uniaxially pressed at 35,000 PSI, and then isostatically pressed at 25,000 PSI. The sample is placed in a Harrop two inch diameter tube furnace, with no temperature gradient, and 250 cm^3 of air flow. The new SBCO schedule reduces the furnace bake time by approximately 130 hours. SBCO crystals are cleaved from the pellet along the 001 plane along which the material easily parts.

YBa₂Cu₃O_{7-x} Monoliths

A. Oxygen Anneal Cycle

In an attempt to reduce cracking introduced during the oxygen anneal process of YBCO crystals, a reduction in furnace temperature was investigated. The furnace setpoint was reduced in increments of approximately 50°C, and after each cycle, magnetic flux-trapping experiments were performed. From the peak magnetic field reading (in the center of the grain if flawless), the J_c of the sample could be calculated. J_c was the criterion chosen for evaluating the effectiveness of the anneal temperature as it is only "material" dependent. The maximum trapped magnetic field as measured on the surface of a sample with a Hall effect probe in the middle of a grain, is dependent not only upon the material properties but also upon the thickness and diameter of the specimen.

The formula used for computing J_c from the measured trapped field intensity and physical dimensions of the YBCO disk is:

$$J_c = \frac{Bc}{2\pi t \ln \frac{a + \sqrt{a^2 + t^2}}{t^2}}$$

where; J_c = current carrying capacity

B = measured trapped magnetic field

t = thickness of disk

a = radius of disk

c and π are constants of proportionality

It is based upon the Biot-Savart law and the Bean model of superconductivity. Results indicated that magnetic flux trapping and J_c are maximized at an anneal temperature of ~425°C. This lower temperature (previously we used ~600°C), not only improves sample J_c but in addition enhances overall physical characteristics by reducing internal porosity and magnitude and frequency of micro-cracking. The complete schedule is: 60°C/HR to 425°C and hold for two hours; then reduce temperature by 0.5°C/HR until 400°C is reached; then drop 30°C/HR to 23°C ambient. It is believed that the enhanced properties of the YBCO pellets are a result of reduced thermal stresses incurred by the 150-175°C lower oxygen anneal temperature. The duration of the

cycle is 72 hours (3 days) for 1" diameter disks by approximately 1/4" thick. However, the thorough annealing may take as long as several months (or more) for crystals 2"-3" in diameter and up to about 1/2" in thickness.

B. Vacuum Assisted Seeding

A method of placing the SBCO single crystal seed coupon upon the YBCO pellet has been developed which shortens the time for "pellet activation" prior to grain growth. The method consists of using a vacuum line connected to a small vacuum pump to securely hold a SBCO seed crystal at the end of an alumina thermocouple rod. The apparatus also consists of a hand switch which allows the vacuum to be turned off at the proper moment to release the SBCO seed. In operation the procedure is to bring the 123 YBCO pellet made from melt quenched powder to well above the melting point of the SBCO seed, which is still outside of the furnace hot zone. This high soak temperature allows the melt quenched powder of the pellet (which consisted of BaCu_2O_2 and Y_2O_3 phases) to form a refined and uniformly dispersed 211 in a barium cuprate-copper oxide liquid phase. After the 1 hour soak the temperature of the furnace is dropped to the temperature of crystal growth in approximately 15 minutes. Then the probe holding the SBCO seed via vacuum is brought down to the surface of the pellet. The seed is then released, and the alumina tube withdrawn. The temperature of the seed is held at 1030-1050°C for 6 minutes, and then lowered at the rate of 20-30°C/HR until about 1000°C is reached.

Figure 1 shows a Crystals Specialties Inc. high temperature superconductor crystal growing furnace. This furnace is located in a class 100 clean room facility. The clean room environment was found to be a necessary requirement in large single crystal growth for the prevention of multiple crystal nucleation sites due to impurities on the sample surface. The atmosphere and thermal conditions are computer controlled parameters with a very high degree of accuracy and reproducibility. Infrared video cameras are used to monitor the crystal growth process. The crystal growing facility can accommodate samples up to 5.5" in diameter and up to 18" long, depending on the required geometry.

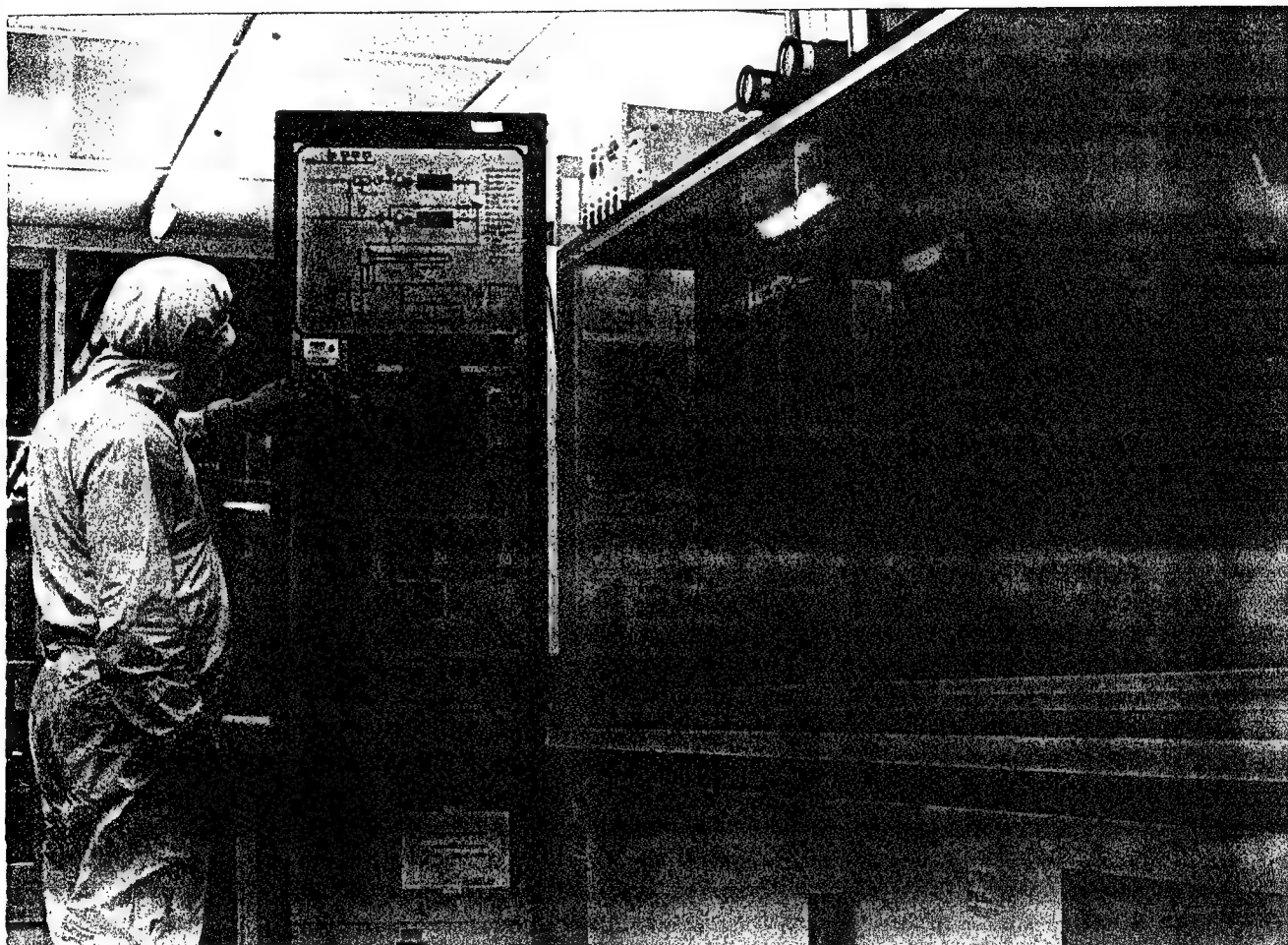


Figure 1. Crystal Specialties Inc. crystal growing furnace in the class 100 clean room.

C. Neutron Back-Scattering

A variety of experimental techniques have been applied in order to investigate the dynamic vortex correlation in high temperature superconducting materials. In contrast to surface imaging techniques, such as decoration with magnetic particles or scanning tunneling microscopy, neutron scattering is sensitive to the entire length of the vortices in the bulk of the material. Neutron scattering measurements can be performed in a magnetic field range of ~ 0.05 to up to several Tesla, a theoretically interesting regime in which the vortices interact strongly. The success of our experiments depended critically on the preparation of a large, high quality single crystal.

The neutron scattering experiments were initiated by B. Keimer at the Princeton University Physics Department and conducted at the Cold Neutron Research Facility of the National Institute of Standards and Technology. The crystal was oriented by x-ray and neutron diffraction and attached to the cold finger of a closed cycle helium refrigerator. The refrigerator was then mounted in an electromagnet capable of achieving fields up to 0.5T. After scattering from the sample, the neutrons were collected by area detector about 15m behind the sample.

Figure 2 reveals the scattering data taken from two different samples which are expected to be a single crystal. One of the samples is identified as a bi-crystal with a tilt angle of ~ 2 degrees. We assume that the seed which was imbedded in the center of the sample was imperfect in terms of its top and bottom (almost parallel planes) surfaces and this led to the formation of two slightly tilted crystals. This shows that bulk characterization of the samples by neutron scattering gives valuable microstructural information. Combination of both transmission electron microscopy and neutron scattering techniques results in a full picture of the interrelation between microstructure and the vortex state in high temperature superconductors.

We are now conducting experiments in order to find a correlation between twinning structure and neutron scattering data. This will enable us to understand flux-pinning mechanisms for development of materials with high flux-trapping properties. Figure 3 is a iso-magnetic contour flux plot of a YBCO disk clearly showing the establishment of circulating currents representing the high trapped fields.

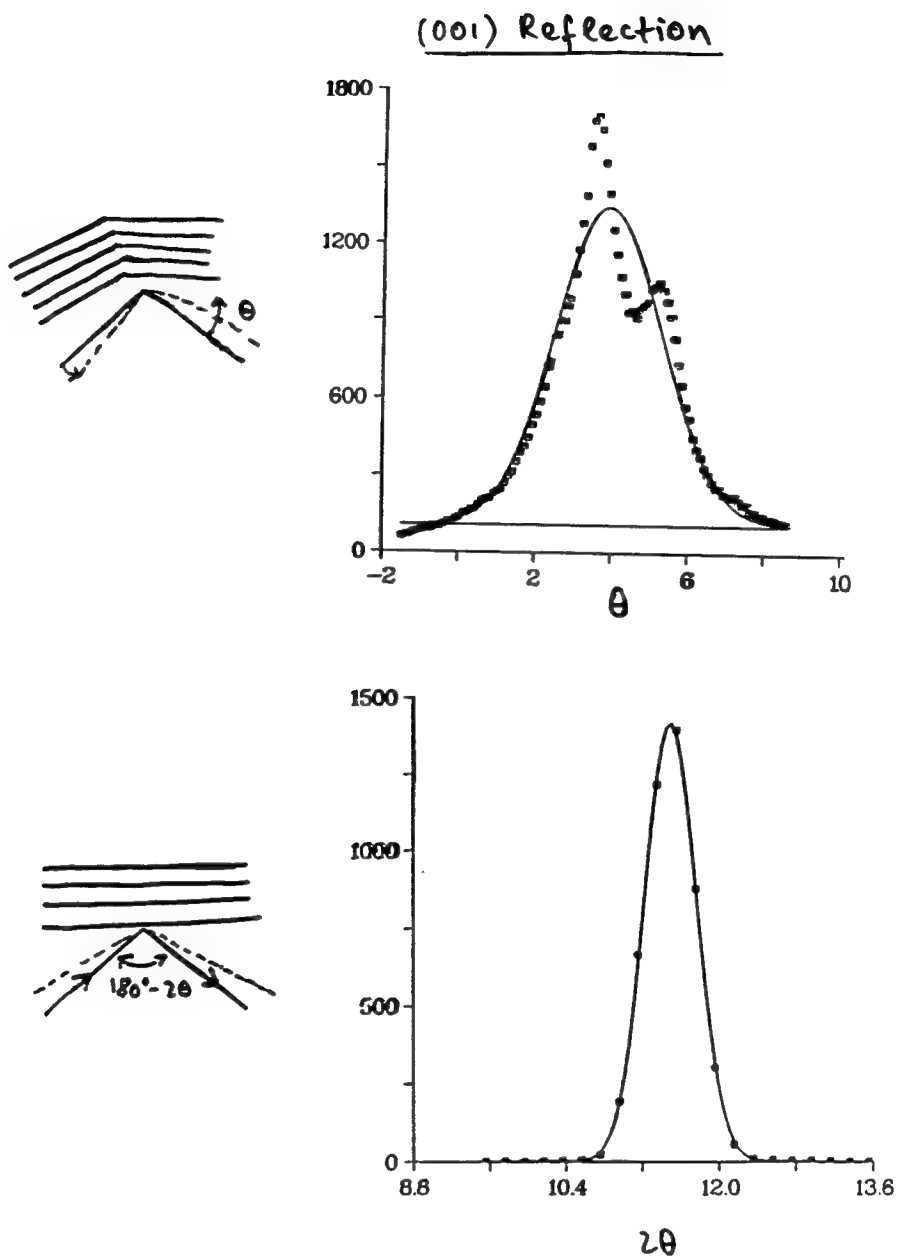


Figure 2. Neutron scattering data taken from two different samples which are expected to be a single crystal.

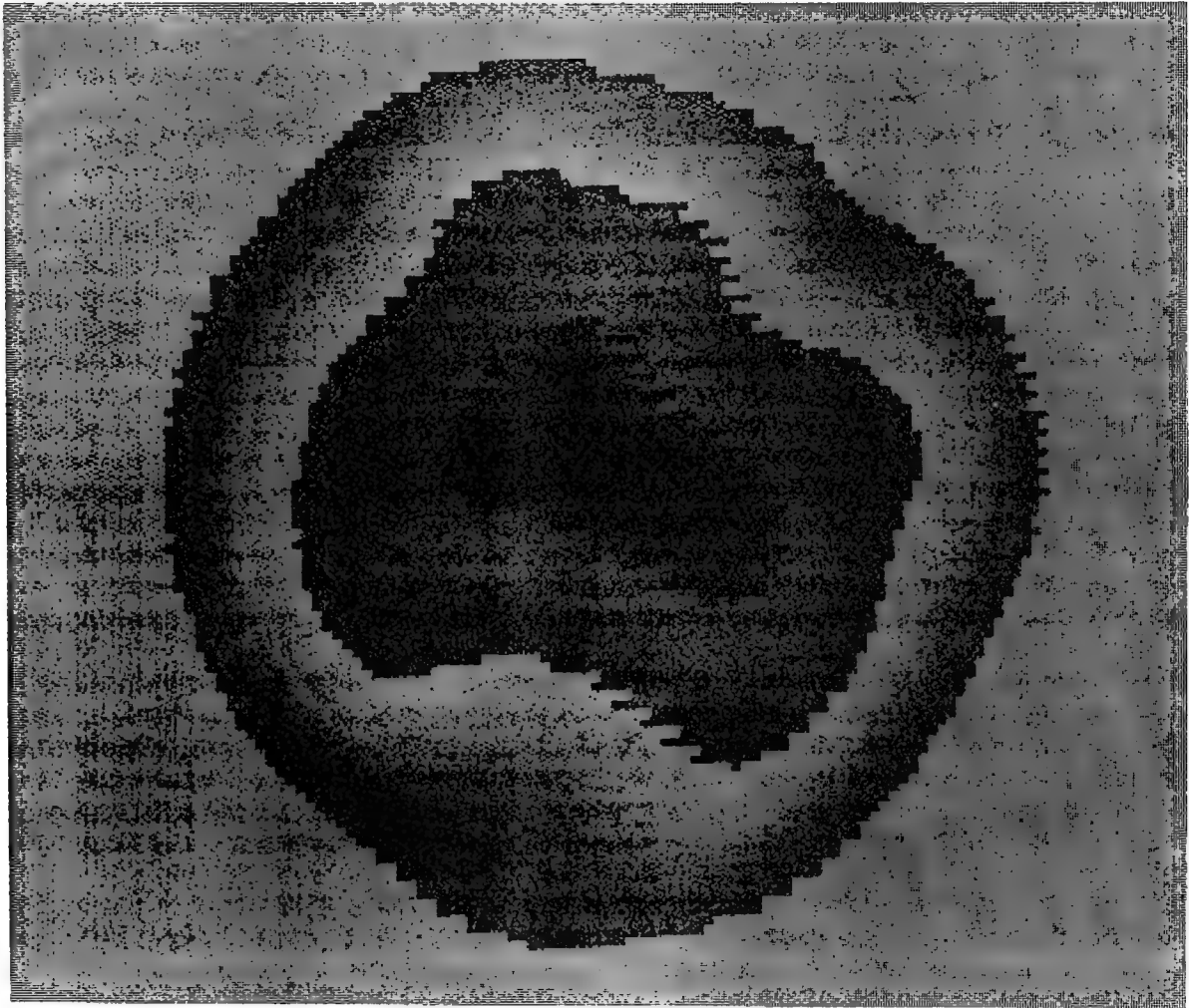


Figure 3. Iso-magnetic contour flux plot of trapped magnetic field in a YBCO disk.

SUPERCONDUCTIVE DEVICE REQUIREMENTS AND DESIGNS

A. Portable Flux-Trap Superconductor Clamp

Permanent magnets find wide use and great diversity in attracting and holding ferromagnetic objects and in clamping non-magnetic objects and assemblies during manufacturing. Permanent magnets are frequently the only feasible way of holding objects in confined areas during fabrication. Besides permanent magnets, large electromagnetic clamps and chucks are being used. In addition to magnetic methods of clamping, vacuum technology is extensively used throughout the manufacturing industry.

High temperature superconductors (HTS) can be magnetically charged by placing them in an applied magnetic field (such as inside a solenoid or in the magnetic field of a permanent magnet), and cooling with liquid nitrogen or a cryocooler below the superconducting transition temperature (92K). By properly orienting polarities and careful design of the magnetic circuit return path (with soft iron, etc.) powerful clamping devices can be configured much as can be done with conventional permanent magnets, such as alnico, samarium-cobalt, or neodymium-iron-boron. However, the magnetic field in the HTS superconductor is far greater than in conventional magnetic materials. Figure 4 shows a comparison between superconducting and permanent magnet clamps. The operational advantage of superconductors is that the magnetic force can be turned off when desired, by warming it up to a temperature above its transition point. Some of the advantages of the superconducting clamp are as follows:

- 1) flux-trap superconducting magnets achieve significantly higher field density (clamping force) as compared to rare earth monolithic permanent magnet (conventional monolithic permanent magnets supply a maximum field of 5000 gauss) Figure 5 shows measured clamp and release forces of existing permanent magnet clamps
- 2) flux-trap superconducting magnets display significantly reduced size and weight as compared to conventional electromagnets
- 3) flux-trap superconducting magnets operate without electrical leads, field windings, or magnet power supplies thus resulting in the simplified design, manufacture, and portability of the superconducting clamp device
- 4) magnetic field of the flux-trap superconducting magnet clamps can be turned off on command, thus releasing the powerful clamping force without need for any mechanical release mechanism

Figures 6a and 6b show a schematic view, and an actual working model of a portable flux-trap superconductor clamp device, revealing the operation of the flux-enhancer core. Figure 7. shows a number of actual working portable superconductor clamp devices made for annual technical review at ARPA's Washington D.C. office. Figure 8 shows a superconductor clamp with a neodymium-iron-boron permanent magnet clamping an actual part.

Comparison of Superconducting vs. Electromagnetic and Permanent Magnet Clamp

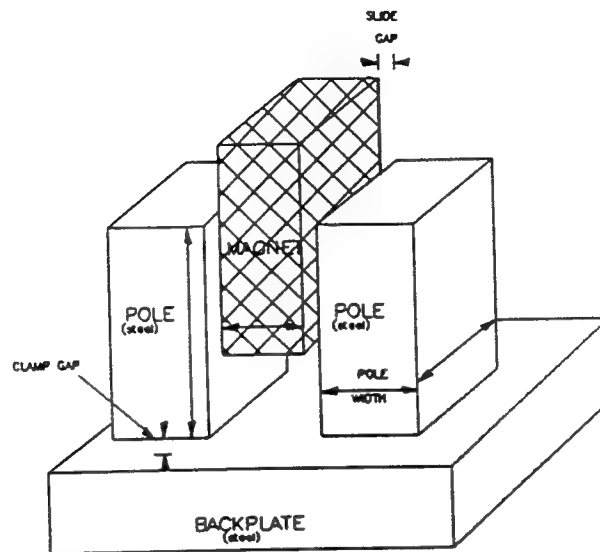
	Permanent Magnet	Electromagnetic	Superconducting
Safety	Relatively Safe	Very Dangerous High Amps; High Voltage	Very Safe
Size	Small	Large, Bulky Very Heavy	Small Lightweight
Portability	No Attached Air Hoses	No Attached Power Cables	Yes
Capital Cost	Approx. \$2K	Approx. \$20-100K	Unknown
Operational Cost	Small	Very Large Due to Large Resistance Losses in Cu Wires	Minimal - No Losses Cryogen Cost
Clamping Force	Very Low Force Required to Remove Clamp	Large	Extremely Large
Reproducibility	Poor Damage to Surrounding Areas	Good	Good
Miscellaneous	Magnetic Field Cannot be Turned Off - Accidental Attachement to Other Parts	Heat Build-Up Due to Resistance in Cu Coil	Magnetic Field Can be Turned Off

Figure 4. A comparison between superconducting and permanent magnet clamps.

Existing Technology

Permanent Magnet Clamp

BASIC CLAMP MODEL



MEASURED CLAMP AND RELEASE FORCES

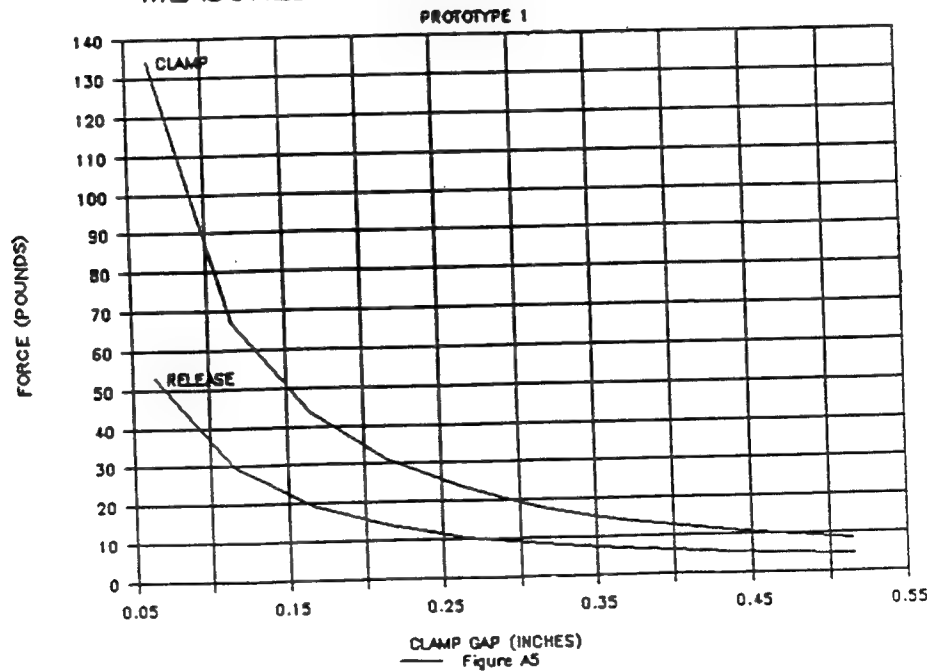


Figure 5. Measured clamp and release forces of existing permanent magnet clamps.

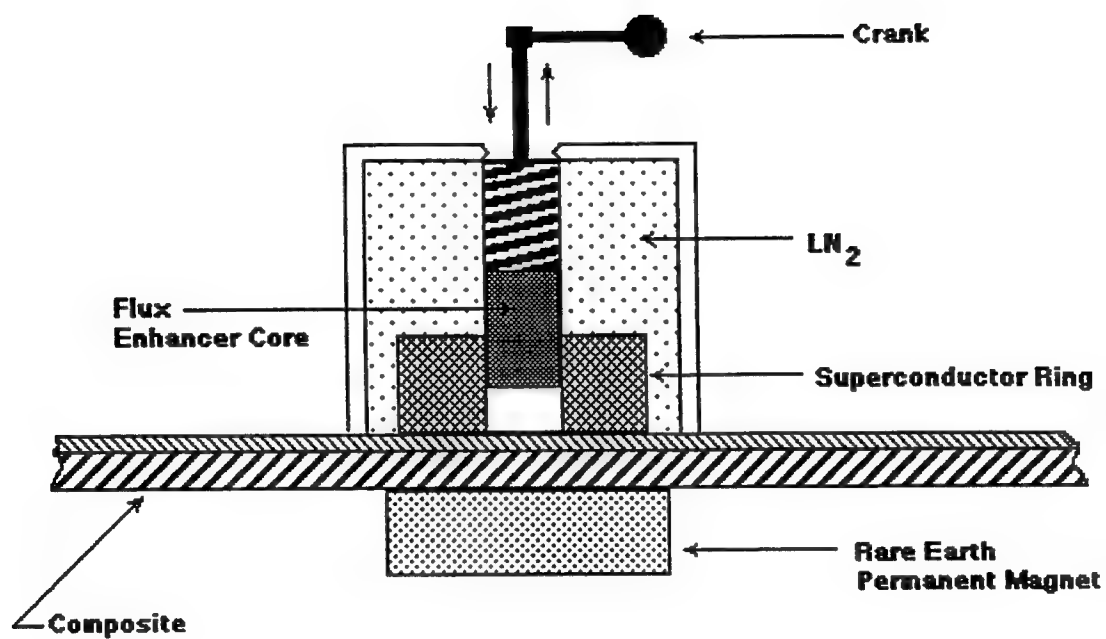


Figure 6a. Schematic operational diagram of portable flux-trap superconductor clamp device with a flux-enhancing core.

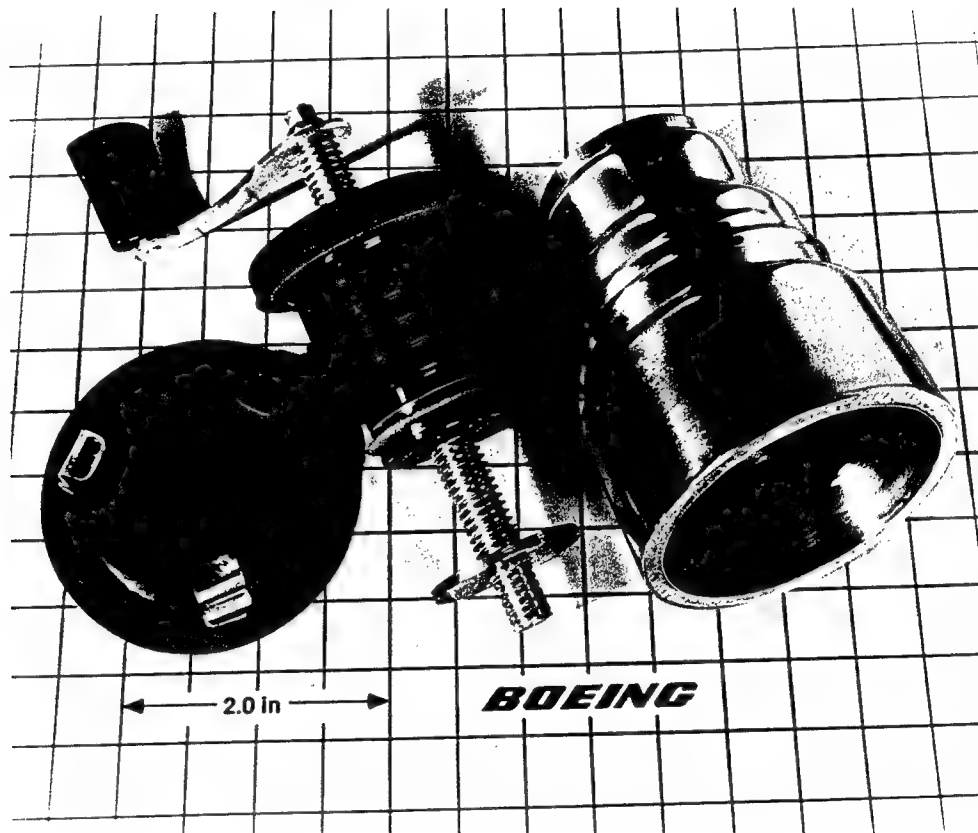


Figure 6b. Dismantled portable flux-trap superconductor clamp device.



Figure 7. Several models of superconductor flux-trap magnet clamps.

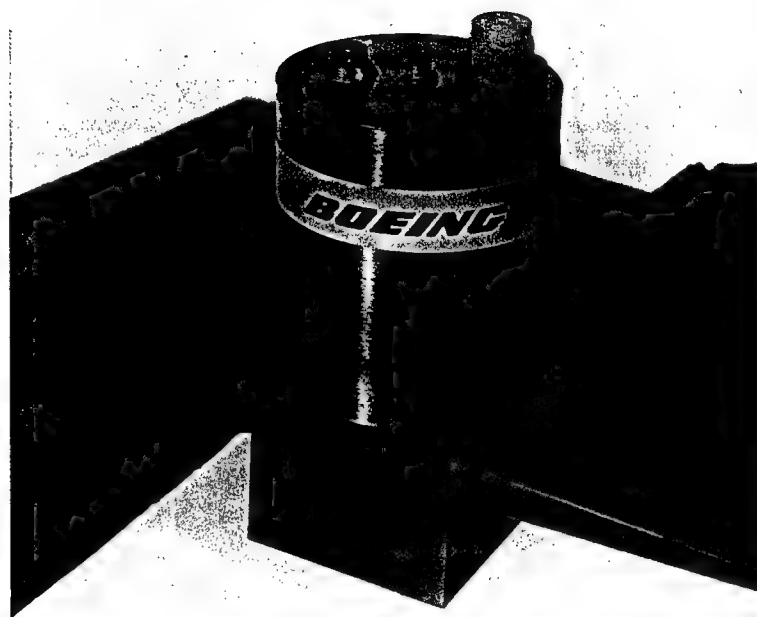


Figure 8. Superconductor clamp coupled with a permanent magnet, clamping an actual part.

B. Adaptive Tooling

Non-recurring tooling costs are a significant fraction of total development cost. Over 25,000 separate tools will be required for the manufacture of the new Boeing 777 airplane. To minimize tooling costs, superconductive adaptive clamp tools are being designed to secure parts during aerospace manufacturing operations.

Figure 9 shows an application for the removal of a buckle during composite structure subassembly with superconductive clamps. Conventional approaches are severely limited by clamping forces and versatility. Figure 10 depicts a superconductor magnet array and a flexible permanent magnet element. The use of high temperature superconductive adaptive clamps enables greater clamping forces and will greatly enhance versatility and significantly decrease costs. These clamps have the potential to increase global competitiveness of all of heavy industry, including auto manufacturing and shipbuilding. Figures 11 and 12 show schematics for proposed superconductive adaptive clamp tools incorporating the following: (1) adaptive tooling concept using high temperature superconducting flux-trap magnet arrays coupled with rare earth permanent magnets; (2) superconducting magnets that will conform to various shaped parts by raising or lowering the individual magnets within an array; (4) superconducting magnets that can be cooled by conventional portable cryocoolers or with liquid nitrogen dewars; (5) superconducting magnet units that can be part of a cryocooled working table on which the working pieces are attached for processing or assembly.

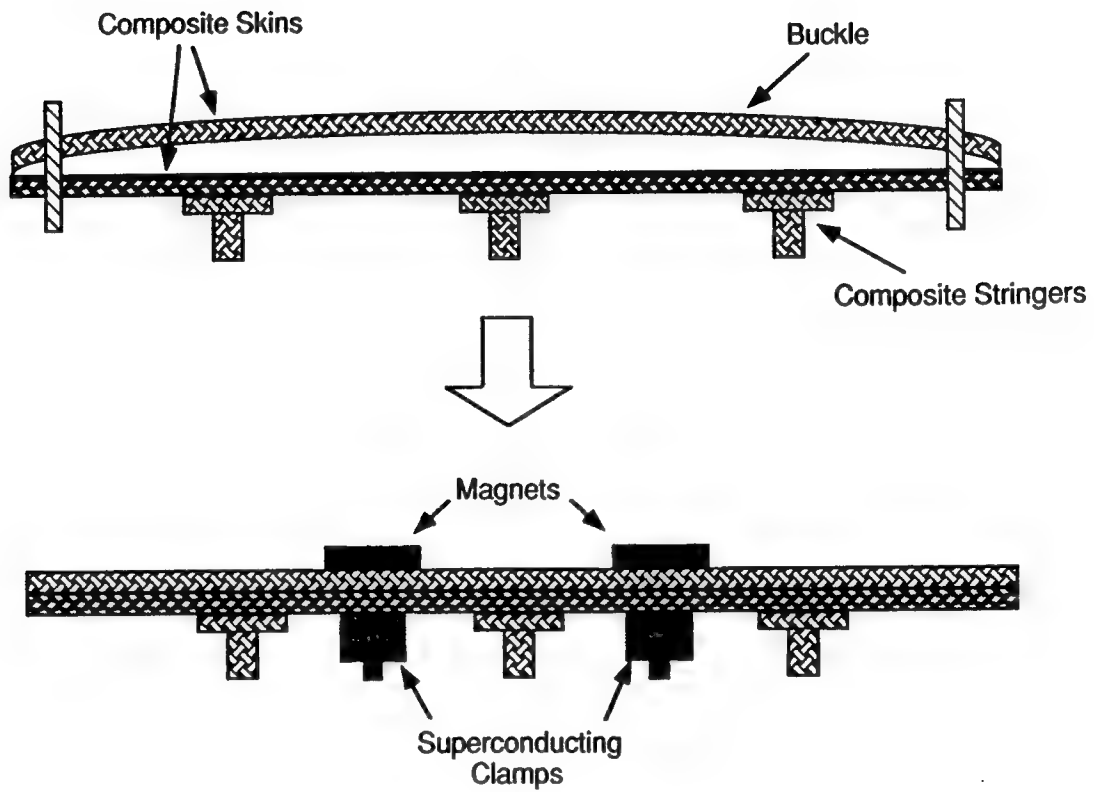


Figure 9. Buckle removal during subassembly of composite structures with superconductor clamps.

ADAPTIVE TOOLING

- reduce cost and increase competitiveness
- flexible tooling - adaptable to contoured parts
- clamping of non-magnetic airplane structures during assembly or service

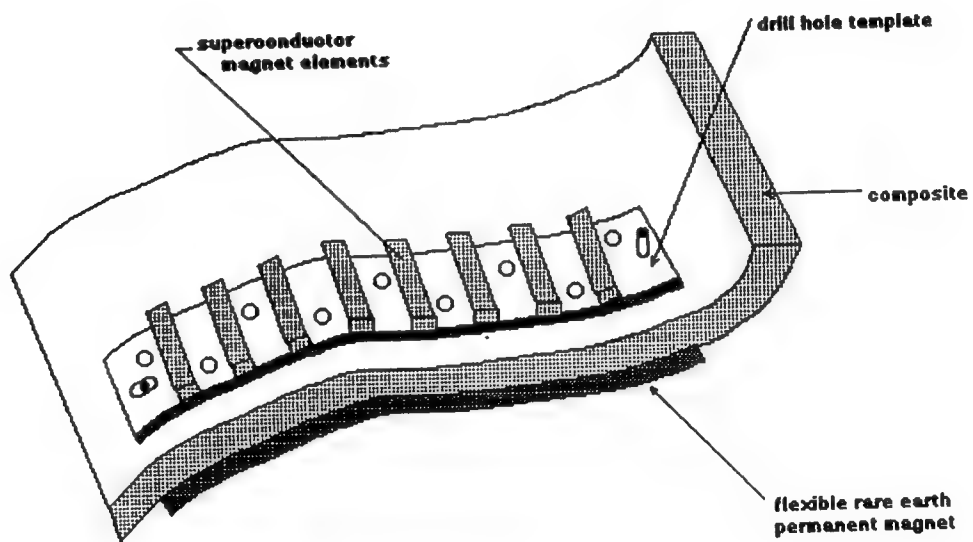


Figure 10. Superconductor array with a flexible permanent magnet latching assembly.

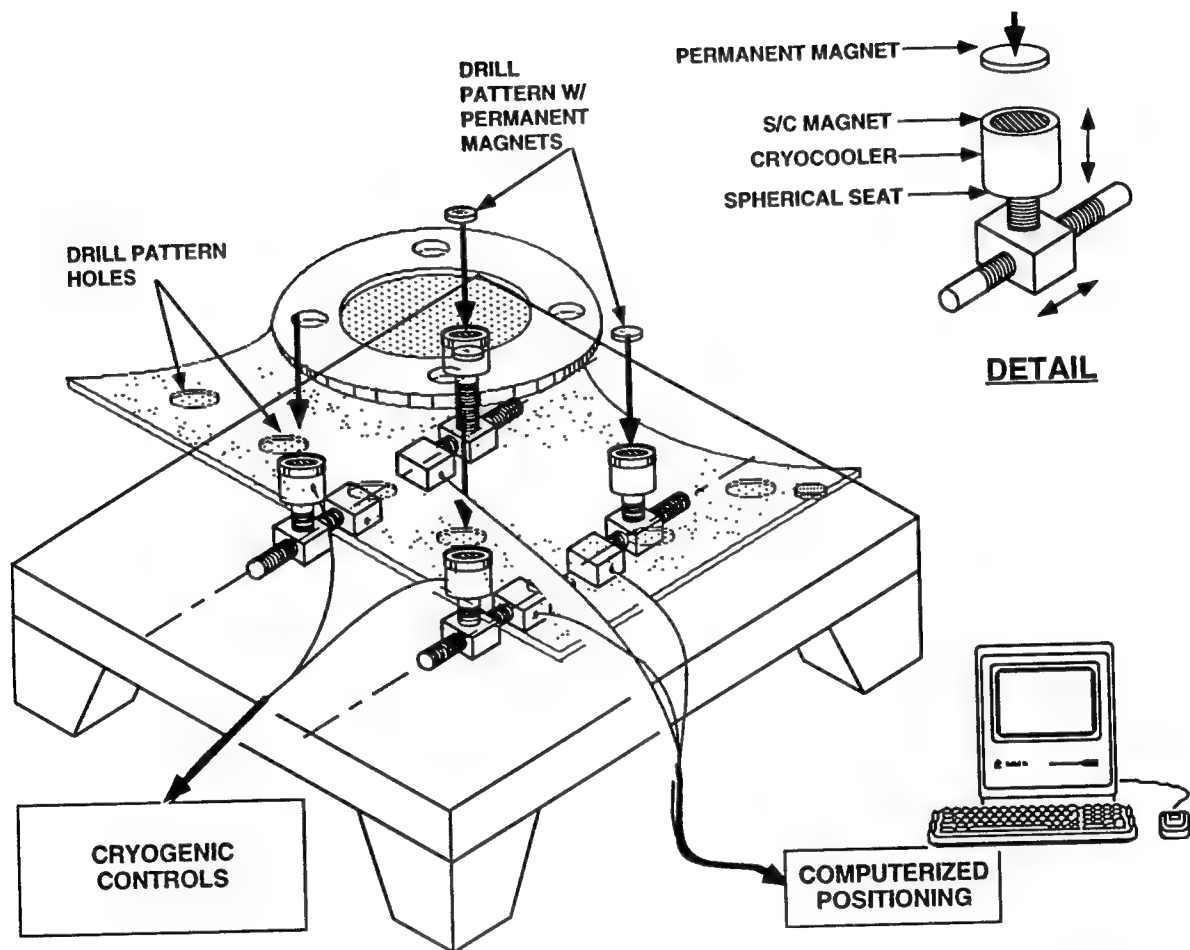


Figure 11. Adaptive tooling concept incorporating high temperature superconductor flux-trap magnet arrays.

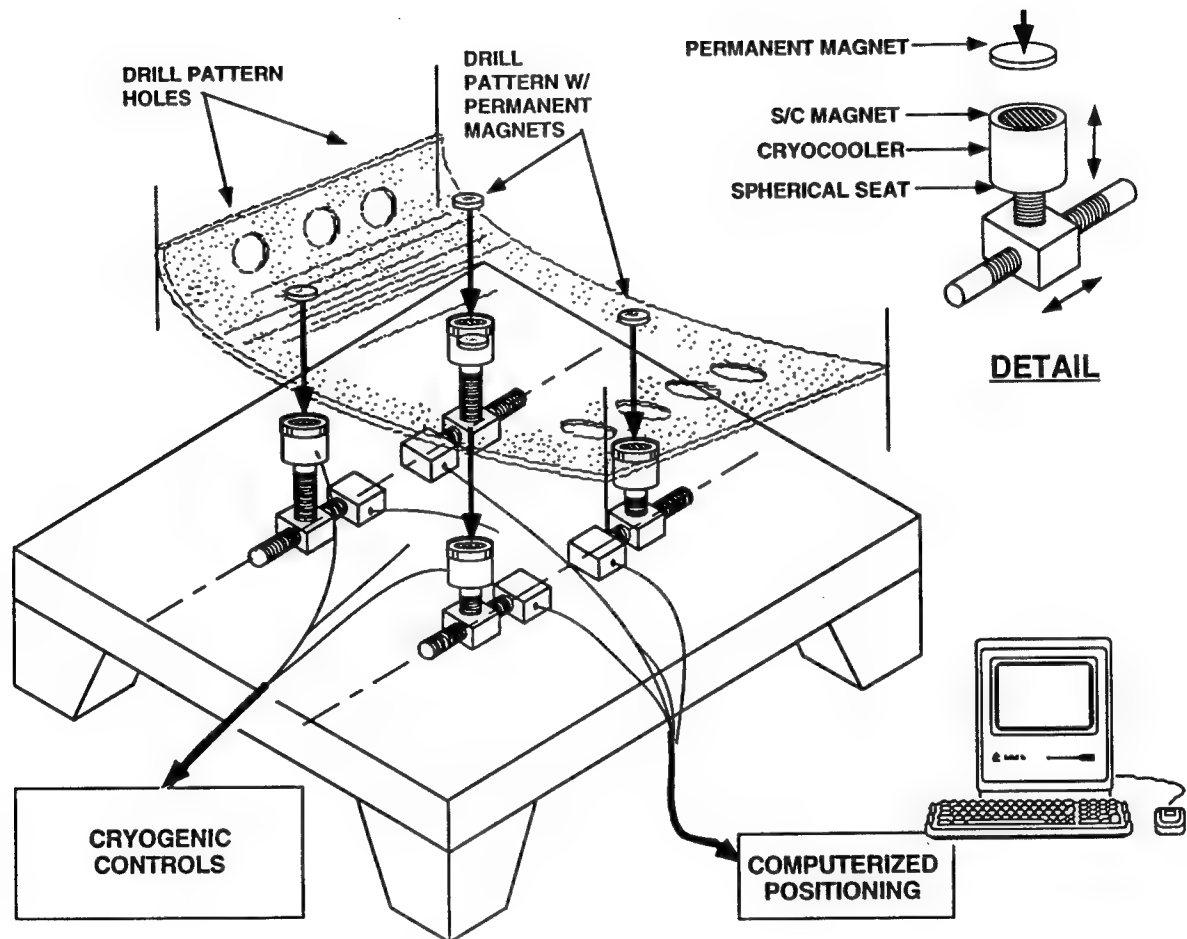


Figure 12. Adaptive superconductor clamp array shown clamping a different shaped part.

The views and conclusions contained in this document are those of the authors and should not be interpreted as necessarily representing the official policies or endorsements, either expressed or implied, of the Defense Advanced Research Projects Agency or the U.S. Government

**PROCESSING, FABRICATION, CHARACTERIZATION
AND DEVICE DEMONSTRATION OF HIGH
TEMPERATURE SUPERCONDUCTING CERAMICS**

Contract No. F49620-90-C-0079

ANNUAL TECHNICAL REPORT

September 30, 1991 - September 30, 1992

Submitted by:

Boeing Defense & Space Group

Sponsored by:

Defense Advanced Research Projects Agency
DARPA Order No. 7476

Monitored by:

AFOSR Under Contract No. F49620-90-C-0079

PM: Dr. Thomas S. Luhman
(206) 773-1991

PI's: Dr. Thomas S. Luhman
(206) 773-1991

Dr. Ilhan A. Aksay
(609) 258-4393

TABLE OF CONTENTS

PROGRAM OBJECTIVE	2
PROGRAM DESCRIPTION	2
SUMMARY	2
MILESTONE SCHEDULE	5a
TECHNICAL RESULTS	6
MATERIALS SYNTHESIS AND CHARACTERIZATION	
YBa ₂ Cu ₃ O _{7-x} Monoliths	6
A. High Temperature Single Crystal Melt Growth	6
i) Melt texturing in a temperature gradient	6
ii) Seeding technique	8
iii) Analysis of melt quenched powders	17
iv) Analysis of non-melt quenched powders	20
B. Low Temperature Processing	23
C. TEM Characterization of 123 Single Crystals	27
D. Dynamic X-Ray Diffraction (DXRD) Studies	30
SUPERCONDUCTING PROPERTIES	
A. Flux-Trapping Experiments	41
B. Theoretical Modeling	45
C. Current Densities	59
DEVICE REQUIREMENTS AND DESIGNS	
A. Flux-Trap Enhancer	69
B. Superconducting Magnetic Clamp	69

PROGRAM OBJECTIVE

To develop material processes and engineering designs for high current applications of $\text{YBa}_2\text{Cu}_3\text{O}_{7-x}$

PROGRAM DESCRIPTION

The goals of our program are to (1) focus on engineering designs and demonstration of flux-trap magnets; (2) develop improved processing and fabrication methods to enhance current densities in strong magnetic fields; (3) optimize processes for grain alignment in bulk and tape samples; and (4) provide a technology base for utilization of flux-trap magnets.

SUMMARY

- a) Among the latest potential applications for early technology insertion in manufacture of military and commercial airplanes is a superconducting clamp based on flux-trap magnets. Permanent magnets are used widely and in diverse applications such as in attracting and holding ferromagnetic objects and in clamping non-magnetic objects and assemblies during manufacturing. Currently, permanent magnets are frequently the only feasible way of holding objects in confined areas during manufacturing. In addition to permanent magnets, larger electromagnetic clamps and chucks are being used extensively throughout the manufacturing industry. Superconducting clamps will allow for the diversity that the electromagnetic clamp provides with the safety and ease of use of a permanent magnet (Invention Disclosure Filed).
- b) Engineering design improvements were a major milestone of this year's work. A superconducting clamp has been developed using single crystal materials with circulating currents (Invention Disclosure has been filed). The superconducting clamp contains a flux magnifier made out of a high permeability metal. The flux magnifier is incorporated into the flux-trap magnet and consists of a plug and/or facesheet and cover for the superconducting cylinder that acts to stabilize the magnetic field as well as magnify its intensity. A flux-trap magnet of 0.85 Tesla strength has been constructed from a single crystal material. This new engineering accomplishment opens up new opportunities for aerospace applications such as magnetic bearings, clutches, motors, and pumps.
- c) Early studies showed that field strengths of only 1 Tesla would be required for a proof-tester to be a working superconducting device. In the proof-testing application,

the dent puller is the only method which can reliably assess joint strength of adhesively bonded aluminum skins; ultrasonic inspection is not able to determine the difference between weakly bonded and securely bonded structures. In addition to flux-trapping, these studies showed the requirement for quenching and flux pumping. Although somewhat limited by adequate sample characteristics, we have recently successfully demonstrated both quenching and flux pumping phenomena in YBCO.

- d) Improvements in the properties and reproducibility of bulk 123 samples with extremely large grains ($> 5 \text{ cm} \times 5 \text{ cm} \times 1 \text{ cm}$) were accomplished this year. These single crystals were successfully prepared by controlling the number of nucleation sites for the growth of 123 grains from the melt-quenched, 211 + liquid region, and following the Japanese approach of seeding (using $\text{SmBa}_2\text{Cu}_3\text{O}_{7-x}$ single crystal seeds) and growth in a temperature gradient. The $\text{SmBa}_2\text{Cu}_3\text{O}_{7-x}$ (SBCO) seeds were grown with the a-b plane parallel to the surface.
- e) Initially, the size of our single crystals was limited to approximately $2.5 \text{ cm} \times 2.5 \text{ cm}$ using melt-quenched stoichiometric 123 powders. SEM-EDS analysis of the area surrounding the single crystal revealed a yttrium depleted region. This condition results from the barium and copper rich liquid phase being swept off at the growth interface of the single crystal. TEM observations have also shown that 211 particles are trapped within the single crystal. According to these results, one can assume that the grain growth is arrested due to the yttrium depletion at the interface. The growth of larger single crystals requires use of melt-quenched 123 powders with excess 211 phase.
- f) Current density measurements on large single crystal materials were performed at Boeing and at the Wright Patterson Air Force Base (by Dr. Gregory Kozlowski). The current density, measured by magnetization, exceeded $1.2 \times 10^4 \text{ A/cm}^2$ at 2 Teslas and 77K, and $7.75 \times 10^5 \text{ A/cm}^2$ at 5 Teslas and 4.2K. The current densities calculated from trapped flux experiments in large single crystals at 77K correlated very well with the magnetization measurements.
- g) A radial gradient furnace was constructed to improve the ability of the temperature gradient to grow large grains in pressed pellets. Single grains were achieved ($5 \text{ cm} \times 5 \text{ cm} \times 1 \text{ cm}$) that grew radially to the edge of the materials, similar to the Nippon Steel approach. Many of these samples were crack-free. The process was reproducible with many large grained samples being produced. Scale-up to 8 cm diameter samples is currently in progress.
- h) A Crystal Specialties Inc. Liquid Phase Epitaxial (LPE)

crystal growing furnace was acquired for crystal grow of large samples. This furnace will allow unprecedented control of processing parameters. The three zone computer controlled furnace is located at the Boeing High Technology Center in a class 100 clean room facility. Modifications are currently being implemented which will allow controlled pulling of YBCO bars through a programmed temperature gradient while monitoring the crystal growth with Infrared cameras. When placed in operation, it should be possible to grow single crystal YBCO of 1 to 4 in² in cross sectional area and 10 in long.

- i) With low temperature texturing we have shown the possibility of preparing textured 123 samples below the peritectic decomposition temperature of the 123 phase. The precursor consists of a mixture of Y_2BaCuO_5 , $BaCuO_2$, and CuO . Texturing was obtained at temperatures between 900 and 1000°C. Precursor powder with a segregated yttria phase was prepared by either melt quenching of 123 or mixing of yttrium oxide, barium cuprate and copper oxide. Addition of silver prevented the formation of pores within the interior of the bulk samples. In our initial experiments, this process was limited to thin samples (tapes). Recently we have shown the feasibility of this low temperature process in preparing thicker textured samples.
- j) Platinum metal additions were explored as a means to limit the particle growth of the yttria-rich phases at the high temperatures, as well as providing flux pinning sites in the finished material. Platinum was added during the melt-quench phase (from the platinum crucible), through addition of fine platinum metal or platinum oxides to the 123, and from a platinum colloid solution during the initial synthesis stage.
- k) Determination of optimum annealing times for the melt textured materials was made using dynamic x-ray diffraction. DXRD measurements on 0.5 mm wafer disks cut from melt textured samples showed the changes in the lattice parameters caused by the diffusion of oxygen through the tetragonal-orthorhombic phase transformation. These measurements were confirmed by electron microprobe analysis on the post-annealed samples.
- l) The 123 bulk and single crystal material is now of sufficient quality to allow us to begin development of a quenching technology. Thermal, high frequency, and high voltage quenching approaches are being tested in these new materials. The full strength quenching demonstration is the most difficult task in our device development program. This task involves quenching in the time frame of 20-30 microseconds in substantially larger samples. We are

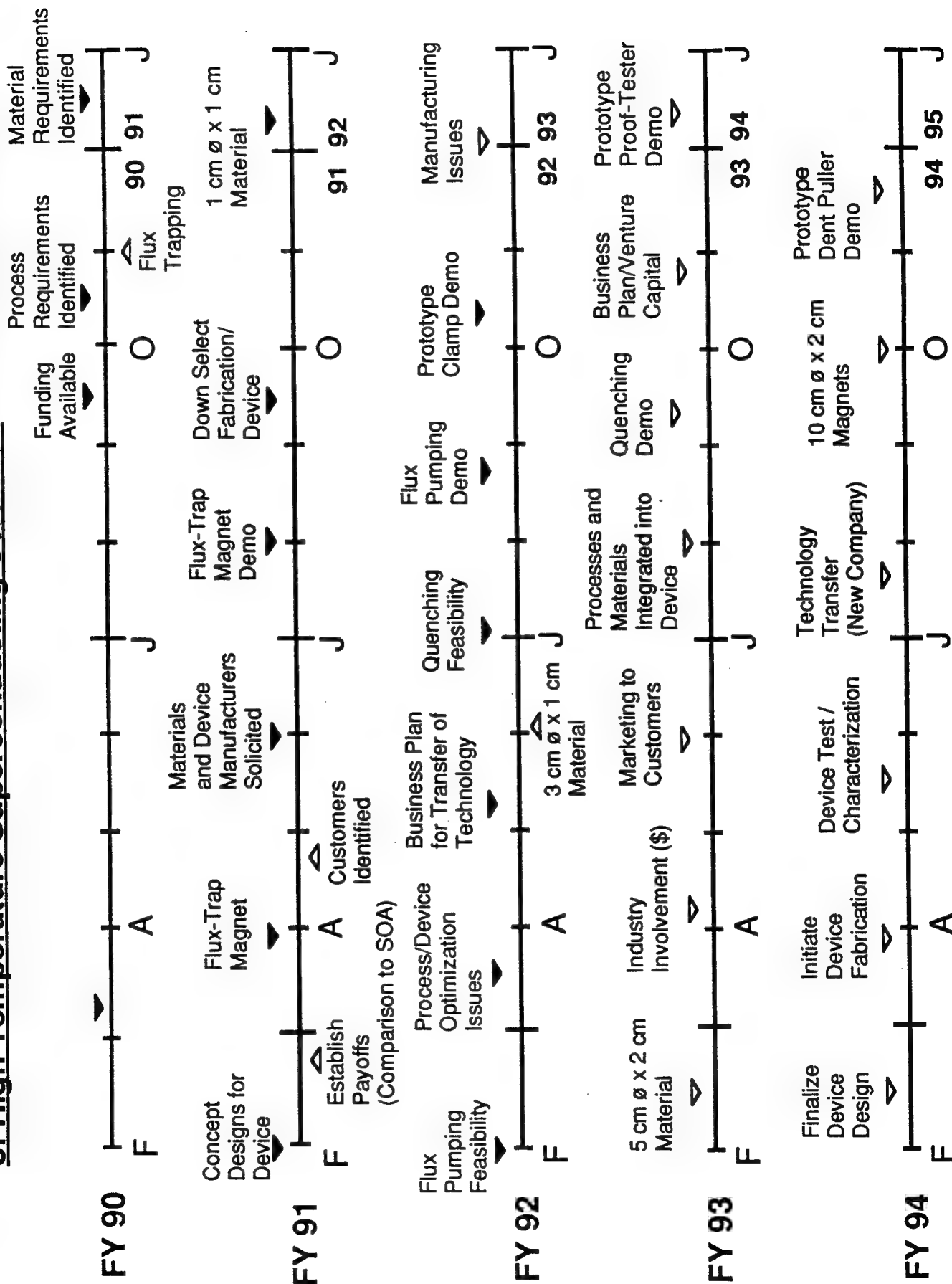
projecting a successful full strength quenching demonstration by the end of September 1993. A prototype proof-tester device is anticipated by 1994.

- m) A Technology Insertion Plan is being actively pursued and implemented. We are continuing discussions with all potential military and commercial customers for the clamp, proof-tester, and dent puller. We are also very actively continuing broader marketing studies on the potential for outside venture capital involvement.

We are in the process of developing a business plan for technology transfer of the large single-crystal growth process to Seattle Specialty Ceramics Inc. (SSC Inc.). Discussions with interested business venture capitalists about a possible new company specializing in superconducting electromagnetic devices are promising.

- n) Dynamic X-Ray Diffraction, which allows for the in-situ acquisition of time-resolved x-ray diffraction spectra, was used to study temperature-time process relationship of various phases formed during the high temperature melt-texturing of the 123. At temperatures above 1150°C, an unidentified phase (there is some evidence that it is a Y-Ba phase contaminated with traces of Pt) nucleates from the melt. This phase will melt after 3-4 hrs at 1350°C and appears to participate in the formation of the 211 phase between temperatures of 1050 and 1150°C, with the net reaction rate being higher at the lower temperature. The concentration of this phase increases dramatically at all temperatures when excess 211 is present.

Processing, Fabrication, Characterization and Device Demonstration of High Temperature Superconducting Ceramics: F49620-90-c-0079



TECHNICAL RESULTS

MATERIALS SYNTHESIS AND CHARACTERIZATION

Processing and Characterization of Textured $\text{YBa}_2\text{Cu}_3\text{O}_{7-x}$ Monoliths

$\text{YBa}_2\text{Cu}_3\text{O}_{7-x}$ Monoliths

The fabrication of textured bulk 123 material is being approached via two processing routes, melt texturing and a low temperature process.

A. High Temperature Melt Growth

Samples with large grain size are required for the high trapped-field device applications. The required large grained samples were prepared by two different methods.

(i) A process involving melt growth in a temperature gradient described in earlier reports. In this case we obtained polycrystalline samples with large grains which trapped magnetic flux lines non-uniformly. Polycrystallinity and crack formation were main sources for degraded properties of these materials.

(ii) Processing of single grained samples by a seeding technique.

The results of these preparation procedures are described below:

(i) Melt texturing in a temperature gradient

The starting 123 powder was melt quenched and milled with 35 mol% 211 and 15 wt% silver. A pressed sample, 27 mm in diameter and 7 mm in thickness, was placed in a tube furnace with a temperature gradient ($\sim 5^\circ\text{C}/\text{cm}$). The sample was heated with $20^\circ\text{C}/\text{min.}$ to 1140°C and held 30 min. Cooling rates to 1025°C , 950°C and room temperature were $0.5^\circ\text{C}/\text{min.}$, $0.01^\circ\text{C}/\text{min.}$ and $2^\circ\text{C}/\text{min.}$, respectively. Flowing air was used during the heat treatment. Oxygenation of the samples was carried out in flowing oxygen with a cooling rate of $3^\circ\text{C}/\text{hr}$ from 600°C to 450°C .

The magnetic flux trap measurements showed that the trapped field in the sample was not uniform. The regions which trapped the highest field about 1500 Gauss was characterized by TEM and compared with another region with ~ 200 Gauss trapped field. Figure 1 shows the crack free grain with higher flux trapped properties contains inclusions of 211 and silver particles. In addition, this high uniformity microstructure displayed twinned grains containing high density of dislocations.



Figure 1. TEM, BF image from the grain with higher flux trapped properties showing no cracks and 211 inclusions.

The region of the sample with poor trapped field revealed microcracking with very high density of dislocations (Figure 2). According to these observations described above, melt texturing in a temperature gradient does not lead to a microstructure with uniform properties throughout the sample, mainly due to microcracking.

(ii) Seeding technique

The seeding of solutions or melts during solidification is a well known process to grow large single crystals. The seeds are usually single crystals of the same material or other materials with the same crystal structure. In our work, we used $\text{SmBa}_2\text{Cu}_3\text{O}_{7-x}$ (SBCO) as seed which has the same crystal structure as YBCO. Due to the higher melting temperature of SBCO ($\sim 1060^\circ\text{C}$) in comparison to YBCO ($\sim 1000^\circ\text{C}$), the melt growth of 123 can be carried out in an intermediate temperature range. Figure 3 reveals DTA of both powders with their melting behavior.

Large grained SBCO samples were prepared by melt texturing in a temperature gradient. Single crystals were cut from bulk samples and placed in the center of 123 precursors during pressing. Melt growth process was carried out in a box furnace under isothermal temperature conditions. Samples were placed on a 123 substrate on the edge to achieve a minimum contact with the substrate. The heat treatment of samples was done in air at 1025°C with heating rates of $10^\circ\text{C}/\text{min}$. and 2 hours dwell time. The cooling rate was $1^\circ\text{C}/\text{hr}$ to 925°C and $2^\circ\text{C}/\text{min}$. to room temperature. A large single grain ($2 \times 2 \text{ cm}$) was obtained according to the XRD analysis (Figure 4).

The resulting large grain was oriented in $[012]$ direction towards the surface which is 45° off the c-axis. Figure 5 shows the polished surface which reveals parallel cracks. It was found, by using XRD from cleaved surfaces and by TEM of electron transparent samples prepared by cleaving and thinning on planes parallel to cracks, that the cracking occurs on (001) planes.

The flux trapping properties of this particular sample exhibited highly uniform field (about 1000 Gauss) but still lower than what might be expected from a single grain without cracks. We concluded that, although we achieved large grain sample with highly homogeneous microstructure and better superconducting properties, we still have to eliminate the formation of microcracks, or to reduce their effect on superconducting properties. Because of the fact that superconducting current flows in (001) planes, if we grow samples with their flat surfaces parallel to (001) plane, the formation of cracks during oxygenation would not severely effect the current flow.



Figure 2. TEM, BF image from the region of low trapped field showing microcracking with high density of dislocations.

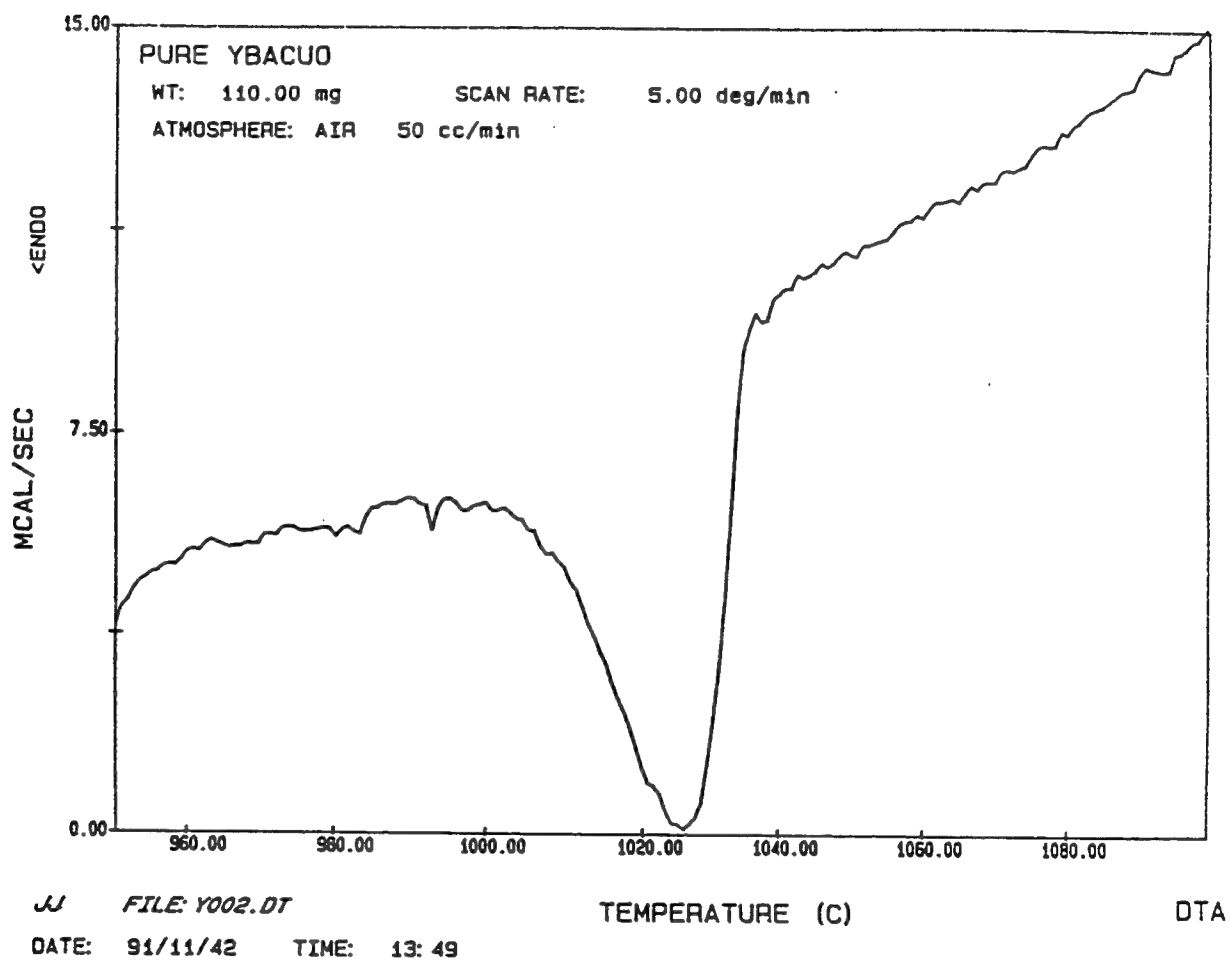


Figure 3a. DTA plot of $\text{YBa}_2\text{Cu}_3\text{O}_{7-x}$ powder showing the melting behavior.

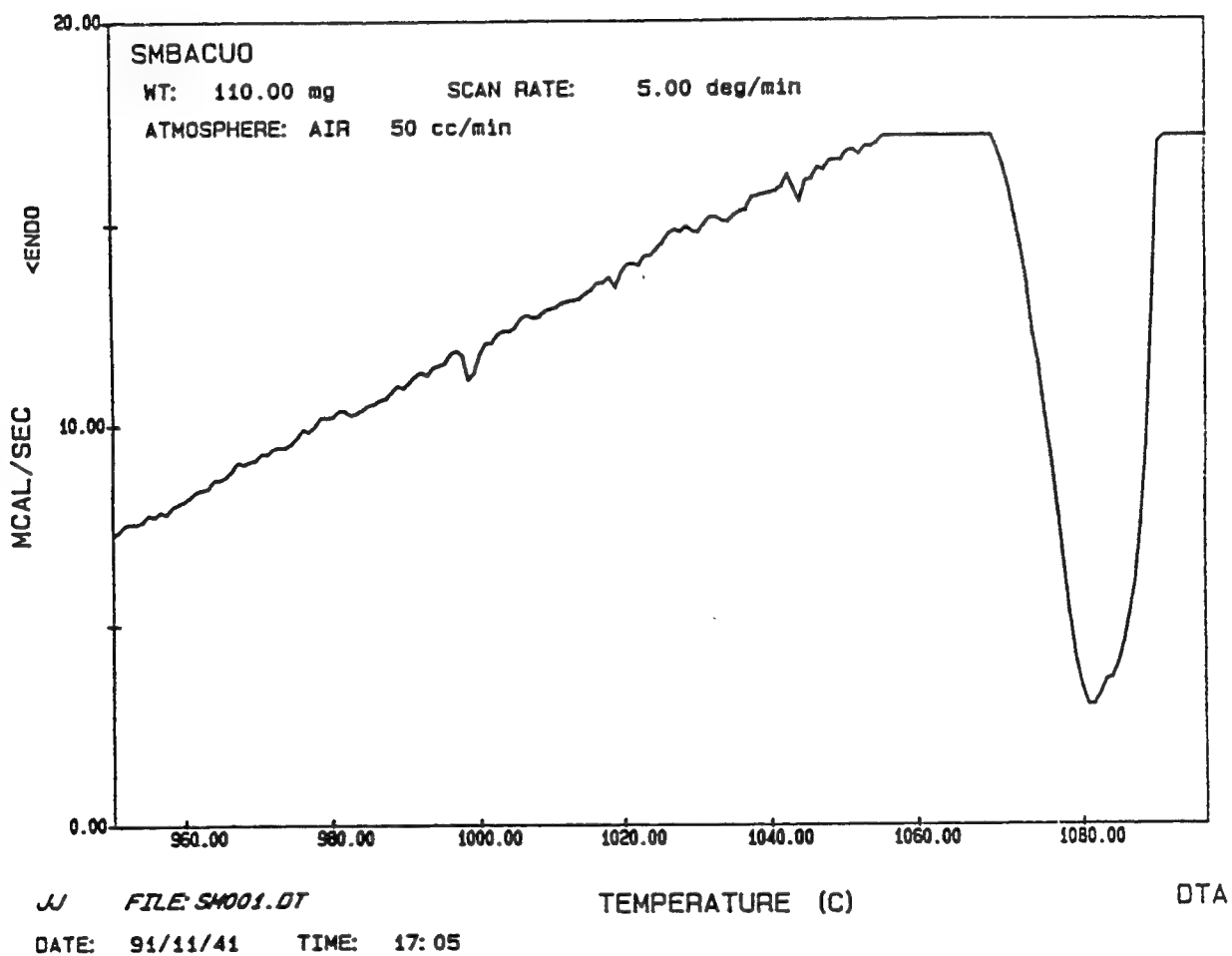


Figure 3b. DTA plot of $\text{SmBa}_2\text{Cu}_3\text{O}_{7-x}$ powder from the surface.

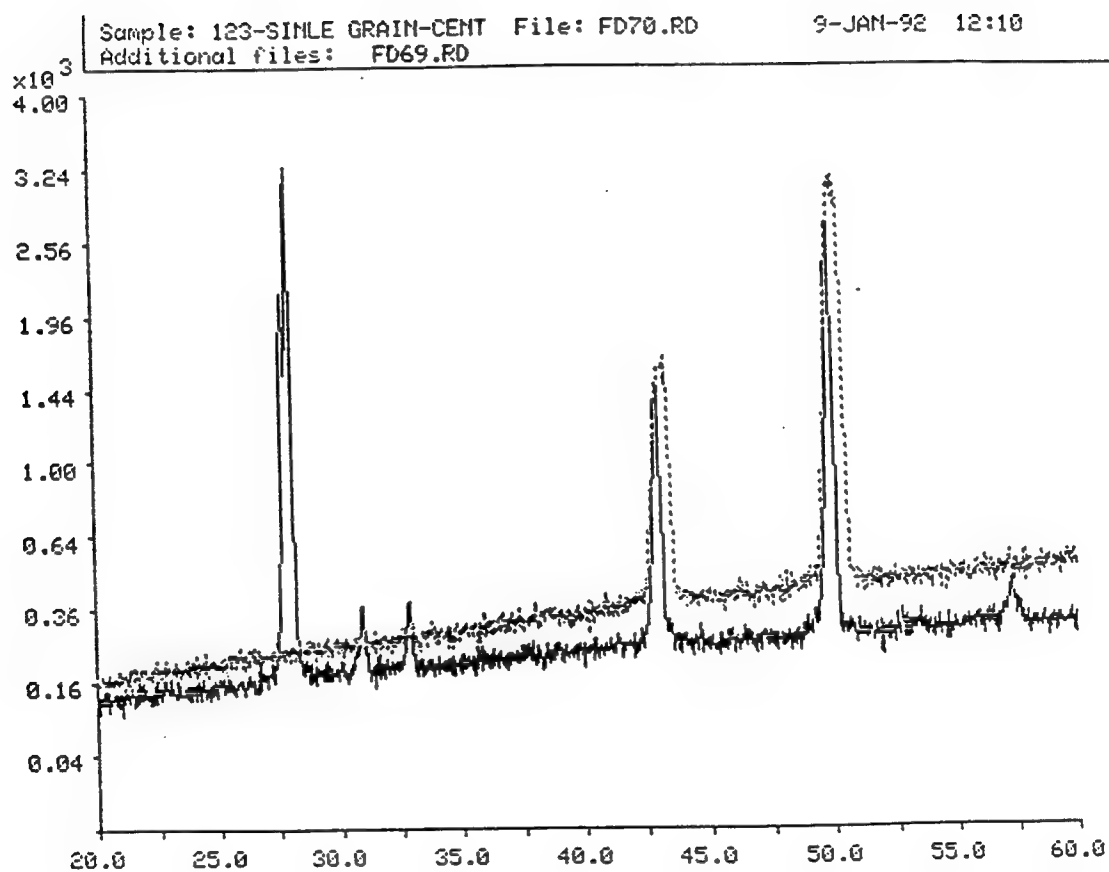


Figure 4. XRD pattern from the surface of a single grained sample showing the [012] orientation. Doted line indicates the reflections of the foil used to mask the sample.



1cm

Figure 5. Photograph of the seeded, single grain YBa₂Cu₃O_{7-x} sample showing parallel cracks along the (001) plane.

In order to obtain a large single grain with c-axis perpendicular to the surface, [001] SBCO seeds are being prepared. The cracks in these samples are expected to be parallel to the surface and, therefore, would not obstruct superconducting current flow significantly. At the present time, processing of the samples using the seeding method described above is in progress.

In order to grow oriented $\text{YBa}_2\text{Cu}_3\text{O}_{7-x}$ single crystals, the $\text{SmBa}_2\text{Cu}_3\text{O}_{7-x}$ seeds were used to induce crystallization during the melt-growth process. The $\text{SmBa}_2\text{Cu}_3\text{O}_{7-x}$ (SBCO) seeds were grown with the a-b plane parallel to the surface. Samples for melt texturing were first pressed uniaxially, followed by pressing cold isostatically with a maximum pressure of 10,000 psi. The oriented seeds were either imbedded in the center of the discs during pressing or placed on the top of a pressed sample. The single crystal was oriented with the c-axis perpendicular to the surface of the sample. Samples with imbedded seeds were either processed vertically or on platinum feet in order to minimize the contact area with the substrate, which can act as an undesirable nucleation site.

Melt-quenched powders were prepared by melting 123 powder at 1450°C for 10 minutes in a platinum crucible. The liquid melt was quenched between two copper plates cooled in liquid nitrogen. The amorphous solid was then manually crushed to 80 mesh followed by attriting with silicon nitride $1/4$ " balls for ten hours in hexane. Analysis of the resulting powder showed it to be composed of particles of approximately 0.5-5 microns and agglomerates of these particles, Figure 6. No evidence of contamination by the grinding media was observed.

Non-melt-quenched powders were prepared by first measuring the desired amounts of fine 123 powder, 211 powder, and platinum powder. Non-melt quenched 123 powder was mixed with 25 wt% 211 and 0.5 wt% Pt powder. The powders are added one at a time to a beaker. Acetone is then added to form a slurry and the mixture is sonicated for a total of 1.5 hours.

The samples were heat treated in a furnace with a radial temperature gradient. In order to achieve a parabolic temperature gradient, a vertical 6 cm diameter and 120 cm length Lindberg tube furnace was used. The temperature profile was measured on a cone shaped refractory material which hung 5 cm above the center of the furnace with chrome-nickel wires, Figure 7. This yielded approximately a $6^\circ\text{C}/\text{cm}$ axial temperature gradient and a 7°C radial temperature difference between the center and the edge of a 5 cm diameter sample. The temperature was measured from the top of the furnace, covered with a pyrex watch glass, using an optical pyrometer. The radial temperature profile was parabolic. The coolest part of the furnace was located at the center of the sample, where the samarium seed was located

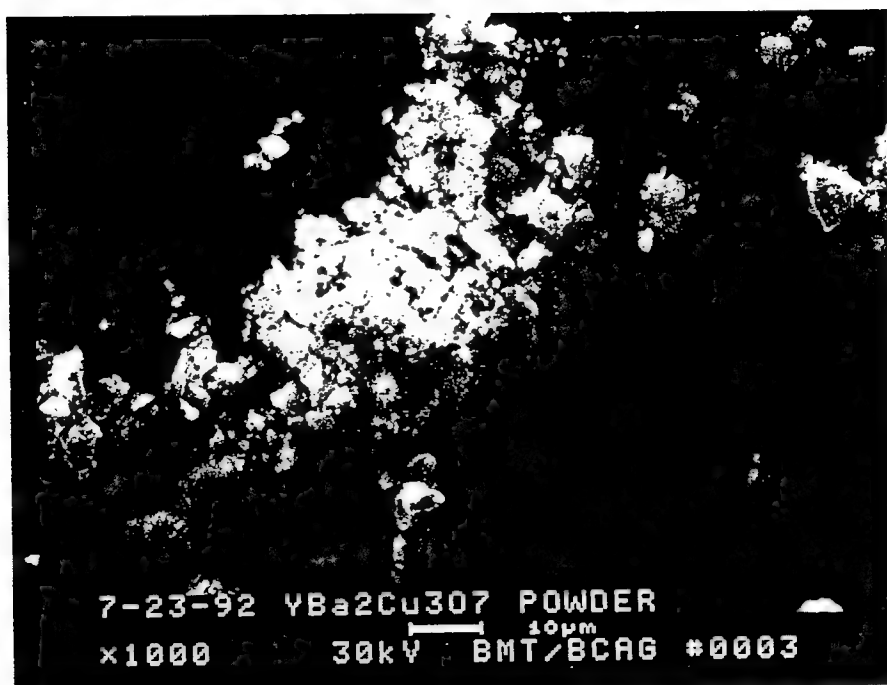


Figure 6. YBCO melt quenched powder that has been attrited in hexane with silicon nitride grinding media for 8 hrs.

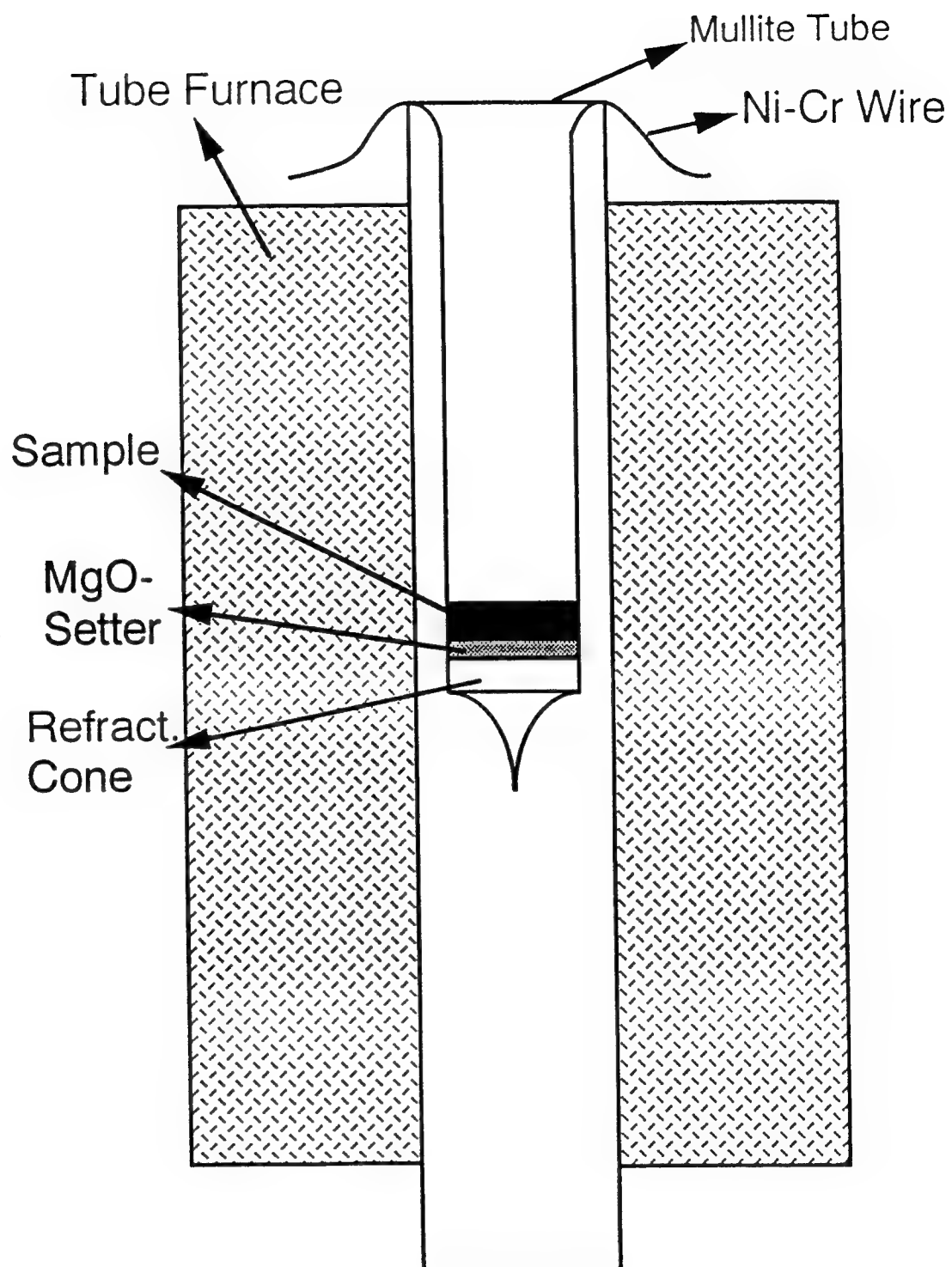


Figure 7. Schematic of radial gradient furnace.

A 10 cm diameter bottom loading furnace was also constructed with an approximate length to diameter ratio of 1.5:1. Useful temperature ranges are restricted to those below 1150°C. Temperature profiles were measured using type K thermocouples cemented into an alumina D tube. Two profiles were measured and temperature contours plotted, Figures 8 and 9. A video camera was built above the furnace for the recording of the crystal growth in situ. Exact furnace temperatures during the initial stage of crystal growth could then be determined. The maximum furnace set temperature could be determined more accurately in order to prevent the superheating of the sample. Excessive loss of the liquid phase could also be avoided by cooling the sample from an optimum temperature.

The heating schedule for these samples was improved to take advantage of the optimum crystal growing region for the mixture. The samples were heated in air to 1020°C for 2 hrs. This was followed by cooling at 15°C/hr to 1010, and a very slow cooling at 0.01°C/min to 990°C. The cooling rate to room temperature was 1°C/min.

Analysis of Melt Quenched Powders:

The following reactions occur during the melt quenching of the YBCO powders and a single crystal grow out of a melt.

< 1200°C



~ 1000°C



Best results to date were obtained from samples prepared from melt quenched powders with stoichiometric 123 composition without excess 211. As discussed previously, a certain amount of 211 particles are still trapped in the crystal due to loss of the liquid phase during processing. In order to obtain larger crystal size, optimum temperature profiles and temperature gradients are necessary. The samples were heat treated in a furnace with a radial temperature gradient. In order to achieve a parabolic temperature gradient, a vertical 6 cm diameter and 120 cm length Lindberg tube furnace was used. The temperature profile was measured on a cone shaped refractory material which was suspended 5 cm above the center of the furnace with chrome-nickel wires, Figure 7. This yielded approximately a 6°C/cm axial temperature gradient and a 7°C radial temperature gradient between the center and the edge of a 5 cm diameter sample. The temperature was measured from the top of the furnace, covered with a pyrex watch glass, using an optical pyrometer. The radial temperature profile was parabolic. The coolest part of the furnace was located at the center of the sample, where the Sm seed was located. This design reduces the likelihood of grain

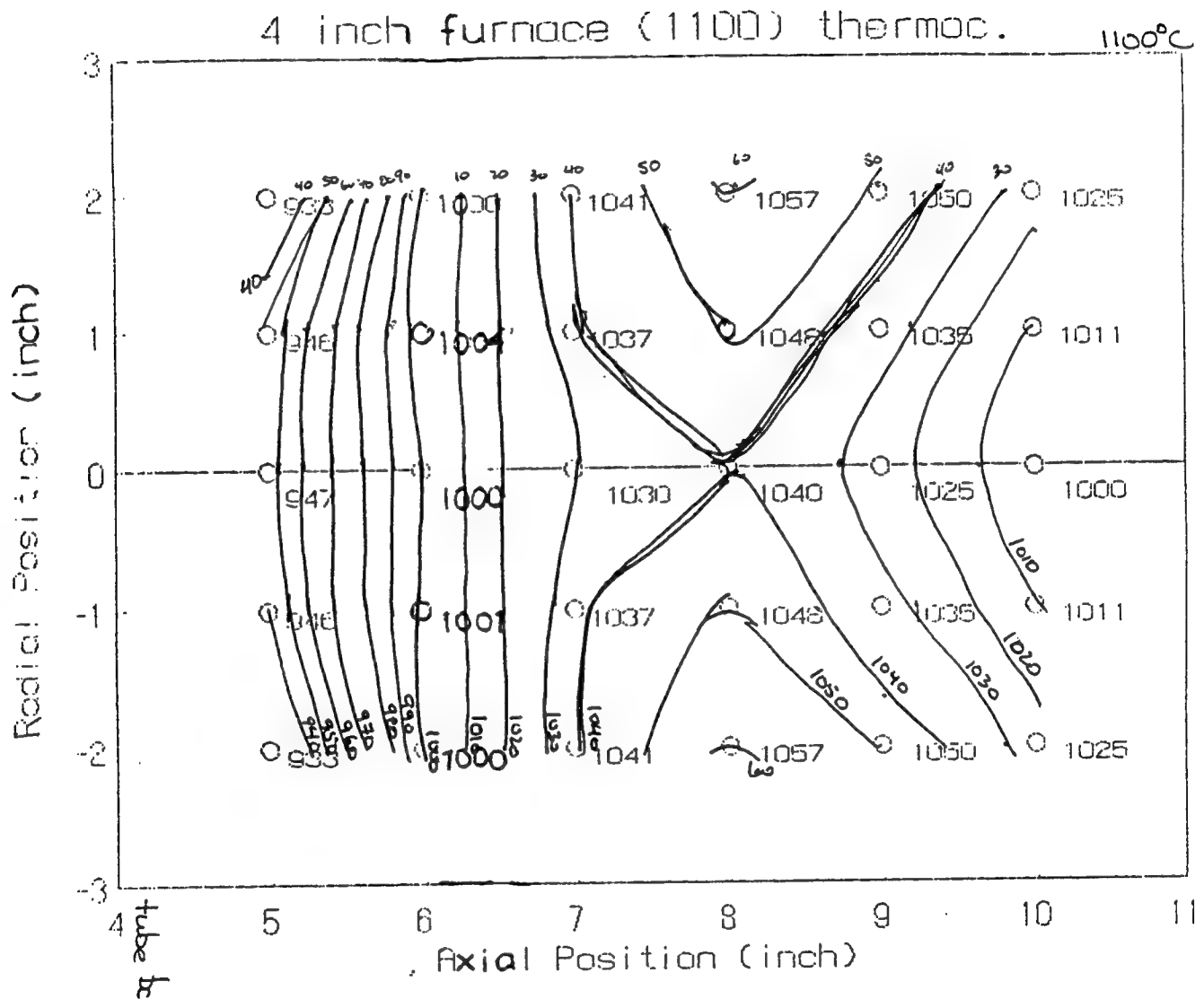


Figure 8. Parabolic temperature gradient profile of bottom loading furnace.

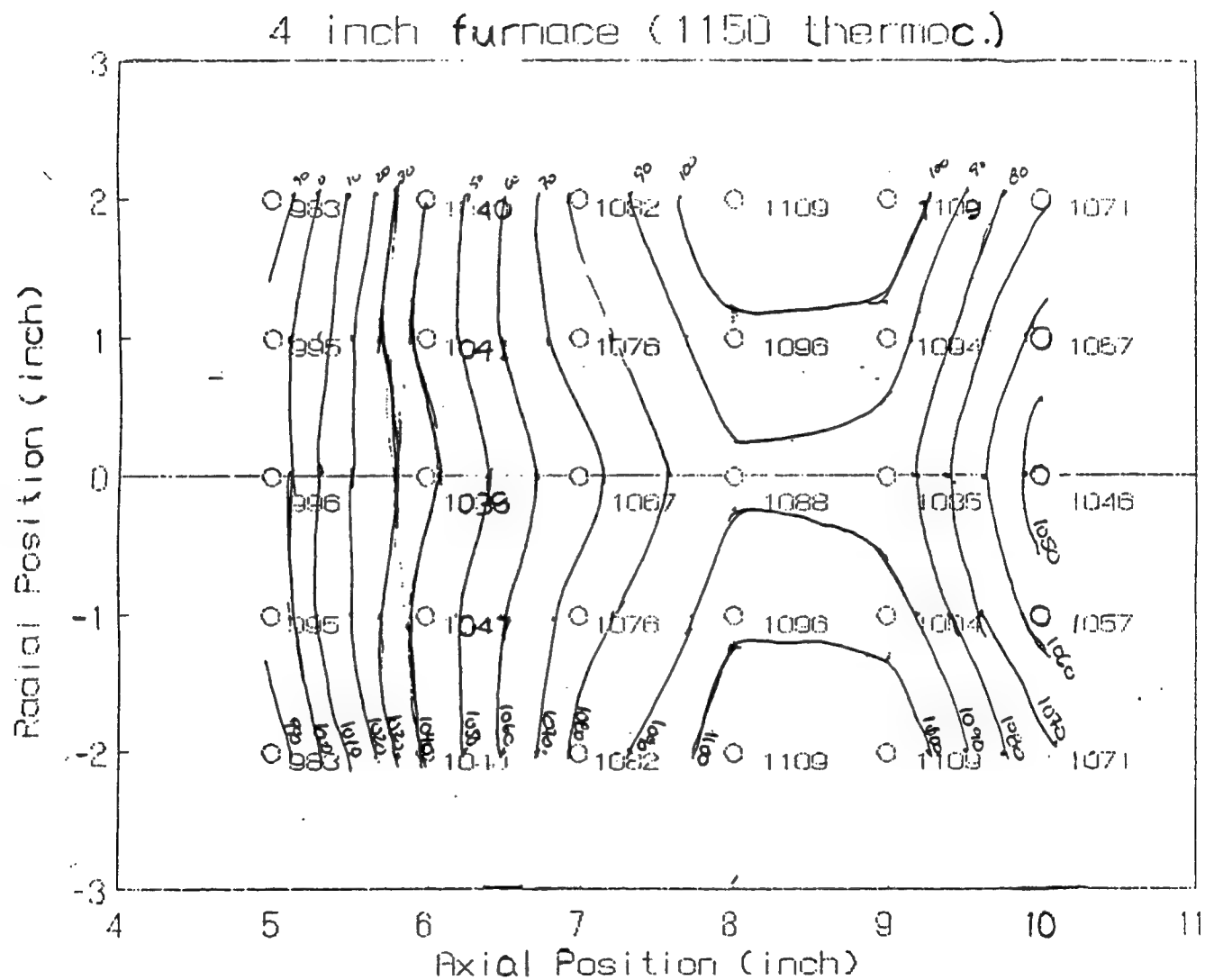


Figure 9. Parabolic temperature gradient profile of bottom loading furnace.

growth at secondary nucleation sites which might be caused by inhomogeneities, impurities or any other unknown inclusions. Platinum is still the substrate of choice, however it may prove uneconomical in the long run. Latest results have shown that the reaction products between platinum and the liquid phase of YBCO can be also used as a setter material. The coarse particles of this Pt-Ba-Cu-O material can therefore be reused. This substrate prevents the sample from reacting with it thus allowing natural shrinking to occur without the buildup of stresses due to difference in the coefficients of thermal expansion of the YBCO and substrate during the heat treatment. Single crystals up to 5 cm in diameter were grown using this technique. Examples of these materials are shown in Figure 10.

Analysis of Non-Melt Quenched Powders:

Previous studies have shown that melt quenched powders were necessary in order to grow large single crystals. However, our recent results show that non-melt quenched powders can also grow large crystals, Figure 11. The role of these added powders in the processing of the samples is not well understood. EDS and WDS analysis by SEM on the polished single crystals, prepared from melt quenched powders, revealed that platinum rich inclusions were trapped throughout the sample. This indicates that the powders contain a small amount of Pt dissolved during melt quenching from platinum crucibles. It is not well understood whether the crystal growth was controlled by the nature of the phase separated melt quenched powder or by the small amount of platinum content.

In order to study the effect of platinum on the growth kinetics of crystals, platinum was added to non-melt quenched powders in the processing of the samples. Platinum powder was prepared from contaminated platinum foils used as setters during the heat treatment of 123 samples. Platinum strips were first cleaned in hydrochloric acid and subsequently dissolved in aqua regia. Platinum hydroxide was precipitated by dropwise addition of ammonia solution. The yellow precipitate was washed with water and heat treated to 700°C to yield an ultrafine metallic powder.

Addition of supplementary platinum is crucial to these powders. Platinum metal is used to limit the particle growth of the yttria-rich phases at the high temperatures, as well as providing flux pinning sites in the finished material. In the melt-quenched powders, platinum is obtained through dissolution of the platinum crucible by the liquid melt. Since this is not possible in the non-quenched powders, a fine platinum powder is added prior to melt quenching. The size of the platinum particles most likely plays a role in determining the properties of the final material. The addition of colloidal platinum is currently being explored, as a means of mimicking the dissolved platinum phase.

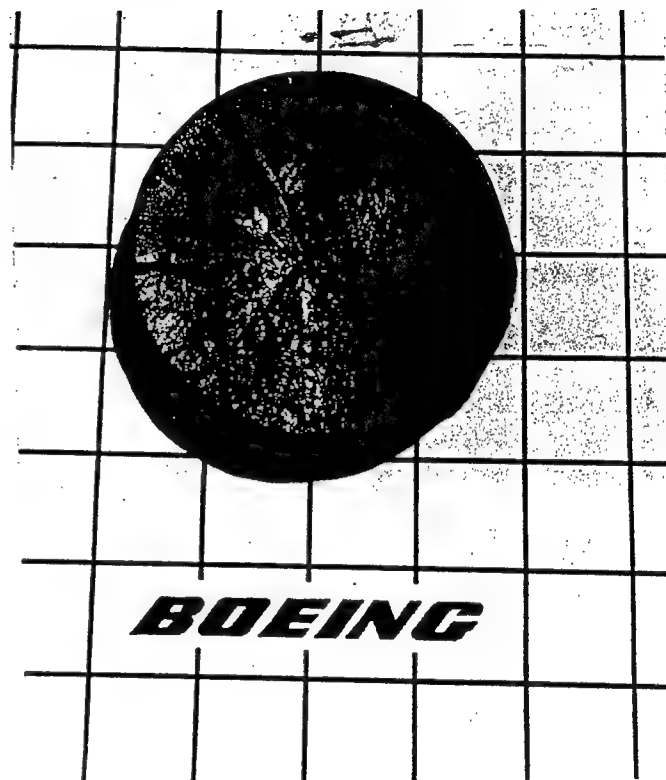
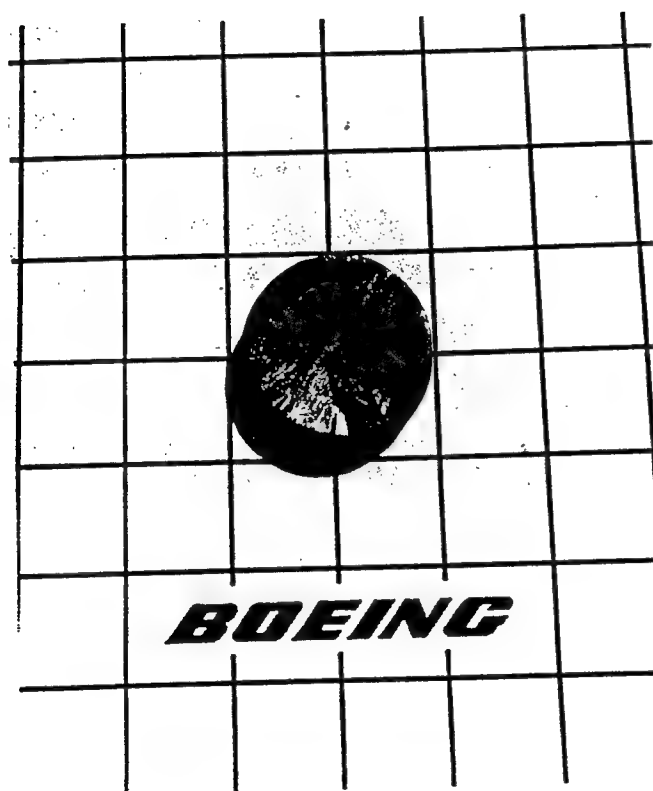


Figure 10. Single crystals grown from melt quenched powders using the SmBCO seeding technique. Gridlines = $1/2$ ".

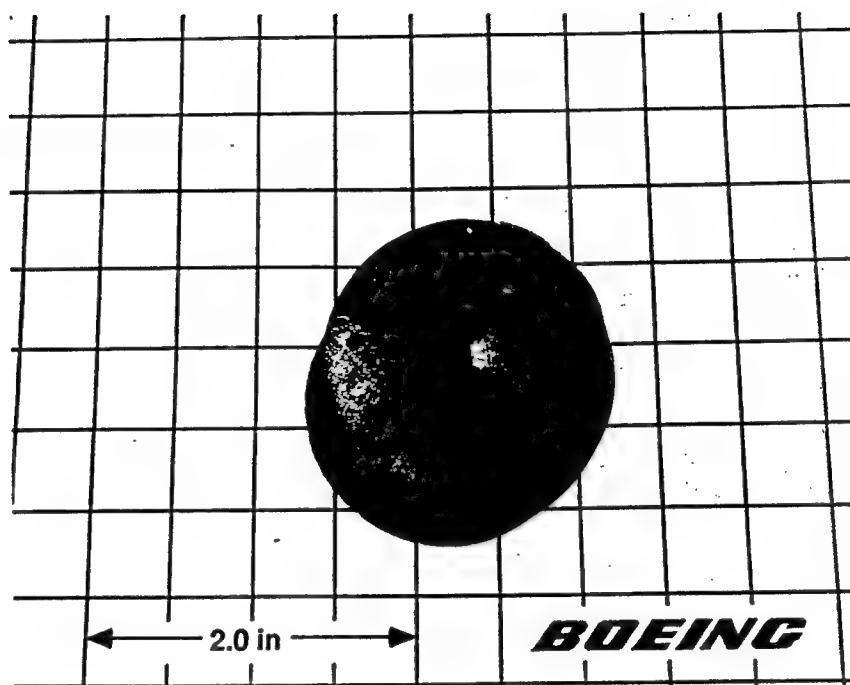


Figure 11. Single crystals grown from non-melt quench powders using the SmBCO seeding technique. Samples contain 25 wt% 211 and 0.5 wt% Pt. Gridlines = 1/2".

Further TEM and SEM studies will be conducted to understand the role of the platinum during the solidification process.

Samples prepared by this method yielded large single crystals extending to the edge of the disk. These results indicate that melt quenched powders are not necessarily needed to be able to grow single crystal grains by the seeding technique. At this stage of the investigation, addition of a small amount of platinum to the powder composition seems to control the growth kinetics of single crystals as large as 4 cm in diameter. The recent results are encouraging with respect to the large size of the crystals.

Addition of excess 211 phase may help in the crystal growth kinetics. At the higher temperatures, the sample consists of a liquid phase plus 211 particulates. As the crystal nucleates, the grain begins to grow and 123 solidifies, consuming most of the 211 phase. However, some of the 211 particulates become encapsulated before they are consumed. Thus, an excess of 211 is necessary to continue grain growth over a large area. If not, the growth is arrested by depletion of the necessary elements prior to 123 formation.

SEM-EDS analysis of the single crystal revealed that the single crystal itself was yttrium rich, in comparison to the area surrounding the crystal, which was barium and copper rich. The limited crystal size is attributed to the compositional change at the interface during the grain growth. Dissolution of 211 particles in Ba-Cu-O rich liquid phase is not fast enough to form 123 and the liquid phase is swept at the interface. The 123 phase with 211 inclusions can no longer be formed when the composition of the interface becomes yttrium depleted.

B. Low Temperature Processing

Although high temperature melt texturing (described in section A) produces 123 monoliths with useful properties, there are several disadvantages associated with this approach (i) difficulties in the retention of sample shape, (ii) variation of chemical composition due to the evaporation of components at high temperatures, and (iii) cracking of samples. In order to alleviate these problems, the feasibility of texturing at a lower temperature was investigated.

Commonly used procedure for texturing 123 grains makes use of the liquid which forms upon the peritectic decomposition of 123 phase at temperatures above 1000°C. This information has led us to believe that lower temperature texturing should be possible if one can introduce liquid at a lower temperature. Specifically, our low temperature processing has been based on the presence of the eutectic liquid which exists between BaCuO₂ and CuO at

temperatures below 1000°C and thus, appropriate precursors were developed to promote the growth of 123 phase in the presence of this low temperature liquid. The two types of initial powder used were (i) a mixture consisting of 211, BaCuO₂, and CuO in the molar ratios needed to form 123 and (ii) quenched powder from Y₂O₃ + liquid region of the phase diagram. TGA and XRD results on the former powder indicate the following path for the formation of 123 phase:



As mentioned previously, our thick sintered samples produced in this manner contained pores in the central portion of microstructure. Presently, we believe that completion of the above reaction (mainly the elimination of the O₂ gas from the system) at the sintering temperature is the key factor in producing pore-free microstructures. This conclusion has been based on two observations; in the first place we have seen that under the same heat treatment condition, the addition of Ag into the precursor powder reduces the number of pores in the final microstructure. From our earlier work on Ag (enhancement of 123 crystallization) this result may be explained in terms of more complete reaction in the above equation and secondly we have also noticed that longer holding times at the sintering temperatures produces microstructures with less pores. Combining these factors, we can now prepare dense and textured 123 samples at temperatures below the melting point of 123 system. Figures 12a and 12b show the SEM microstructures from the sample which has been sintered at 985°C and cooled at the rate of 3°C/hr to 900°C. As it can be seen the number of pores has been decreased significantly. in comparison to our earlier samples. We were also able to control the grain size in these samples with the use of seeding technique.

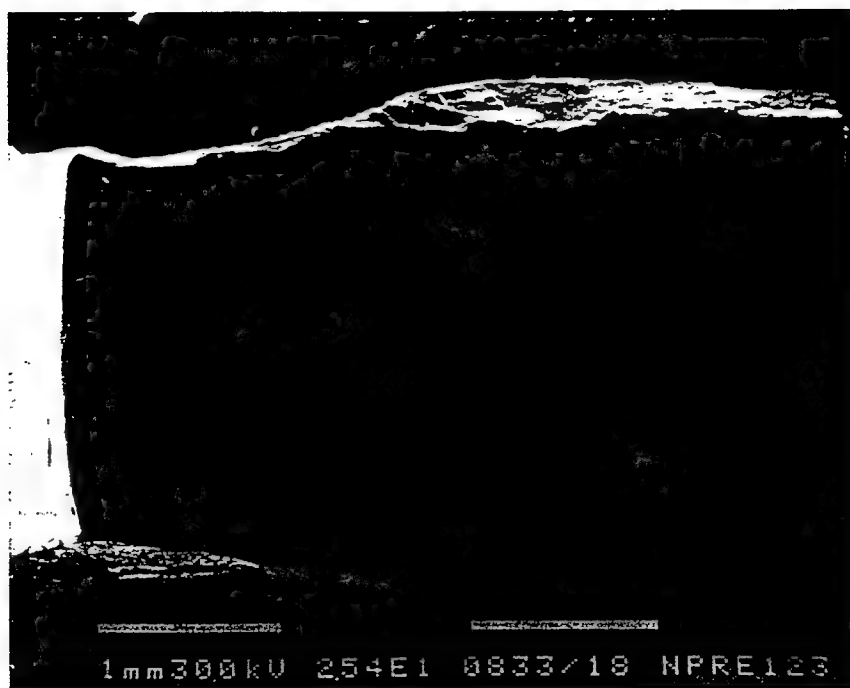


Figure 12a. SEM micrograph showing a polished cross sectional view from the sample sintered at 985°C.

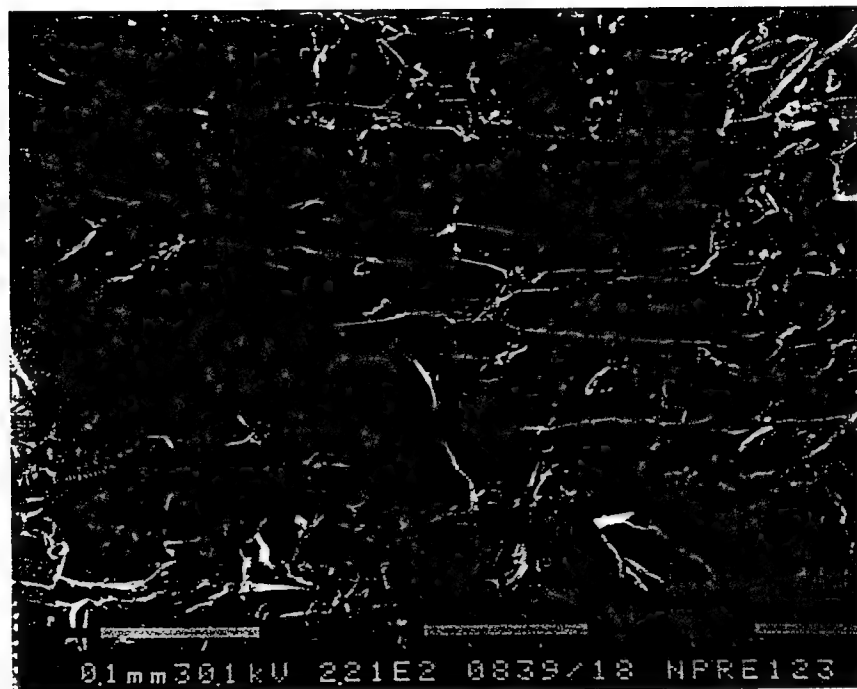


Figure 12b. Fracture SEM view from the sample in Fig. 12a.

C. TEM Characterization of 123 Single Crystals

The objective of TEM characterization is to identify the nature of the pinning centers and to understand the mechanism of a single crystal growth process. The approach is to study the microstructure and the composition of the material as a function of position across the sample and as a function of different crystallographic orientation. The microstructural observations were also performed on samples prepared by different processing routes to understand the influence of the melt-quenching step and other processing parameters.

In this study, powders from different processing routes have been characterized: melt quenched powders; melts quenched, 950°C treated powders; melt quenched and remelted powders; melt quenched, remelted and annealed powders; and melt quenched powders with extra 211 phase. The purpose is to find fine defects in the materials and the stability of these defects under heat treatment necessary for grain growth.

It is generally observed that there are some fine structural defects in the melt quenched powders, which are not present in powders through the non-melt process. First, fine nanometer sized precipitates are observed, Figure 13. These precipitates are identified as either 211, yttria, or cuprate compounds. Anisotropic strain contains are also observed. In these powders, the twin structures are usually not well defined. However, annealing the materials at high temperature tends to reduce the density of the defects.

Characterization of large grains:

Figure 14 is a typical single crystal microstructure perpendicular to the c axis. Typical large 211 precipitates are observed with some strains around the particles. Two twinning variations are also observed. In all of the samples, planar defects perpendicular to the c-axis were observed. These defects are usually associated with a high density of strains. Streaking of the diffraction indicates that the defects are like "stacking faults" in the a-b plane.

The fine precipitates, planar defects, and strains may be responsible for high flux trapping. However, the planar defects can also cause the sample to crack along the a-b plane.



Figure 13. Fine precipitates in melt-quenched powders.



Figure 14. TEM image perpendicular to c-axis.

D. Dynamic X-Ray Diffraction (DXRD) Studies

The initial focus has been directed at fundamental studies of the tetragonal-orthorhombic phase transformation during oxygen annealing. Specifically, "cycling" experiments have been conducted in order to determine whether the desired net tetragonal-orthorhombic phase transition could be affected by cycling the temperature between low temperatures and a progressively decreasing high value. The objective was to determine whether the transition was kinetically limited so that it could be considered as one means of controlling crack propagation due to the volume change during the phase transition. The results with powdered samples have been encouraging: no kinetic limitations were observed between ranges of 680 and 550°C during 30 second cycles, even at atmospheres containing only 5.4% oxygen.

The cycling experiments start with pure phase 123. The sample is heated in air to 850°C for 5-15 minutes to assure complete transformation to the tetragonal phase and then switched to the desired atmosphere prior to cooling to the initial "high" temperature (T_{start}) of the cycle range. Figure 15 shows a schematic (Temperature - Time) of the cycling experiments. The upper temperature was lowered at a rate of 1-2 deg/min while the lower temperature was maintained constant (T_{min}) for any given experiment. The sample temperature was then cycled between the upper and lower temperatures at about 1 cycle/min, a sufficient time to obtain a complete scan at both the upper and lower temperatures during each cycle. The upper temperature, was lowered at the designated rate until a pre-selected end point temperature, T_{stop} , was reached. Another data point in Figure 15 is the temperature, T^* , at which the 123 phase at the upper temperature was no longer tetragonal, but rather, the orthorhombic^I phase; i.e., an orthorhombic phase with a lower oxygen content than the superconducting orthorhombic^{II} phase.

The following Table I shows the results of the cycling experiments. In all cases the phase transitions were sufficiently rapid (less than 20 seconds) so that thermodynamic conditions prevailed at both the upper and lower temperatures. Thus the existing 123 phase at the upper temperature was always tetragonal until the temperature reached T^* , at which point it was orthorhombic^I.

TABLE I

Expt	Atmos	Deg/min	T_{start}	T_{stop}	T_{min}^*	T^*
PT7	O ₂	1	680	630	600	650
PT8	air	2	650	570	550	606
PT9	5.4% O ₂	2	580	555	550	567

The 123 phase at this temperature was O^I in PT7 and O^{II} in PT8 and PT9

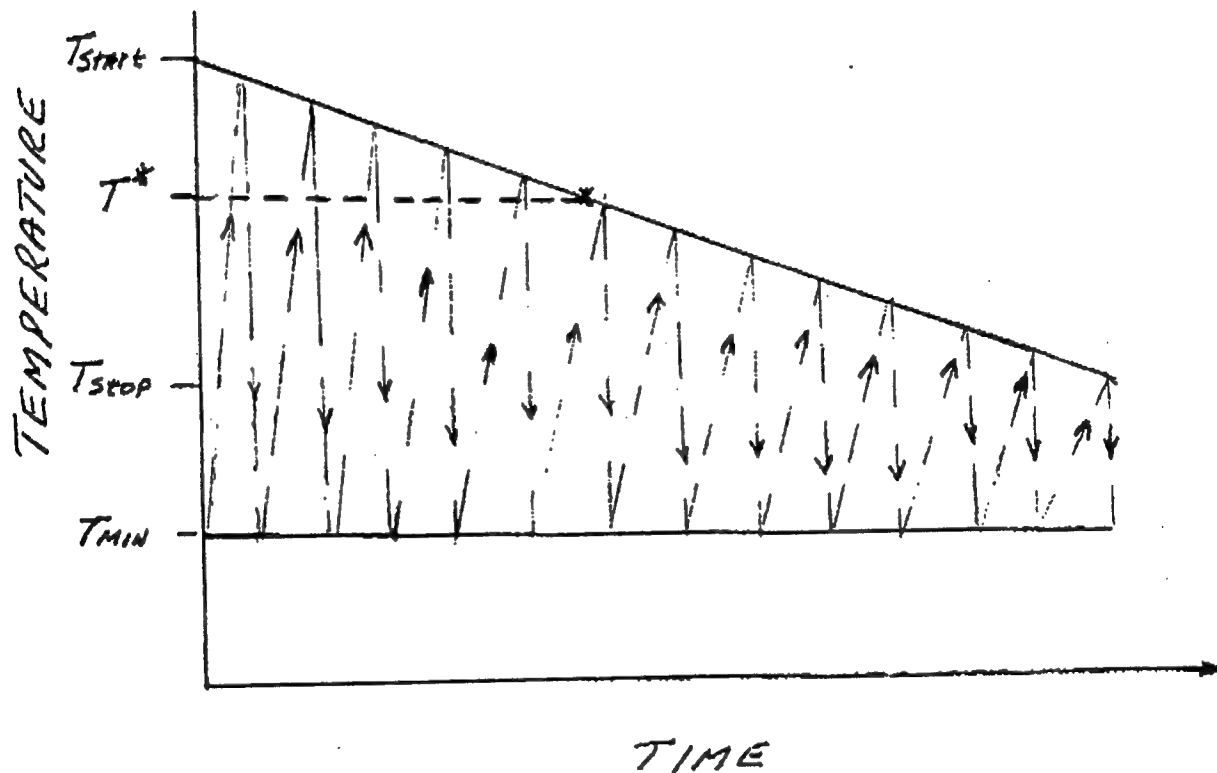


Figure 15. Temperature-Time scheme for cycling experiments.

After the initial studies we have initiated DXRD experiments with melt textured 123 wafers. Although microscopy and electron microprobe measurements indicated that the surfaces of the wafers were not phase pure, promising results were obtained with both electron microprobe oxygen scans as well as with DXRD experiments. Even though oxygen transport rates could be obtained via the electron microprobe measurements, this method has been discarded due to its expense and time consuming nature. DXRD measures changes in the lattice parameters as oxygen is added to the 123 phase and, by fitting the data to a diffusion model, calculations of oxygen transport rates and, ultimately, annealing times as a function of temperature were conducted.

Technical Problems.

Because of the high densities of melt textured 123 pellets, the rates of the tetragonal-orthorhombic phase transformation are diffusion limited and very slow. The major difficulty with XRD experiments is that the x-rays only penetrate about 3 μm and thus it is difficult to extrapolate these results to a pellet that is 2 cm in diameter. We are hopeful that, by mathematically modelling the diffusion process, we can successfully fit the limited XRD data to the model and thereby increase the chances of successful extrapolation.

General Methodology.

We attempted to obtain information on the extent of the tetragonal-orthorhombic phase transition during oxygen annealing of melt textured samples. The objective was to measure the rates of this transformation and then extrapolate them so that information can be obtained on the temperature-time processing conditions required to achieve an orthorhombic HTSC. These measurements are being made by DXRD techniques (which can only monitor the transformation over the first 3 μm of the surface of the pellet) and by electron microprobe measurements to quantify the oxygen content as a function of distance from the oxygen-exposed surface.

Technical Results.

Four thin "wafers" of melt textured 123 were prepared. Two of the samples were grown using a samarium seed and two were grown without the seed. The wafers are about 2 cm in diameter and 1.6 mm thick. Prior to DXRD measurements, XRD scans were taken of both surfaces ('A' and 'B', in Figure 16) and one sample (no samarium seed) was cut with a diamond saw as shown in the sketch and then examined by means of microscopy as well as by electron microprobe.

An optical microscope revealed the extreme and right and left hand sides of the sample (the portion of the wafer exposed to

air) to be very heterogeneous while the middle of the cross section is reasonably homogeneous. Various "islands" of separated phases were found in regions of the sample and were analyzed by EDAX with the following results:

Phase 1 - Consists of Y, Ba, Cu and Pt (throughout sample).

Phase 2 - Consists primarily of Cu and O, slight Y and Ba (at both ends).

Phase 3 - Probably barium cuprate (brown and at isolated points in the main phase)

Phase 4 - This phase is the 123 phase (throughout the mid section of the cross section).

Figures 17 and 18 show oxygen scans along scan lines 1 and 2, respectively. Although there is quite a bit of data scatter, an oxygen profile is evident along scan line 1 and appears to be flat along scan line 2. This is what would be expected since both edges of scan line 1 would have been exposed to oxygen during cool down (Surfaces 'A' and 'B') and would have been expected to transform to the oxygen rich orthorhombic phase.

As mentioned earlier, we can get at the rate of oxygen transport in two ways: by means of the oxygen gradient in the sample (as in Figure 18) or by measuring the changes in the lattice parameters as the tetragonal-orthorhombic phase transition takes place. The former method is expensive and exceedingly time consuming since we would have to deal with quenched samples. The more preferable method is to use DXRD to follow the oxygen transport in-situ. To date we have not been very successful using DXRD, primarily due to phase heterogeneity near the surfaces. That is, the penetration depth of the x-rays is only about 3 μm and this is the region where the maximum heterogeneity exists. This is illustrated in Figure 19 which shows x-ray scans of the samples along with the sample exposed ('A' Surface) to helium at 650°C for 30 minutes and then cooled and held in air at 450°C for 2 hours. The standard for c-axis aligned orthorhombic 123 is also shown for comparison purposes. As can be seen, the XRD peaks at the outer surface are not phase pure, c-axis aligned 123. However there are changes as the sample was heated and cooled, indicating that the detection of the phase transition might be possible if we were to start with phase pure 123.

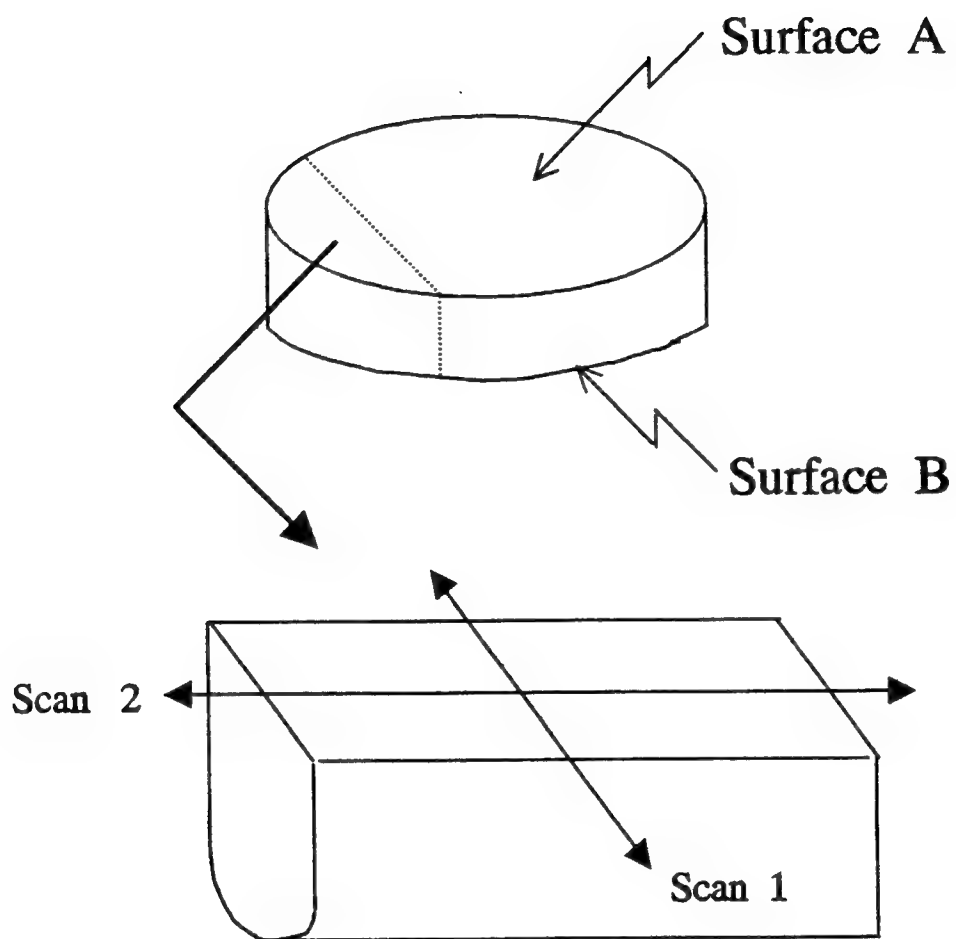


Figure 16. Wafer sample and configuration for DXRD analysis.

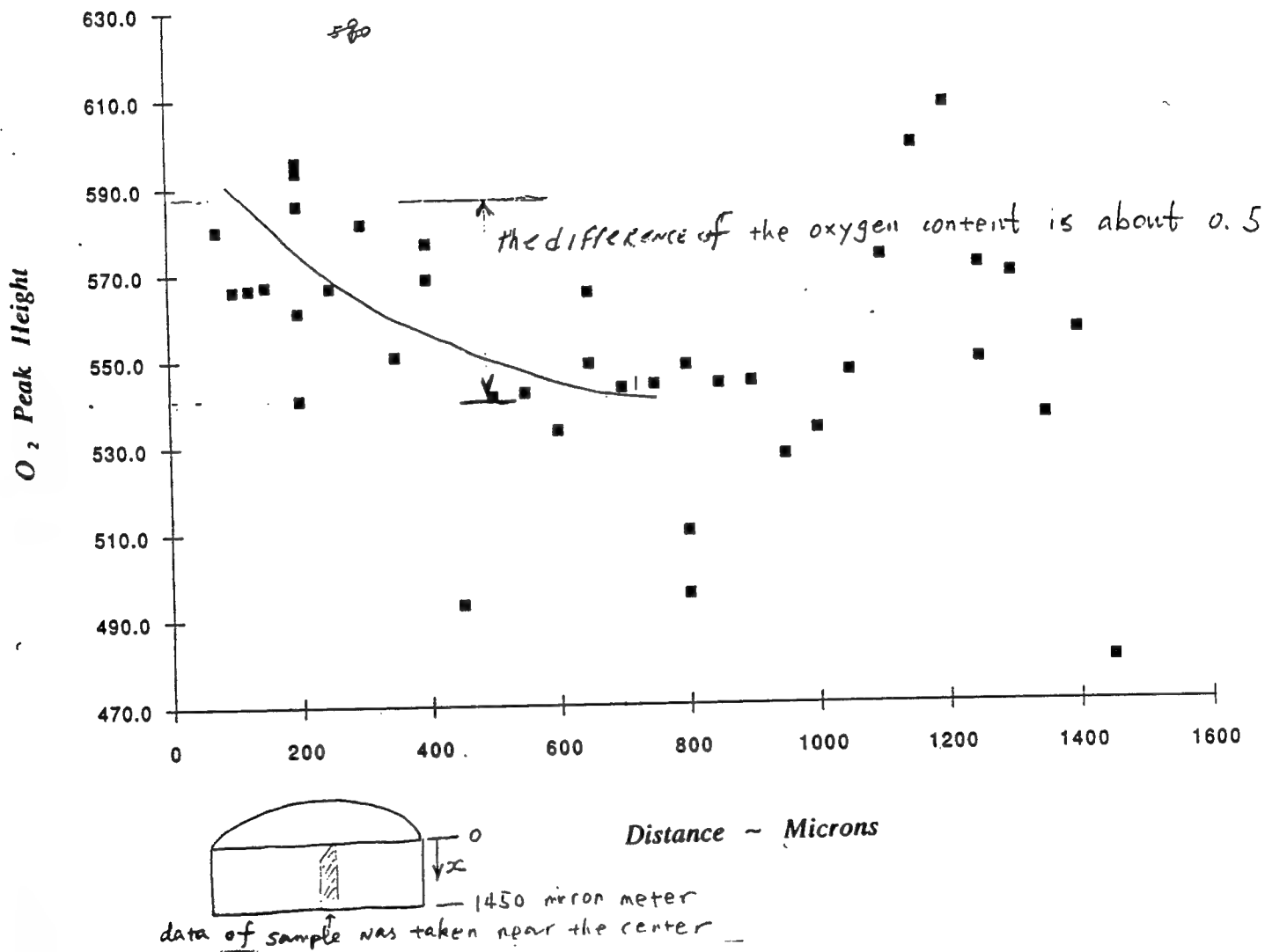


Figure 17. Oxygen profile along scan line one.

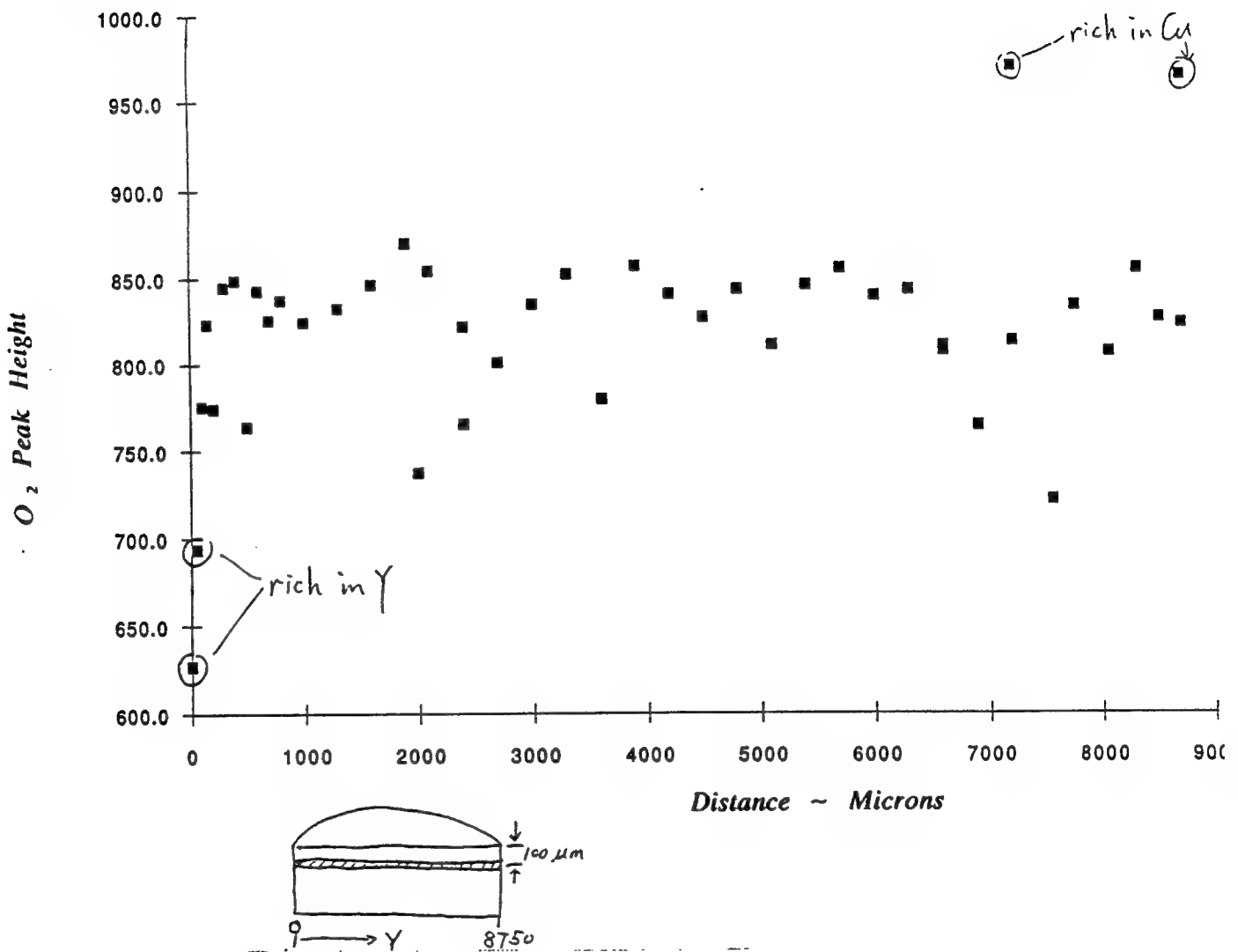


Figure 18. Oxygen profile along scan line two.

5000

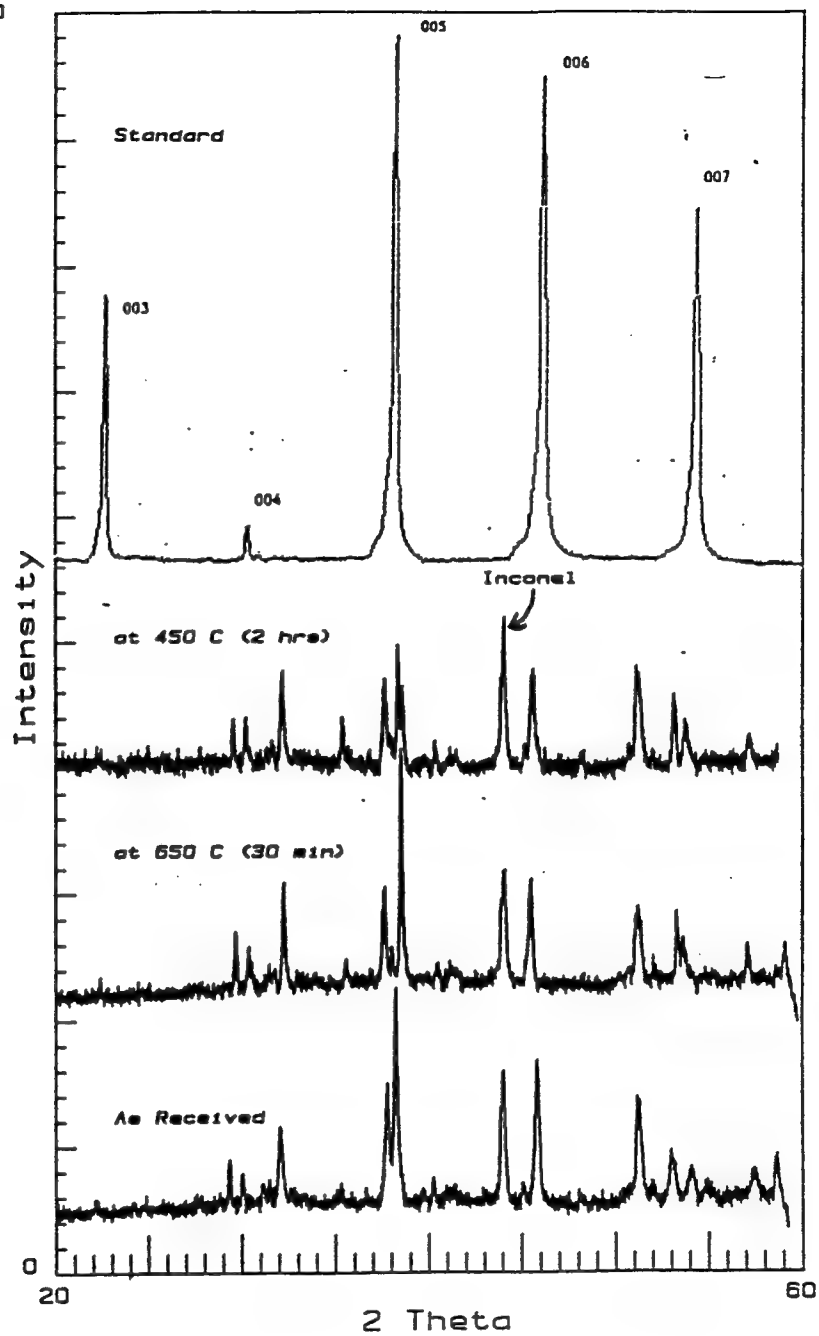
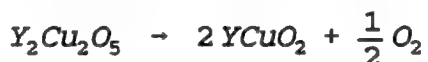


Figure 19. DXRD results for samples exposed to helium at 650°C for 30 min followed by cooling in air to 450°C for 2 hrs.

A systematic study has been conducted to determine the effects of particle size and gaseous oxygen on the reaction paths leading to the Y-Ba-Cu (123) HTSC. Using Dynamic X-Ray Diffraction (DXRD), three binary reaction sets having two different particle sizes (nm and μm) were reacted in both air and helium environments. Results indicate that the absence of oxygen leads to lower reaction temperatures and to different products in the Y-Cu and Ba-Cu binaries. Particle size comparisons show, not only a higher reactivity in the nm system, but also different products due to the diffusion limitations in the μm system. Comparisons between the binary and ternary reactivities show that the Ba-Cu binary is the most critical for assuring high quality HTSC.

Figure 20 shows one of the more significant effects of particle size wherein it is clear that in the nm size system it is the α -BaCO₃ phase which reacts with Y₂O₃ whereas it is the β phase which reacts in the μm system. The effect is even more pronounced in the Y-Cu binary as can be seen in Figure 21. Note that in the nm sized system, the final products are Cu₂O, YCuO₂ and Y₂O₃ whereas, in the μm system there is only Cu₂O and Y₂O₃. The reason here is due to the fact that the reaction



is inhibited in the μm system by the presence of small concentrations of O₂ which is unable to diffuse away from the reaction site. This same effect was noted in all of the intermediate reactions involving oxygen as a product gas.

The fact that such a relatively small difference in particle size could actually produce different product species points to the importance of oxygen diffusion in all of the reaction leading to the formation of the 123 HTSC.

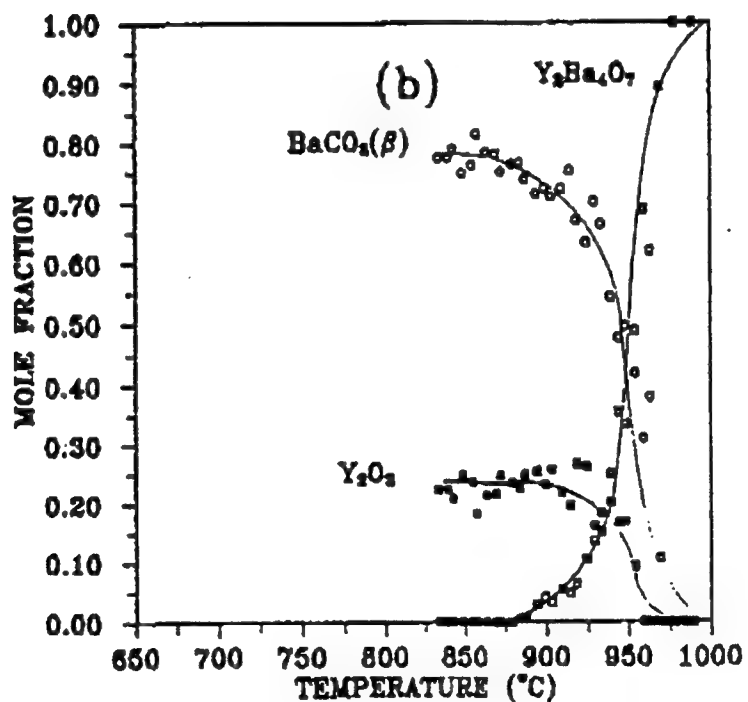
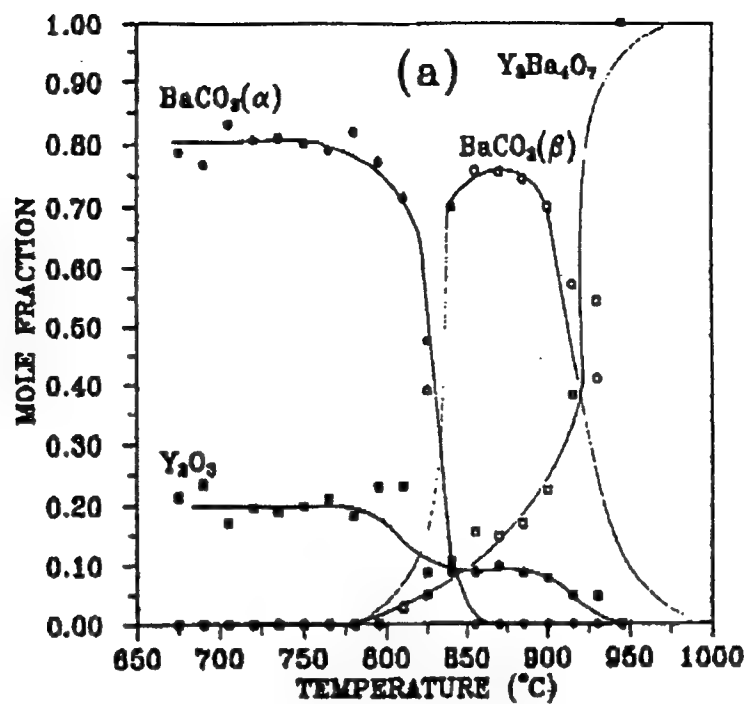


Figure 20. Y_2O_3 - $BaCO_3$ Binary: 5°C/min in air
 (a) nm particles
 (b) μm particles

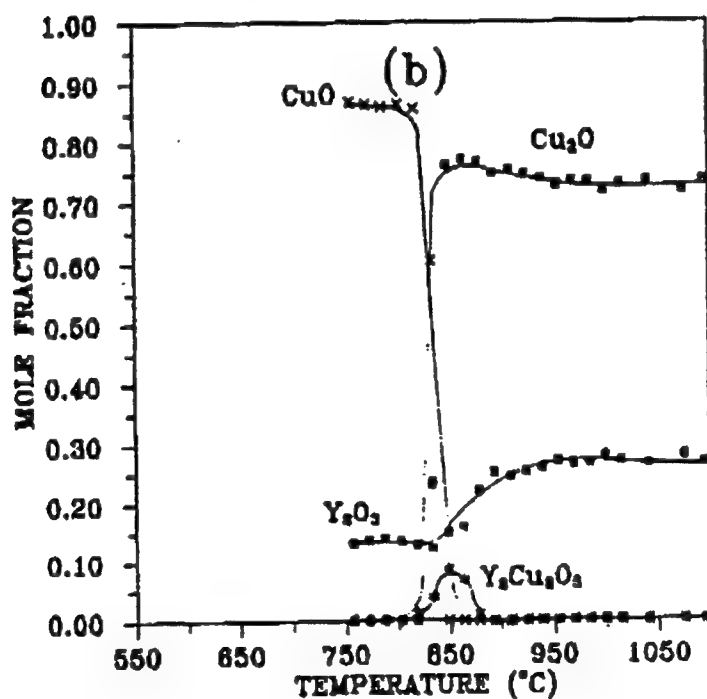
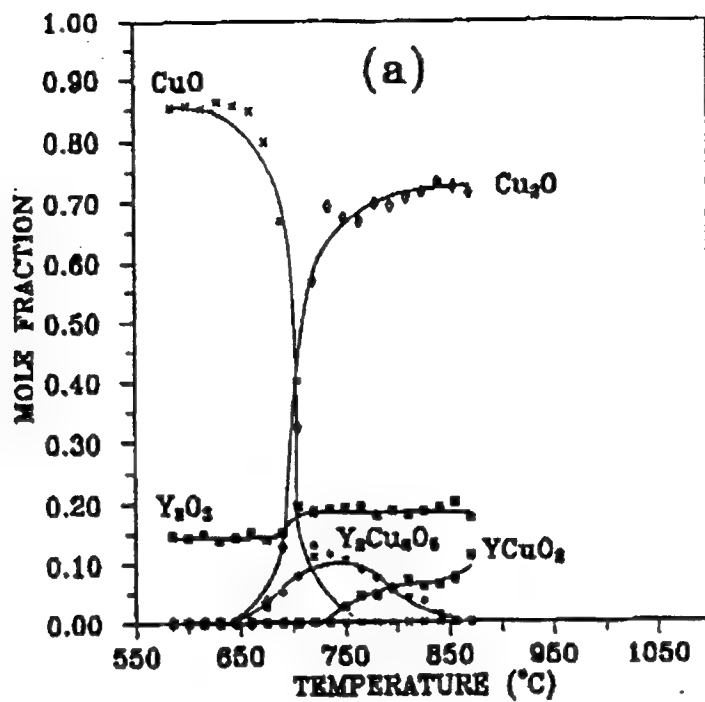


Figure 21. Y₂O₃-CuO Binary: 5°C/min in helium
 (a) nm particles
 (b) μm particles

SUPERCONDUCTING PROPERTIES

A. Flux-Trapping Experiments

Flux-trapping measurements were carried out on the seeded, single crystal $\text{YBa}_2\text{Cu}_3\text{O}_{7-x}$ samples as a function of applied field and orientation of the applied field. Experiments were performed both on the solid monoliths as well as on cylindrical single crystals to establish amount and profile of induced circulating currents required for the operation of the electromagnetic devices.

Fields of up to 2400 Gauss were trapped at 77K in the initial single grain sample (6 mm thick and 15 x 15 mm square). Figure 22 shows a result of flux-trapping capability of the single grain 123 as a function of applied field up to 2 Teslas. As can be seen, the current density of the single crystal sample is independent of applied field up to a tested field of two Teslas. The percentage of trapped field in this sample is about 100% up to 2100 Gauss of applied field. This corresponds exactly with calculated values for this size grain as will be explained in the following section.

The amount of trap field is also dependent on the direction of applied field. As is well known, the micro-cracking in the 123 crystals occurs along the a-b planes during the tetragonal-to-orthorhombic phase transformation. The microcracking is believed to cause the observed decrease in the current density and hence lower flux-trapping capabilities of these samples. As observed in Figure 23, the trapped field is significantly lower in a single crystal with cracking along the a-b plane when the applied field is parallel with cracks. When the magnetic field is applied in perpendicular to a-b planes, thus inducing current along the a-b direction, the trapped-flux is about 3 times higher than in the previous case. This experiment shows the importance of an alignment of a-b planes in a single crystal during growth process. Figure 24 shows a trapped field profile across the single crystal 123. The gradient toward the sample edge was approximately constant, indicating establishment of Bean's critical state conditions. From the profile in Figure 24 with the trapped field peaking at the center of the grain, we can establish presence of a circulating current within the sample.

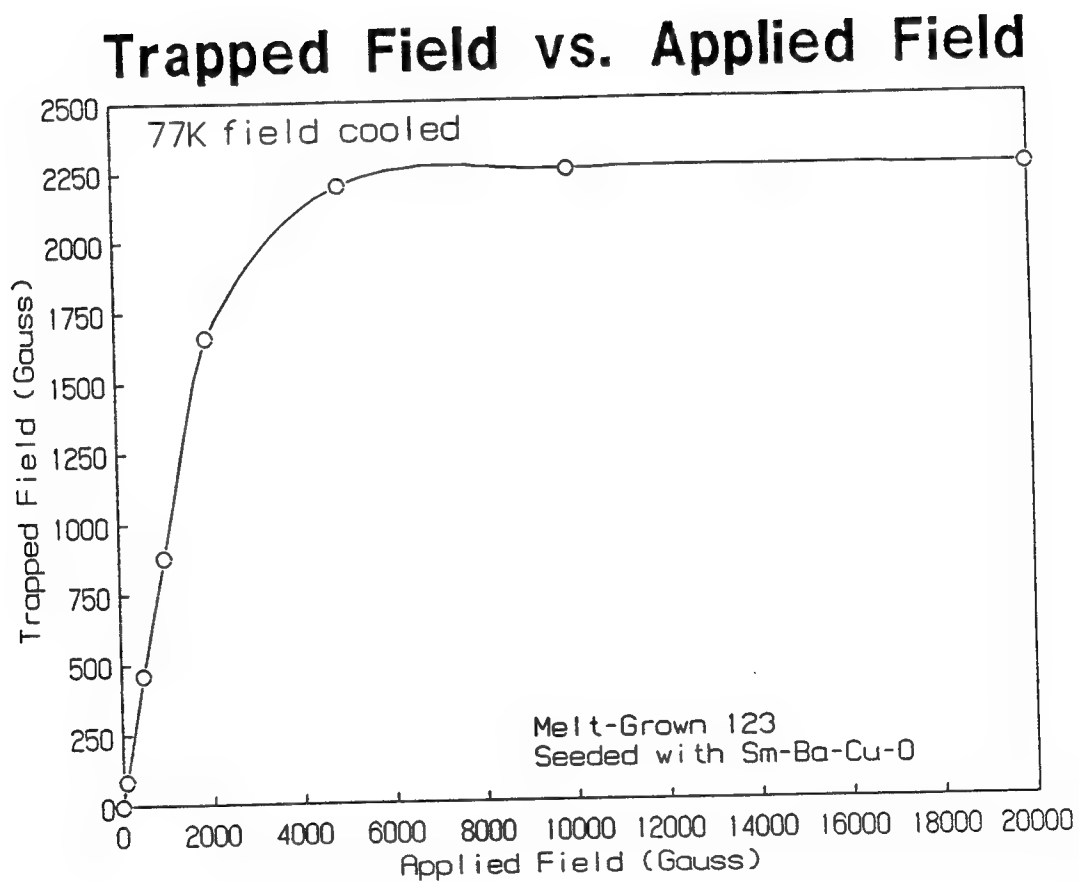


Figure 22. Trapped field vs. applied field for a $\text{YBa}_2\text{Cu}_3\text{O}_{7-x}$ grown via seeding technique.

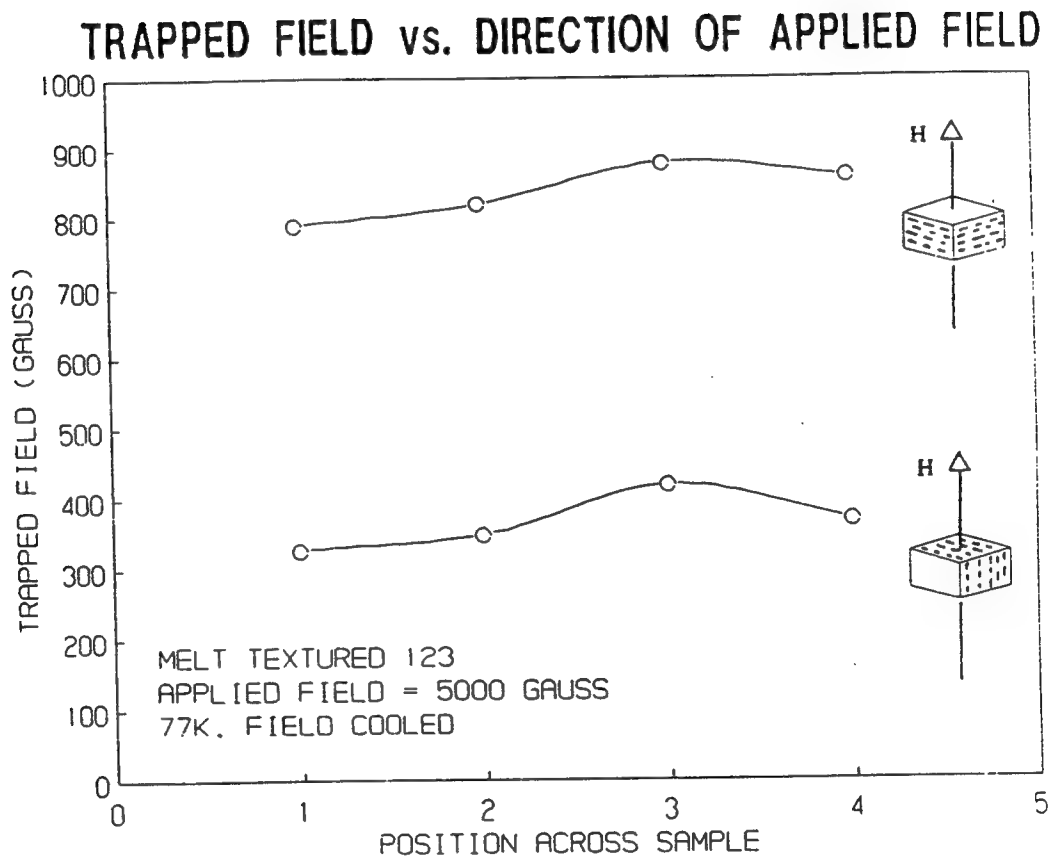


Figure 23. Trapped field vs. direction of applied field in melt-grown 123 crystal.

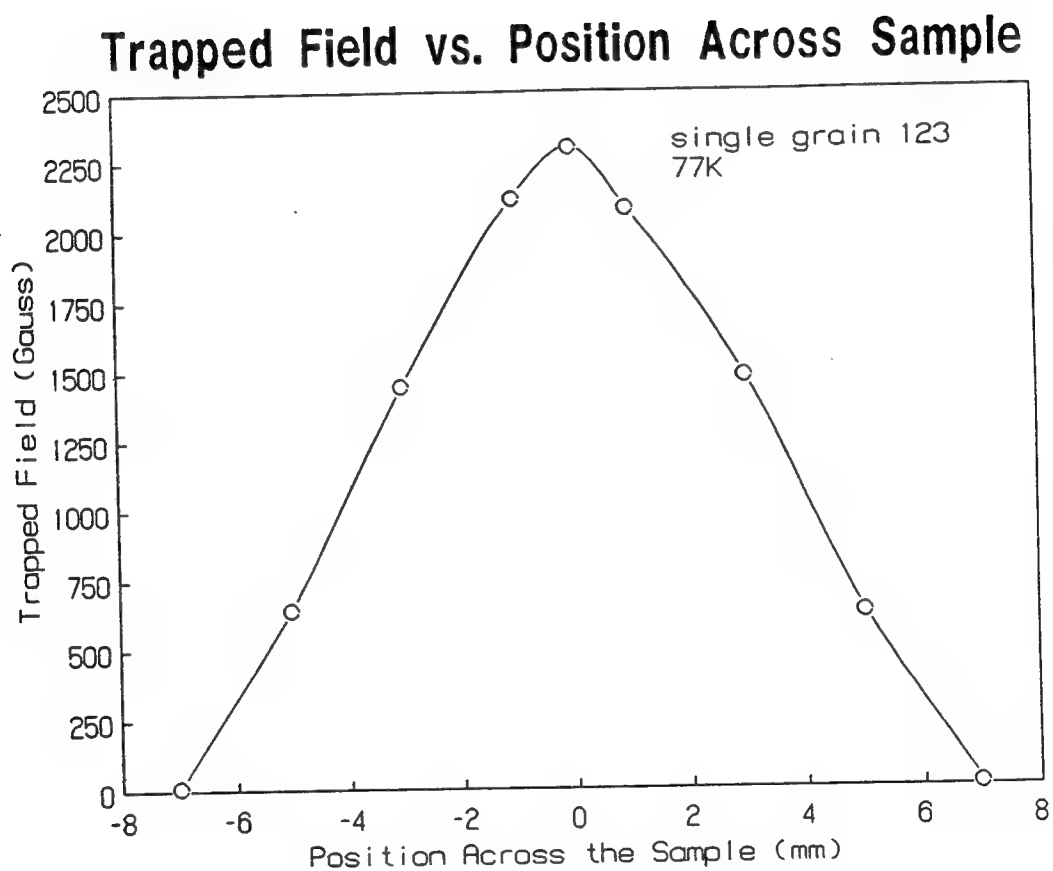


Figure 24. Surface magnetic flux density profile of a single grain seeded 123 sample.

B. Theoretical Modeling

From the maximum trapped density and the size of the sample, it is possible to calculate the overall J_c of the sample using the critical state model. Using a Bean model and Biot-Savart's law, we can express the magnetic flux density (B) at the center of the solid disc surface as follows:

$$B = \frac{\mu J l}{2} \ln \frac{1 + \sqrt{1 + \left(\frac{l}{r}\right)^2}}{\left(\frac{l}{r}\right)}$$

where J is the overall current density in the disc, l is the thickness, r is the radius of the disc and μ is the magnetic susceptibility in the vacuum. Substituting for the observed trapped magnetic flux density (2500 Gauss) at the center and the size of the disc, the J_c was calculated to be about 6.5×10^3 A/cm² in the single grain. This result directly compares to the J_c obtained by researchers at Nippon Steel Corporation, who are world leaders in amount of trapped flux in a single pellet. This result shows that our samples were limited only by the grain size and not by current density of the samples. The following calculations show theoretical trapped fields calculated for different current densities, thicknesses and radii of 123 monoliths.

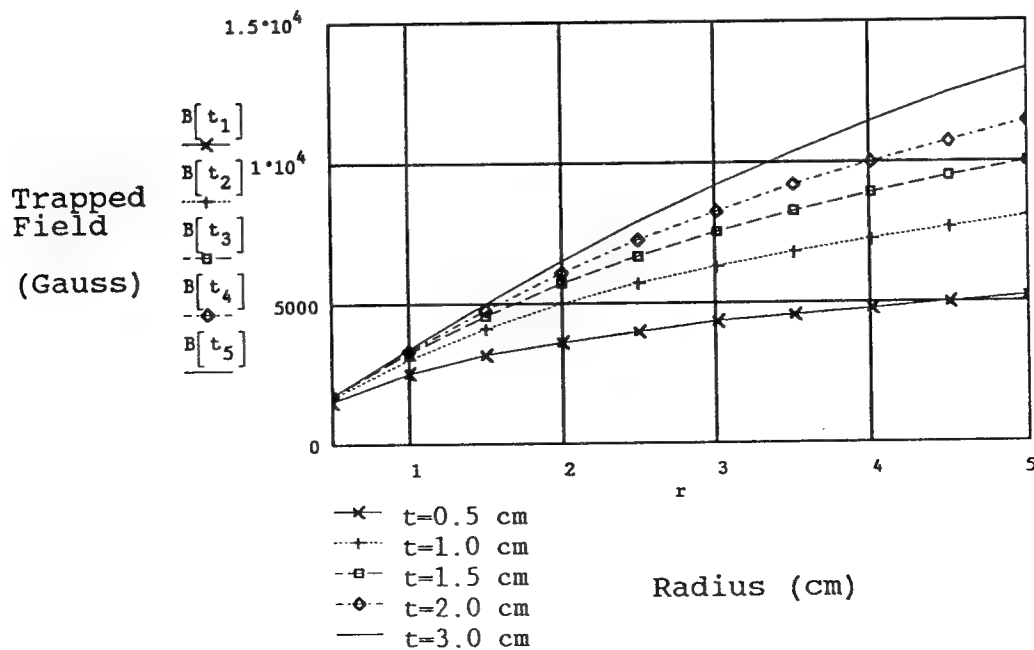
Trapped Field in a 123 Monolith.

t = thickness of 123 cylinder (cm)
r = radius of 123 cylinder (cm)
Jc = current density of 123 monolith (A/cm²)
B = trapped field in 123 monolith (Gauss)

$$r := 0.5, 1 \dots 5 \quad Jc_1 := 5500 \quad \mu := 1.256 \cdot 10^{-6}$$

$$B[t] := \mu \cdot Jc_1 \cdot 10^4 \cdot \frac{t}{200} \cdot \ln \left(\frac{1 + \sqrt{1 + \left(\frac{t}{100} \right)^2}}{\frac{t}{100}} \right) \cdot 10^4$$

$t_1 := 0.5$		$t_2 := 1$		$t_3 := 1.5$		$t_4 := 2$		$t_5 := 3$	
r	$B[t_1]$	r	$B[t_2]$	r	$B[t_3]$	r	$B[t_4]$	r	$B[t_5]$
0.5	1522	0.5	1662	0.5	1697	0.5	1709	0.5	1719
1	2493	1	3044	1	3239	1	3324	1	3393
1.5	3140	1.5	4127	1.5	4566	1.5	4788	1.5	4986
2	3618	2	4986	2	5692	2	6089	2	6478
2.5	3994	2.5	5690	2.5	6651	2.5	7237	2.5	7859
3	4303	3	6281	3	7479	3	8253	3	9133
3.5	4566	3.5	6790	3.5	8204	3.5	9159	3.5	10305
4	4795	4	7235	4	8846	4	9973	4	11384
4.5	4997	4.5	7631	4.5	9421	4.5	10708	4.5	12380
5	5178	5	7987	5	9942	5	11379	5	13303

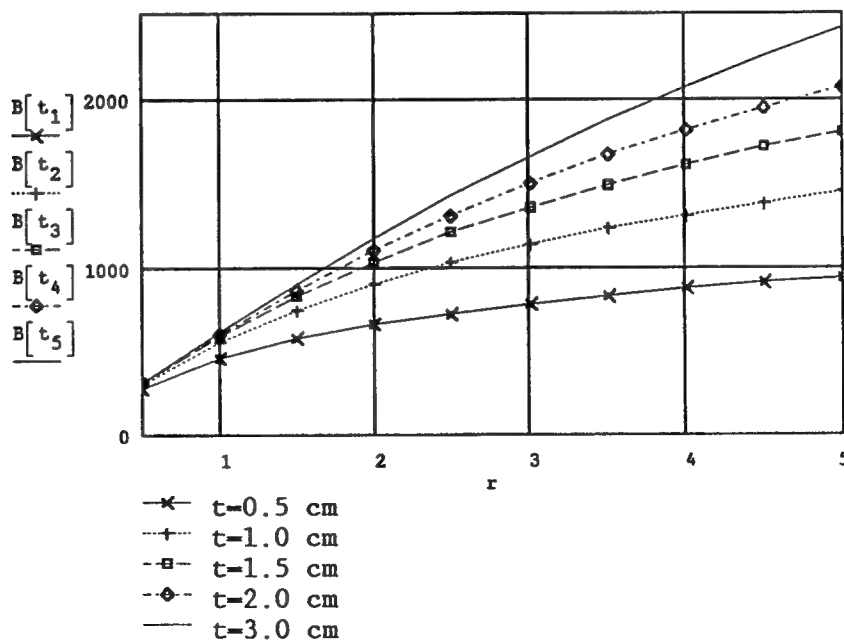


$$Jc_2 := 1000$$

$$B[t] := \left[\mu \cdot Jc_2 \cdot 10^4 \cdot \frac{t}{200} \cdot \ln \left(\frac{1 + \sqrt{1 + \left(\frac{t}{100} \right)^2}}{\frac{t}{100}} \right) \right] \cdot 10^4$$

$t_1 := 0.5$		$t_2 := 1$		$t_3 := 1.5$		$t_4 := 2$		$t_5 := 3$	
r	$B[t_1]$	r	$B[t_2]$	r	$B[t_3]$	r	$B[t_4]$	r	$B[t_5]$
0.5	277	0.5	302	0.5	308	0.5	311	0.5	313
1	453	1	554	1	589	1	604	1	617
1.5	571	1.5	750	1.5	830	1.5	871	1.5	907
2	658	2	907	2	1035	2	1107	2	1178
2.5	726	2.5	1034	2.5	1209	2.5	1316	2.5	1429
3	782	3	1142	3	1360	3	1501	3	1661
3.5	830	3.5	1234	3.5	1492	3.5	1665	3.5	1874
4	872	4	1315	4	1608	4	1813	4	2070
4.5	909	4.5	1387	4.5	1713	4.5	1947	4.5	2251
5	941	5	1452	5	1808	5	2069	5	2419

Trapped
Field
(Gauss)

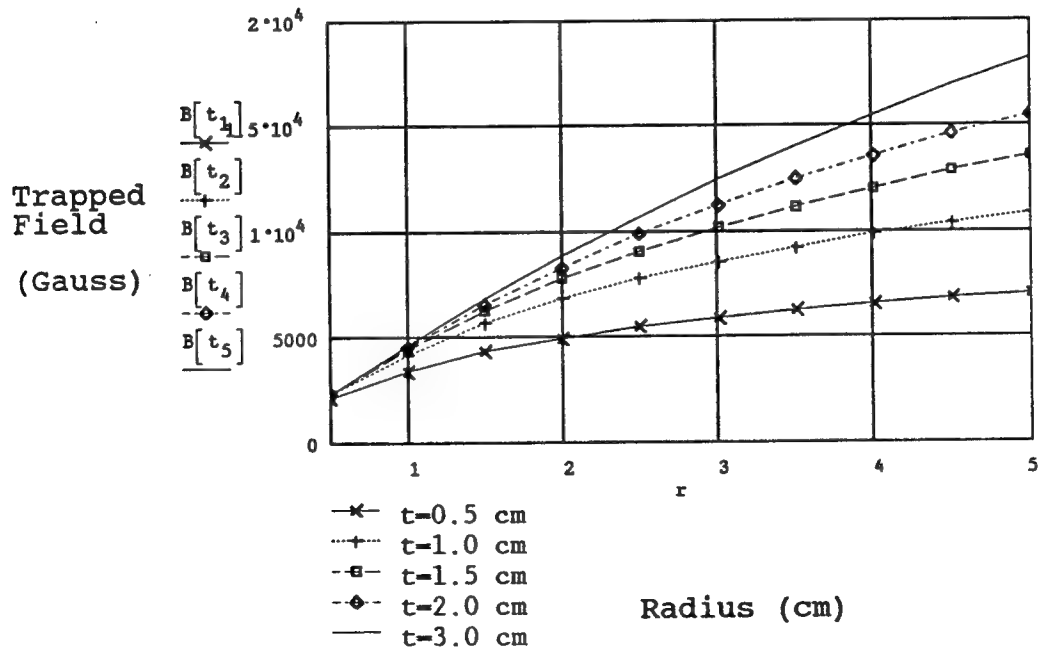


Radius (cm)

$$Jc_3 := 7500$$

$$B[t] := \left[\mu \cdot Jc_3 \cdot 10^4 \cdot \frac{t}{200} \cdot \ln \left(\frac{1 + \sqrt{1 + \left(\frac{t}{100} \right)^2}}{\left(\frac{t}{100} \right)} \right) \right] \cdot 10^4$$

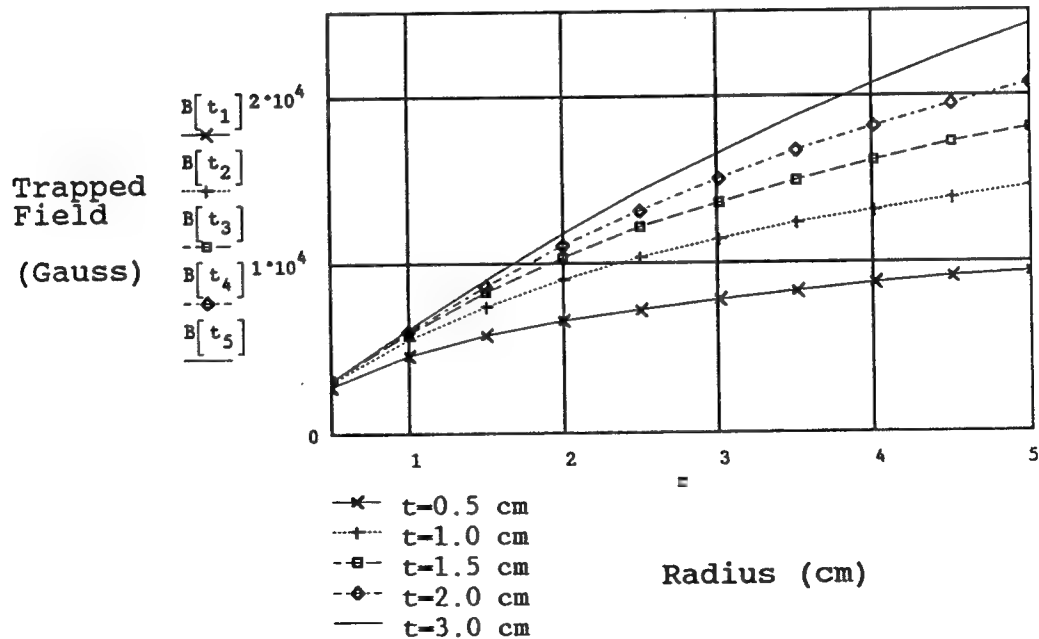
$t_1 := 0.5$		$t_2 := 1$		$t_3 := 1.5$		$t_4 := 2$		$t_5 := 3$	
r	$B[t_1]$	r	$B[t_2]$	r	$B[t_3]$	r	$B[t_4]$	r	$B[t_5]$
0.5	2076	0.5	2267	0.5	2313	0.5	2331	0.5	2344
1	3400	1	4151	1	4417	1	4533	1	4627
1.5	4282	1.5	5627	1.5	6227	1.5	6529	1.5	6800
2	4933	2	6800	2	7762	2	8303	2	8833
2.5	5446	2.5	7758	2.5	9070	2.5	9868	2.5	10717
3	5868	3	8565	3	10199	3	11255	3	12454
3.5	6227	3.5	9259	3.5	11187	3.5	12490	3.5	14052
4	6539	4	9866	4	12063	4	13599	4	15523
4.5	6814	4.5	10406	4.5	12847	4.5	14602	4.5	16882
5	7061	5	10892	5	13557	5	15517	5	18140



$$Jc_k := 10000$$

$$B[t] := \left[\mu \cdot Jc_k \cdot 10^4 \cdot \frac{t}{200} \cdot \ln \left(\frac{1 + \sqrt{1 + \left(\frac{t}{100} \right)^2}}{\left(\frac{r}{100} \right)} \right) \right] \cdot 10^4$$

$t_1 := 0.5$		$t_2 := 1$		$t_3 := 1.5$		$t_4 := 2$		$t_5 := 3$	
r	$B[t_1]$	r	$B[t_2]$	r	$B[t_3]$	r	$B[t_4]$	r	$B[t_5]$
0.5	2768	0.5	3022	0.5	3085	0.5	3108	0.5	3126
1	4533	1	5535	1	5889	1	6044	1	6169
1.5	5710	1.5	7503	1.5	8303	1.5	8706	1.5	9066
2	6577	2	9066	2	10349	2	11070	2	11778
2.5	7261	2.5	10345	2.5	12093	2.5	13158	2.5	14290
3	7824	3	11420	3	13599	3	15006	3	16605
3.5	8303	3.5	12345	3.5	14916	3.5	16653	3.5	18736
4	8718	4	13155	4	16084	4	18132	4	20698
4.5	9085	4.5	13875	4.5	17130	4.5	19470	4.5	22509
5	9414	5	14522	5	18076	5	20689	5	24187



$$J_{c5} := 15000$$

$$B[t] := \left[\mu \cdot J_{c5} \cdot 10^4 \cdot \frac{t}{200} \cdot \ln \left(\frac{1 + \sqrt{1 + \left[\frac{t}{100} \right]^2}}{\left[\frac{t}{100} \right]} \right) \right] \cdot 10^4$$

$t_1 := 0.5$		$t_2 := 1$		$t_3 := 1.5$		$t_4 := 2$		$t_5 := 3$	
r	$B[t_1]$	r	$B[t_2]$	r	$B[t_3]$	r	$B[t_4]$	r	$B[t_5]$
0.5	4151	0.5	4533	0.5	4627	0.5	4662	0.5	4688
1	6800	1	8303	1	8833	1	9066	1	9254
1.5	8565	1.5	11255	1.5	12454	1.5	13059	1.5	13599
2	9866	2	13599	2	15523	2	16605	2	17667
2.5	10892	2.5	15517	2.5	18140	2.5	19737	2.5	21435
3	11736	3	17130	3	20399	3	22509	3	24908
3.5	12454	3.5	18517	3.5	22375	3.5	24980	3.5	28103
4	13077	4	19732	4	24126	4	27198	4	31047
4.5	13628	4.5	20812	4.5	25695	4.5	29205	4.5	33764
5	14122	5	21783	5	27114	5	31034	5	36280

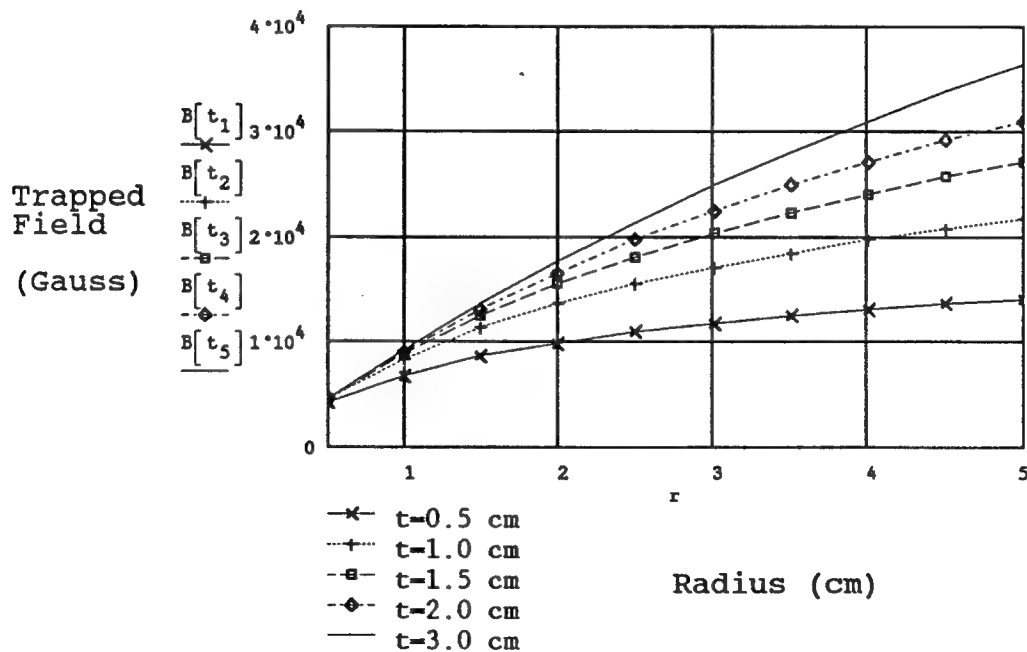


Figure 25 shows a time dependence of trapped flux in a seeded single grain of 123 in applied field of 1000 and 4500 Gauss. As can be observed, the logarithmic decay of trapped flux is very significant at 4500 Gauss due to flux creep from poor pinning properties. The flux creep at 1000 Gauss is negligible. When the temperature during flux-trapping experiments is lowered from 77K to 74K (Figure 26) we can see a significant decrease in flux creep at that temperature. From our previous calculations and resulting experiments we concluded that our samples are limited by grain size rather than current density. To prove this conclusion, we trapped field in two single grain samples piled on top of each other, hence doubling the grain size. From Figure 27 it is obvious that this conclusion was accurate, as we trapped almost double field, as predicted accurately by our calculations.

Large YBCO single crystals require very long oxygen annealing treatments due to high density and slow oxygen diffusion rates. The oxygen annealing time vs. trapped field results for a 1" diameter single crystal are shown in Figure 28.

Fields of up to about 4900 Gauss were trapped at 77K in the best 1.3" diameter single crystal sample (Figure 29). As expected, the current density of the single crystal sample is independent of an applied field up to a tested field of two Teslas. In contrast to earlier samples, the magnetic field in the single crystals was very uniform over the surface of the sample (Figures 30-31). This profile clearly shows a presence of a circulating current in a one turn single crystal conductor, with macroscopic current densities exceeding 1.2×10^4 A/cm² at 77K in an applied field of up to at least 2 Tesla.

Time Dependence of Trapped Flux in 123

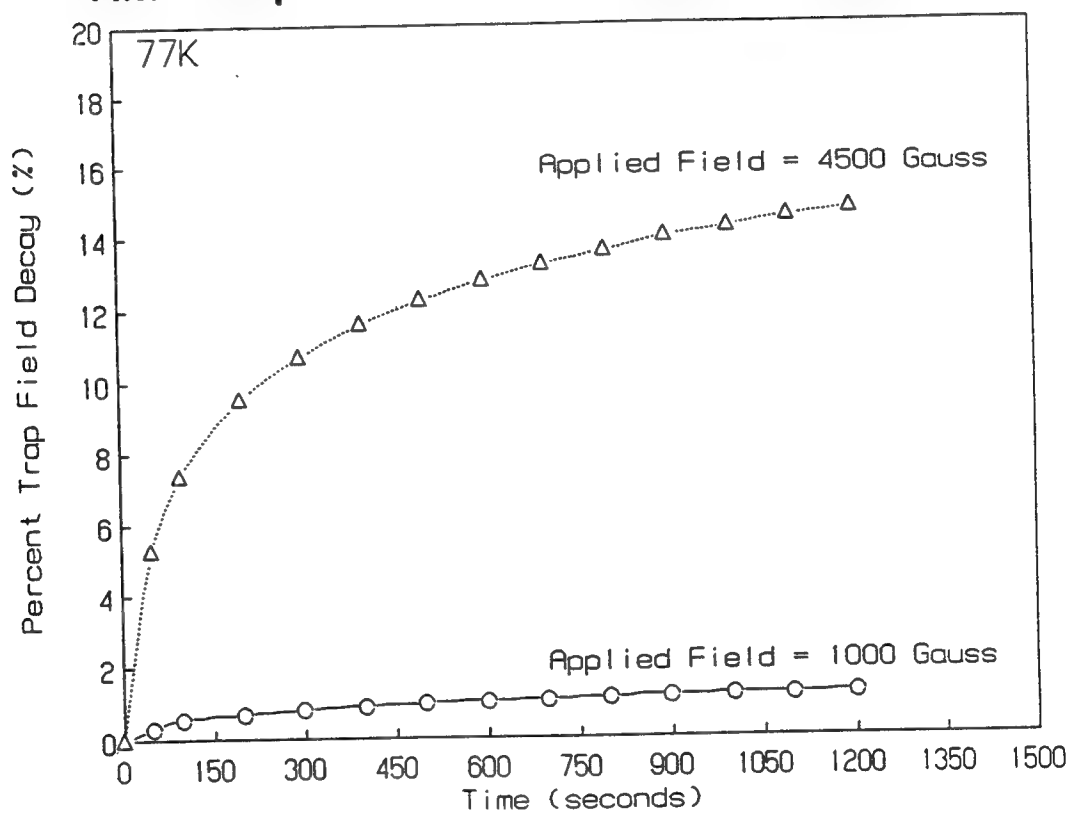


Figure 25. Time dependence of trapped flux in single crystal 123.

Time Dependence of Trapped Flux in 123

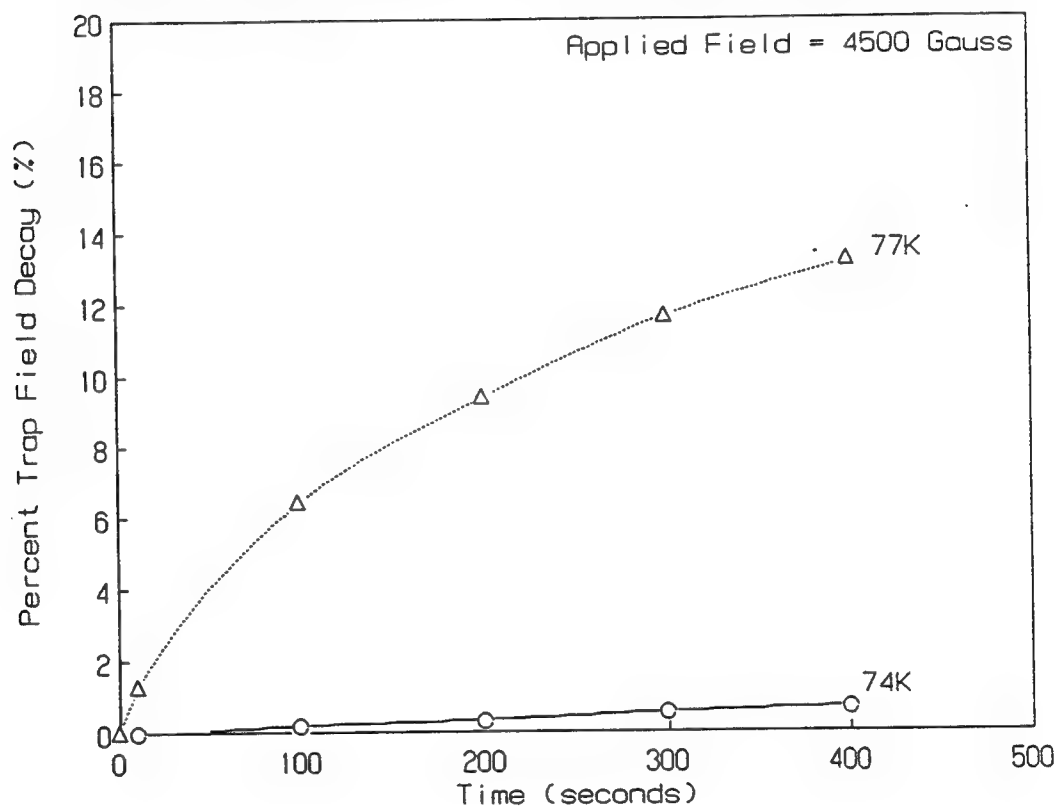


Figure 26. Time dependence of trapped flux in single crystal 123 as a function of temperature.

Trapped Field vs. Applied Field

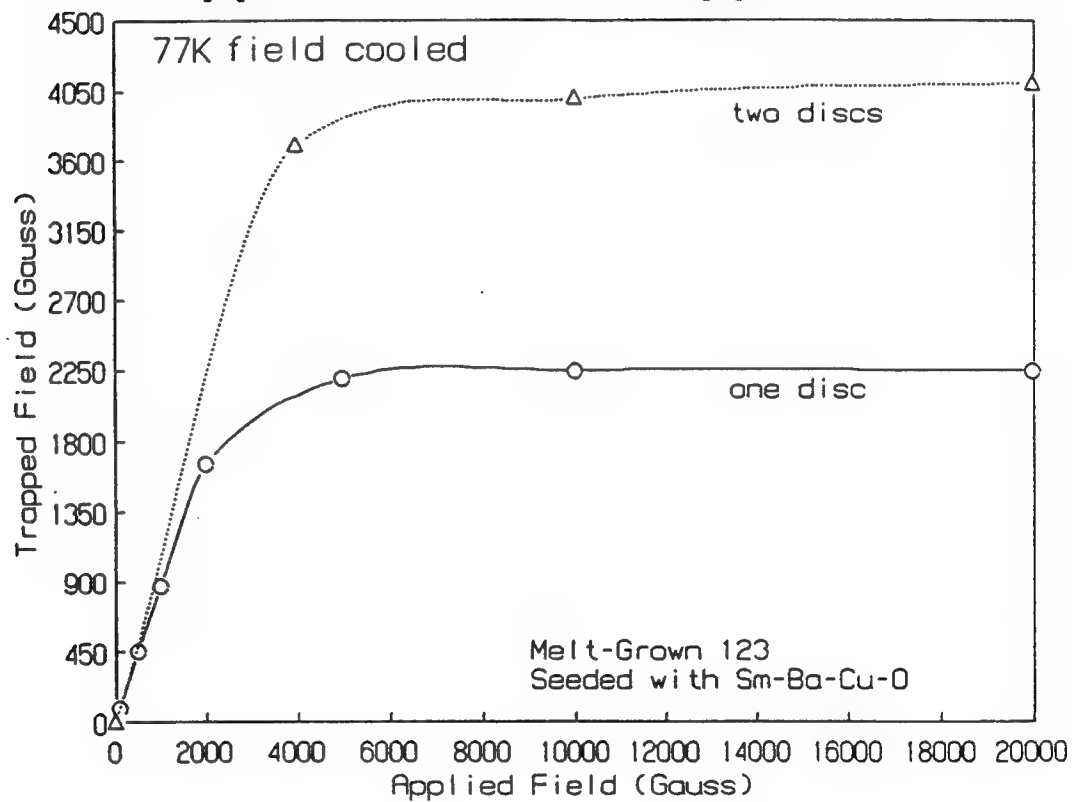


Figure 27. Trapped field vs. applied field for single and double piled single crystal 123.

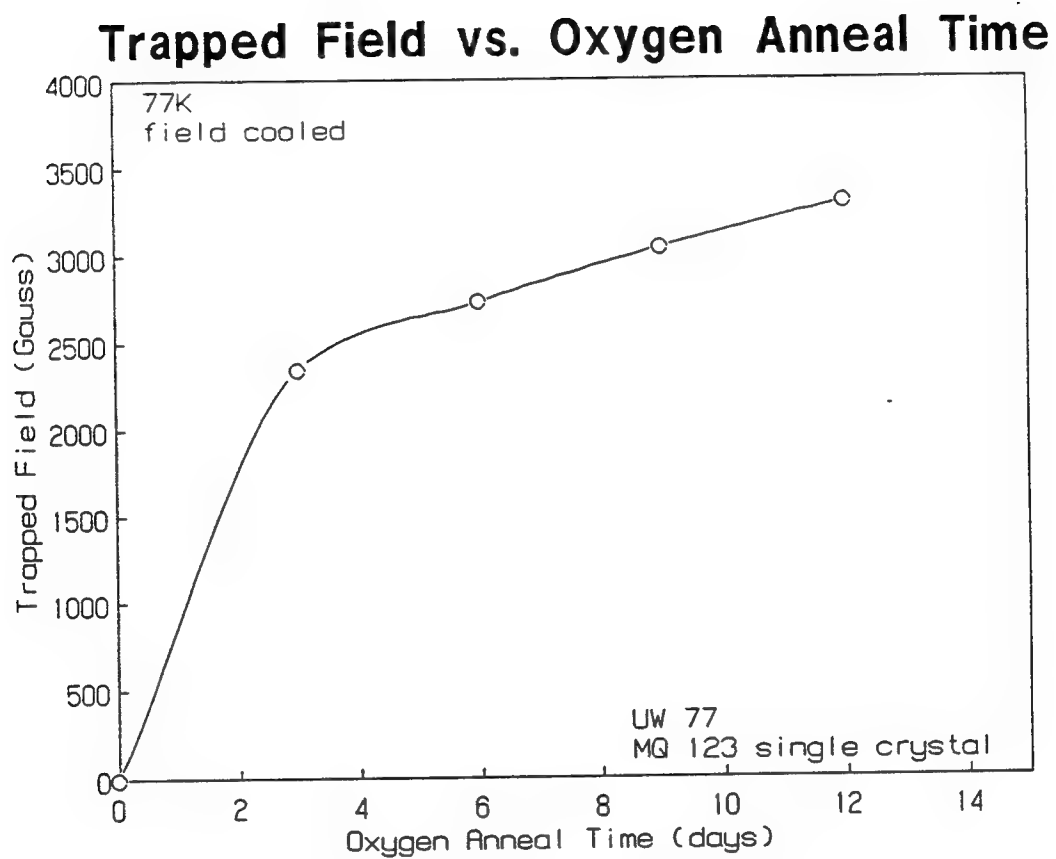


Figure 28. Trapped field as a function of oxygen annealing time in a single crystal 123 disk.

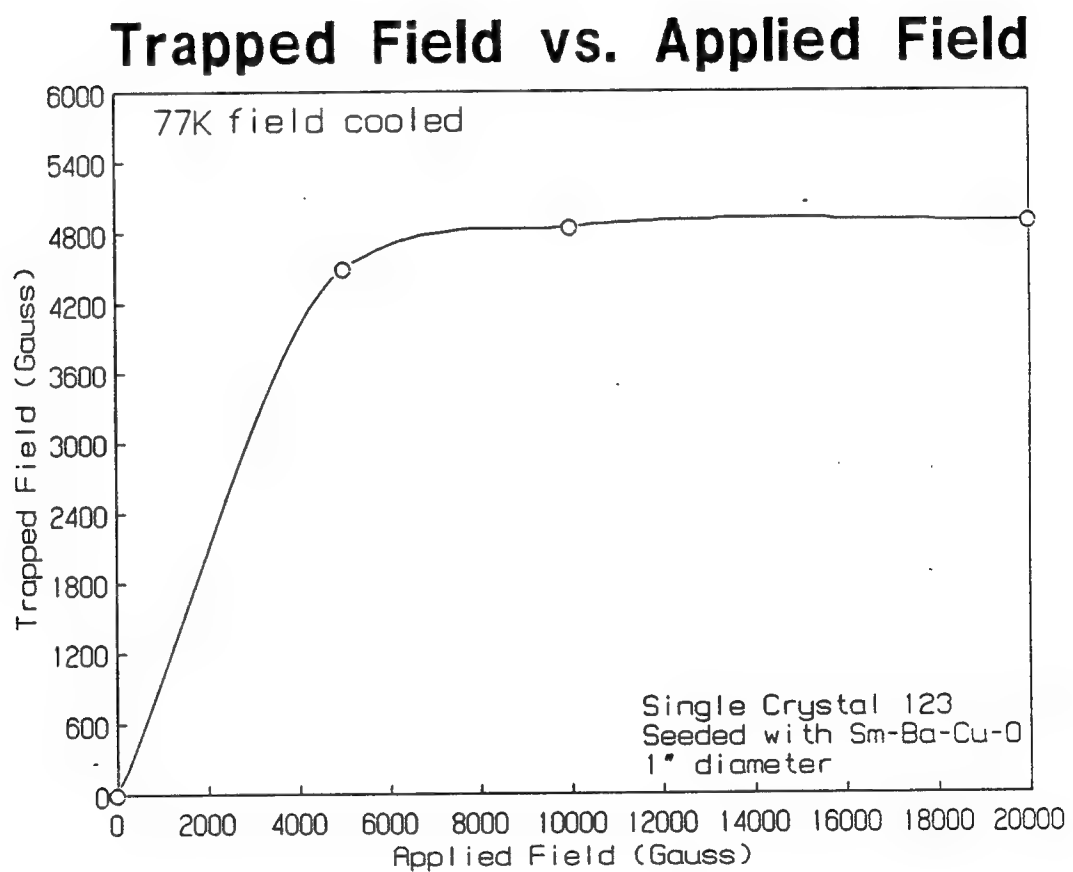


Figure 29. Trapped field vs. applied field for latest $\text{YBa}_2\text{Cu}_3\text{O}_{7-x}$ single crystal grown via seeding technique.

Trapped Field in 123 Disk

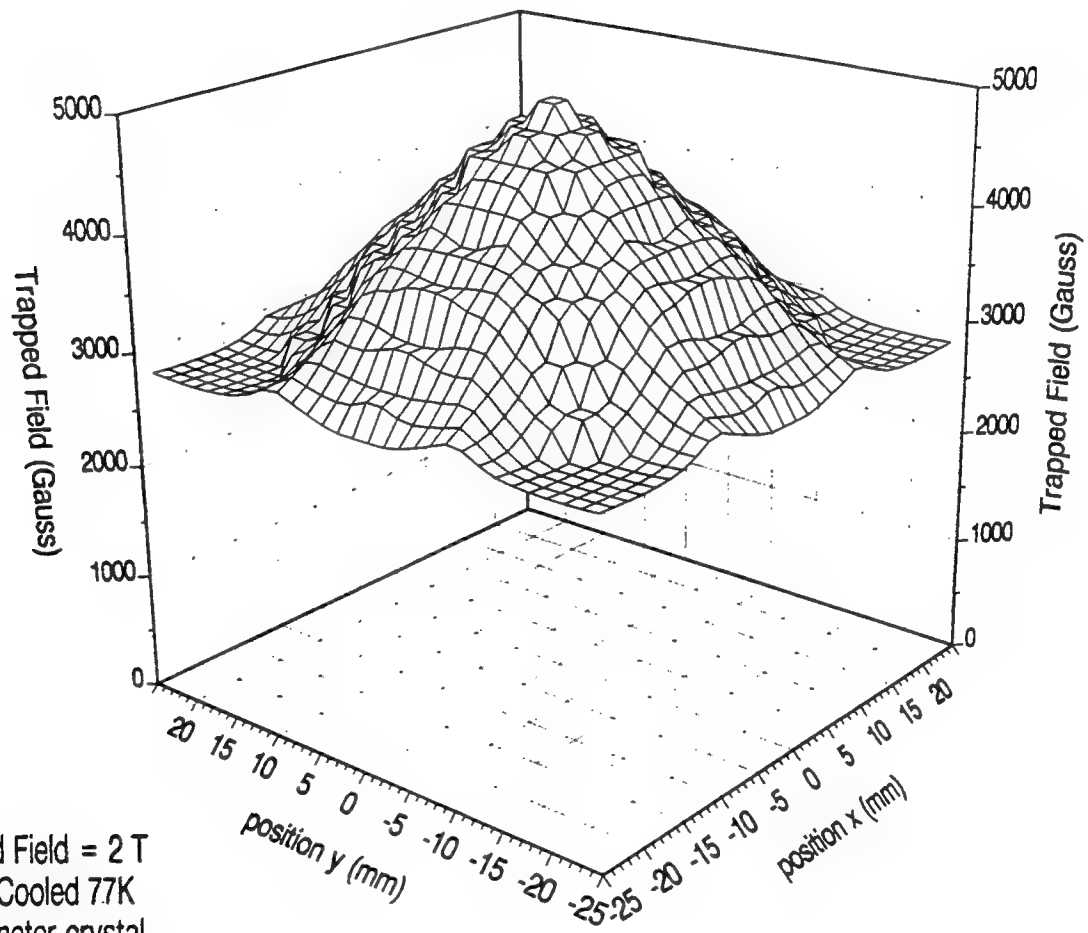


Figure 30. Surface magnetic flux density profile of a single crystal 123 sample from Figure 29..

Trapped Field vs. Position Across Sample

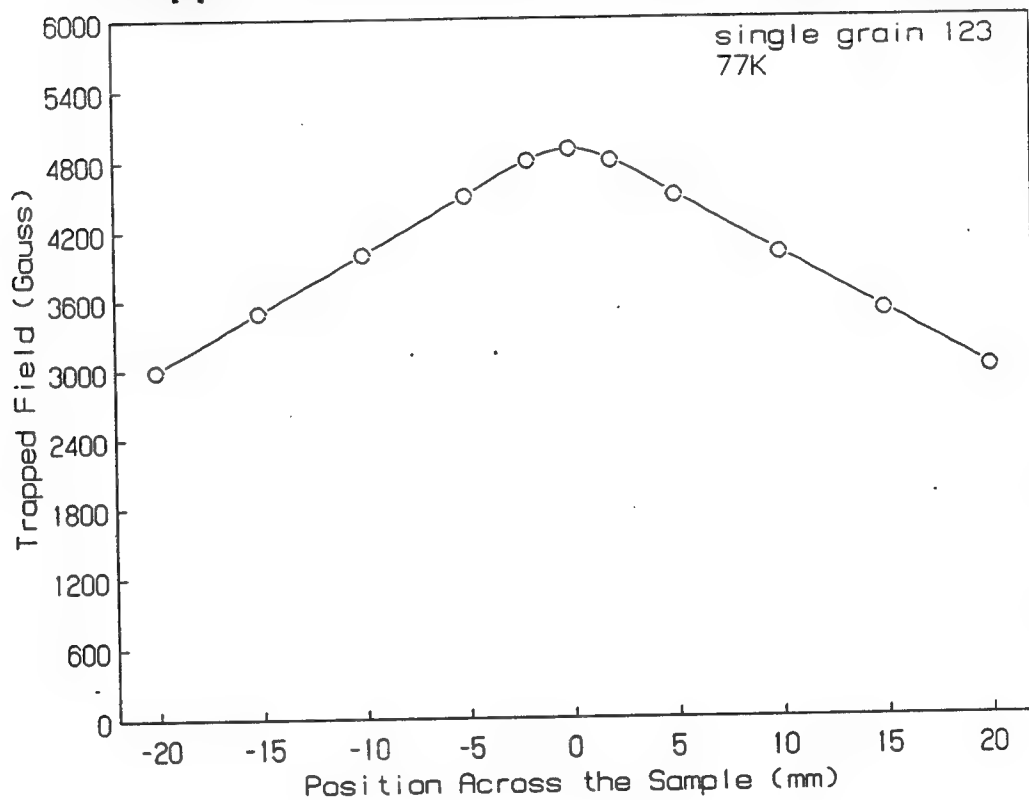


Figure 31. Surface magnetic flux density profile of a single crystal 123 sample from Figure 30.

C. Current Densities

Critical current density measurements were performed at Boeing and at Wright Patterson Air Force Base by Dr. Gregory Kozlowski. The current densities were measured in 1" diameter single crystals by magnetization up to a field of 9 Teslas at temperatures ranging from 4.2K to 85K. The current densities were also calculated in 1" and 2" crystals from the trapped flux measurements.

Figures 32-33 shows current densities of large single crystal YBCO as a function of applied magnetic field. The magnetic field was applied parallel with the c-axis. The current densities measured when field was applied at the direction perpendicular to the c-axis were lower by a factor of three from the parallel direction. Figure 34 shows a relationship of current density versus temperature. The current density exceeds 3×10^4 A/cm² at 0 Tesla and 77K, 1.2×10^4 A/cm² at 2 Tesla and 77K, and 7.75×10^5 A/cm² at 1 Tesla and 4.2K. As can be seen from the Figure 33, the current density at temperatures from 4.2-40K is almost independent of the applied magnetic field up to a measured field of 8 Teslas. This shows that the single crystals are very pure lacking the common weak links often associated with bulk YBCO samples. The current densities calculated from trapped flux experiments in large single crystals at 77K correlated very well with the magnetization measurements.

Figures 35-40 show magnetization results of YBCO single crystals grown by a seeding technique. As can be seen again, the current density is almost independent of the applied field in the 4.2-40K temperature range. These single crystals are also very cryostable at the measured current densities and temperatures against flux jumps, as there is no evidence of a thermal instability even at 4.2K up to a field 8 Teslas. However, one single crystal sample, not fully oxygenated, exhibited flux jumps at 4.2K and 4 Teslas (Figure 40).

Current Density vs. Applied Field

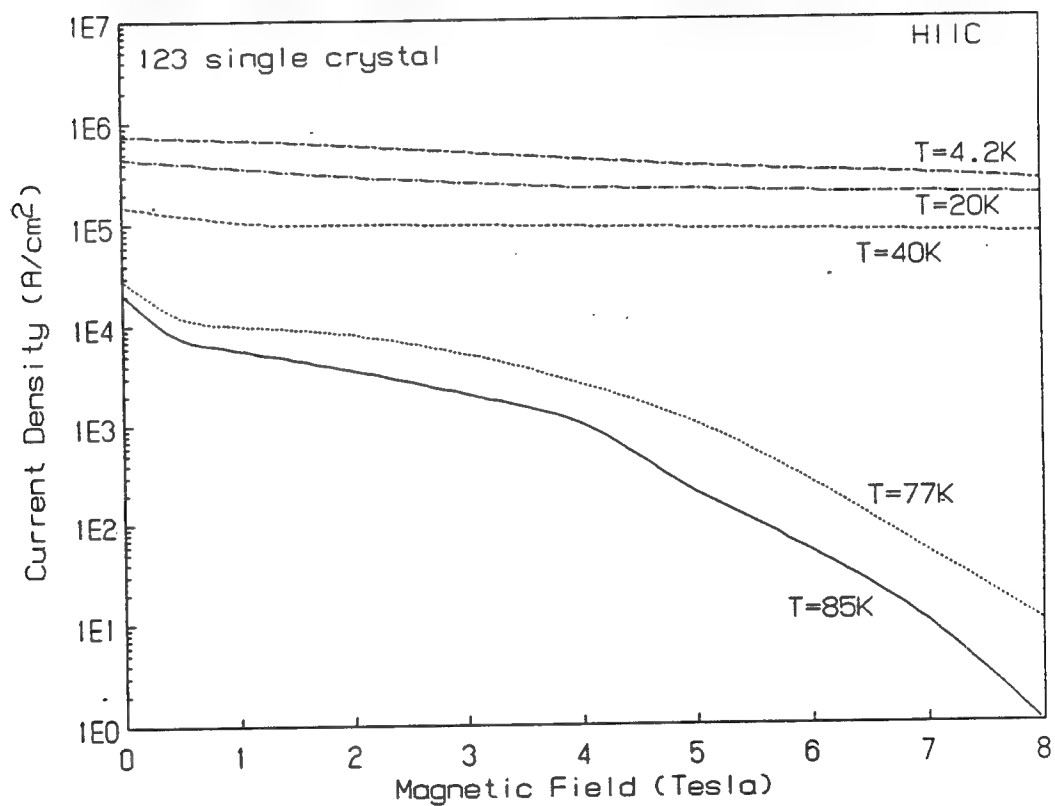


Figure 32. Current density vs. applied field in a single crystal YBCO.

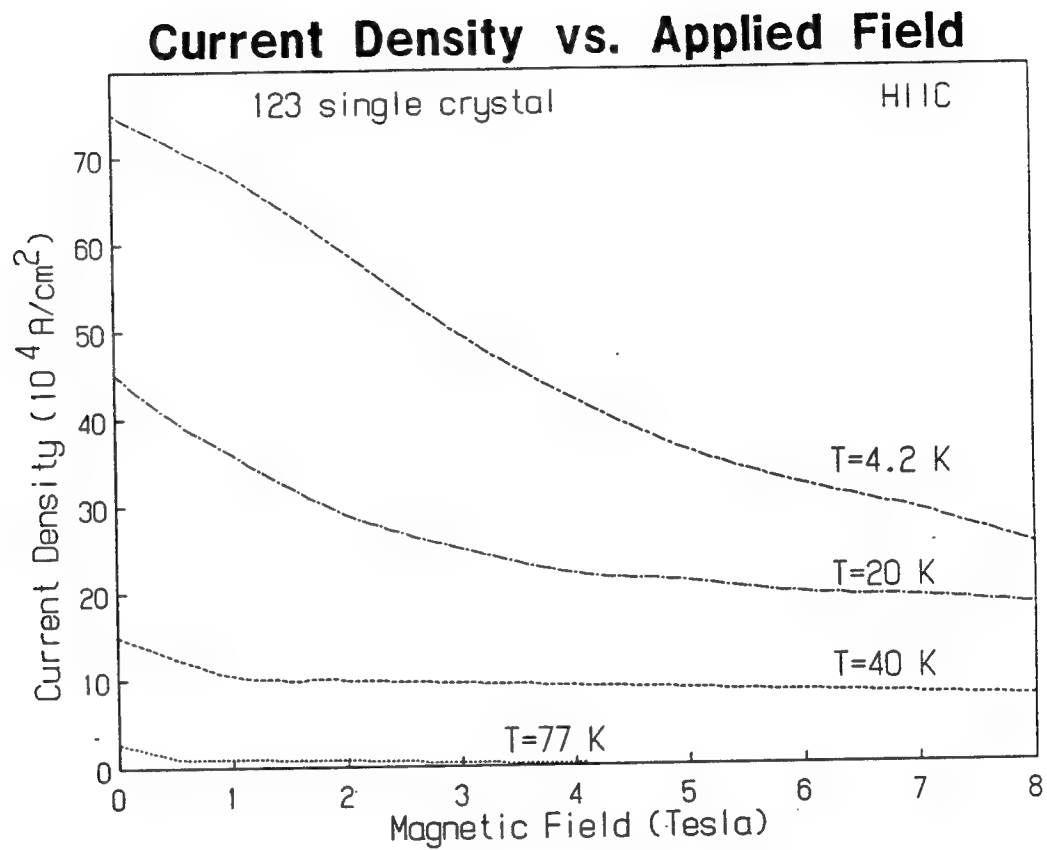


Figure 33. Current density vs. applied field in a single crystal YBCO.

Current Density vs. Temperature

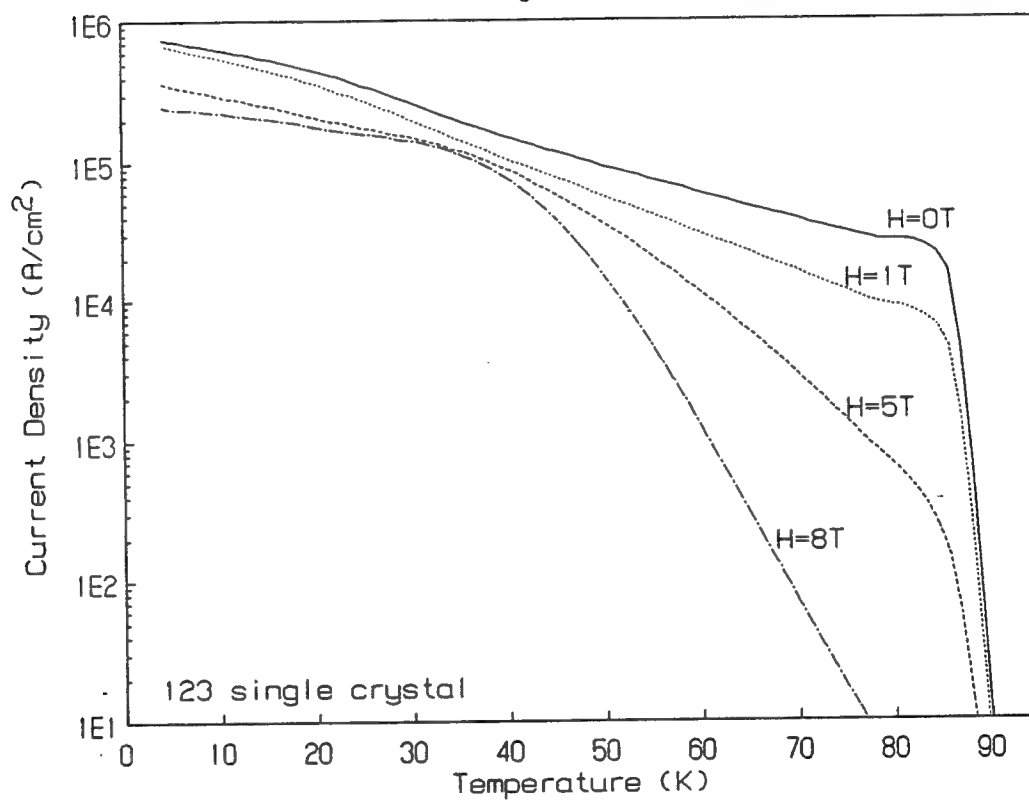


Figure 34. Current density vs. temperature in a single crystal YBCO.

YBa₂Cu₃O_x (SINGLE CRYSTAL)
T=85K (H || C)

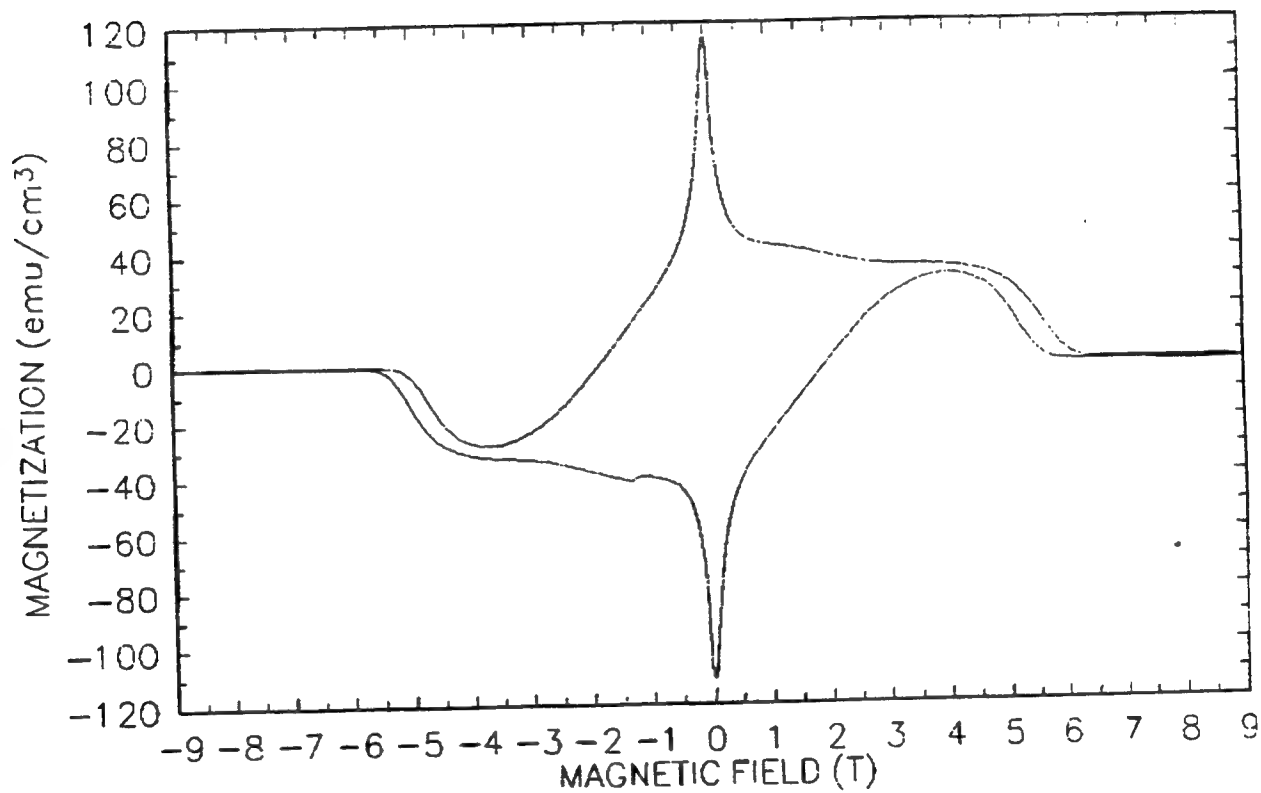


Figure 35. Magnetization curve of YBCO single crystal at 85K.

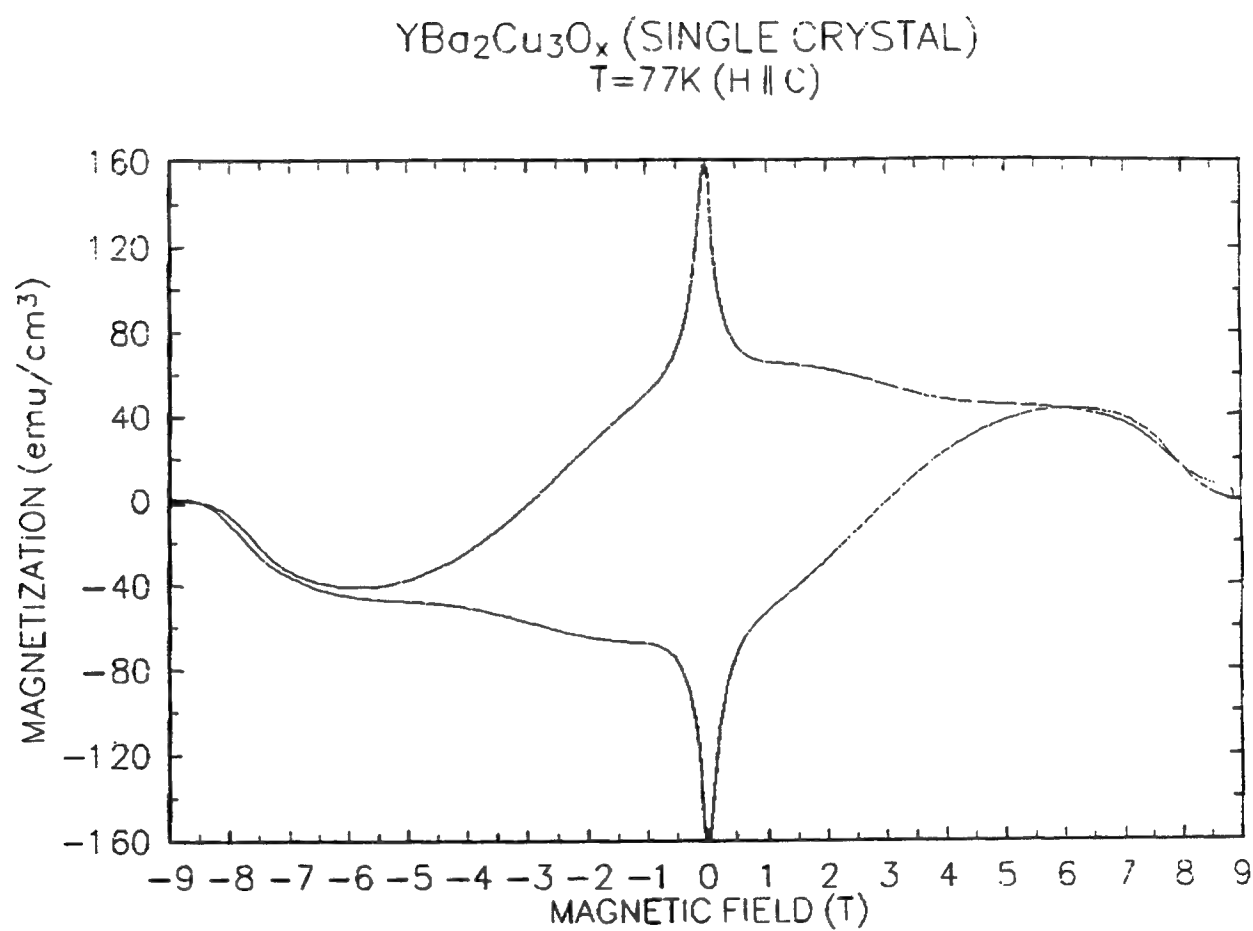


Figure 36. Magnetization curve of YBCO single crystal at 77K.

YBa₂Cu₃O_x (SINGLE CRYSTAL)
T=40K (H || C)

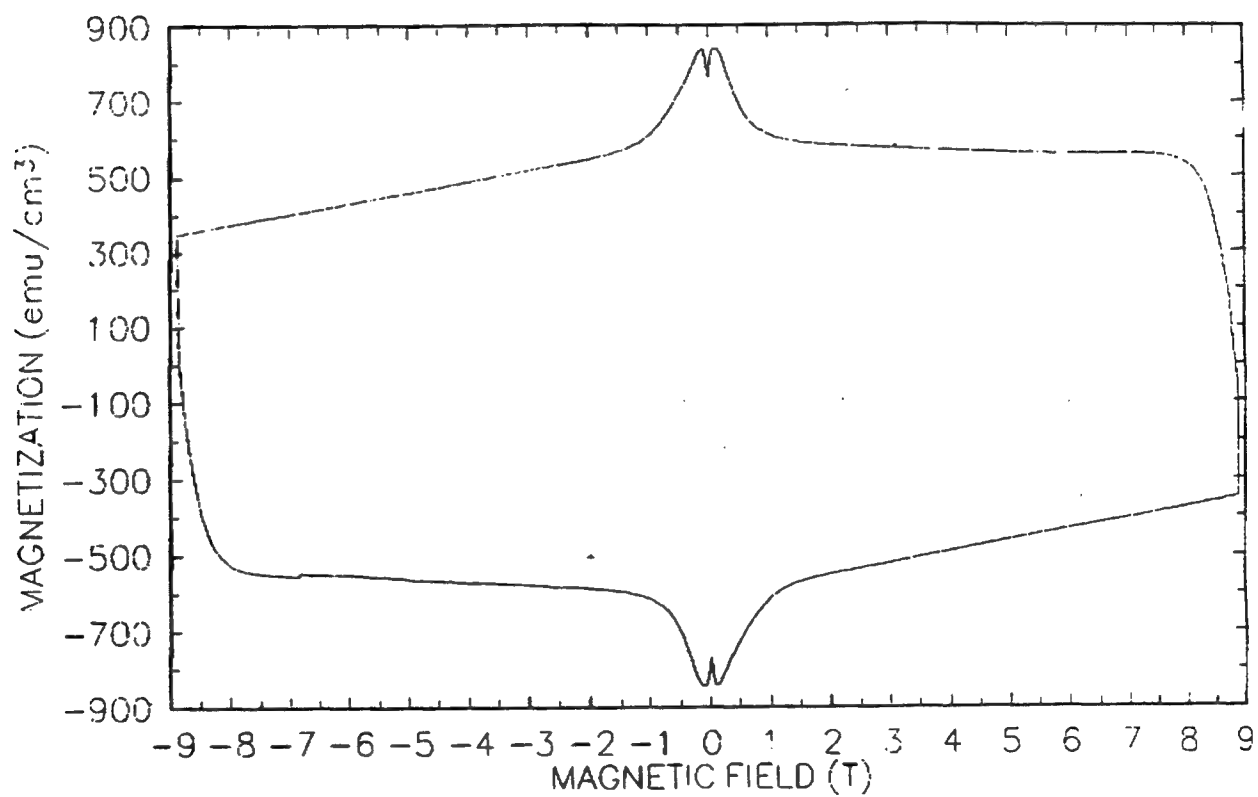


Figure 37. Magnetization curve of YBCO single crystal at 40K.

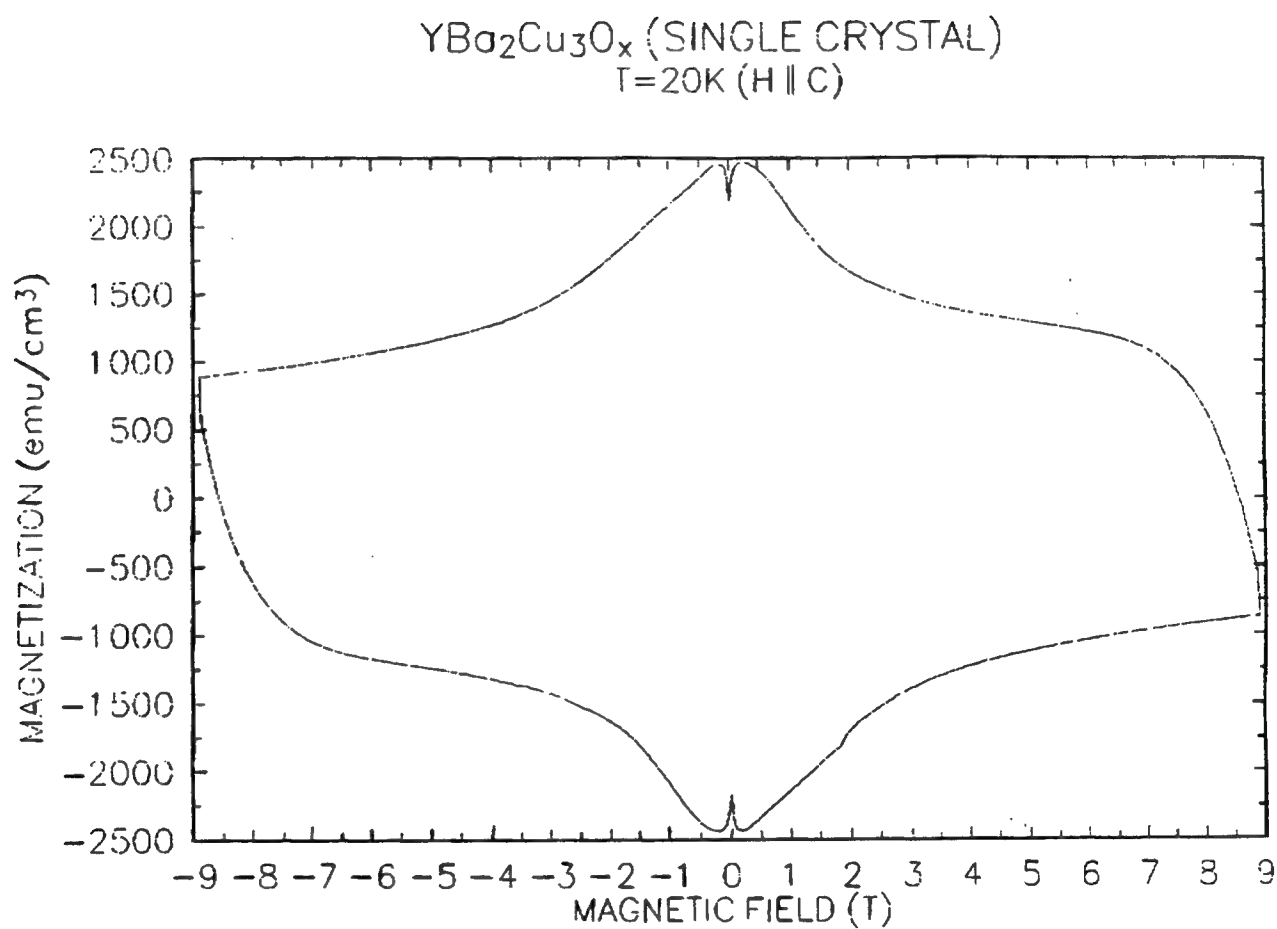


Figure 38. Magnetization curve of YBCO single crystal at 20K.

YBa₂Cu₃O_x (SINGLE CRYSTAL)
T=4.2K (H || C)

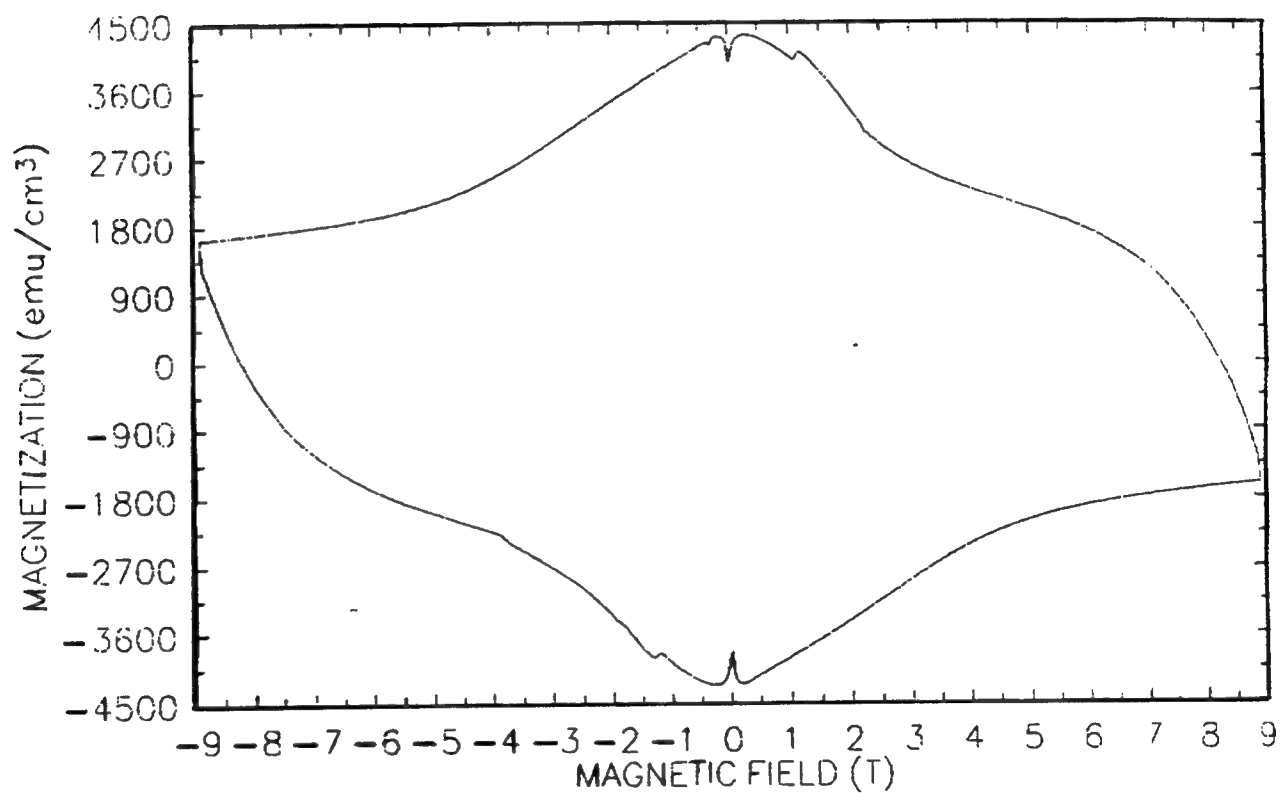


Figure 39. Magnetization curve of YBCO single crystal at 4.2K.

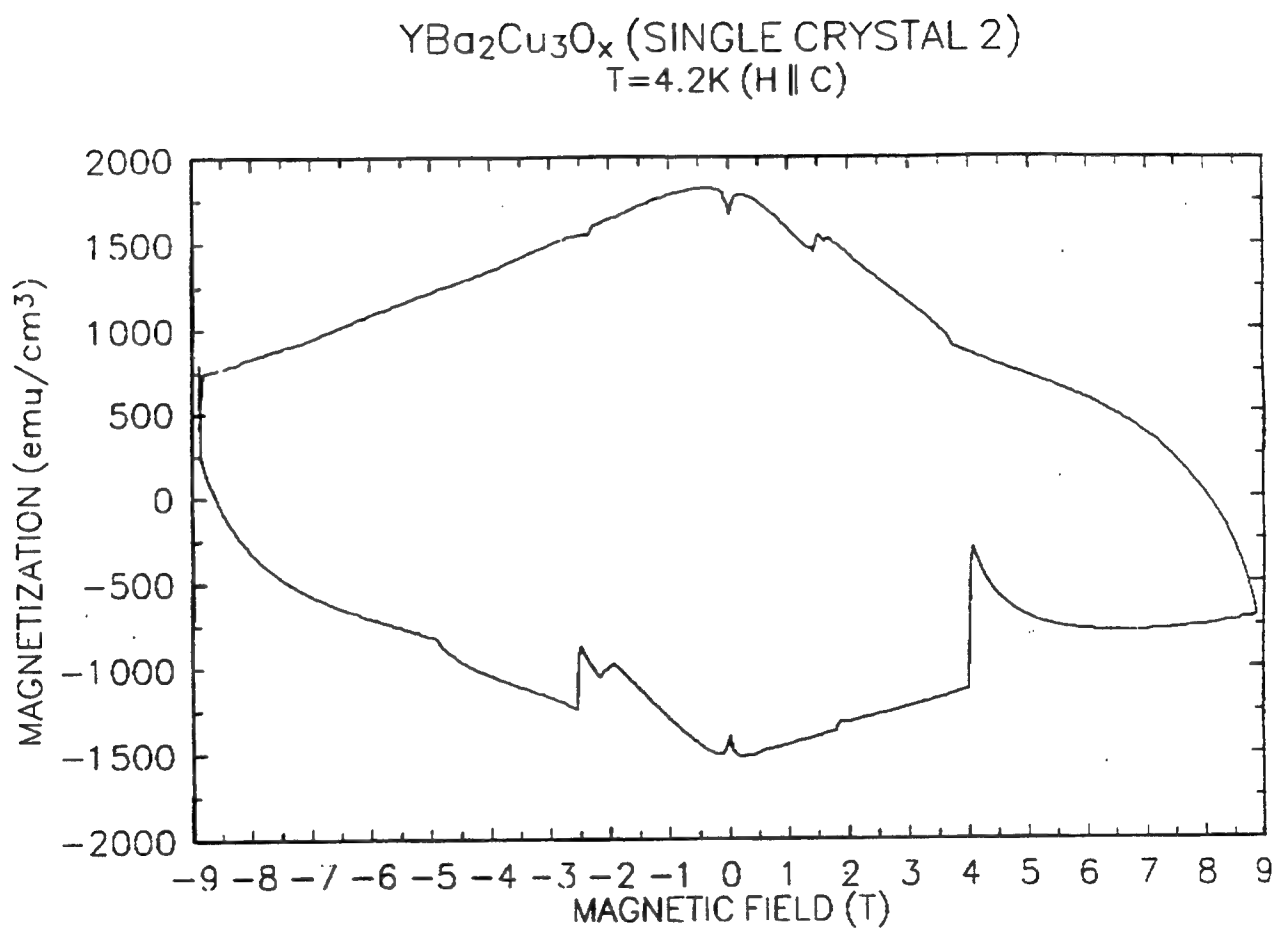


Figure 40. Magnetization curve of partially oxygenated single crystal at 4.2K.

DEVICE REQUIREMENTS AND DESIGNS

A. Flux Trap Enhancer

In experimenting with ways to increase the flux capacity of our existing materials, a method to amplify or enhance the attractive force of the flux-trap magnets was developed. Enhancement of the flux-trapping capabilities is accomplished by inserting a core of high permeability material (with a high saturation field) such as soft iron, superalloy, mu metal, permendur, etc., into a hole within a cylinder, ring, or other shape of high temperature superconductor. The trapped field, B, within the core of the superconductor is then enhanced according to

$$B = \mu_0 \cdot \mu_r \cdot I$$

where: I = current carried by the superconducting ring
 μ_0 = magnet permeability of free space
 μ_r = relative magnetic permeability of core material
material at the field of the superconductor
with a free space core

The core field can be enhanced up to the magnetic saturation of the core material. One example was a 1.3 inch diameter sample was tested and measured to have a flux trapping capability of 4000 gauss. When a flux enhancer plug was inserted into the center of the cylinder and the identical test was repeated, the usable field increased to over 8500 gauss (Figure 41). It is expected that similar enhancements will be observed for even better samples. Figure 42 illustrates the flux trapping setup experiment used to test the usable magnetic field in these samples.

The implications of this discovery are vast. This method makes it possible to have a much greater usable field available in the superconducting disks for use in superconducting magnets, clamps, and actuating devices requiring larger magnetic forces.

B. Superconducting Clamp

Among the latest potential applications for early technology insertion in manufacture of military and commercial airplanes is a superconducting clamp based on flux-trap magnets (Figure 43). Permanent magnets are used widely and in diverse applications such as in attracting and holding ferromagnetic objects and in clamping non-magnetic objects and assemblies during manufacturing. Currently, permanent magnets are frequently the only feasible way of holding objects in confined areas during manufacturing. In addition to

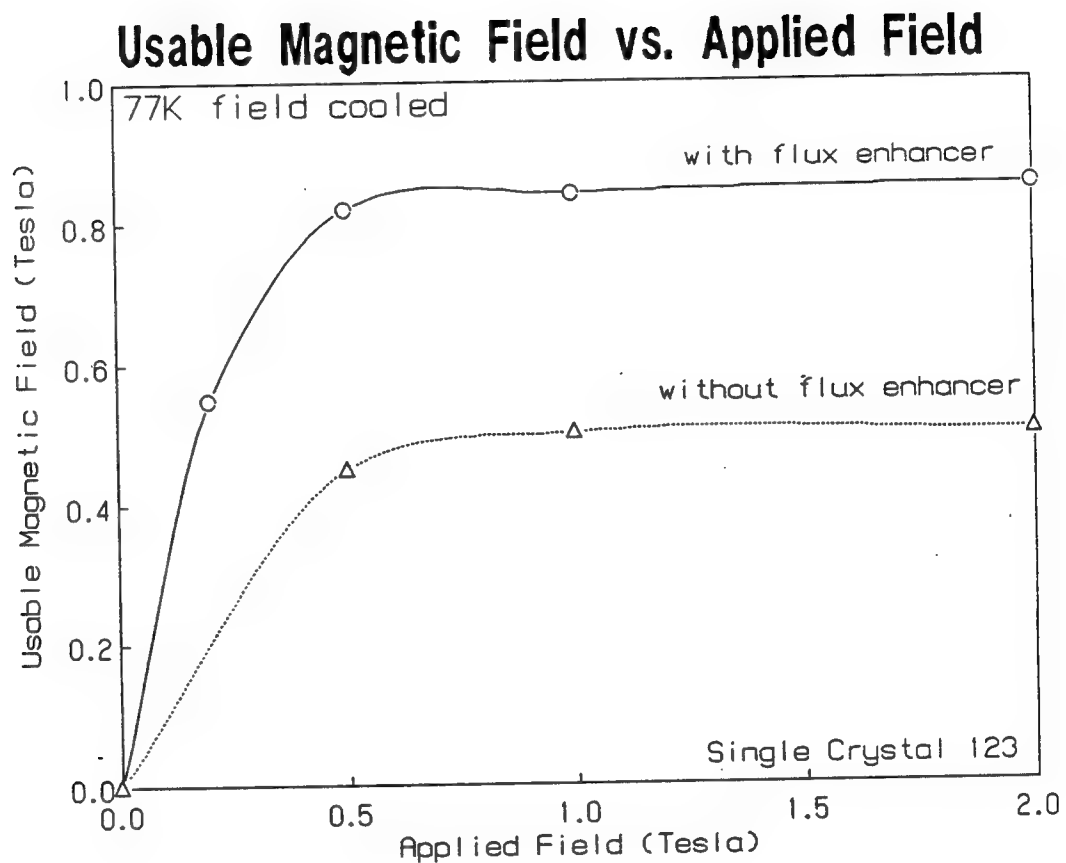


Figure 41. Usable magnetic field vs. applied for superconducting clamp with and without the flux-enhancer manufactured from single crystal 123 cylinder.

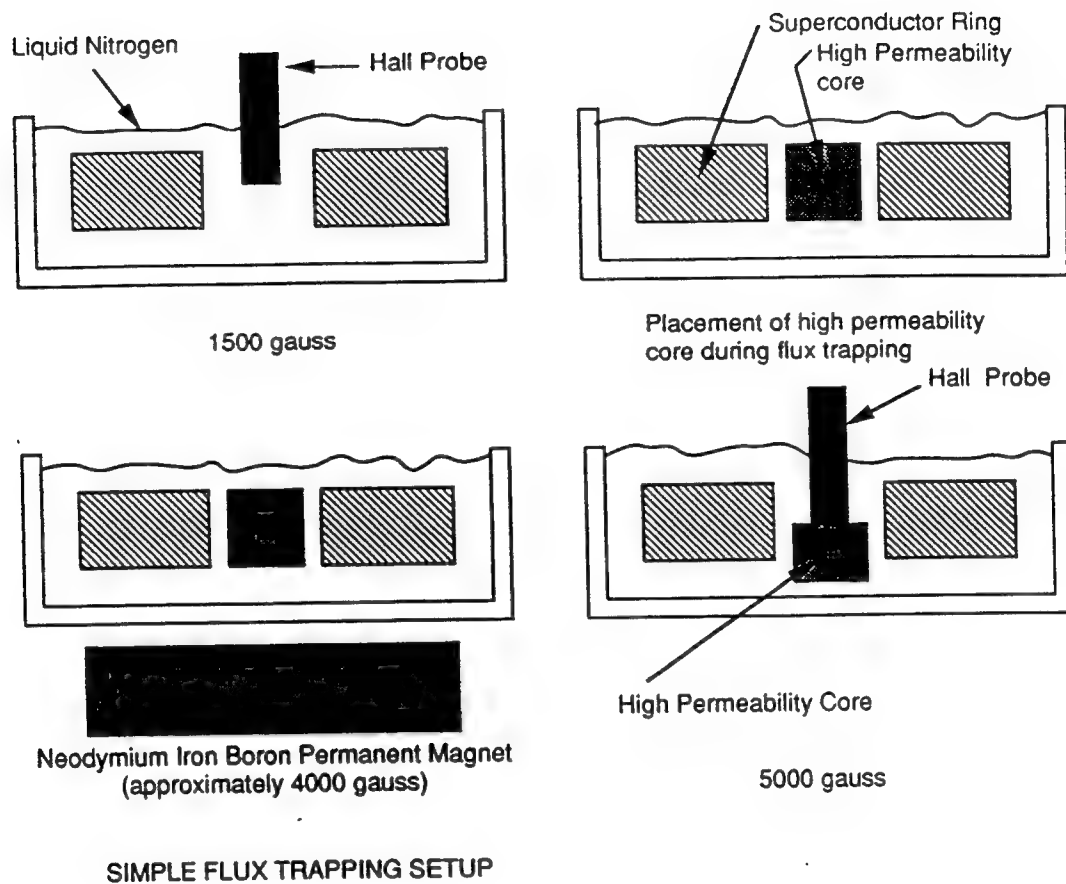
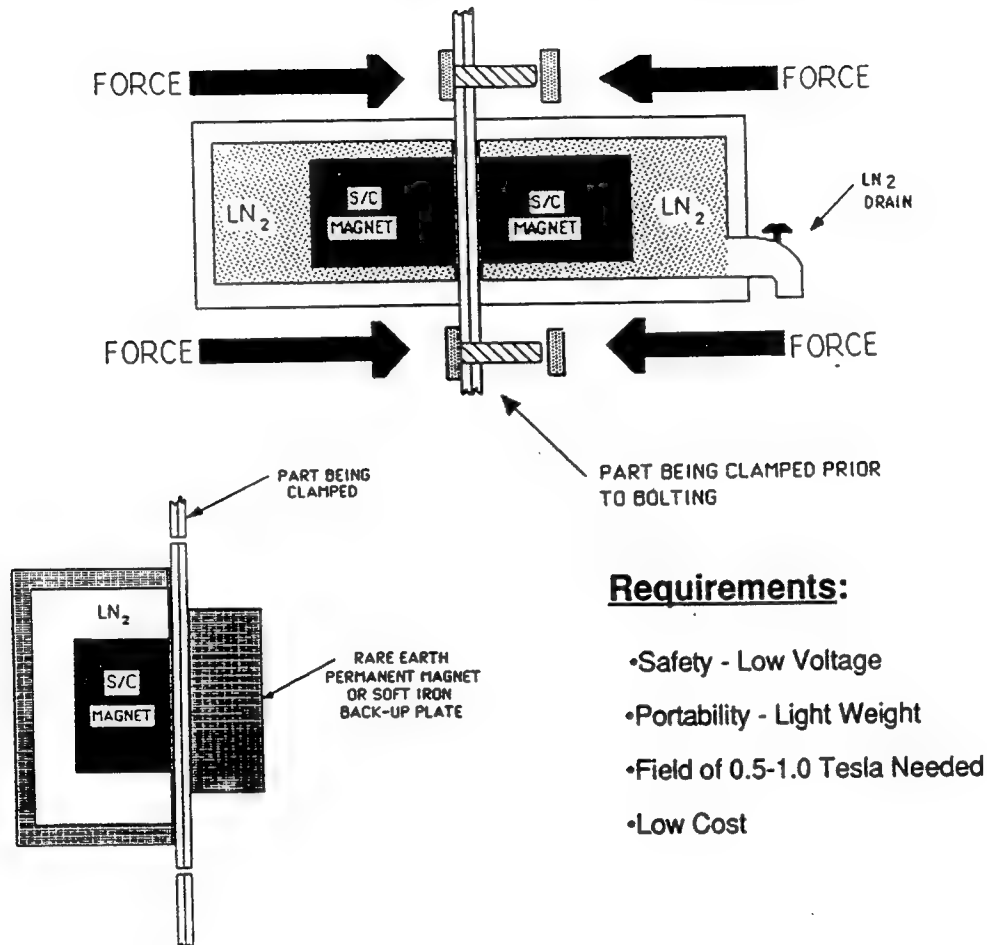


Figure 42. Flux trapping setup for measuring the usable field in a superconducting flux-trap magnet with a flux enhancement core.

SUPERCONDUCTING CLAMP



Requirements:

- Safety - Low Voltage
- Portability - Light Weight
- Field of 0.5-1.0 Tesla Needed
- Low Cost

Figure 43. Schematic diagram of a superconducting magnetic clamp.

permanent magnets, larger electromagnetic clamps and chucks are being used extensively throughout the manufacturing industry. Superconducting clamps will allow for the diversity that the electromagnetic clamp provides with the safety and ease of use of a permanent magnet. Figure 44 shows a comparison of several operational factors for superconducting vs. electromagnetic and permanent magnet clamps.

Magnetic clamping and latching devices can easily be fabricated from these bulk superconducting cylinders, both with and without the flux enhancing core. Figure 45 shows a clamp device which allows a latch pin to 'meld' with the superconductor ring and an iron enhancement slug to complete the magnetic circuit for maximum holding force while the flux-trap superconductor is in the superconducting state. This also allows for a large surface area for latching during the clamping operation. One novel clamp configuration works in conjunction with a permanent magnet such as rare earth samarium cobalt or neodymium iron boron types. The permanent magnet is placed on one side of a surface to be clamped with the superconductor clamp device (with flux enhancer) on the other. The moment the superconductor is cooled to below its transition temperature the clamp is in the operational mode, obviating the need for pre-charging (i.e. the S/C) in a high magnetic field.

An alternate clamp design includes a simple lever device to retract the soft iron core material thereby greatly reducing the clamping force at the surface (Figure 46). This retractable lever thus obviates the need to quench the superconductor flux-trap magnet. This allows the device to be continually charged and ready for use. Even though the magnetic field can be very high in the core, the iron core itself can be retracted fairly easily along the axial direction. Variations of the device could be used for drive shafts in liquid nitrogen and magnetic clutches for cryogen circulators and pumps.

Comparison of Superconducting vs. Electromagnetic and Permanent Magnet Clamp

	Permanent Magnet	Electromagnetic	Superconducting
Safety	Relatively Safe	Very Dangerous High Amps; High Voltage	Very Safe
Size	Small	Large, Bulky Very Heavy	Small Lightweight
Portability	No Attached Air Hoses	No Attached Power Cables	Yes
Capital Cost	Approx. \$2K	Approx. \$20-100K	Unknown
Operational Cost	Small	Very Large Due to Large Resistance Losses in Cu Wires	Minimal - No Losses Cryogen Cost
Clamping Force	Very Low Force Required to Remove Clamp	Large	Extremely Large
Reproducibility	Poor Damage to Surrounding Areas	Good	Good
Miscellaneous	Magnetic Field Cannot be Turned Off - Accidental Attachment to Other Parts	Heat Build-Up Due to Resistance in Cu Coil	Magnetic Field Can be Turned Off

Figure 44. Comparison of superconducting vs. electromagnetic and permanent magnet clamp.

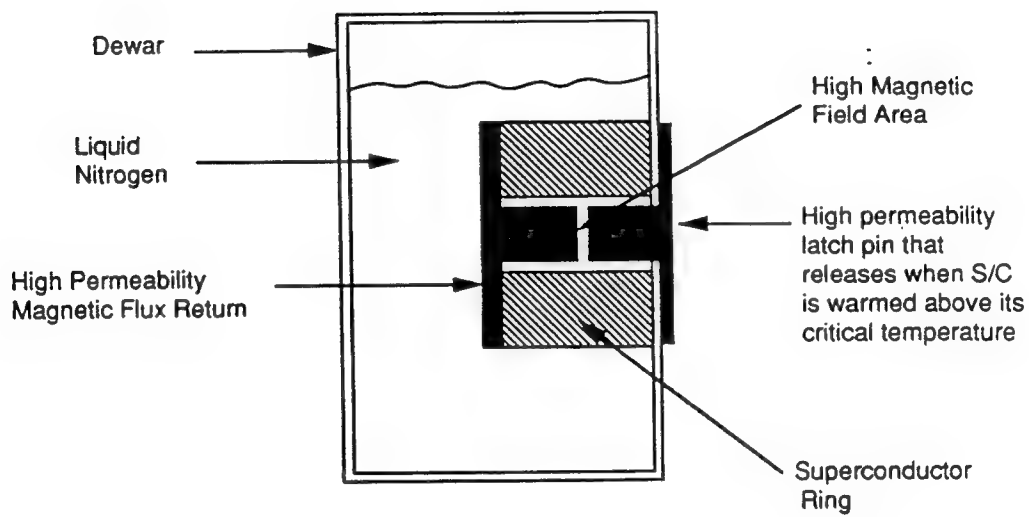


Figure 45. Superconductor flux-trap magnet clamp latching configuration.

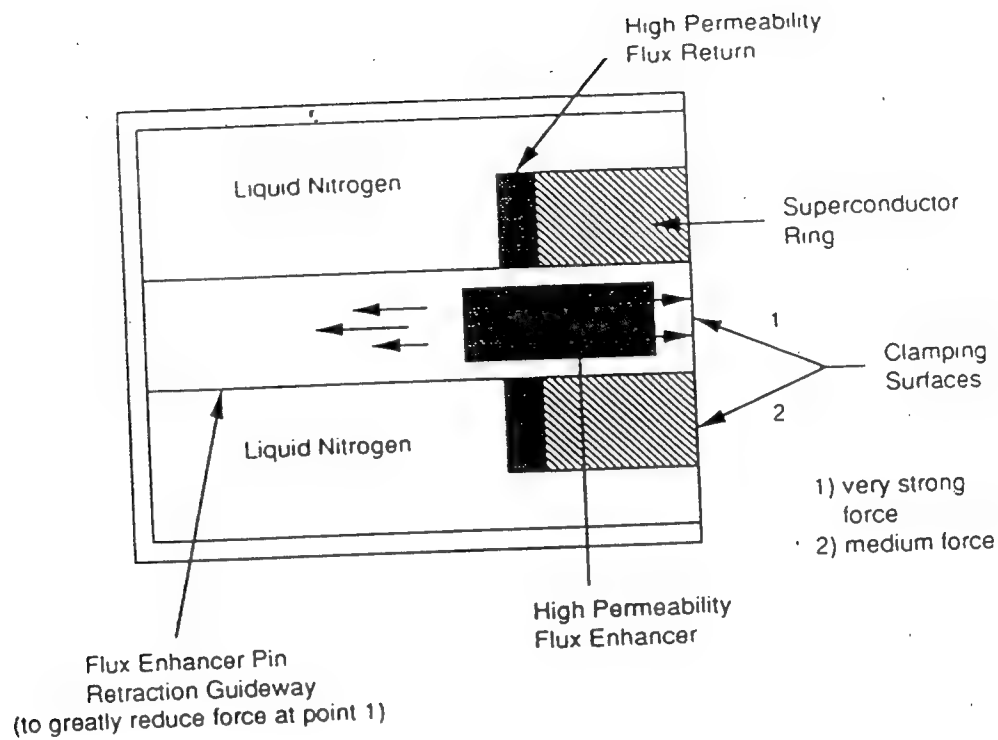


Figure 46. Superconductor flux-trap magnet clamp with retractable flux enhancer.

The views and conclusions contained in this document are those of the authors and should not be interpreted as necessarily representing the official policies or endorsements, either expressed or implied, of the Defense Advanced Research Projects Agency or the U.S. Government

**PROCESSING, FABRICATION, CHARACTERIZATION
AND DEVICE DEMONSTRATION OF HIGH
TEMPERATURE SUPERCONDUCTING CERAMICS**

Contract No. F49620-90-C-0079

ANNUAL TECHNICAL REPORT

September 15, 1990 - September 30, 1991

Submitted by:

Boeing Defense and Space Group

Sponsored by:

Defense Advanced Research Projects Agency
DARPA Order No. 7476

Monitored by:

AFOSR Under Contract No. F49620-90-C-0079

PM: Dr. Thomas S. Luhman
(206) 773-1991

PI's: Dr. Thomas S. Luhman
(206) 773-1991

Dr. Ilhan A. Aksay
(206) 543-2625

TABLE OF CONTENTS

PROGRAM OBJECTIVE	1
PROGRAM DESCRIPTION	1
SUMMARY	1
MILESTONE SCHEDULE	6
TECHNICAL RESULTS	6
MATERIALS SYNTHESIS AND CHARACTERIZATION	
A. $\text{YBa}_2\text{Cu}_3\text{O}_{7-x}$ Tapes	6
B. $\text{YBa}_2\text{Cu}_3\text{O}_{7-x}$ Monoliths	6
1. High Temperature Texturing	34
2. Powder Preparation	43
C. Low Temperature Processing	48
D. Dynamic X-Ray Diffraction Studies	56
SUPERCONDUCTING PROPERTIES	69
A. Flux-Trapping Experiments	69
B. Quenching Experiments	90
DEVICE REQUIREMENTS AND DESIGNS	99
A. Operational Principles and Designs	99
1. Superconductivity - Relevant Parameters	99
2. Flux Shielding and Trapping	104
3. Flux Pumping	107
4. Switching Processes	110
B. Applications	132
1. Technology Insertion Plan	132
2. Dent Puller/Proof-Tester	136
3. Clamp	142

PROGRAM OBJECTIVE

To develop material processes and engineering designs for high current applications of $\text{YBa}_2\text{Cu}_3\text{O}_{7-x}$

PROGRAM DESCRIPTION

The goals of our program are to (1) focus on engineering designs and demonstration of flux-trap magnets; (2) develop improved processing and fabrication methods to enhance current densities in strong magnetic fields; (3) optimize processes for grain alignment in bulk and tape samples; and (4) provide a technology base for utilization of flux-trap magnets.

SUMMARY

- a) In the processing of textured bulk 123 samples our focus has been on two major issues: (i) elimination of cracks; (ii) understanding and comparing the microstructural evolution in the samples prepared using either pure 123 or yttria-rich initial powder. With respect to the first problem, we have shown that higher oxygenation temperatures, thinner samples, and the addition of silver are all very effective in lowering the number of cracks. The second part of our study was devoted to understanding microstructural modifications caused by the long term high temperature melt-texturing needed to fabricate large-grained samples. The two main conclusions from this study were (i) that long periods of high temperature heat treatment resulted in the removal of fine defect structures (believed to be responsible for the high flux trapping) from the 123 grains and (ii) excess yttria was necessary to maintain the fine defect structures.
- b) With low temperature texturing we have shown the possibility of preparing textured 123 samples below the peritectic decomposition temperature of the 123 phase. The precursor consists of a mixture of Y_2BaCuO_5 , BaCuO_2 , and CuO . Texturing was obtained at temperatures below 985°C . In our initial experiments, this process was limited to thin samples (tapes). Recently we have shown the feasibility of this low temperature process in preparing thicker textured samples.
- c) We have explored other methods such as torch flame and plasma spraying in preparing the powders for texture processing of 123 bulk samples. TEM structural investigation on these powders clearly indicated the presence of fine, well-dispersed, second phase particles within the primary matrix particles.

- d) Bulk 123 samples with extremely large grains ($> 1 \text{ cm} \times 1 \text{ cm} \times 0.4 \text{ cm}$) were successfully prepared by controlling the number of nucleation sites for the growth of 123 grains from the 211 + liquid region. Samples were characterized using XRD, optical, and electron microscopy. A single set of diffracting planes in the XRD pattern was evidence for the formation of a large grain. Microscopic observation revealed that the samples consist of a single grain containing 211 precipitates. In addition to large grains and 211 precipitates, a number of cracks within the large grain were observed. The presence of these cracks was detrimental to the superconducting properties of our samples.
- e) In an attempt to increase the fracture toughness of the 123 monoliths and prevent cracking, composite samples containing 123 and a ductile phase (metallic Ag powder) were prepared. After the peritectic reaction ($211 + \text{liquid} \rightarrow 123$) was completed, the sample was cooled to room temperature and kept in the tetragonal state; this step was taken to understand the point in the processing sequence at which cracking occurs. The sample was examined by SEM with no visible cracks detected at this stage. Thus the cracking must occur during the oxygenation phase.
- f) Dynamic X-Ray Diffraction, which allows for the in-situ acquisition of time-resolved x-ray diffraction spectra, was used to study temperature-time process relationship of various phases formed during the high temperature melt-texturing of the 123. At temperatures above 1150°C , an unidentified phase (there is some evidence that it is a Y-Ba phase contaminated with traces of Pt) nucleates from the melt. This phase will melt after 3-4 hrs at 1350°C and appears to participate in the formation of the 211 phase between temperatures of 1050 and 1150°C , with the net reaction rate being higher at the lower temperature. The concentration of this phase increases dramatically at all temperatures when excess 211 is present.
- g) Among the potential applications we have been exploring for the early technology insertion of 123 ceramic superconductors is an electromagnetic dent puller. Two major areas of use for the dent puller are in airplane manufacture and proof-testing of adhesively bonded aerosurface skins. The dent puller has the potential to significantly improve cost and productivity in manufacturing of military and commercial airplanes.

In the manufacture of commercial and military airplanes, dent pullers are used for removing inadvertent damage during manufacture. Significant time and cost savings could be realized with the availability of safe, portable dent

pullers. The airline industry will also benefit tremendously in terms of cost and time savings in repairing airplanes dented in service.

In the proof-testing application, the dent puller is the only method which can reliably assess joint strength of adhesively bonded aluminum skins; ultrasonic inspection is not able to determine the difference between weakly bonded and securely bonded structures. Significant amounts of bonded composites are currently used on military airplanes, with increasing use predicted for commercial airplanes. Proof-testing with an electromagnetic device (which utilizes rapidly collapsing magnetic fields) is the only reliable method in use at the present time. These conventional electromagnetic systems are very large, not easily transportable (1000 pounds for the capacitor unit), and very dangerous (495 Volts and 30,000 Amperes) in operation. They require large cables connecting the capacitors to the hand-held unit, making the accessibility of the dent puller very impractical or sometimes impossible. In our proposed high temperature superconducting system, the capacitors are replaced by magnetic energy stored in flux-trapped magnets. Advantages of the superconducting system include safety, portability, simple operation under hazardous and remote conditions, and improved productivity and reproducibility. Early studies show that field strengths of only 1 Tesla would be required for this to be a working superconducting device. Trapped fields of this magnitude are predicted in 123 material before the end of 1991.

- h) Among the latest potential applications for early technology insertion in manufacture of military and commercial airplanes is a superconducting clamp based on flux-trap magnets. Permanent magnets are used widely and in diverse applications such as in attracting and holding ferromagnetic objects and in clamping non-magnetic objects and assemblies during manufacturing. Currently, permanent magnets are frequently the only feasible way of holding objects in confined areas during manufacturing. In addition to permanent magnets, larger electromagnetic clamps and chucks are being used extensively throughout the manufacturing industry. Superconducting clamps will allow for the diversity that the electromagnetic clamp provides with the safety and ease of use of a permanent magnet (Invention Disclosure Filed).
- i) A technology Insertion Plan for a Superconducting Dent Puller, Proof Tester, Electromagnetic Clamp and a Rivet Gun was developed. Payoffs and benefits of these superconducting electromagnetic devices were identified. Potential customers and markets for the superconducting devices were identified (U.S. Military, Airplane

Manufacturers, Airlines, Auto Manufacturers). Among the potential customers initially contacted were the Air Force, Navy, Boeing, McDonnell Douglas, United, American, Northwest, Delta, and Continental Airlines. Industrial involvement in the Technology Insertion Plan was outlined.

- j) The superconducting properties related to the experimental design issues for Boeing's devices were evaluated by performing flux-trapping experiments. Flux-trapping measurements were carried out on the melt-textured samples as a function of applied field. Fields of up to 2,300 Gauss (with an applied field of 20,000 Gauss) were trapped in the melt-textured samples (5 mm thick x 30 mm long x 8 mm wide) containing additional 211 phase (up to 20 at % 211). We investigated the effects of (a) initial powder state (quenched vs. non-quenched), (b) pure vs. 211 doped powder, and (c) amount of added silver, on the magnitude of trapped field.
- k) Several geometrical (thickness, grain orientation, grain size, trapped field as a function of distance from the sample surface) factors affecting the flux trapping abilities of the melt-textured samples were also investigated.
- l) The concept of obtaining mechanical work from the collapsing field in a high temperature superconducting "permanent" magnet was evaluated. A light, compact, low voltage, electro-mechanical rivet gun and dent puller would be of considerable interest to the aerospace industry. Such devices should be able to deliver a peak force of about 90 kNt (20,000 lb) in 1 msec.
- m) Quenching experiments of trapped flux were designed with respect to a superconducting dent puller and a rivet gun device. DC thermal switching experiments were designed and conducted in a rectangular 123 monolith with embedded Ni-Cr heater coil. A trapped field of 1000 Gauss was quenched thermally in 25 msec.
- n) An alternative quenching mechanism, "Weak Link Collision Quench" was designed and initial experiments were conducted. In this unique technique, the detrimental weak link properties of the 123 system were used to the advantage where a circulating current is suddenly forced to flow through the grain boundaries (weak links) by externally applied ac field (Invention Disclosure Filed).

- o) New operational designs of the dent puller and proof tester were developed. The alternative design employs a magnetic shutter, where all the magnetic field from a superconducting flux-trap magnet is blocked by a high permeability metal shield. The shutter would operate at microsecond speeds, as required for the operation of the dent puller and proof tester, thereby eliminating a need for quenching the superconducting flux-trap magnet (Invention Disclosure Filed).
- p) Various schemes to repetitively flux pump, i.e. magnetically charge, hollow cylindrical shapes and then discharge them in the required time frame was examined. The possibility of combining the charge and discharge methods, what engineering data will have to be collected, and what materials properties will have to be attained, in order to build such a device, was analyzed.

FY 90

F

A

J

Funding Available

Action

Judgment

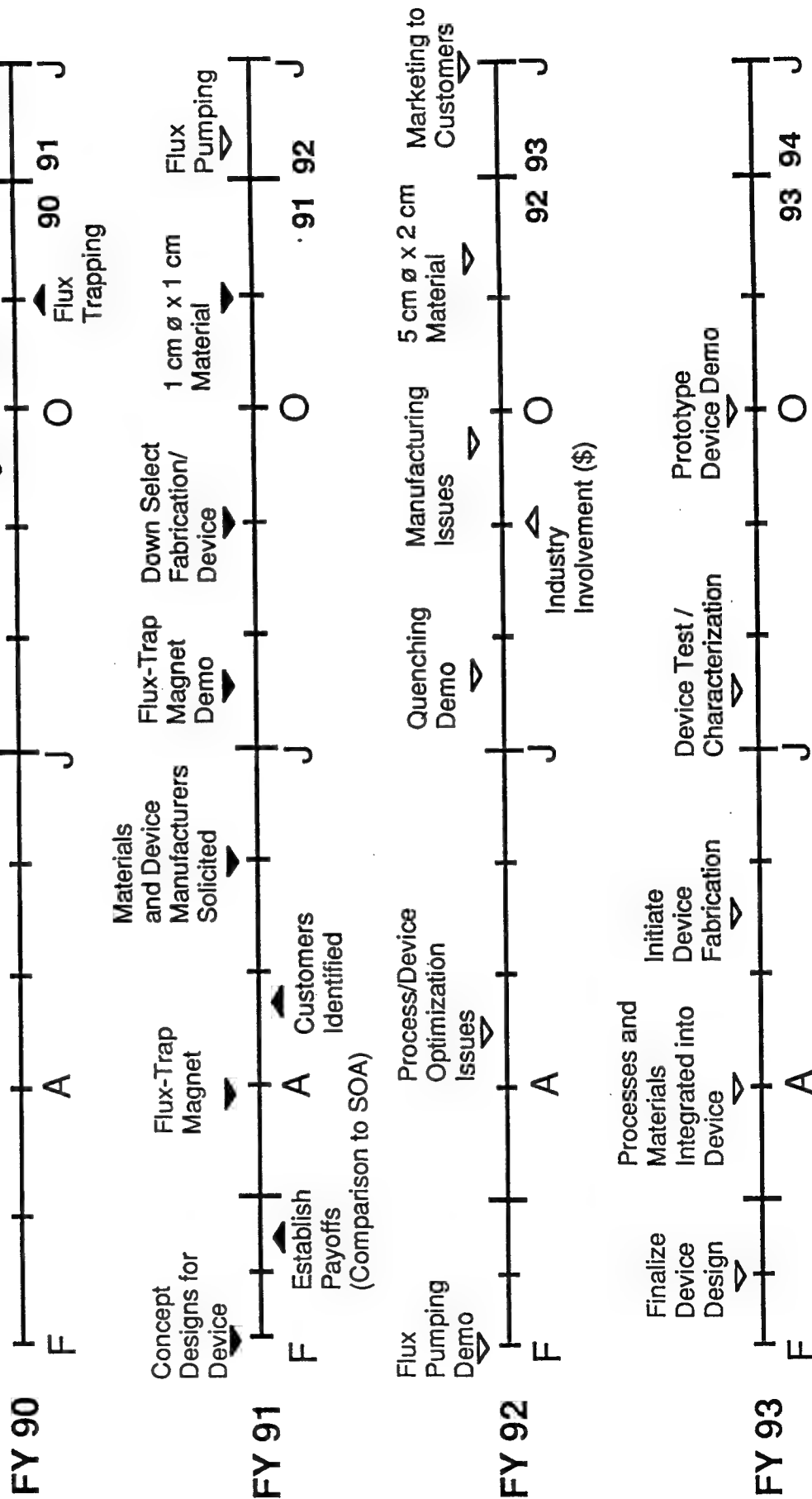
Material Requirements Identified

Process Requirements Identified

Flux Trapping

90 91

J



TECHNICAL RESULTS

MATERIALS SYNTHESIS AND CHARACTERIZATION

Processing and Characterization of Textured $\text{YBa}_2\text{Cu}_3\text{O}_{7-x}$ Tapes and Monoliths

A. $\text{YBa}_2\text{Cu}_3\text{O}_{7-x}$ Tapes

Preparation of tapes started by suspending 40 vol. percent of 123 powder in a solvent composed of methylethylketone and ethyl alcohol. The particles were dispersed by the addition of an appropriate amount of Menhaden fish oil which was determined from sedimentation study. Flexibility and strength to the unfired tape were provided by the addition of poly-vinyl butyral resin. The resulting stable suspension was cast onto a mylar film using a doctor blade technique.

$\text{YBa}_2\text{Cu}_3\text{O}_{7-x}$ tapes with thicknesses in the range of 0.15 mm to 0.55 mm were prepared following the doctor blade approach. These tapes were then sintered at 950°C for 6 hrs in oxygen atmosphere. After sintering experiments, the transport current density measurements were performed on these samples. The result from this test is shown in Figure 1. As is evident from this graph, there is an indirect relationship between thickness of the tapes and the critical current density values. This behavior is apparently due to overall increase in the degree of texturing as the sample thickness decreases. This behavior can be interpreted by considering the effect of self fields on the current density measurements. The current density increases as the thickness of the sample decreases due to lower self fields generated by lower transport current carried through the sample.

B. $\text{YBa}_2\text{Cu}_3\text{O}_{7-x}$ Monoliths

The fabrication of textured bulk 123 material is being approached via two processing routes, melt texturing and a low temperature process.

Melt texturing

In the first quarter we have concentrated on improving and modifying existing synthetic methods for the manufacture of large grained melt textured pieces. Our major synthetic efforts have stemmed from two principle techniques: the Salama¹ and Murakami² methods.

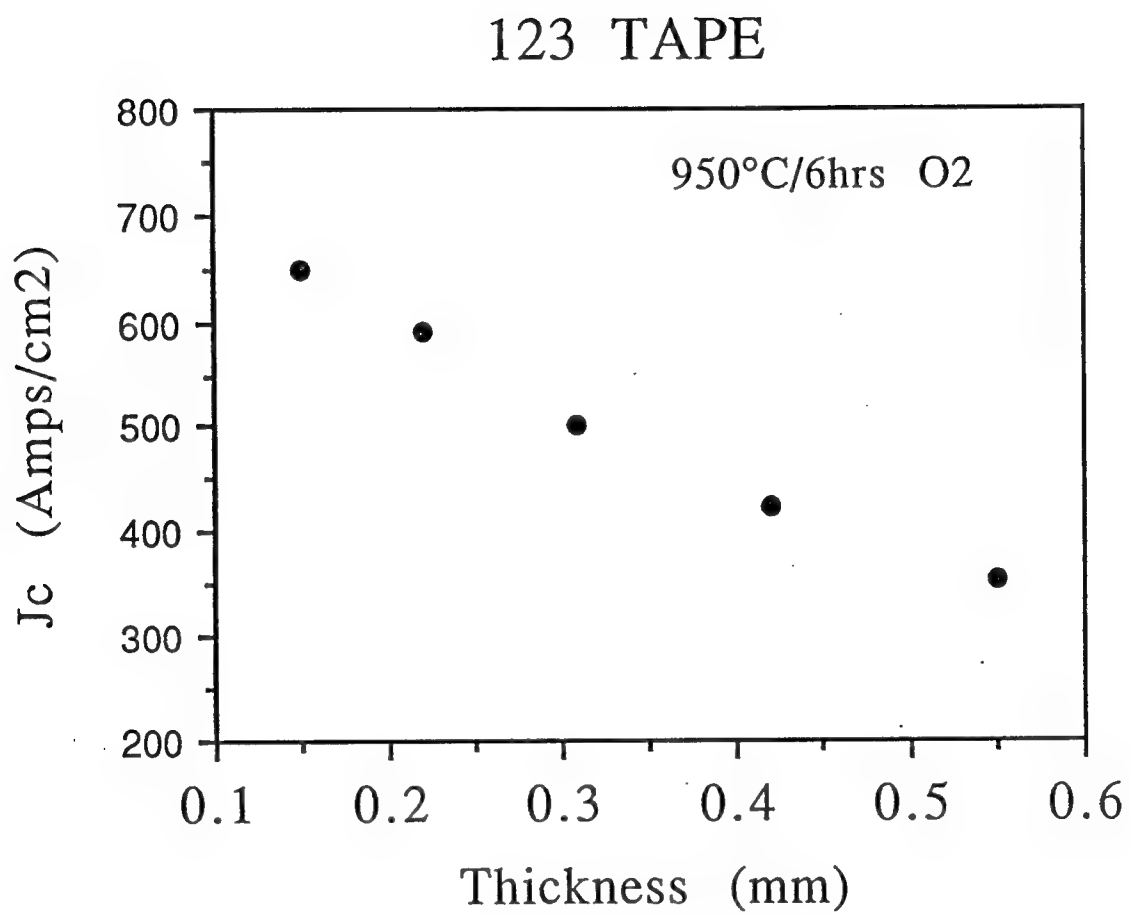


Figure 1. Critical Current density as a function of sample thickness for 123 tapes.

1. Recrystallization from 211 + liquid region

The Salama (University of Houston) method concentrates on slow cooling of 123 samples through the peritectic region resulting the formation of long, platelike grains. This method may be carried out under isothermal conditions or in a gradient depending upon what is required in the final microstructure.

Following this technique, the sample was quickly heated to 1100°C in an oxygen atmosphere. After a period of ten minutes, the sample was quenched to 1030°C. The heat treatment then changed to very slow cooling (1°C/hr) through the peritectic transformation to 980°C. After holding at 980°C for 12 hours, the sample was subjected to a long oxygen anneal step where slow cooling from 600-400°C was carried out over a period of three days. The effect of cooling rates (6 and 1°C/hr) through the peritectic region on the microstructure and superconducting properties were investigated. The SEM micrographs obtained from fracture surfaces of these samples are shown in Figures 2a and 2b, respectively. As shown in these micrographs this process leads to formation of long, oriented plate like grains. It is also observed that grain size and the width of oriented domains increases as the cooling rate decreases from 6 to 1°C/hr. The superconducting properties of these samples were evaluated by performing flux trapping experiments. The results of this test are presented in Figures 3a and 3b, respectively. As shown in this Figure, the magnitude of trapped field is higher in the sample with larger grains (sample with slower cooling rate). Presently we are investigating the effect of processing variables such as method of oxygenation (to minimize cracking), magnitude of thermal gradient and powder composition on the flux trapping capability.

2. Recrystallization from Y_2O_3 + liquid region

The second method used for the production of high quality melt textured material is based on work done by Murakami of ISTEC in Tokyo, Japan. It consists of the melt-powder-melt-growth process. Using this technology, researchers in Japan have been able to trap fields of up to 0.5 Tesla in their materials, sufficient for many useful applications.

There are many key factors important in successfully carrying out this processing technique. The method consists of flash melting prepared 123 powder at temperatures around 1450°C for two minutes. The melt is then quenched onto a copper plate in liquid nitrogen resulting in almost instantaneous cooling of the liquid sample. At this point, the melt has to be recrushed into a powder. This step is very critical in getting high quality material at the end of the melt texture cycle. It is crucial that the 211 inclusions within the matrix are of micron to submicron size. Otherwise, transformation into 123 from the [211 + liquid] phase, see phase

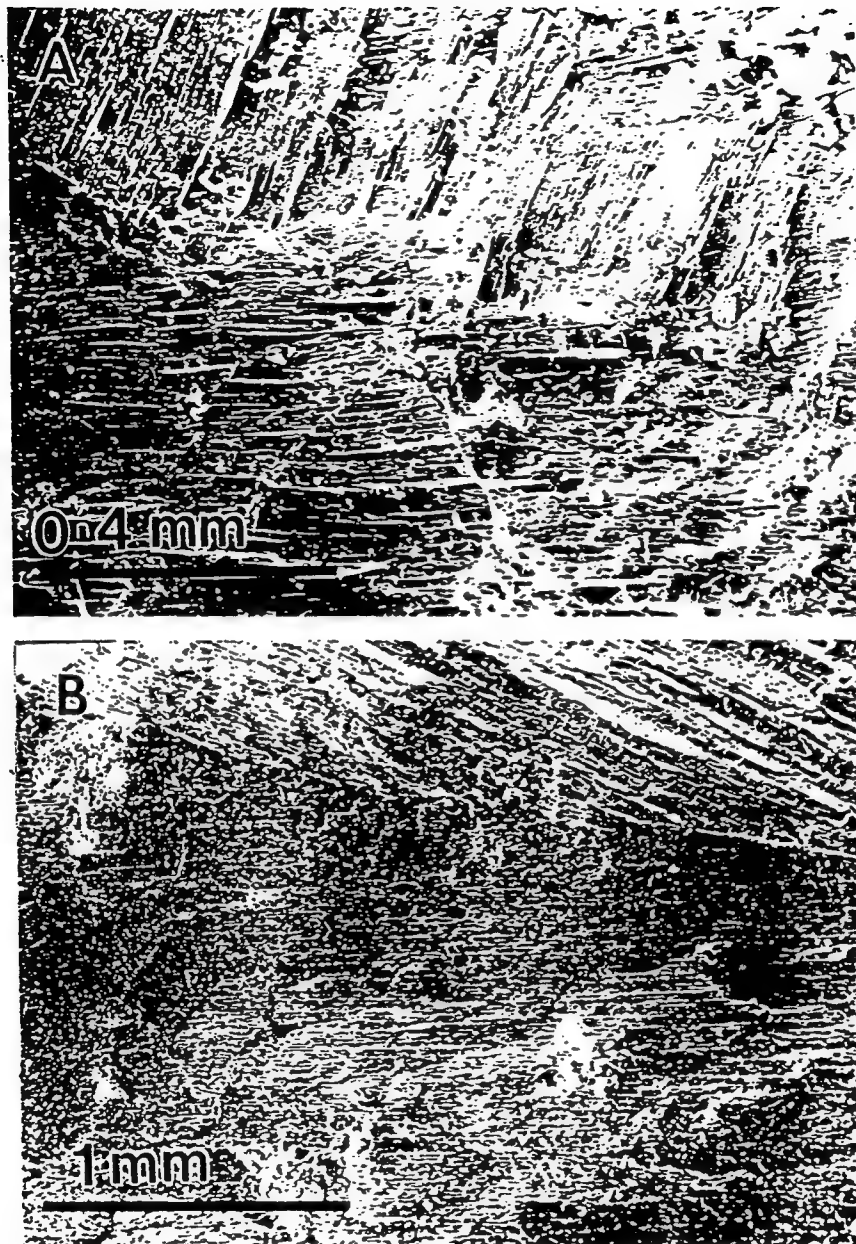


Figure 2. (a) SEM micrograph from sample cooled at the rate of 6°C/hr through the peritectic region.
 (b) SEM micrograph from sample cooled at the rate of 1°C/hr through the peritectic region.

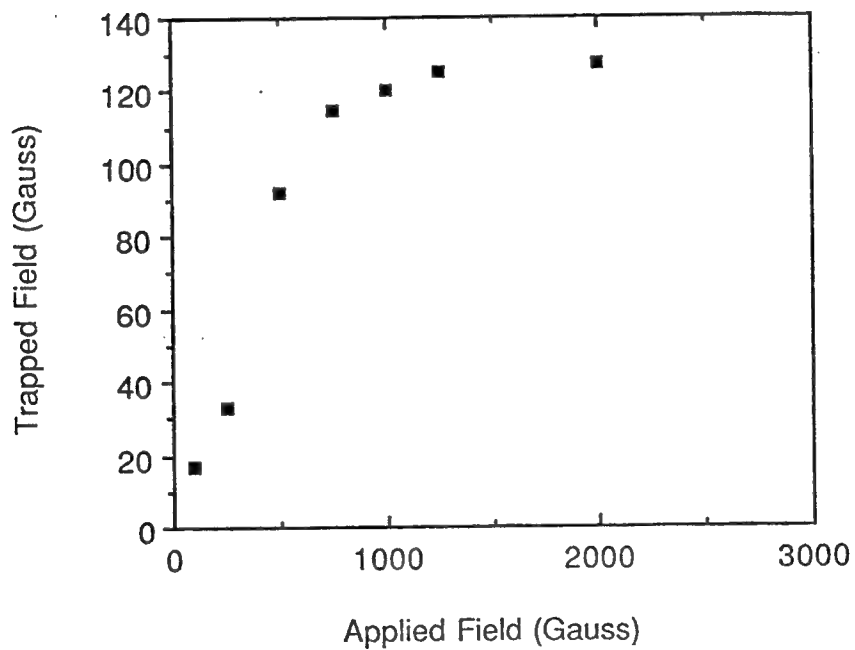
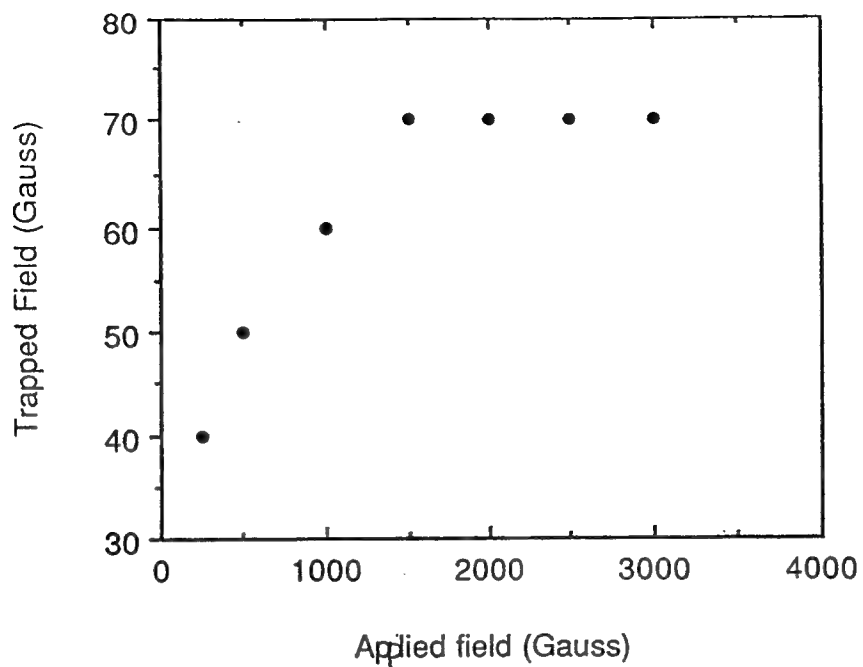


Figure 3. (a) Flux trapping data for sample 2a
(b) Flux trapping data for sample 2b.

diagram in Figure 4, would be hampered by extremely slow solid state diffusion processes. Unfortunately, in obtaining micron and submicron sized particles, we have had problems with contamination from the grinding media. Recent experiments with a high speed attritor equipped with a Teflon coating vessel and 3/16" zirconia balls indicate that obtaining very small high purity powders by this method should be possible.

After the melt has been crushed, it is pressed into a bar or pellet and subject to the second part of the heating cycle. The sample is once again quickly heated to 1065-1150°C, the exact temperature dependent on the qualities desired in the final ceramic, and held there for 10 minutes. This process is carried out in flowing air. The sample is then cooled at 100°C/hr to 1000°C followed by a very slow cooling at 1°C/hr to 900°C. It is in this slow cool region that the liquid phase and the 211 continue transformation into 123 material and grain growth occurs. This process may be carried out under isothermal conditions or in a gradient, with the gradient being responsible for larger, more aligned grain structures. After cooling to room temperature, the sample is reoxygenated over a three day period at temperatures from 600-400°C. An optical and SEM micrographs taken from this sample are displayed in Figures 5a and 5b respectively. Sample of this material was evaluated for flux trapping capability. The result of such test is shown in Figure 6. As indicated in this plot this process has improved the magnitude of flux trapping significantly. Materials based on pure 123 were formed as well as materials incorporating 5-20 % of additional 211 phase. Excess 211 phase is thought to increase the transformation of the liquid phase to 123 resulting in larger amounts of superconducting material.

Samples were characterized by microprobe analysis. The microstructures based on a pure 123 formulation, as well as those doped with an excess of 211, showed small ($< 5 \mu\text{m}$) inclusions of 211 within the 123 grains or matrix. As would be expected, the samples with added 211 showed more of these inclusions than did the pure material. Areas rich in copper (as CuO) and barium (most likely as BaCO_3) existed resulting from the incomplete transformation of the liquid phase into 123. This is most likely due to the fact that the material needed from the 211 phase was tied up in the middle of the larger 211 pieces. Access to this material could only occur through solid state diffusion, a very slow process at these temperatures. Thus, extra copper and barium is present in the mixture which has no chance to transform. If the 211 particulates were smaller with a larger surface area, a larger percentage of them would react, resulting in consumption of all of the liquid phase. Thus, addition of extra 211 can help alleviate this problem and still result in the inclusion of small 211 particulate, which may act as pinning sites in the final material.

To compare our results with other laboratories, a sample of 123 melt textured material from CPS, in Boston, MA was examined by x-

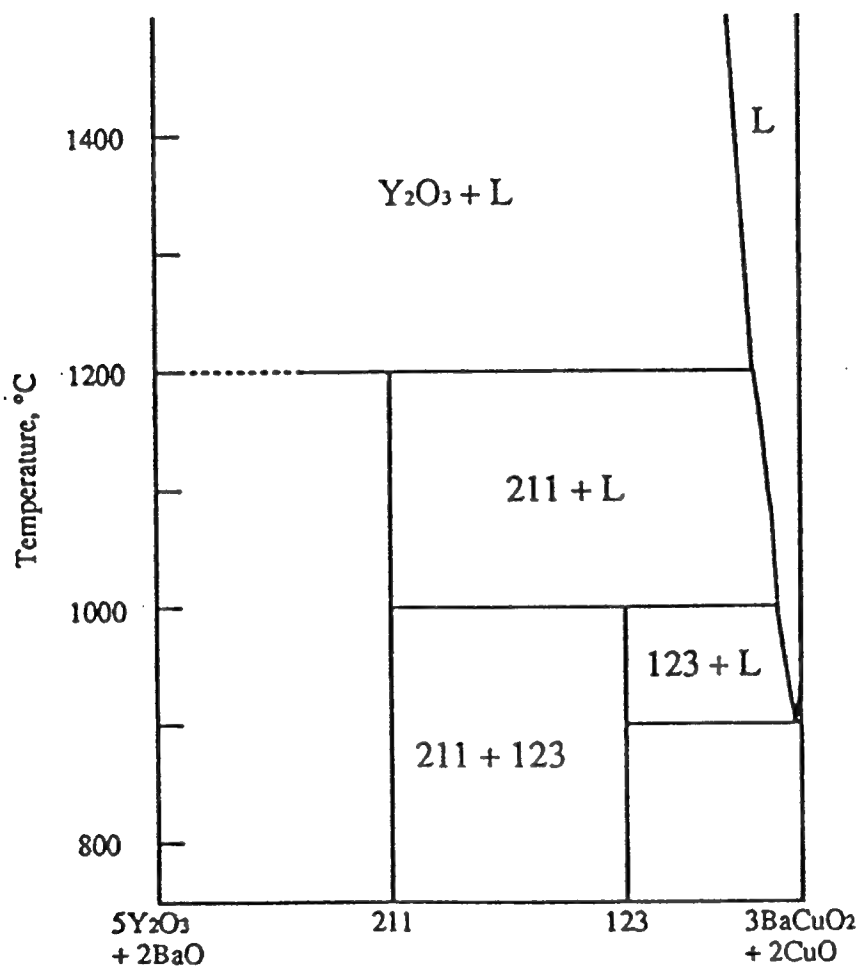


Figure 4. Pseudo-binary phase diagram of the Y-Ba-Cu-O system along the Y_2BaCuO_5 - $\text{YBa}_2\text{Cu}_3\text{O}_{7-x}$ tie line.

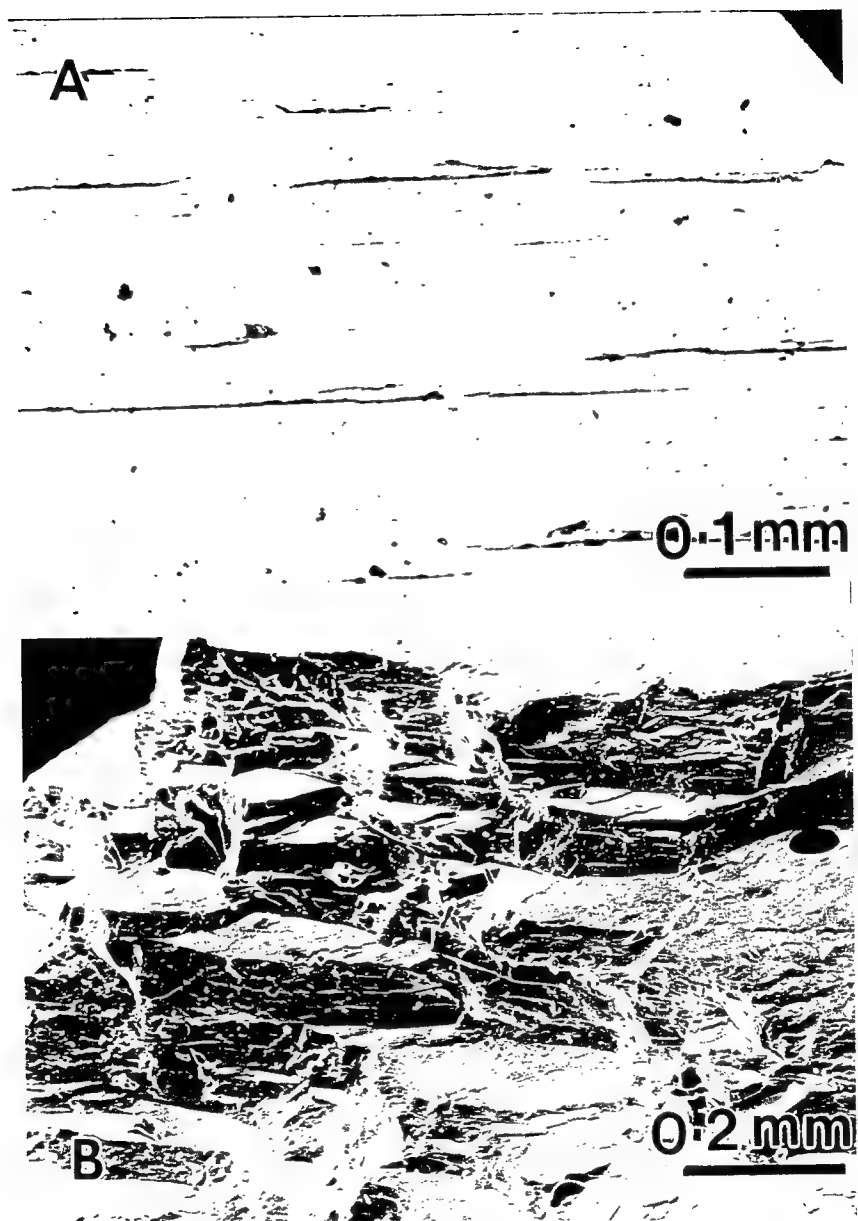


Figure 5. (a) Optical micrograph from the sample prepared using the Y_2O_3 + Liquid approach.
(b) SEM micrograph of the same

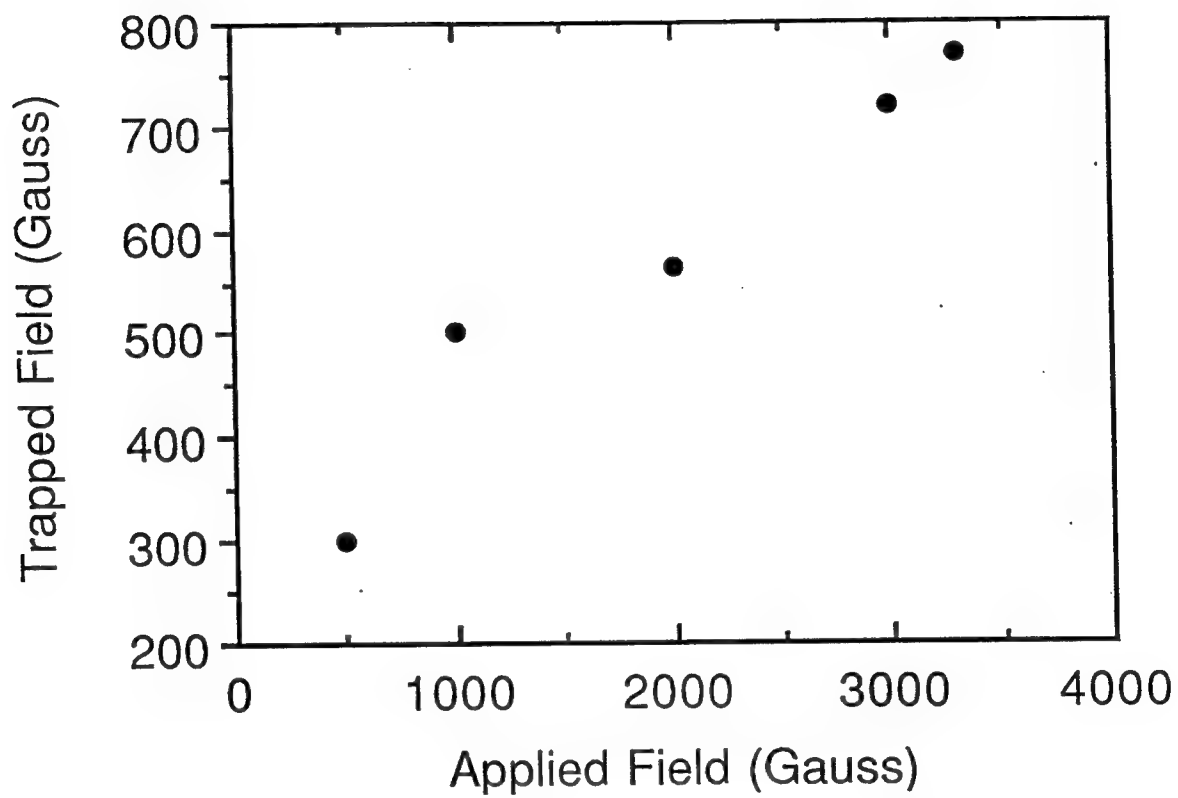
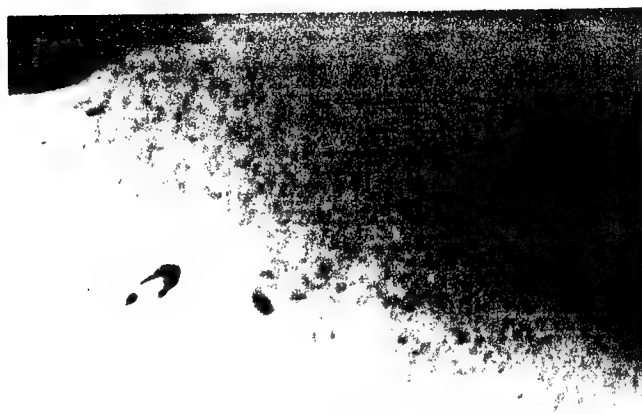


Figure 6. Flux trapping data for sample shown in Figure 5.

ray microprobe. This particular sample had fairly large grains, on the order of one centimeter, and exhibited good superconducting properties. As can be seen in Figures 7a and 7b, this material showed large areas of 123 material, within the grains, as well as amounts of intergranular material. 211 inclusions were observed within the 123 grains of sizes ranging from 1-5 μm . The intergranular material was once again areas of CuO and BaCO_3 , the latter being very porous in nature. This would indicate that these regions are leftover from the liquid phase after all the 211 particulates had been encapsulated by solid 123.

A vertical, thermal gradient furnace with a movable hot zone was constructed for processing samples by melt-texturing. The furnace system incorporates state-of-the art transparent furnace technology which will allow direct observation and monitoring of the visual onset of grain nucleation and growth. The sample is located inside a heater coil which in turn is contained within a mirror tube. The mirror tube consists of a glass tube with a thin layer of gold deposited on the inner surface. The mirror tube reflects the heat back into the furnace while allowing visible light to transmit through. The complete furnace assembly is enclosed within a sealed, water-cooled stainless steel shell. Visual observation is augmented by a microscope/camera installation.

Two different types of powder have been used to prepare melt textured 123 monoliths, (a) preformed 123 and/or 123+211 mixture and (b) 123 and/or 123+211 powder heated to Y_2O_3 + liquid region and quenched from this state. The quenching step is necessary to produce a supersaturated liquid which will precipitate out fine particles in the final stage of melt texturing process. These particles are then expected to act as flux-pinning sites in the microstructure. TEM imaging, spectroscopy, and diffraction have been performed on the quenched powder. The results can be summarized as follows: (1) an amorphous matrix with 123 composition with embedded 211 and/or Y_2O_3 particles. The bright field image and the corresponding spectra are shown in Figures 8 and 9a-9c, respectively; (2) the phase separation in the Y_2O_3 + liquid region results in the formation of large Y_2O_3 particles as shown in Figure 10. The process of melt texturing starts by first preparing a pressed bar-shaped sample with the dimensions of 40 mm x 6 mm x 6 mm using powder (a) or (b). The pressed bar is then placed in a tube furnace horizontally, and heated to the 211 + liquid region (1100°C). After holding at this temperature for 20 minutes, the sample is recrystallized into 123 phase following a peritectic reaction. TEM analysis of the melt textured samples shows several important structural features; (1) elongated plate-like 123 grains with some localized weak coupling between the grains (Figure 11); (2) 211 particles with trapped Y_2O_3 particles inside, these 211 particles are usually 1 μm or larger in diameter (Figure 12). There are two unusual features which are only observed in the melt textured samples; first, the 123 matrix contains ultrafine particles (50 - 100 Å) in diameter which are homogeneously



100nm

Figure 8. Bright Field TEM image showing an amorphous matrix containing 211 and/or Y_2O_3 particles.

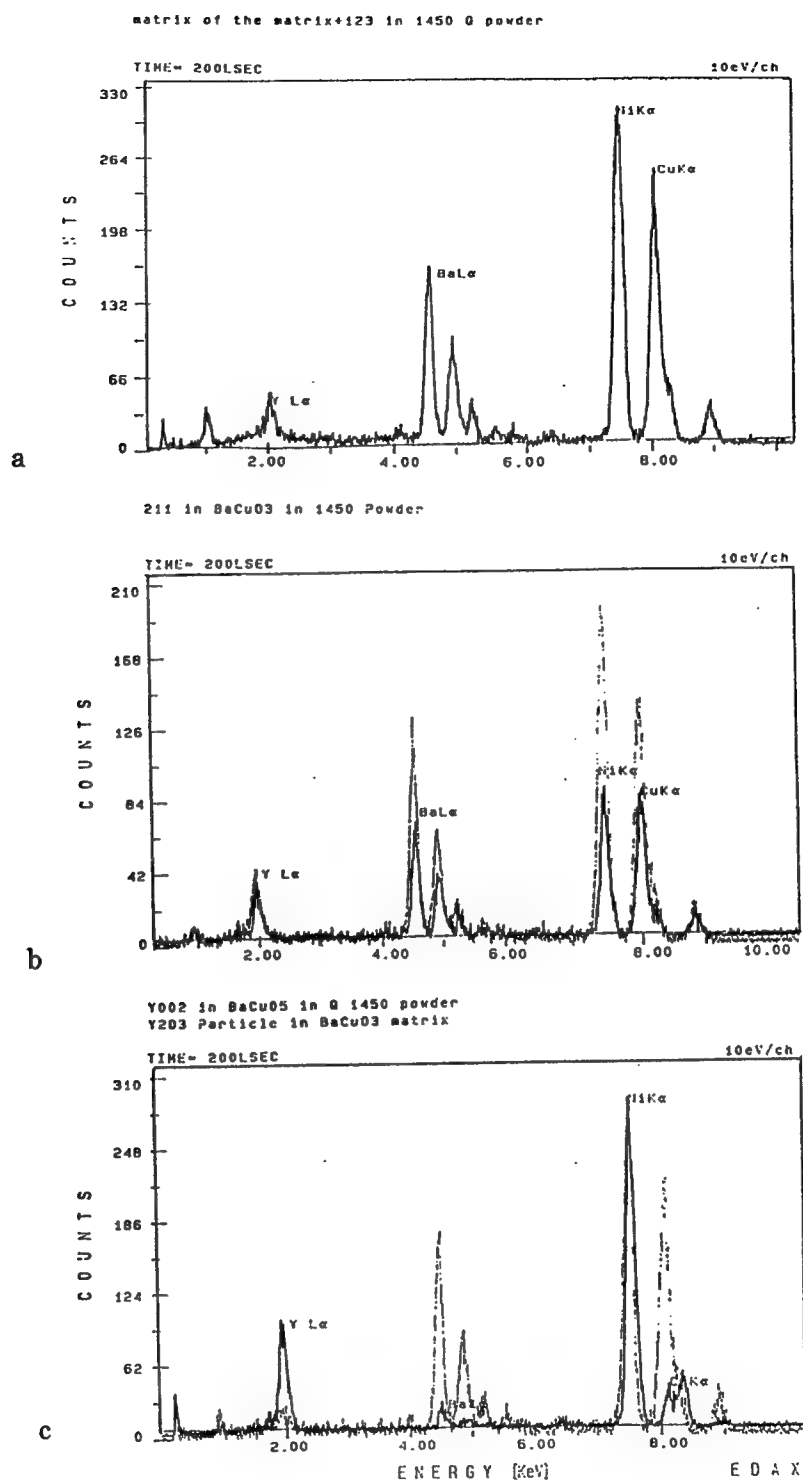



Figure 9. EDAX spectra

- (a) from the amorphous region shown in Figure 8.
- (b) from 211 particles within the amorphous region.
- (c) from Y_2O_3 particles within the amorphous region.



0.5 μm

Figure 10. BF TEM image showing large Y_2O_3 particles.



Figure 11. BF TEM image showing elongated 123 grains with localized weakly coupled grains.



Figure 12. BF TEM image showing Y_2O_3 particles trapped within 211 phase.

distributed within the grains (Figure 13); second, a linear contrast is present along the long axes of the grains which are believed to be related to strains along [001] direction (Figure 14). The origin of these features, which may turn out to play an important role in controlling the superconducting properties, is being investigated.

Samples were characterized by microprobe analysis. The microstructures based on a pure 123 formulation, as well as those doped with an excess of 211, showed small ($< 5 \mu\text{m}$) inclusions of 211 within the 123 grains or matrix. As would be expected, the samples with added 211 showed more of these inclusions than did the pure material. Areas rich in copper (as CuO) and barium (most likely as BaCO_3) existed resulting from the incomplete transformation of the liquid phase into 123. This is most likely due to the fact that the material needed from the 211 phase was tied up in the middle of the larger 211 pieces. Access to this material could only occur through solid state diffusion, a very slow process at these temperatures. Thus, the extra copper and barium present in the mixture has no chance to transform. If the 211 particulates were smaller with a larger surface area, a larger percentage of them would react, resulting in consumption of all of the liquid phase. Addition of extra 211 can help alleviate this problem.

The 123 powder used in fabricating textured monoliths was initially heated to Y_2O_3 + liquid region and quenched from this state. The quenching step was undertaken to produce supersaturated liquid which will then precipitate fine particles in the final stage of the melt texturing process. These particles are subsequently expected to act as flux-pinning centers in the microstructure.

The bulk sample synthesis was started by first preparing a pressed disk-shaped sample with the dimensions of 25 mm x 3 mm using the quenched powder. The pressed sample was then introduced in a tube furnace horizontally and heated to the 211 + liquid region (1100° - 1150°C). After holding at this temperature for 20-35 minutes the sample was recrystallized into 123 phase by a peritectic reaction. It is our experience that the size of the 123 grains in the melt textured microstructure is determined by the choice of recrystallization temperature; the higher the recrystallization temperature the larger the grains will be in the final microstructure. Using this knowledge, it was possible to prepare samples with grains $> 1 \text{ cm} \times 1 \text{ cm} \times .3 \text{ cm}$ in size. The XRD pattern (Figure 15) taken from transverse cross section of one such large grain showed only a single set of diffracting planes; strong evidence for the formation of large single grain. After pulverizing the large grain, resulting XRD pattern (Figure 16) showed randomly oriented 123 phase with 211 as the major 2nd phase. Formation of large single grains, as determined by XRD, is an important advancement toward achieving material properties required for the superconducting electromagnetic devices. However, the flux

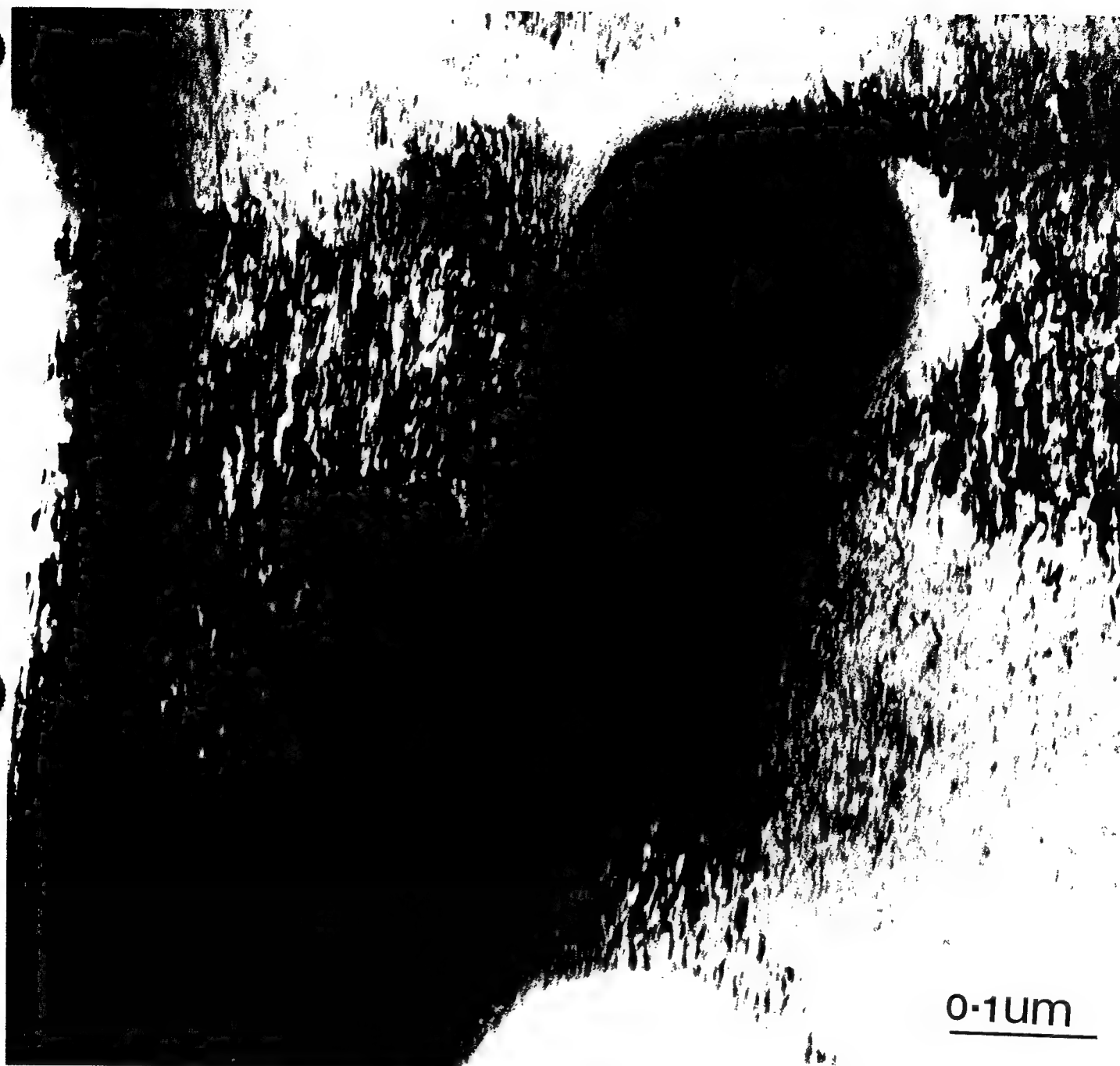


Figure 14. BF TEM image showing the linear contrast along the long axes of the grains.

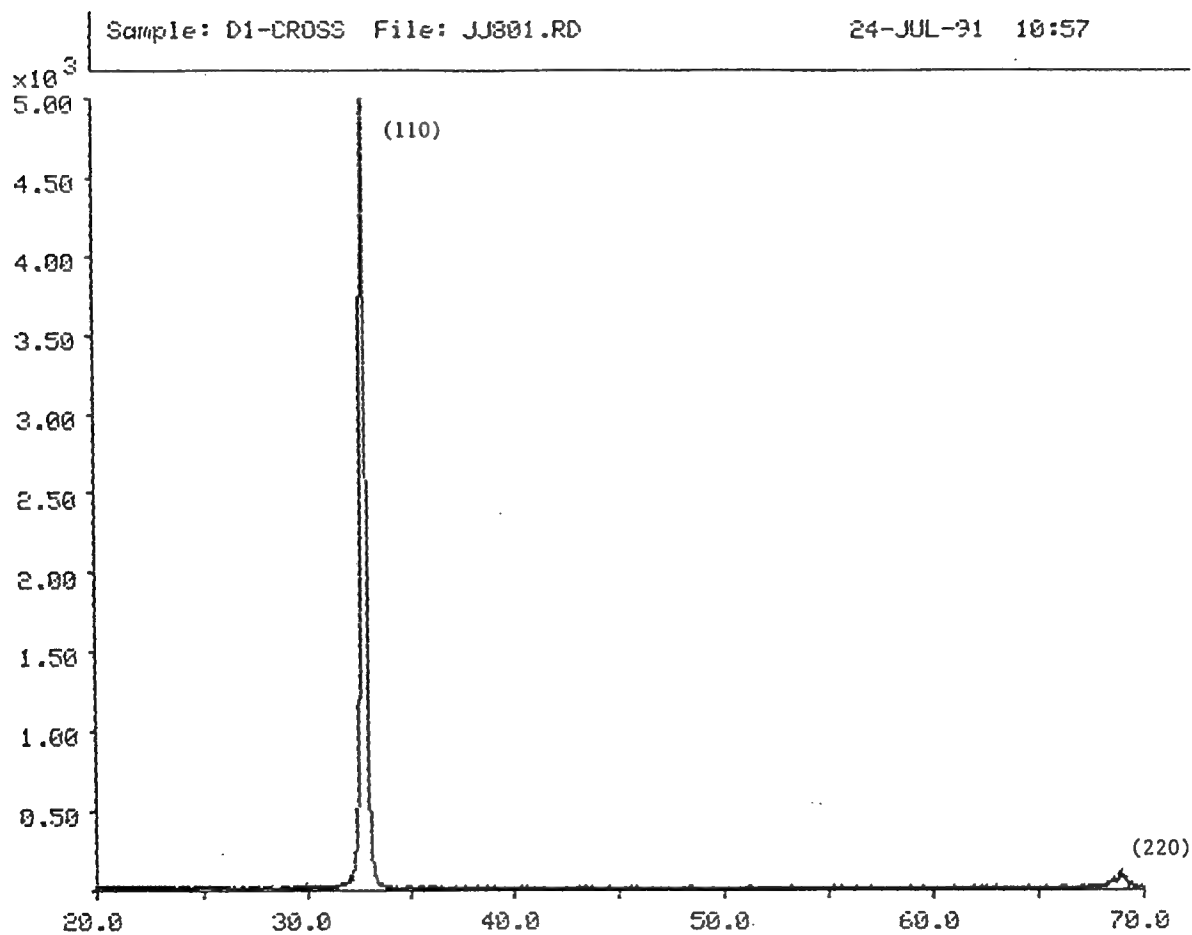


Figure 15. XRD pattern from transverse cross section of the large grain showing a single set of diffracting planes.

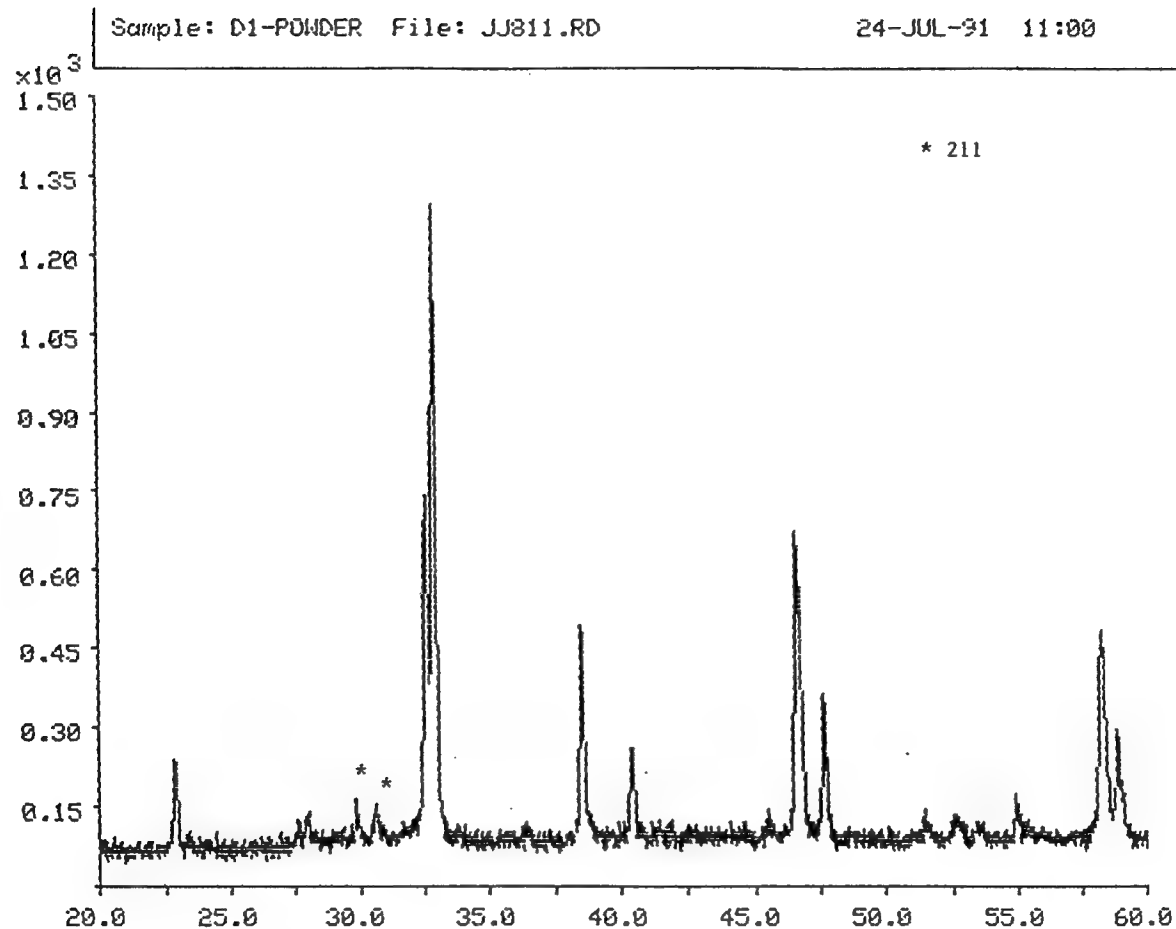


Figure 16. XRD pattern from pulverized large grain showing the presence of 123 and 211 as the major and secondary phases, respectively.

trapping capability for this sample was poorer (only 850 Gauss) in comparison with our earlier samples having smaller grains (2000 Gauss).

Microstructural investigation was undertaken to understand the cause of deterioration in superconducting properties. In Figure 17 we present an optical micrograph taken from transverse cross section of the sample. One feature of interest in this microstructure is the 211 precipitates distributed within the large grain. Our previous TEM analysis on textured samples revealed the presence of much finer particles (50-100 Angstroms) within the 123 grains (please see our second technical report for details). The second point of interest in this micrograph, and the one shown in Figure 18, is the presence of numerous cracks within the grain. We believe that these cracks are responsible for lack of macroscopic circulating current within the sample.

Cracking can occur at two stages of sample processing: (1) during solidification, and (2) during phase transformation from tetragonal to orthorhombic state. In order to understand the dominant point in the processing sequence at which cracking occurs, the microstructure of the sample before oxygenation was examined. The particular sample in this case was a composite containing 123 and Ag powder. After the peritectic reaction ($211 + \text{liquid} \rightarrow 123$) was completed this sample was cooled to room temperature in the tetragonal state. The microstructure of this sample was examined by SEM (Figure 19) and only a few isolated cracks were observed at this stage of processing. Figure 20 shows the microstructure of this same sample after oxygenation. The number of cracks increased during oxygenation, as seen in Figure 20. However, if this micrograph is compared with the microstructures shown in Figure 17 and 18, it is seen that the incorporation of Ag has reduced the number of cracks.

The reduction in the number of cracks improved the flux-trapping capability of this sample (Figure 21). From these results it was concluded that cracking occurs during oxygenation and we believe this is the result of a stress gradient generated by volume shrinkage during the tetragonal to orthorhombic phase transformation. The reduction in cracking with the addition of Ag may be the result of enhanced oxygen diffusion rate and/or improved fracture toughness of the sample. Another important result of Ag addition was the reduction in the size of 211 precipitates as shown in Figure 22. The maximum precipitate size is on the order of $5 \mu\text{m}$ as compared to $40\text{-}50 \mu\text{m}$ in sample without Ag addition (Figure 17). It is clear that the Ag has an important effect on the microstructure and properties of 123 system. However, in order to utilize Ag most effectively its exact role must be understood.



Figure 17. An optical micrograph taken from transverse cross section of the large grain showing 211 precipitates and a number of cracks.

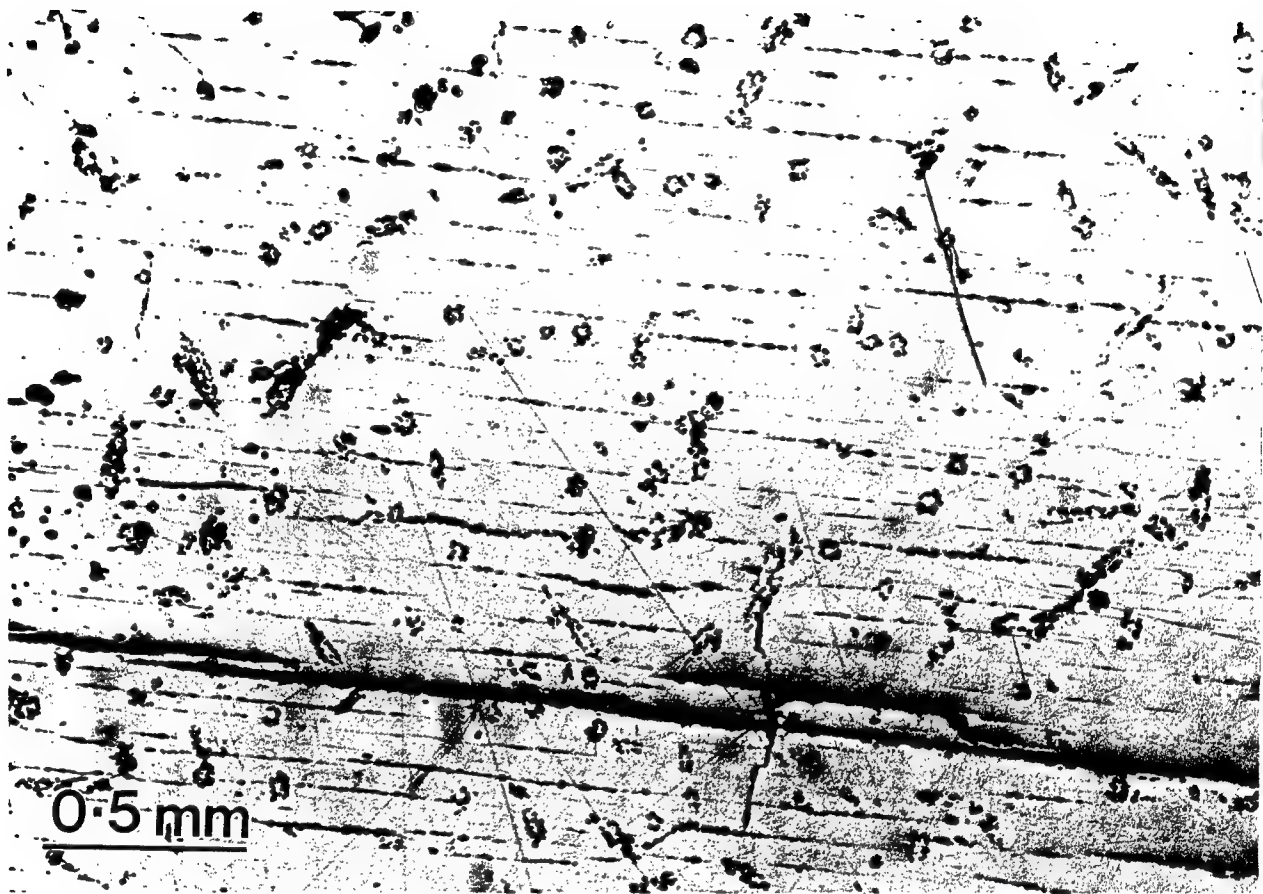


Figure 18. An optical micrograph taken from transverse cross section of the large grain showing a number of cracks within the large grain.

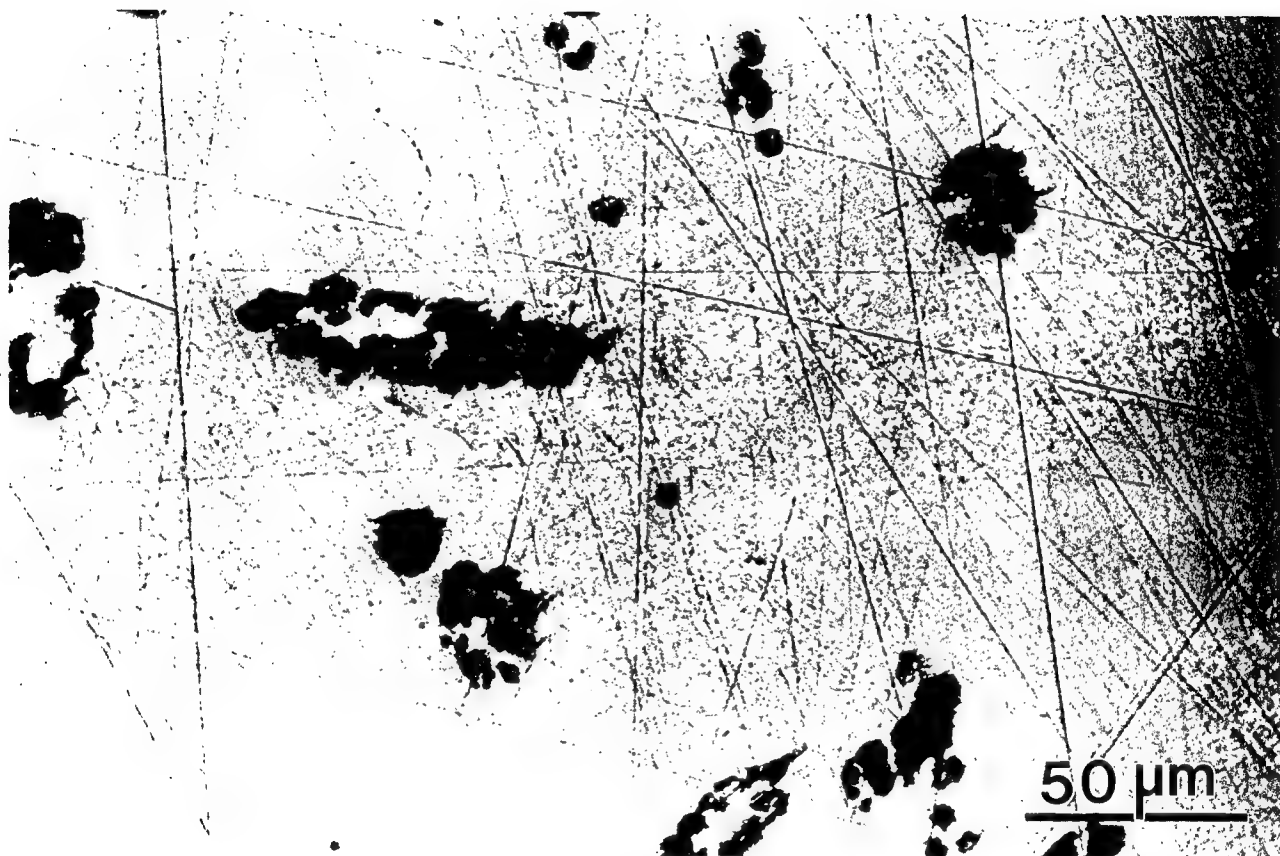


Figure 19. SEM micrograph showing the microstructure of 123/Ag sample before oxygenation.

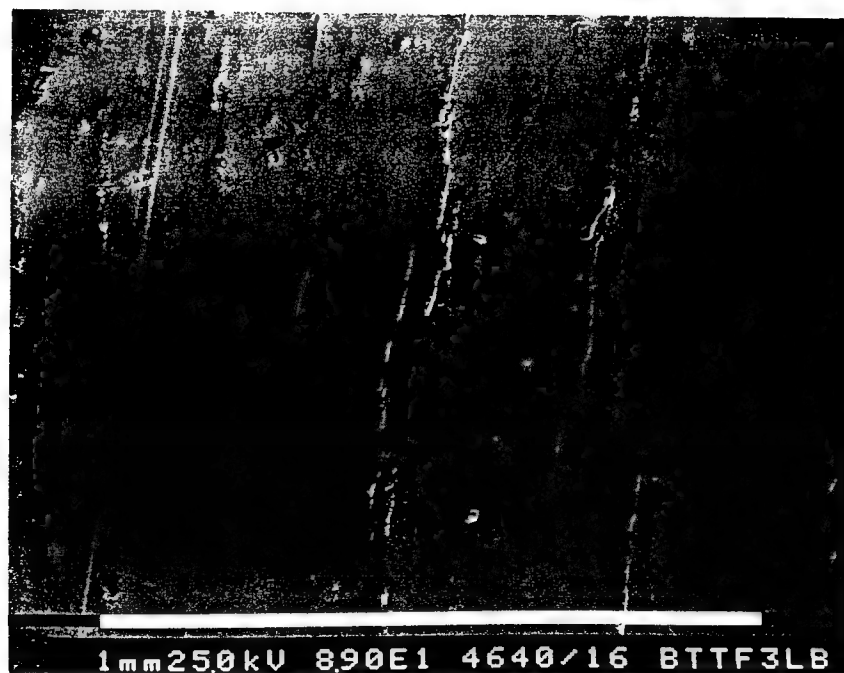


Figure 20. SEM micrograph showing the microstructure of 123/Ag sample after oxygenation.

Trapped vs Applied Field

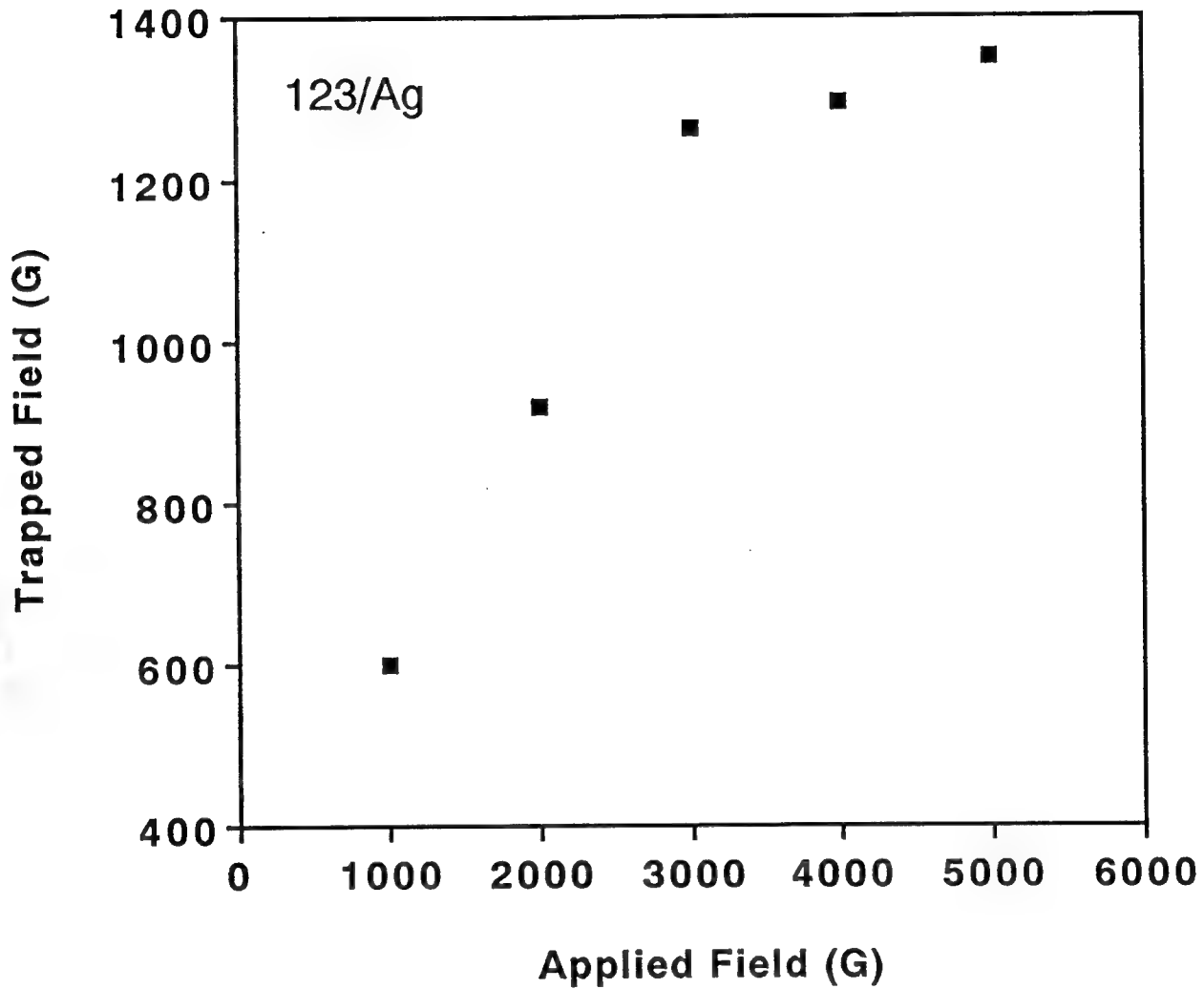


Figure 21. Trapped-flux vs. applied field for 123/8 wt. % Ag monolith.

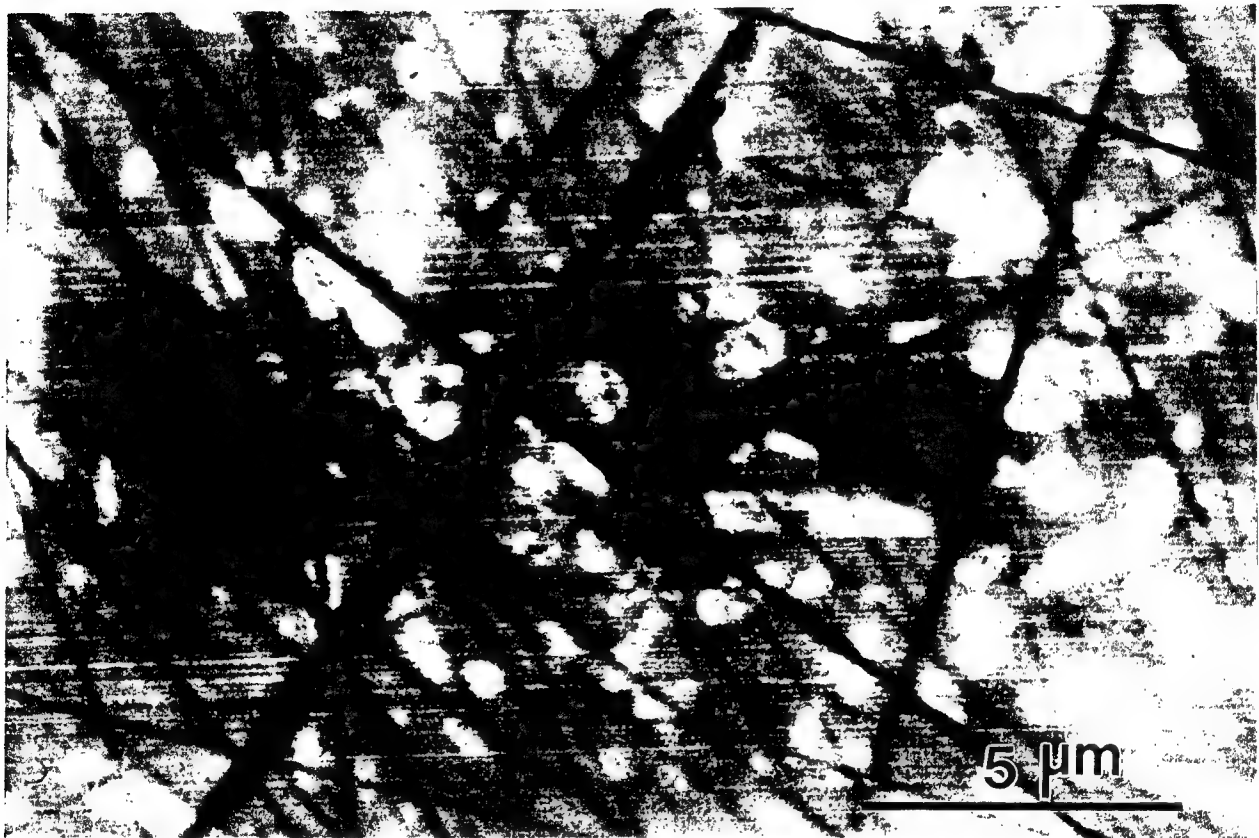


Figure 22. A higher magnification SEM micrograph of 123/8 wt. % Ag monolith showing the 211 precipitates.

In the processing of textured bulk 123 samples our focus has been on two major issues: (i) elimination of cracks; (ii) understanding and comparing the microstructural evolution in the samples prepared using either pure 123 or yttria-rich initial powder. With respect to the first problem, we have shown that higher oxygenation temperature, thinner samples, and the addition of silver are all very effective in lowering the number of cracks. The second part of our study was devoted to understanding microstructural modifications caused by the long term high temperature heating needed to fabricate large-grained samples. The two main conclusions from this study were (i) that long periods of high temperatures results in the removal of fine defect structures (believed to be responsible for the high flux trapping) from the 123 grains and (ii) excess yttria was necessary to maintain the fine defect structures.

I. High Temperature Texturing

In our previous discussion we described the processing methodology for the preparation of textured bulk 123 monoliths. Briefly, the samples have been prepared using either preformed and/or quenched 123 powders. In the latter method, 123 powders were heated to temperatures at which Y_2O_3 plus a liquid phase are stable, then quenched. We also reported that the samples prepared using quenched powder showed superior properties to samples prepared by Salama method. However, the samples could not maintain circulating current. The reason proposed was the presence of weak links between the textured grains and domain boundaries.

Our next step was therefore to grow large grains, in excess of one centimeter on each axis. Large-grained 123 monoliths were successfully grown by controlling the number of nucleation sites for the 123 grains. XRD analysis suggested single grain structures but flux trapping values were lower than those observed in samples with smaller grains. Microstructural analysis of the large-grain samples revealed the presence of numerous cracks within the grains. These were believed to be the cause of lower flux trapping values. Thus, in the processing of textured 123 samples our focus has been on two major issues (i) elimination of cracks (ii) understanding and comparing the microstructural evolution in the samples prepared using either pure 123 or yttria-rich initial powder. With regard to the first problem we have already shown the effectiveness of silver incorporation in lowering the number of cracks from the microstructure. To further improve the microstructure, separate studies were initiated to examine the effects of oxygenation temperature and sample thickness on the cracking behavior. As was reported earlier, the cracking is the result of phase transformation from tetragonal to orthorhombic state. To reduce the stress generated at this stage we thought of minimizing oxygen gradient between the outer and inner portions of the sample by incorporating the oxygen at the highest possible temperature. In order to determine the highest temperature for oxygen uptake, TGA

experiments were carried out on the tetragonal melt-textured samples. These isothermal oxygenation experiments were done at temperatures of 475°, 600° and 650°C in oxygen. The results of these tests are shown in Figure 23. As seen in this plot the maximum oxygen uptake occurs when the process is carried out at temperatures near 600°C.

In a parallel study we observed that thinner samples were less susceptible to cracking. Based on the information gathered from the above studies we prepared thin silver-containing samples. The test results on these samples still showed that they also exhibited low flux trapping values. Since cracking was no longer a major problem (confirmed by SEM observations), we suspected microstructural modifications caused by long term high temperature exposure (needed for grain growth) to be the cause of poor properties. In order to understand these modifications, further studies focussing on the evolution of microstructure in the melt-processed samples were planned.

We chose the quenched 123 powder as our starting point and analyzed the microstructure of this powder after various post-heat treatment schedules. The examination of the bright field (BF) images taken from the as quenched powder (Figures 24a and 24b), revealed that the as-quenched powder contains well-dispersed nanometer-sized particles within an amorphous matrix. The particles have been identified as 211 and/or Y_2O_3 by energy dispersive spectroscopy (EDS); the matrix had a composition which was rich in barium and copper. This sample was later heated to 930°C and held at this temperature for 6 h.

After heat treatment the powder was examined under TEM; the resulting micrograph is shown in Figure 25. The conversion of quenched powder into 123 phase (presence of twins) is apparent. The other important feature is the trapped fine particles within the 123 grains. These particles were determined to be rich in yttrium by EDS analysis. In a separate experiment, the as-quenched powder was heated to the 211 + liquid region (1140°C) and cooled to room temperature at the rate of 1°C/min. The TEM micrographs after this heat treatment are shown in Figures 26a and 26b. As indicated in Figure 26a, after this heat treatment the microstructure develops features which are believed to be related to the presence of strain in the matrix. The exact nature of the strain contrast is not clear at this point.

In addition to strain contrast, the microstructure contains very fine particles as shown in Figure 26b. In our next experiment, the powder after being held at 1140°C for 15 minutes, was cooled to 930°C and held at this temperature for the period of 8 h. As noted above, high temperature annealing was necessary to prepare large-grained samples. The microstructure of the sample after this heat treatment is presented in Figure 27. The most striking consequences of long high temperature exposure was the

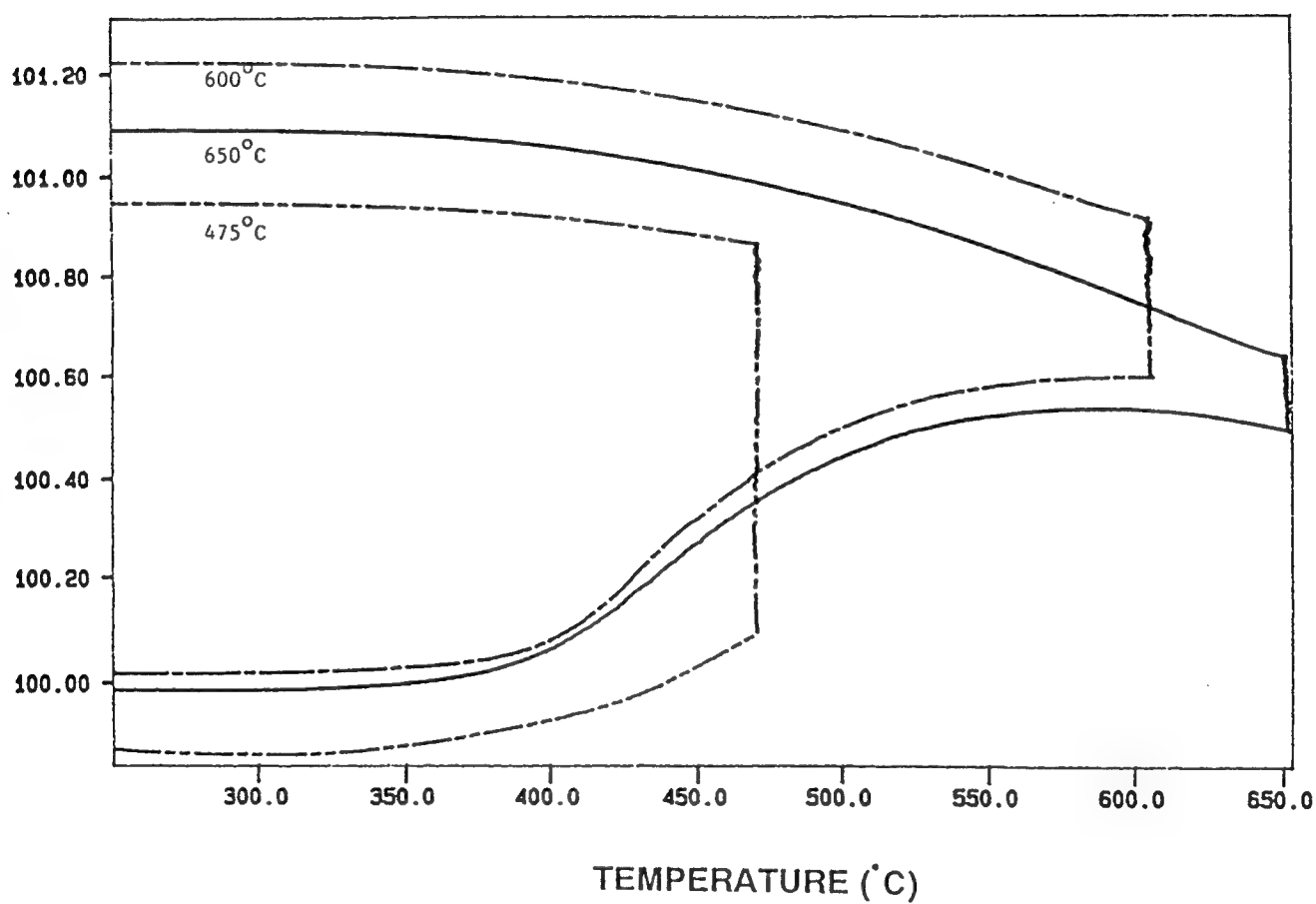


Figure 23. TGA plots showing oxygenation behavior for a bulk textured sample at 475°, 600° and 650C.

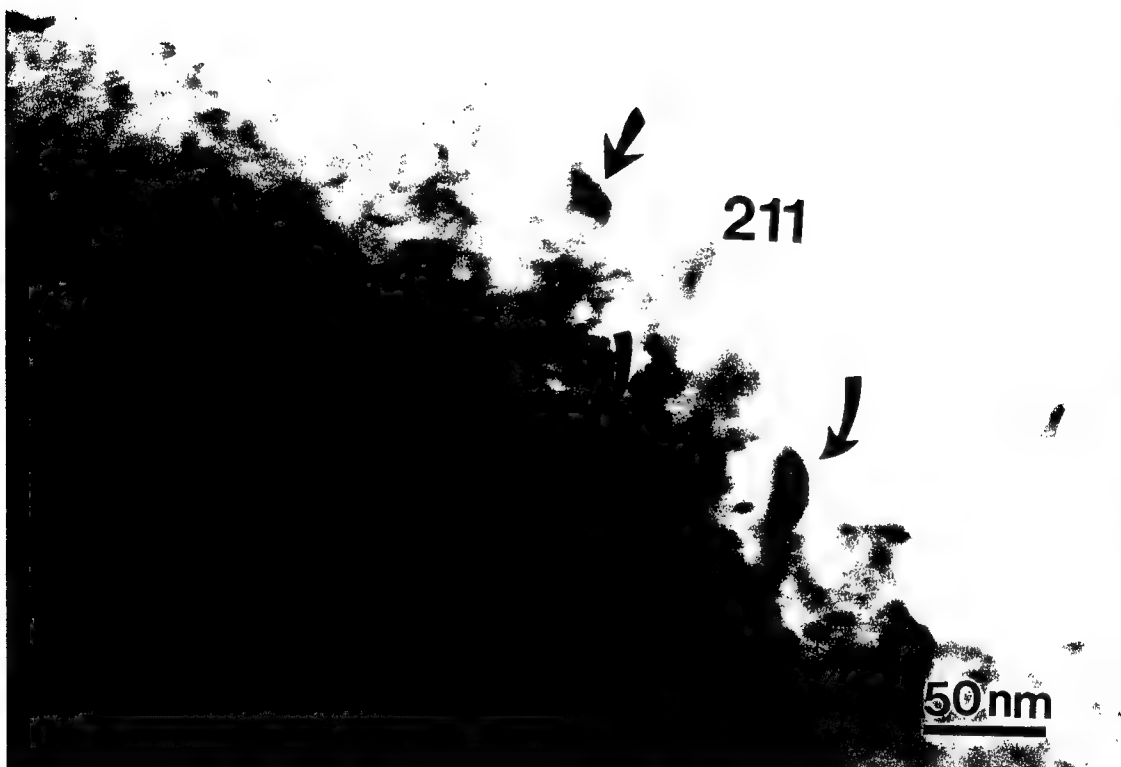


Figure 24a. BF TEM image from as quenched powder showing 211 particles trapped in an amorphous phase rich in Ba and Cu.

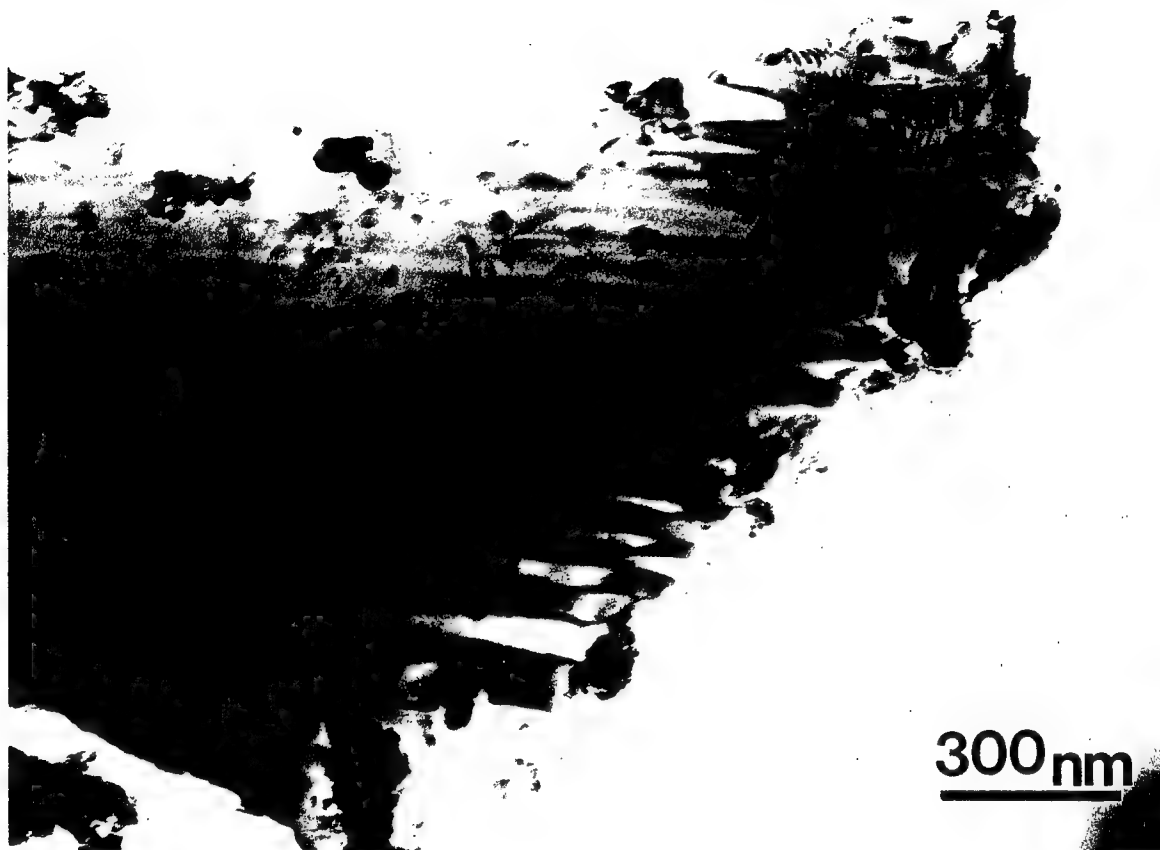


Figure 25. BF TEM image showing as quenched powder following a post heat treatment at 930°C.



Figure 26a. BF TEM image from as quenched powder following a post-heat treatment at 1140°C. This micrograph shows the presence of strain contrast.



Figure 26b. BF TEM image from as quenched powder following a post-heat treatment at 1140°C. This micrograph shows nano scale precipitates within the 123 grains.



Figure 27. TEM image from as quenched powder following a post-heat treatment at 1140°C and 8 h hold at 930°C.

disappearance of both the nano-size particles and the strain contrast from the 123 grains. We believe that the elimination of these features from the microstructure was responsible for the poor flux-trapping values observed in the large-grained samples prepared using quenched 123 powder doped with silver.

The next problem was to learn how to trap these fine features in large-grained bulk materials. This problem was addressed by modifying the composition of the initial powder with the addition of excess yttrium. The powder used was a mixture of 123 and 211 in a 50-50 molar ratio. The powder was heated to 211 + liquid region, cooled to 930°C, and held at this temperature for 8 h before cooling to room temperature. As seen in the BF TEM image shown in Figure 28, the presence of excess yttrium led to the retention of the fine structures such as the nanosized particles and the strain contrast within the 123 grains. This is an important observation as it will enable us to control the microstructure and thus the properties.

Next, the knowledge obtained in the preceding studies was applied in the preparation of a bulk 123 sample. The quenched powder used was a mixture containing 123 + 211 (12vol.%) + 10 wt.% Ag. The microstructure of the bulk sample prepared using this powder is shown in Figure 29. As indicated in this micrograph the use of excess Y_2O_3 led to the retention of nanometer-sized precipitates and strain contrast. This sample exhibited no circulating current under high applied field. We believe the reason for this behavior is the presence of microcracks in the microstructure of the sample as visible in Figure 29. Presently our effort is focussed on optimizing the 211 and Ag content of our monoliths with the aim of preventing the formation of microcracks.

III. Powder Preparation

The superior properties observed in the bulk samples prepared using quenched powder motivated us to explore different methods for preparing such powders. Initially, platinum crucibles were used in the preparation of quenched powder. In addition to being nonpractical, this approach also led to platinum contamination of the 123 powder. To avoid contamination and to simultaneously produce a less agglomerated powder, we have studied other means of producing powder such as torch flame and plasma spraying which retains the entrapped nano-meter sized second phase particles. Figure 30, shows the x-ray diffraction pattern (XRD) from 123 powder exposed to an $H_2 - O_2$ torch flame. As indicated in Figure 30, using this simple process we were able to quench the powder from the Y_2O_3 + liquid region of the phase diagram. The as quenched powder transformed into 123 orthorhombic phase upon 3h heat treatment at 950°C (see the XRD pattern shown in Figure 31) which indicates there was no loss of components in this process.

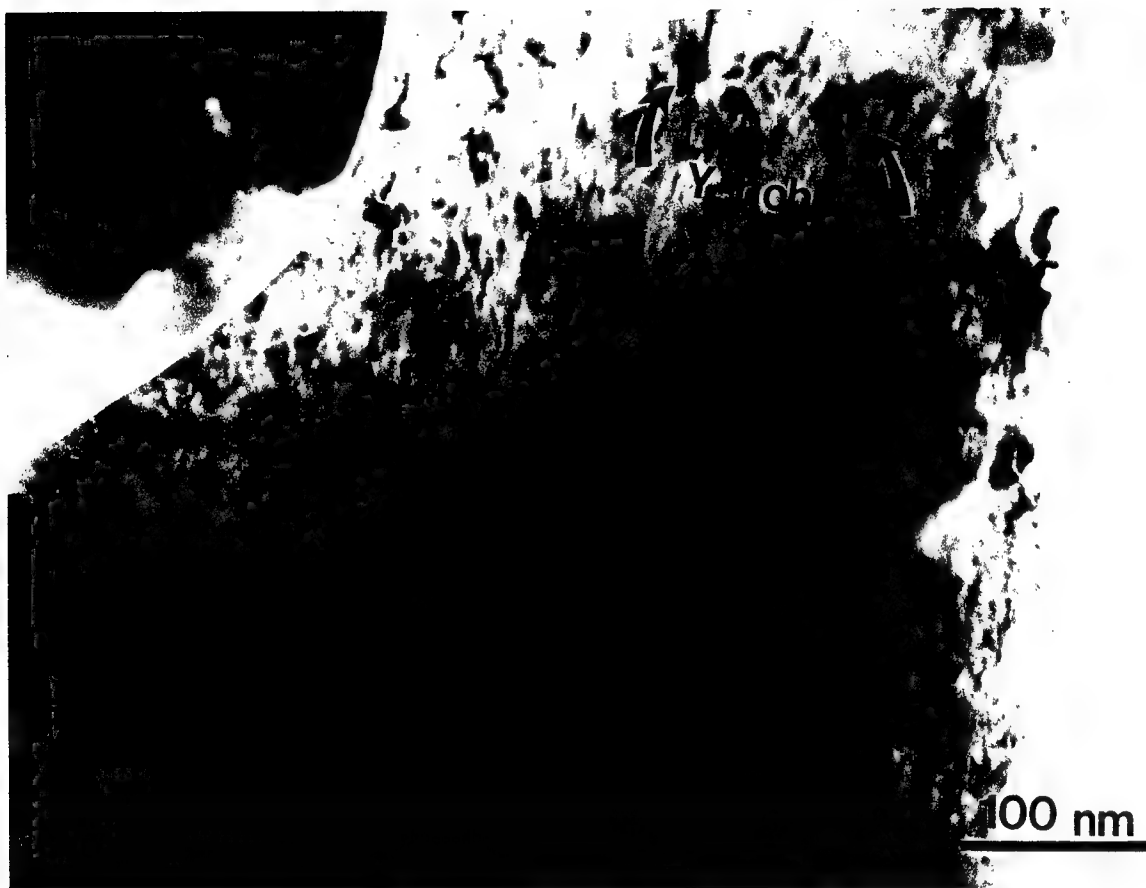


Figure 28. TEM image from as quenched 123/211 powder following a post-heat treatment at 1140°C and 8h subsequent hold at 930°C.



Figure 29. TEM image from a bulk textured sample prepared using 123 + 211 (12vol.%) + 10 wt.% Ag.

Sample: 123 BAR H2-O2 File: JJ841.RD

2-OCT-91 18:22

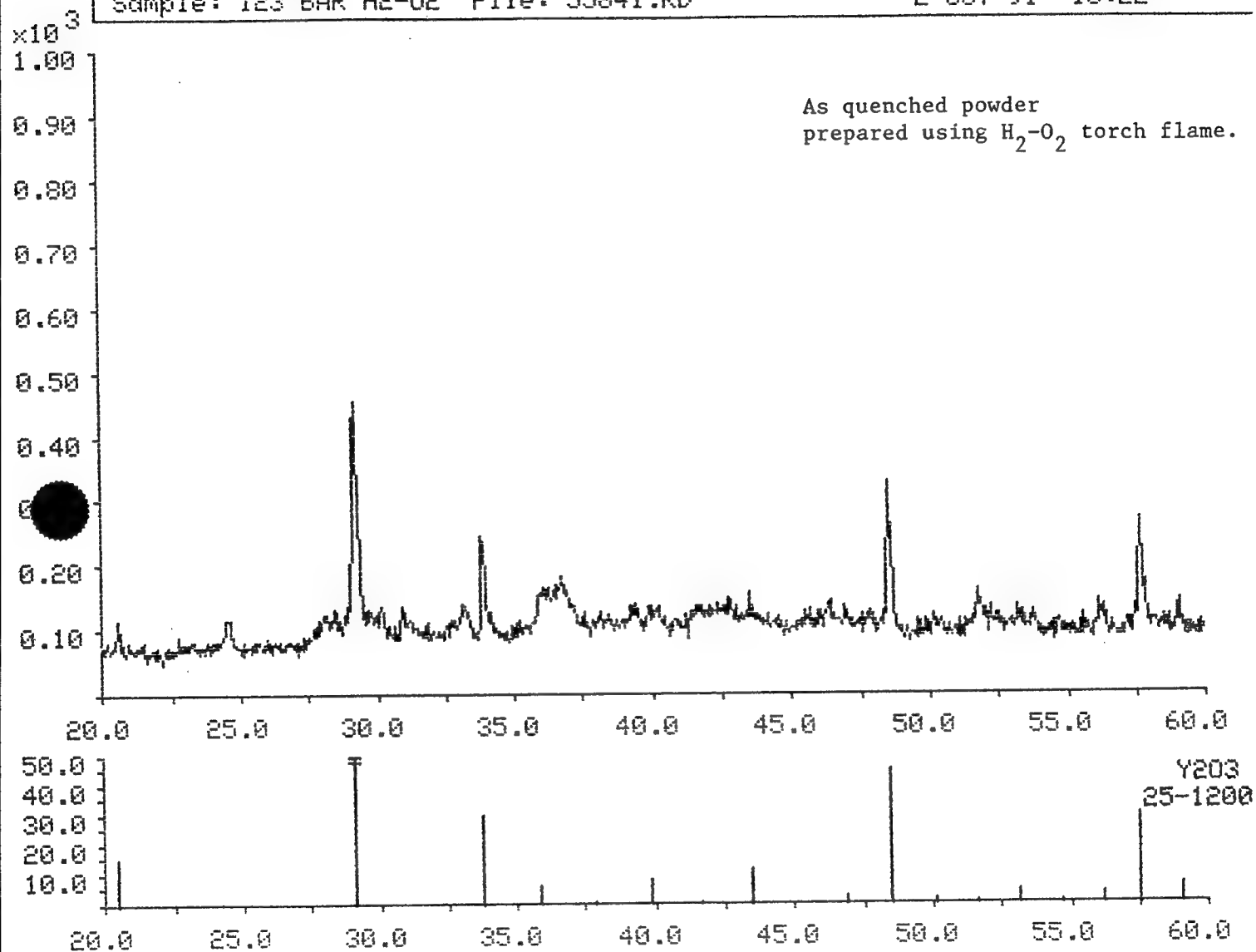


Figure 30. XRD pattern from as quenched powder prepared using H_2-O_2 torch flame process.

Sample: 123 H2-02 +950/3HRS File: JJ842.RD

2-OCT-91 18:27

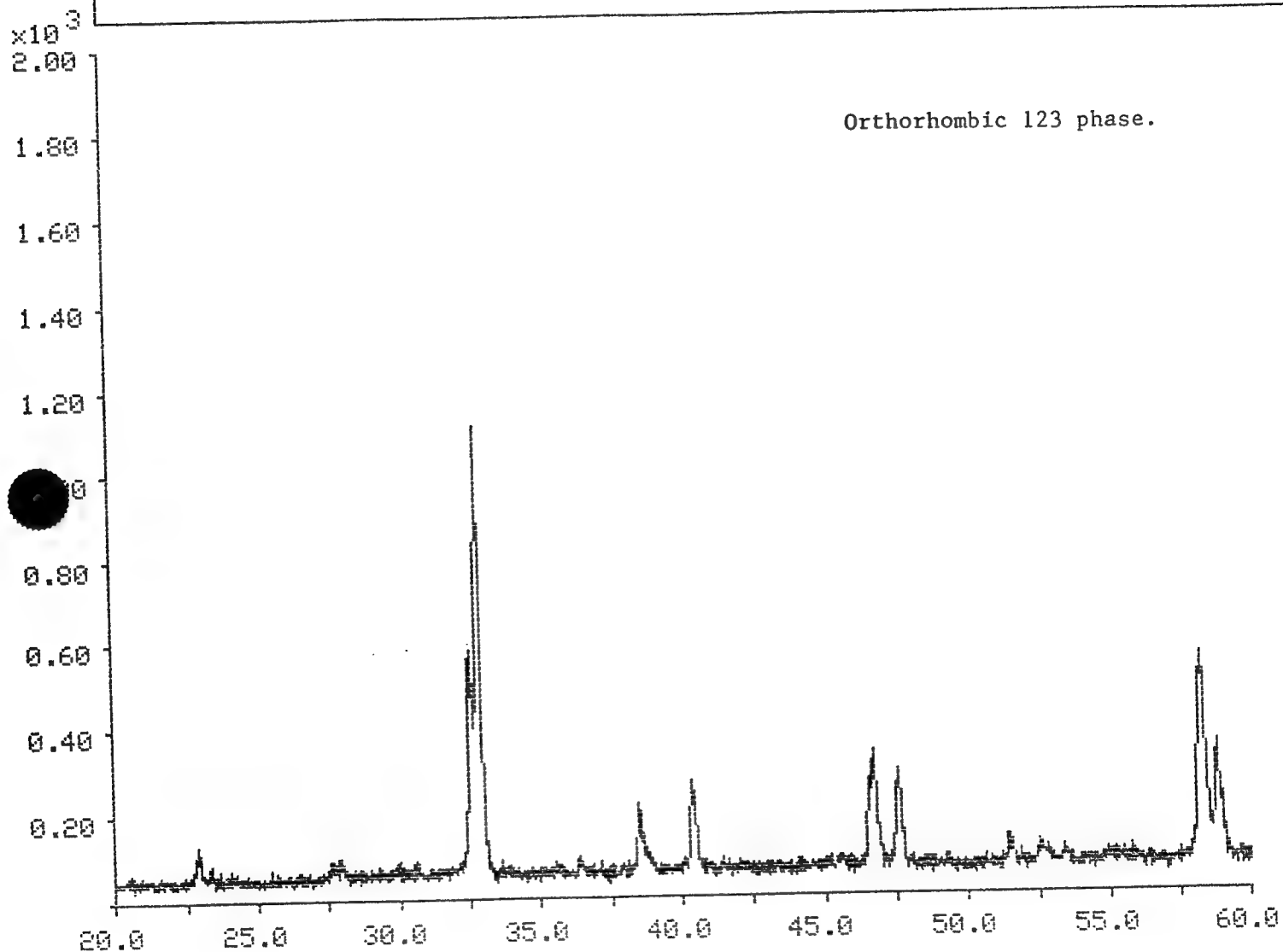


Figure 31. Powder in Figure 30, after calcination at 950°C for 3 h.

B. Low Temperature Processing

Although high temperature melt texturing (described in section A) produces 123 monoliths with useful properties, there are several disadvantages associated with this approach (i) difficulties in the retention of sample shape, (ii) variation of chemical composition due to the evaporation of components at high temperatures, and (iii) cracking of samples. In order to alleviate these problems, the feasibility of texturing at a lower temperature was investigated.

In the previous section of this report we described two approaches for melt texturing. An important common aspect of these two methods is that the growth of large 123 grains and their alignment is achieved in the presence of a liquid phase. This observation implies that a low temperature texturing should be possible if one can introduce liquid at a lower temperature.

The examination of BaO-CuO , $\text{BaO-Y}_2\text{O}_3$, and $\text{Y}_2\text{O}_3\text{-CuO}$ phase equilibria reveals that the mixture containing 2 moles of BaO and 3 moles of CuO (2B3C) provides a low temperature liquid phase (at temperatures less than 1000°C). The phase diagram describing this situation is shown in Figure 32. The success of the low temperature texturing using 2B3C will be dependent on the ability to form and retain a large quantity of a liquid phase during the growth of 123 grains. The low temperature liquid phase is formed through the reaction between BaO and CuO . The liquid phase is consumed by reacting with Y_2O_3 , and at this stage the rate of the liquid phase consumption is governed by the size of the Y_2O_3 particles. When finely mixed 2B3C is combined with coarse Y_2O_3 particles, low temperature texturing can be expected.

In order to examine this hypothesis, coarse Y_2O_3 particles were mixed with a finely mixed $2\text{BaCO}_3 \cdot 3\text{CuO}$. The mixture was dried and pressed into pellets uniaxially. The pressed pellets were sintered without a temperature gradient at 1000°C and 1050°C for 12 hours in ambient air and cooled at $1^\circ\text{C}/\text{min}$ to room temperature. The microstructures from the fracture surfaces were observed with SEM.

When the mixture was sintered at 1000°C (below the melting point of 123) for 12 hours, the outer region of the sample showed domains of large, textured 123 grains, although the central region did not show any visual sign of texturing (Figure 33). When the sample was sintered at 1050°C for 12 hours, the texturing of the outer region was improved, and even the central region exhibited noticeable alignment (Figure 34). These results clearly demonstrate that the texturing of 123 monoliths, as expected, is possible by employing properly designed raw materials. One problem associated with texturing in the presence of a liquid phase is the motion of the liquid phase. The detrimental effect from the liquid motion is the formation of large pores as shown in Figure 35. When the liquid migrates due to gravitational or capillary forces, the

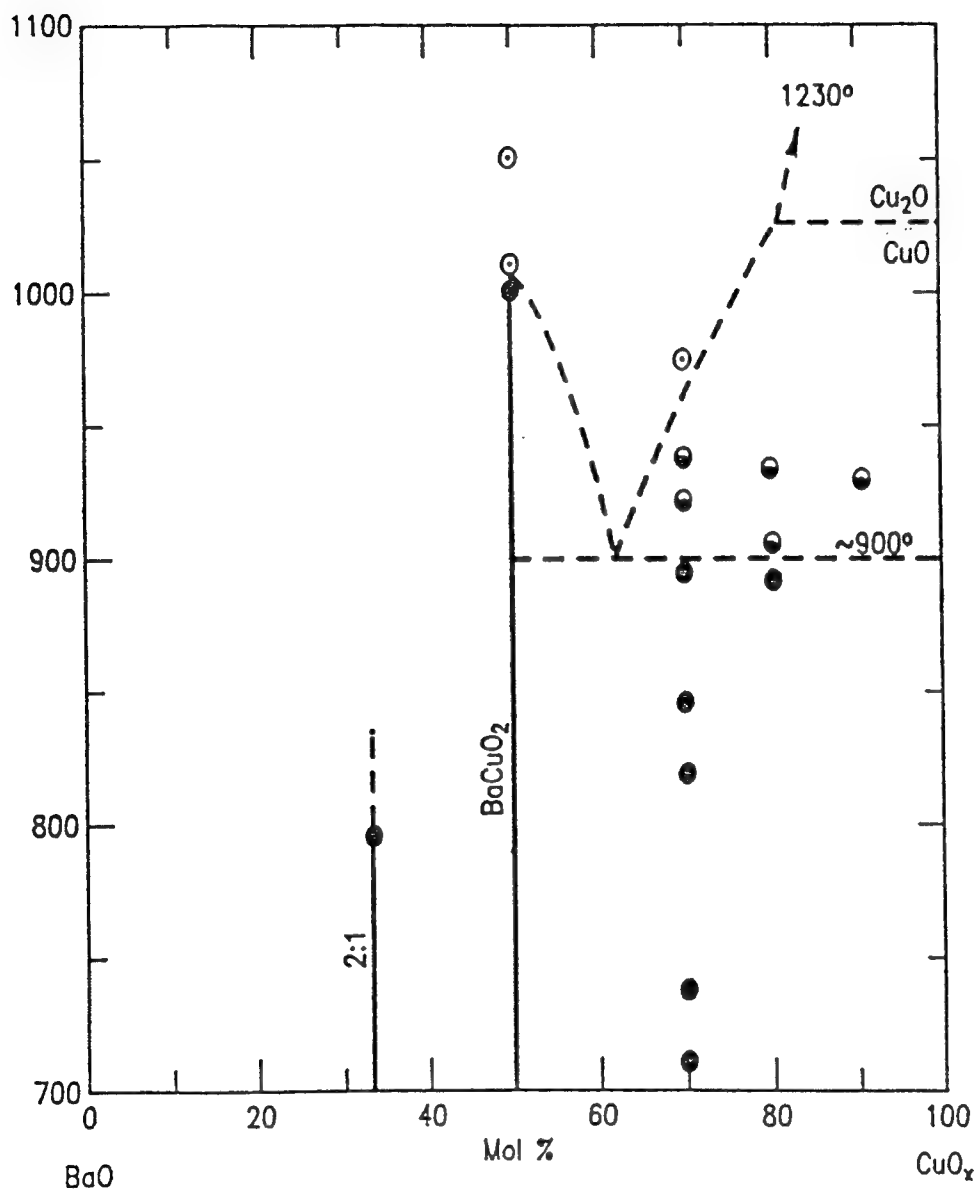


Figure 32. Phase diagram of a BaO-CuO binary system.

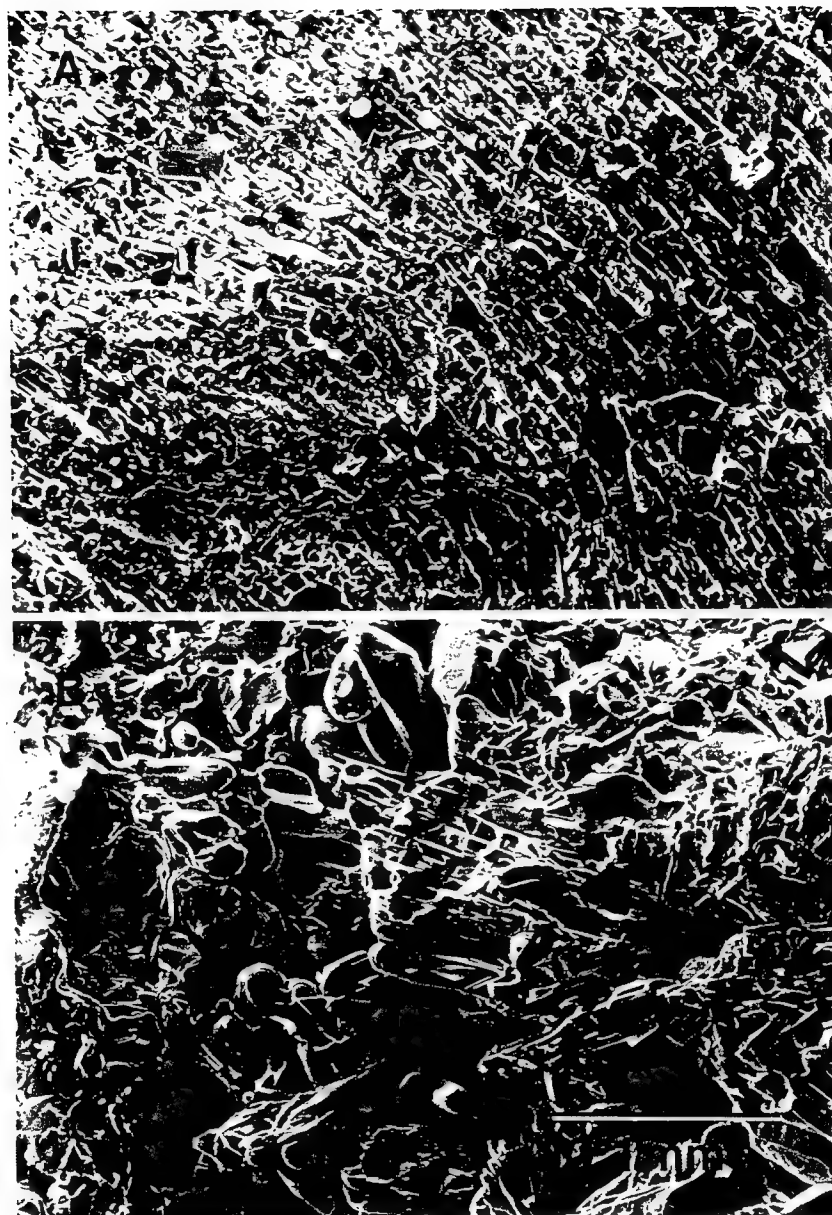


Figure 33. SEM micrograph taken from the mixture of Y_2O_3 and $2BaCO_3 \cdot 3CuO$ sintered at $1000^\circ C$ for 12 hours in ambient air. (a) edge (b) center

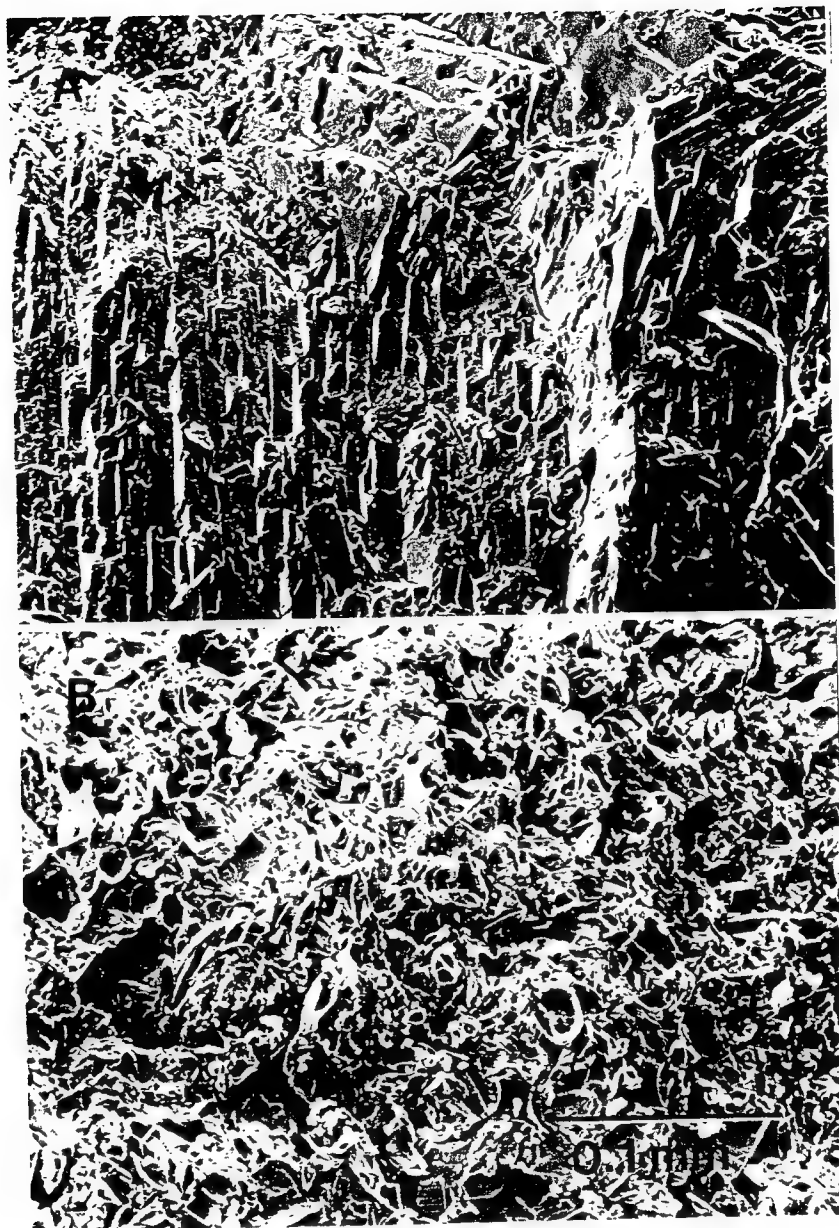


Figure 34. SEM micrograph taken from the mixture of Y_2O_3 and $2BaCO_3 \cdot 3CuO$ sintered at $1050^\circ C$ for 12 hours in ambient air. (a) edge (b) center

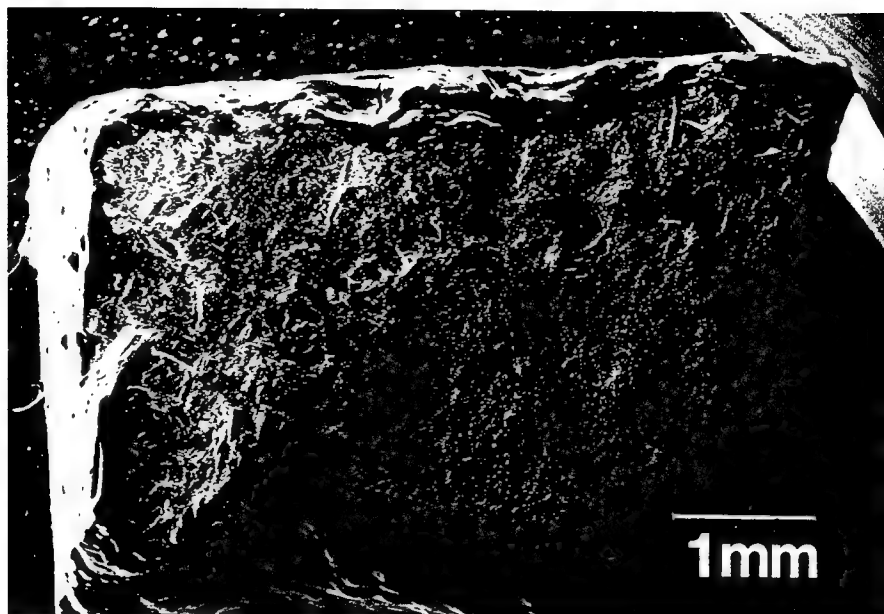


Figure 35. SEM micrograph taken from the mixture of Y_2O_3 and $2BaCO_3 \cdot 3CuO$ sintered at $1000^\circ C$ for 12 hours in ambient air.

volume initially occupied by the liquid phase remains in a form of pores. Research is in progress to alleviate the problem associated with the liquid motion and to produce completely textured 123 monoliths by this lower temperature method.

An important aspect of high temperature melt texturing is that the growth of large 123 grains and their alignment is achieved in the presence of a liquid phase. This observation implies that a low temperature texturing should be possible if one can introduce liquid at a lower temperature. One source of such low temperature liquid could be the eutectic reaction between BaCuO_2 and CuO which occurs at a temperature below 1000°C . A new precursor was developed to confirm the above idea; this precursor is a mixture which consists of Y_2BaCuO_5 , BaCuO_2 , and CuO in proper molar ratios to form 123. To prepare textured samples the powder mixture was pressed into a 2 mm thick pellet and heated to 985°C , held at this temperature for 12 hrs. Figure 36 shows the fracture surface view from the heat treated sample. The important features in this micrograph are the presence of an aligned region near the surface and porosity in the central portion of the sample. The reason for the development of pores in this process is not clear, but might be due to the decomposition of precursor powder into CO_2 containing compounds. To investigate this point, the precursor powder was calcined at intermediate temperatures of 750, 850, and finally at 950°C . The XRD patterns from these samples showed no sign for the decomposition of initial precursor powder. These results show that decomposition of compounds such as BaCO_3 are not the cause for the development of pores in the microstructure. Recently, we investigated the effect of sample thickness on microstructural development. Figures 37a and 37b are the fracture surface views from a 0.15 mm thick sample which has been sintered at 985°C for 12 hrs. As shown in this micrograph, it is possible to prepare a dense, textured sample at temperatures below the melting of 123 phase. Presently our efforts are focussed toward understanding the source and elimination of pores from the thicker samples.

With low temperature texturing we have previously shown the possibility of preparing textured 123 samples below the peritectic decomposition temperature of the 123 phase. However, at the time this process was limited to thin samples (tapes). Recently we have shown the feasibility of this low temperature process in preparing thicker textured samples. In addition we have explored other methods such as torch flame and plasma spraying in preparing powders for texture processing of 123 bulk samples. TEM structural investigation on these powder clearly indicated the presence of fine well-dispersed second phase particles within the primary matrix particles.

Recently, the focus of the work has been on the elimination of pores from the thicker samples. One approach toward achieving this goal has been the use of Ag as sintering aid. We have already shown the beneficial effects of Ag on the crystallization as well

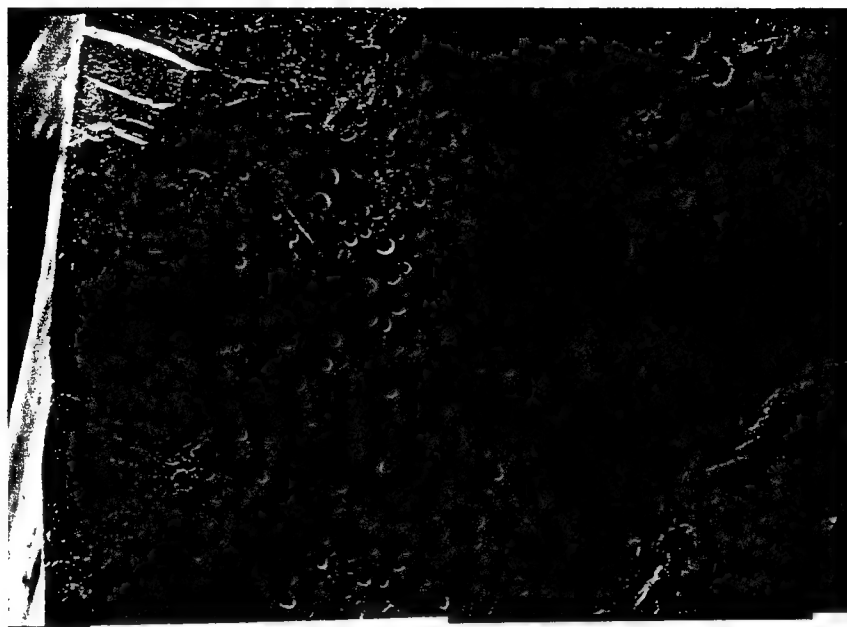


Figure 36. SEM micrograph taken from the mixture of 211, BaCuO_2 , and CuO sintered at 985°C for 12 hrs in air.

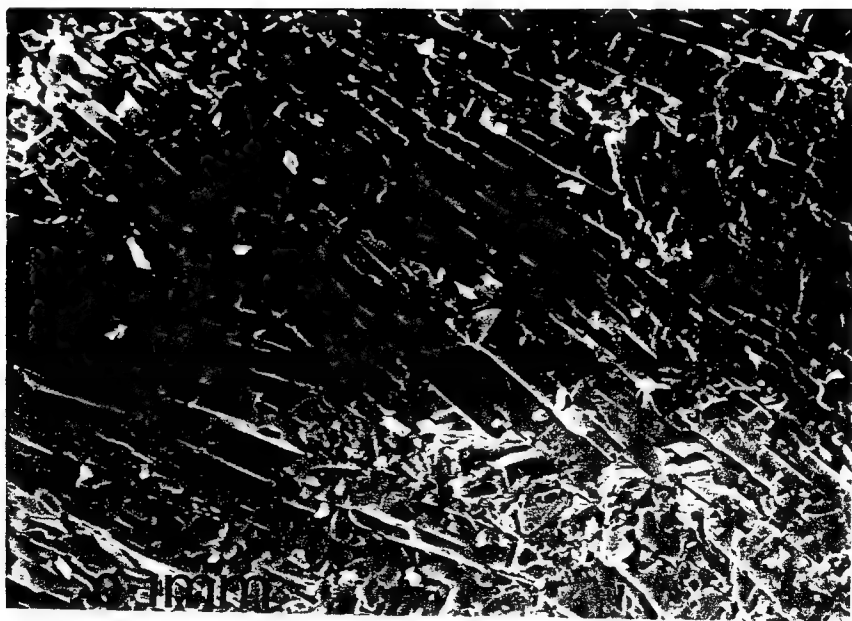
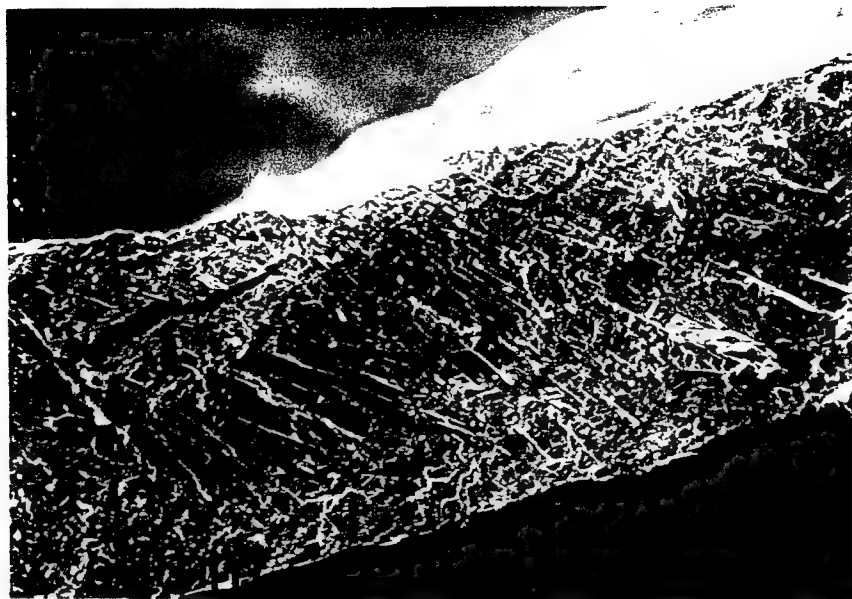


Figure 37. (a) SEM micrograph taken from a thin sample prepared using 211, BaCuO_2 , and CuO . This sample was sintered at 985°C for 12 hrs in air (b) magnified

as in the sintering of 123 compounds. Figure 38 shows a fracture surface view from a 1mm thick sample prepared using our new precursor doped with 10wt.% Ag. As seen in this micrograph the microstructure is highly aligned and the number of pores has reduced significantly in comparison to the thick samples prepared without adding silver. An SEM micrograph from such a sample is shown in Figure 39 for comparison. One reason for the improvement in microstructure by adding Ag may be the presence of excess liquid (from the melting of Ag). Whatever the reason, the advantage of Ag addition is clearly seen when comparing Figures 38 and 39. At this point we are studying the effect of varying Ag amounts upon further improvements in the microstructure of this and thicker samples.

C. Dynamic X-Ray Diffraction (DXRD) Studies

Samples and Experimental Conditions

Experiments have been conducted with pure phase 123 powders and with 123 precursors including a "flashed nitrate" precursor, and a citrate sol-gel precursors with stoichiometric as well as excess 211 (5% and 15%). These samples have been monitored by DXRD at temperatures between 925°C and 1350°C for times ranging from minutes to hours. A number of these samples were also subjected to staged heating-cooling; that is, heated to high temperatures for a prescribed length of time and then cooled to lower temperatures.

Typical Phase Sequencing

Figure 40 shows the disappearance and evolution of various phases for a pure phase 123 sample which was heated to 1350°C in 20 seconds, held there for 3 minutes, and then subsequently cooled to 1300°C and 1100°C for 60 and 300 min, respectively. As can be seen, Y_2O_3 continues to crystallize up to the point where the 211 phase begins to form. It is also interesting that Ba_2CuO_3 forms at the same time. This also occurred with pure phase 123 when cooled to 1150°C but did not occur when the citrate precursors with excess 211 was subjected to the same heating/cooling conditions. The implications of unreacted Y_2O_3 and Ba_2CuO_3 on the successful formation of melt textured 123 are not clear at this point. It may be that different temperatures are required to insure that the remaining Y_2O_3 reacts with it to form pure phase 211. Another matter of interest is the rapid formation of an unknown phase, tentatively labeled as $Y_xBa_yO_z$, at 1350°C and its disappearance coincident with the formation of the 211.

While the above results are typical for high temperatures, a number of experiments were also conducted at lower temperatures. For example, in the case of the citrate sol-gel precursor (5% excess 211) we employed DXRD in the "fast scan" mode to follow the decomposition of the 123 phase; determining that it decomposed to 211 at 1000°C in about 4 minutes and at 1050°C in a matter of seconds.

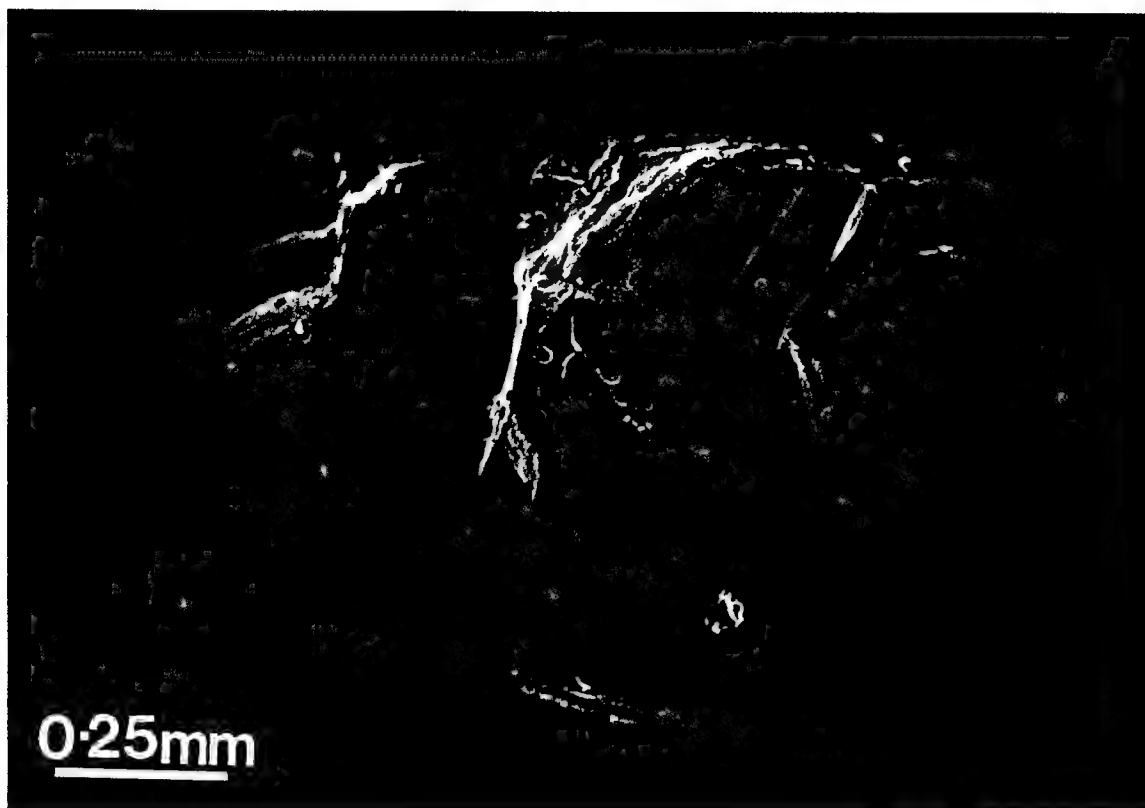


Figure 38. Cross-sectional SEM view from a bulk sample prepared using 211, BaCuO_2 , CuO and 10 wt.% A. This sample was sintered at 985°C for 12 h.

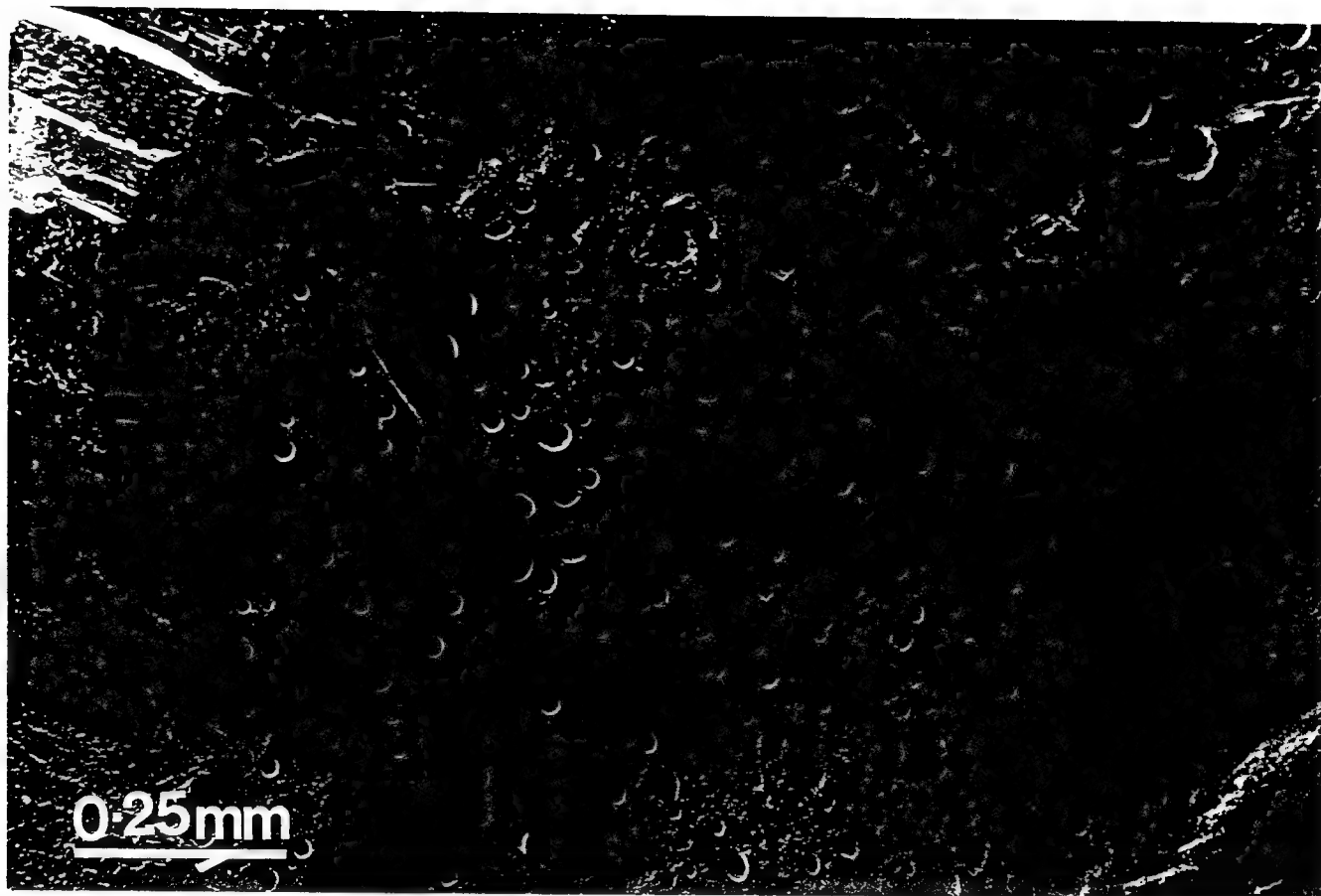


Figure 39. Cross-sectional SEM view from a bulk sample prepared using 211, BaCuO_2 , CuO . This sample was sintered at 985°C for 12 h.

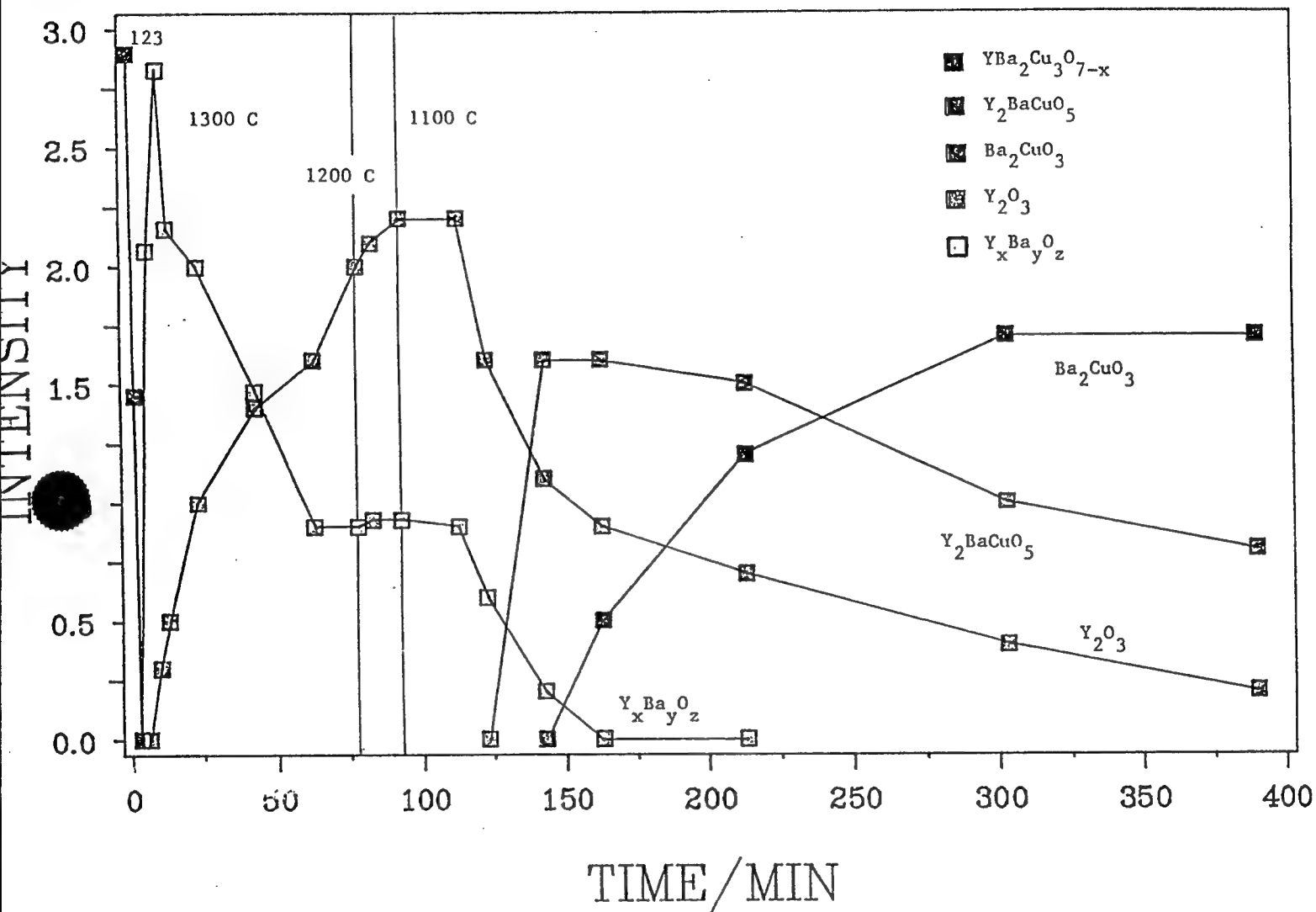


Figure 40. Phase sequencing: Pure Phase 123

Unidentified Phase Formation

During the course of these experiments a number of unknown phases were observed to form. At lower temperatures (925-1000°C) we have tentatively assigned one of these phases to tetragonal Ba_2CuO_3 . However the most interesting phase (and still unidentified) is one that occurs at temperatures at or above 1150°C. The characteristics of this phase are the following:

- It forms from either precursors or pure phase 123 at or above 1150°C.
- It will slowly melt at about 1350°C (takes ~ 4 hrs)
- When formed at 1350°C and then cooled to 1150°C, it continued to crystallize for about 30 min after which it slowly disappears (> 90 min). It appears to be involved in the formation of 211 at this temperature.
- When formed at 1350 and cooled to 1050°C, it disappears rapidly (6 min)
- An electron micrograph of a sample quenched from 1150 (after being held there for 60 min) showed flat crystals which are suspected to be this unknown phase. EDAX of this crystal indicated that it primarily contained Y and Ba (Cu peaks are either non-existent or extremely small) with trace quantities of Pt).
- This phase is far more dominant (at all temperatures) when there is excess 211 present and is proportional to the percent excess 211.

Since this phase does have trace quantities of Pt, it is not clear whether its presence is due to the presence of the Pt heating strip or whether it is a normal intermediate phase under these operating conditions.

Formation of 211 Phase

The 211 phase can be formed from any of the starting materials and at all temperatures between 1000 and 1150°C. In all cases, needle-like grains are formed, although the macro-morphology appears to depend on the processing conditions. For example, the samples heated directly to 1000°C form needle crystals which are distributed evenly with an interlocking texture. When heated directly to 1150°C, the morphology consists of a texture comprised of needle crystals emanating from a common center to form spherules. When the samples are first heated to 1350°C and then cooled to 1150°C, the needle crystals are longer and thinner.

Samples and Experimental Conditions

During the last quarter we initiated studies on the effects of precursor preparation and processing conditions on the high temperature phase chemistry of the 123 HTSC system. Three

different samples were investigated: pure phase 123, a 123 precursor with excess Ba and Cu, and a 123 sample which had been previously heated to 1450°C for 2 minutes and then rapidly quenched in liquid nitrogen and re-ground. Each sample was heated in air to 1350°C for 6 min and then rapidly cooled to 1100°C and held at that temperature for 20 minutes or more. In addition, the pure phase 123 was subjected to a slower heating program, but in an oxygen-deficient (helium) environment. When heated in air to 1300°C, both the melt quenched sample and the pure phase 123 produced both Y_2O_3 and the unknown phase reported earlier. However, the melt quenched sample produced much higher quantities of highly crystalline Y_2O_3 . As a result, when the melt quenched sample was cooled to 1100°C for 20 minutes, it produced highly crystalline 211 as well as small but significant quantities of the unknown "Z" phase. The significance of the Z phase to the formation of melt textured 123 is an unanswered question at this point. The results for processing in helium were quite different. That sample appeared to melt at about 1000°C and formed Y_2O_3 , BaO, and at least two new unidentified phases.

Technical Problems

We were attempting to obtain information on the temperature-time process conditions which lead to the optimal Y_2O_3 particle size when it nucleates out of the melt and to then determine the optimal process conditions to form an adequate 211 phase which will lead to melt textured 123.

Figure 41 is a comparison of the XRD spectra for the four experiments after being held at 1300°C for 6 minutes. As can be seen in Figure 41, only Y_2O_3 and unidentified phases are formed when pure phase 123 is heated in air to 1300°C for 6 minutes whereas the same sample heated in an oxygen-deficient environment produces only the unidentified phase. It should be pointed out that this phase (Z in Figure 41) is the same phase as reported earlier and has yet to be identified. It is possible that this phase is either a nonstoichiometric 211 phase or a crystalline variation of 211. It is interesting that the sample with excess Ba and Cu is almost completely melted and produces only small quantities of crystalline 211 phase and no crystalline Y_2O_3 . On the other hand, it is clear that the previous high temperatures to which the melt quenched sample has been exposed results in highly crystalline Y_2O_3 and small, but significant, quantities of the unknown Z phase.

Figure 42 shows the results for the same four experiments after the samples had been cooled to 1100°C and held there for 3 minutes. First of all, it is interesting that all four spectra, including the 123 sample processed in helium, exhibit crystalline Z phase. The fact that the Z phase appears in that sample as well as in the sample with excess Ba and Cu when it was absent at 1300°C (see Figure 41), indicates that the Z phase may be an equilibrium phase at this temperature. This is given further credence when it is

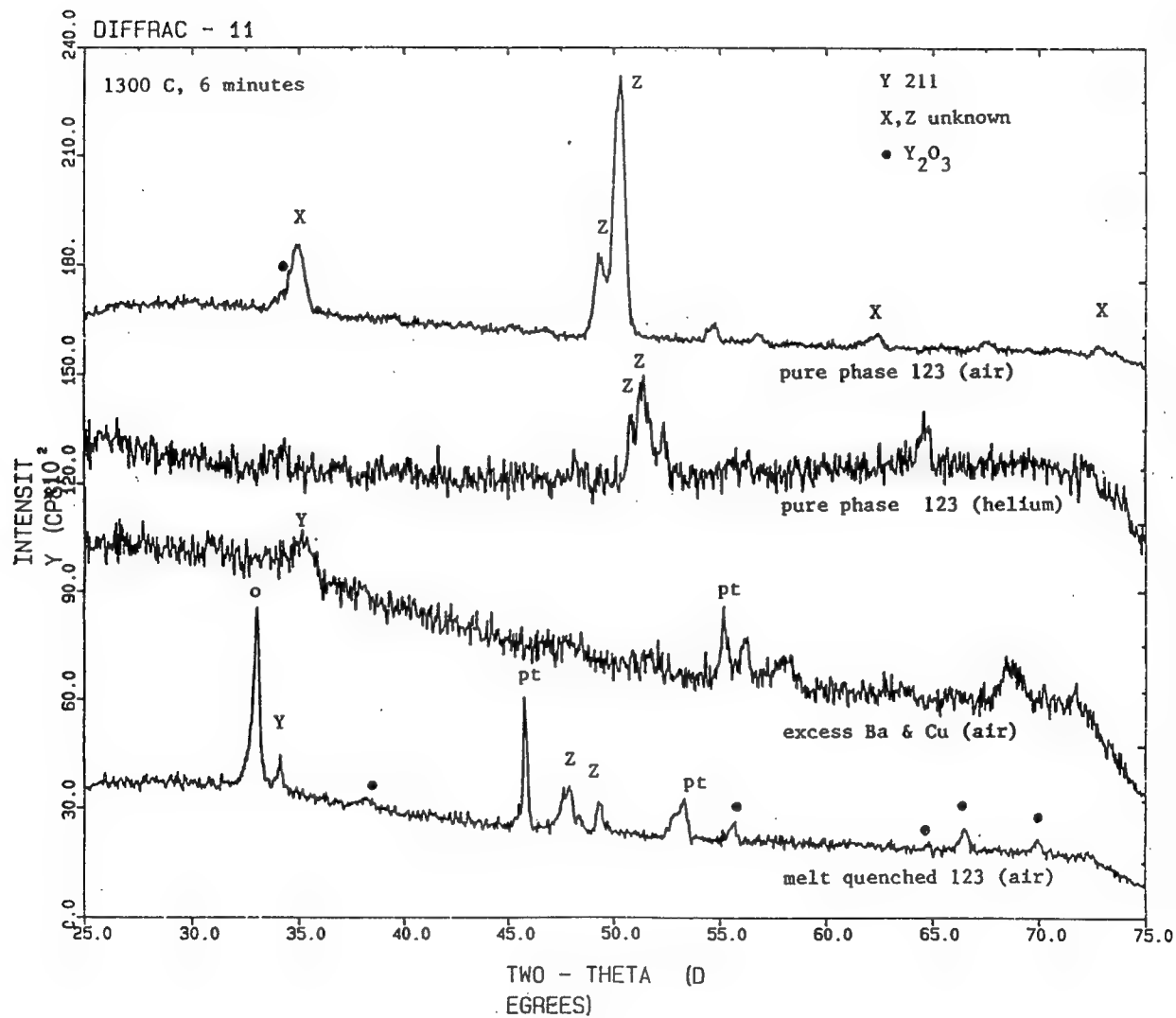


Figure 41.

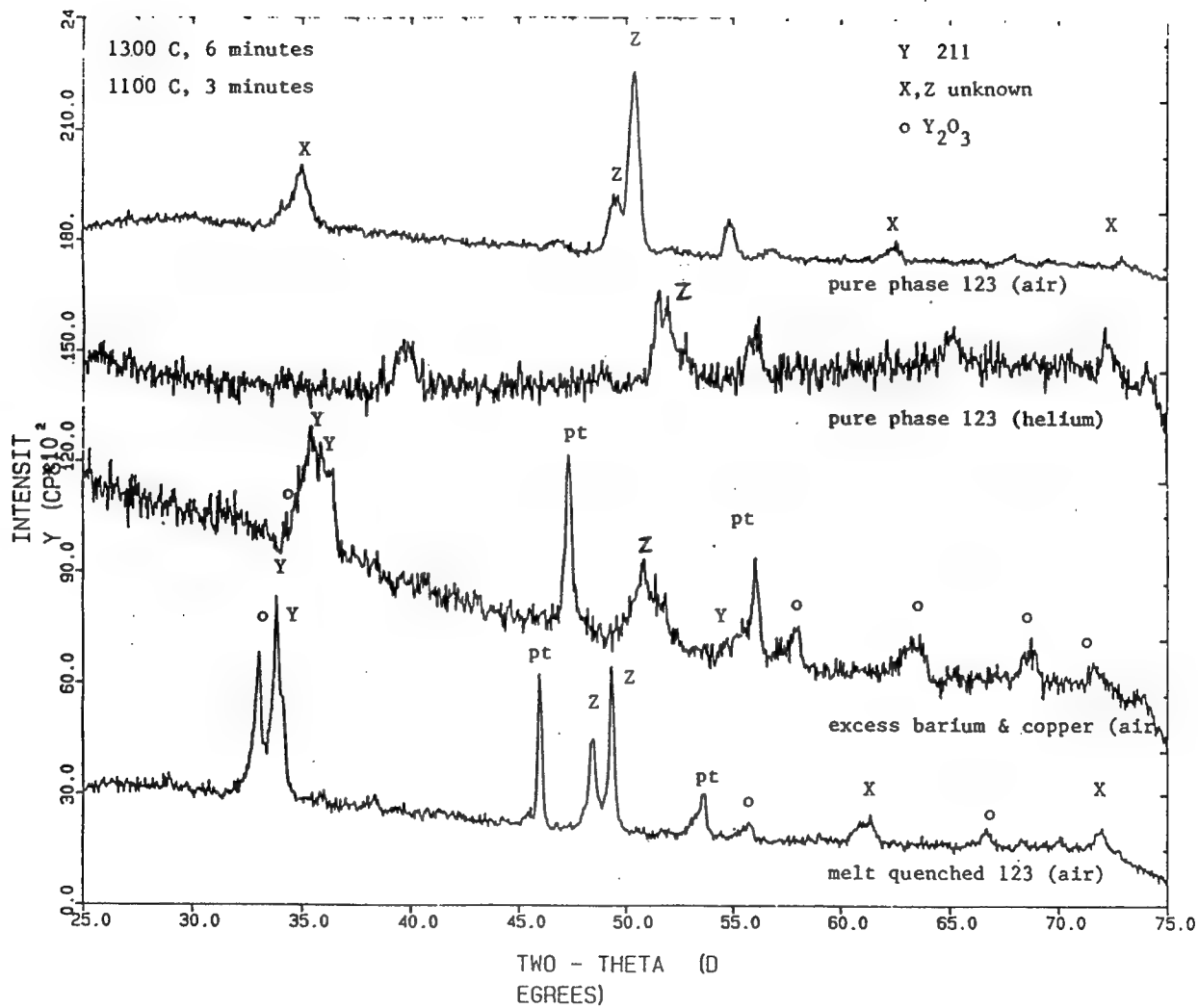


Figure 42.

realized that the Z phase grows upon cooling from 1300°C to 1100°C in the case of the melt quenched sample. The other observation of note is that the melt quenched sample produces the largest quantities of highly crystallized 211 with somewhat less formed in the case of the sample with excess Ba and Cu. The efficacy of the melt quenched sample for forming large grained 211 is more evident in the data presented in Figure 43, which compares the three air-processed samples after being held at 1100°C for 20 minutes. However, it should be noted that the unknown Z phase is still present and, if single phase 211 is necessary to produce melt textured 123 at lower temperatures, its presence may have serious implications.

The pure phase 123 was also processed in helium in order to determine the temperatures at which melting would occur and to see the extent to which the phase chemistry would differ from processing in air. Figures 44A-44C show the DXRD spectra as the sample was heated at 15°C/min from 1050°C to 1300°C, held at 1300°C for 6 min and then cooled to 1100°C and held for 6 min. As can be seen, the sample appears to have melted between 1000°C and 1050°C and new phases nucleate, starting at about 1100°C. There are at least three unidentified phases formed at high temperatures: The X phase grows steadily up to 1250°C at which point it appears to form another phase (Δ) which grows and persists even after cooling to 1100°C and quenching to room temperature. A third unidentified phase, the Z phase, nucleates and grows from 1100°C to 1300°C, but disappears upon cooling to 1100°C. At 1300°C and particularly when cooled to 1100°C, there is some evidence of the formation of 211 along with Y_2O_3 and BaO, the latter being formed at temperatures as low as 1200°C. The former is surprising since, in air, 211 melts above 1200°C.

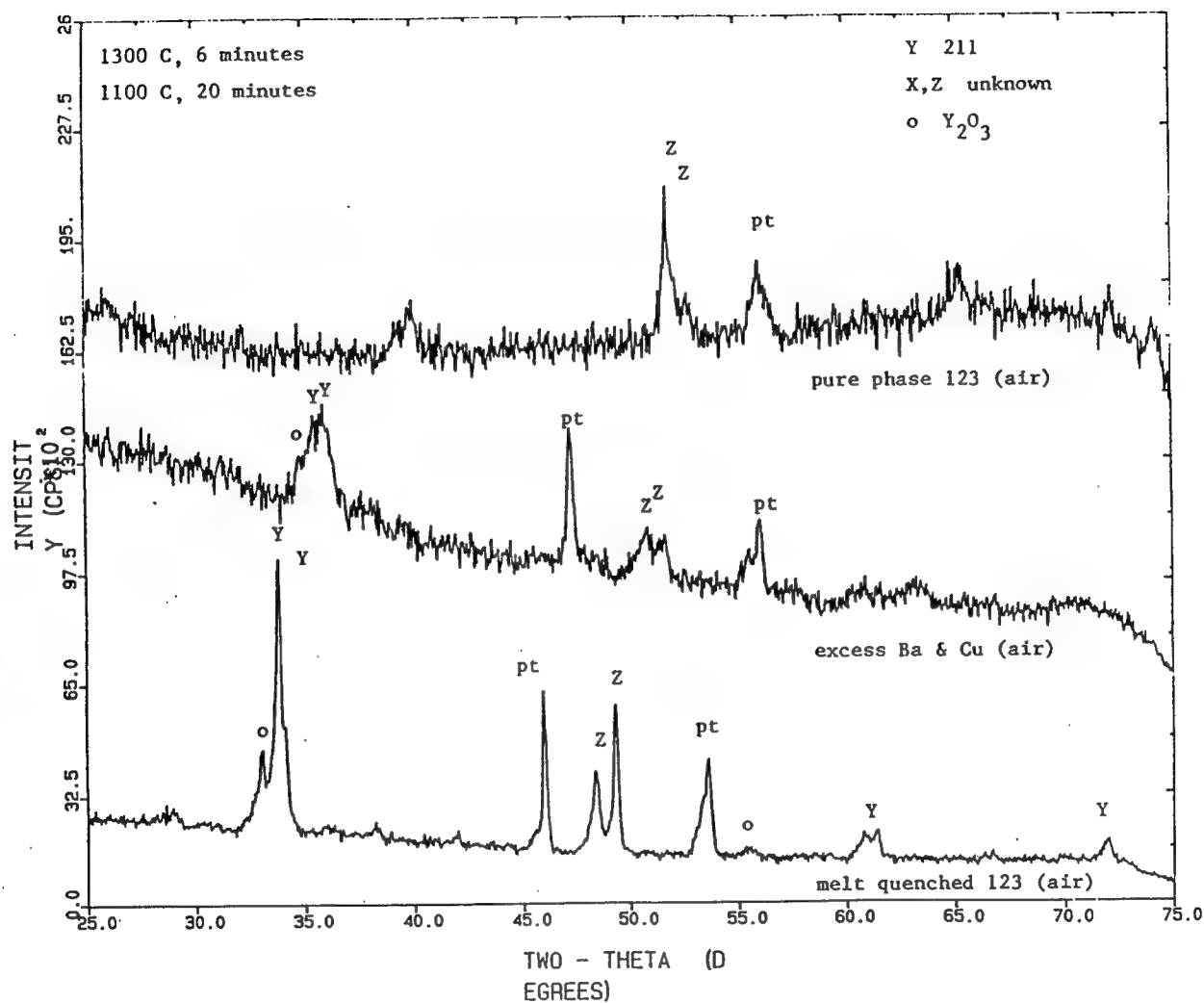


Figure 43.

Legend: \circ BaO, χ , \blacktriangle unknown, \bullet Y_2O_3 , ψ 211

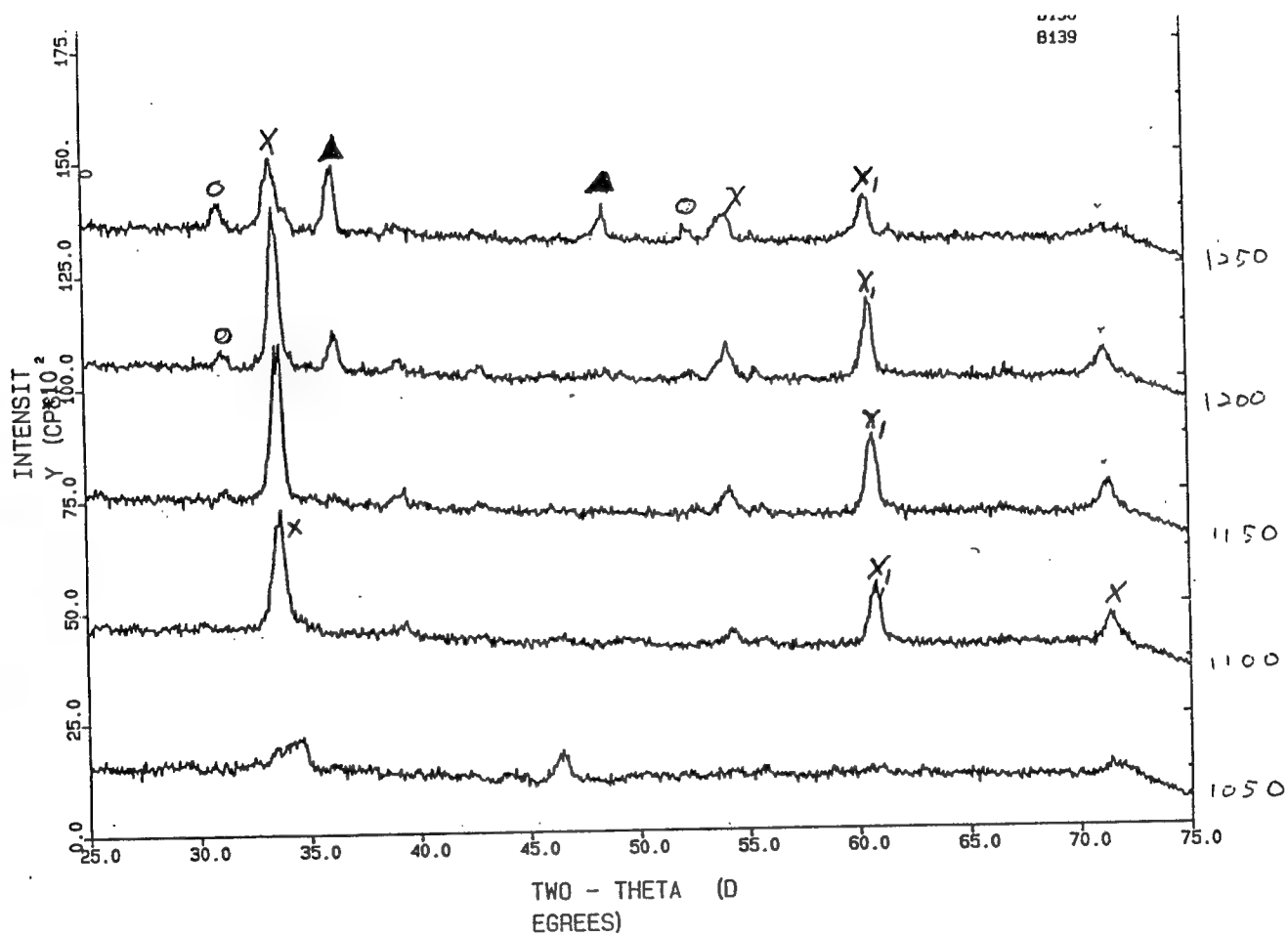


Figure 44a.

Legend: ○ BaO, X, ▲ unknown, ● Y₂O₃, ψ 211

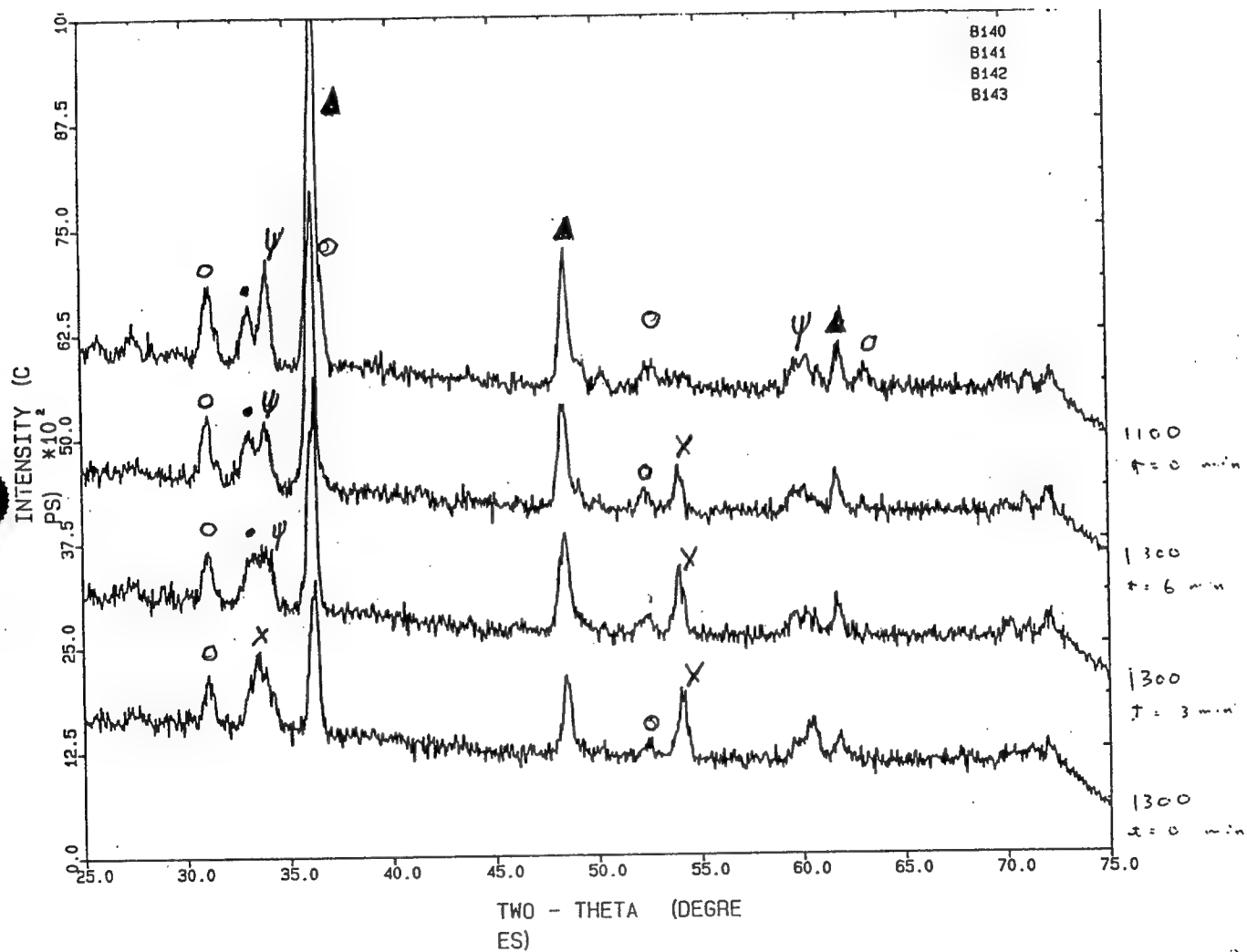
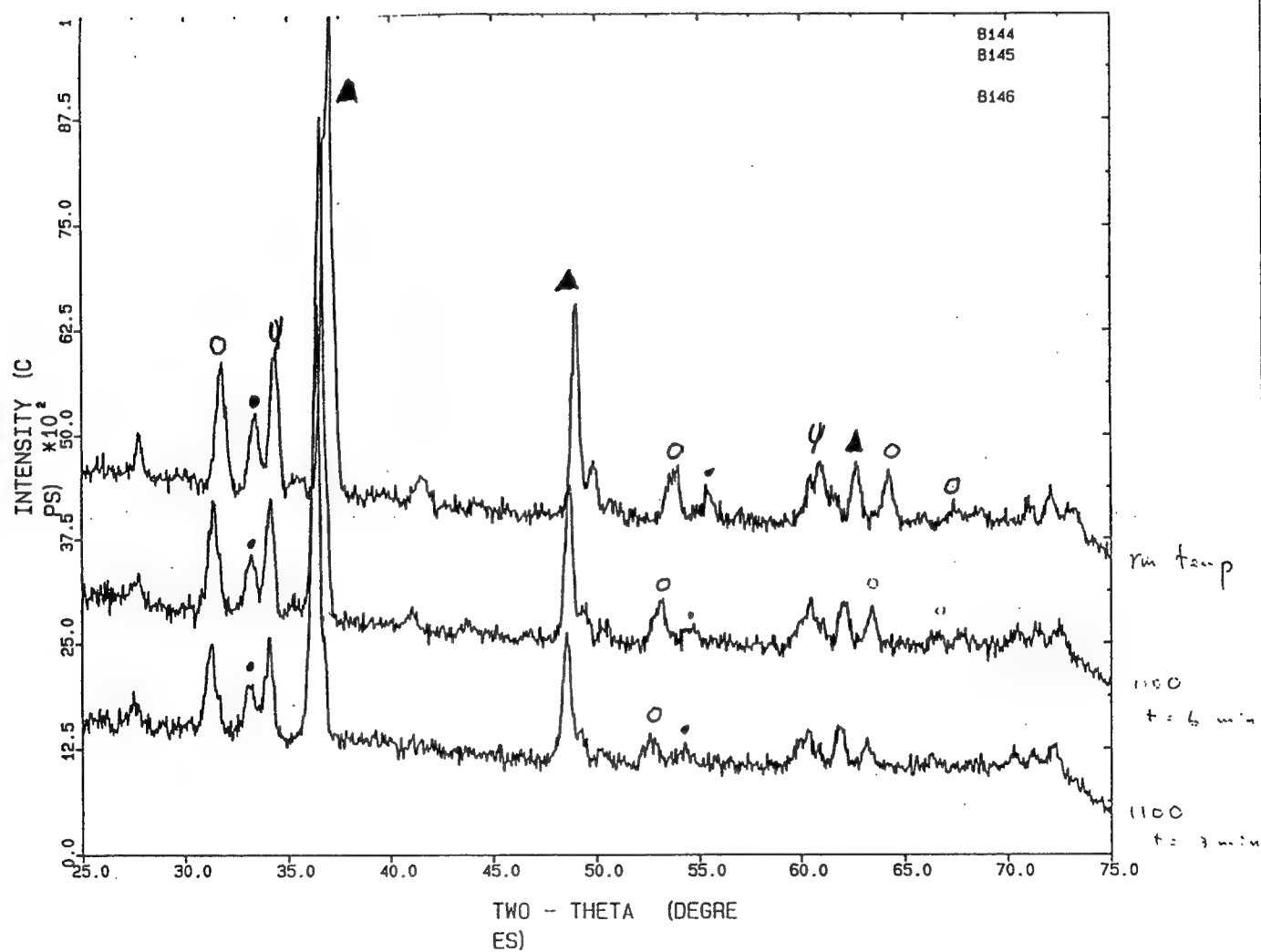


Figure 44b.

Legend: ○ BaO, X, ▲ unknown, ● Y₂O₃, ψ 211



1010-4

Figure 44c.

SUPERCONDUCTING PROPERTIES

AC susceptibility data of the melt-textured samples prepared by both techniques exhibited a T_c onset of 93K with a very narrow delta T_c range (Figure 45). In fact, ac susceptibility studies have shown to have limited usefulness in characterizing these melt textured compounds in the magnetic fields available with our current instrumentation. This is because all of the melt textured materials show essentially similar T_c curves, due to the large intragrain currents available in these samples.

Current densities of up to 1.0×10^5 A/cm² (corrected for self field effects) were obtained using transport current measurements (Figure 46). Current density measurements on these materials are difficult at zero field because of the large amount of current that passes through the sample. Over 100 amperes of current was passed through one of these samples at which point difficulty was encountered in the system setup. While the current contacts were still marginally operational, current leads that had not been properly cooled were destroyed. In the future, transport current density measurements at higher fields should suffice for characterization of these samples.

A. Flux-Trapping Experiments

Flux-trapping measurements were carried out on the melt-textured samples as a function of applied field. Fields of up to 1280 Gauss were trapped initially in the melt-textured samples (5 mm thick x 30 mm long x 8 mm wide) containing additional 211 phase (up to 10 at % 211, Figure 47). The trapped flux in the 211 rich sample (10 at.% 211) was 50 % higher than in the pure 123, possibly due to increased number of flux pinning sites represented by small 211 inclusions within the 123 phase, as suggested by Murakami et. al. The percentage of the trapped flux was decreasing with an increased applied field as shown in Figure 48. This percentage was, however, very similar for pure and 211 rich $YBa_2Cu_3O_{7-x}$ samples. This result is most likely related to the current density behavior in a magnetic field. Current density decreases rather rapidly even in a small applied magnetic field due to weak links, reaching a plateau at a higher field, where current density is only weakly dependent on applied field. This behavior of current density is in turn related to the amount of flux trapped in the sample. A flux profile map, Figure 49, of one such sample indicates regions of high trapping ability occurring in the regions of larger, oriented grains. Several geometrical (thickness, grain orientation, grain size, trapped field as a function of distance from the sample surface) factors affecting the flux trapping abilities of the melt-textured samples are also being investigated (Figure 50).

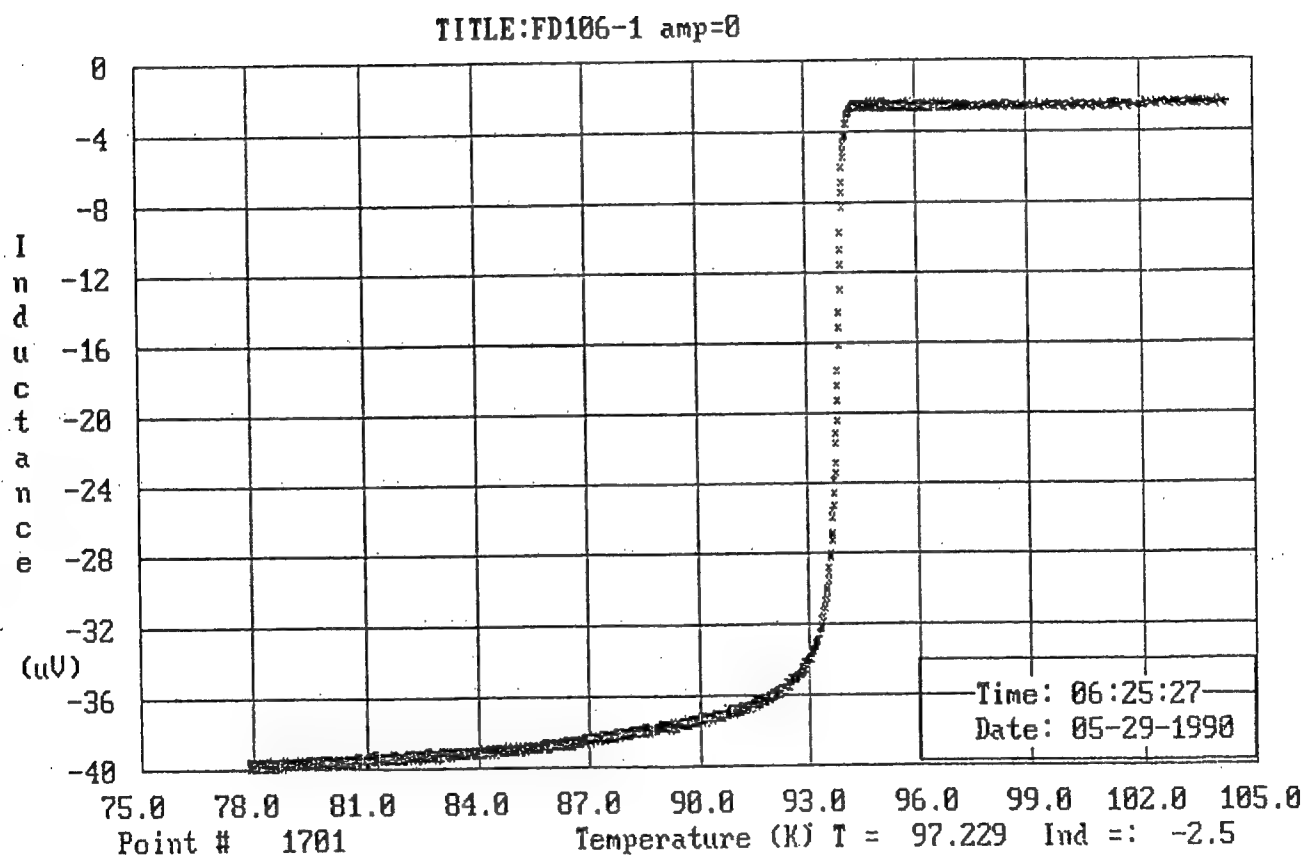


Figure 45. Transition temperature curve for melt-textured $\text{YBa}_2\text{Cu}_3\text{O}_{7-x}$ at 0.3 Gauss.

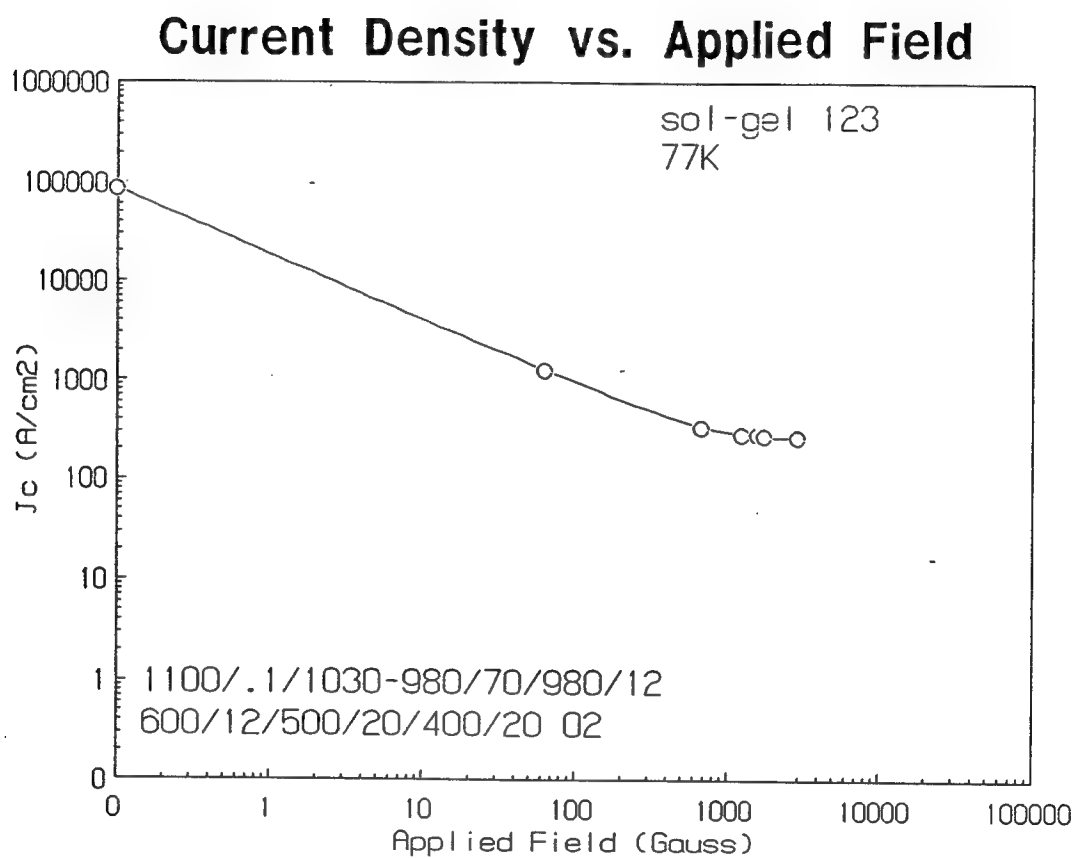


Figure 46. Current density vs. applied field for a melt textured $\text{YBa}_2\text{Cu}_3\text{O}_{7-x}$ measured at 77K.

Trapped Field vs. Applied Field

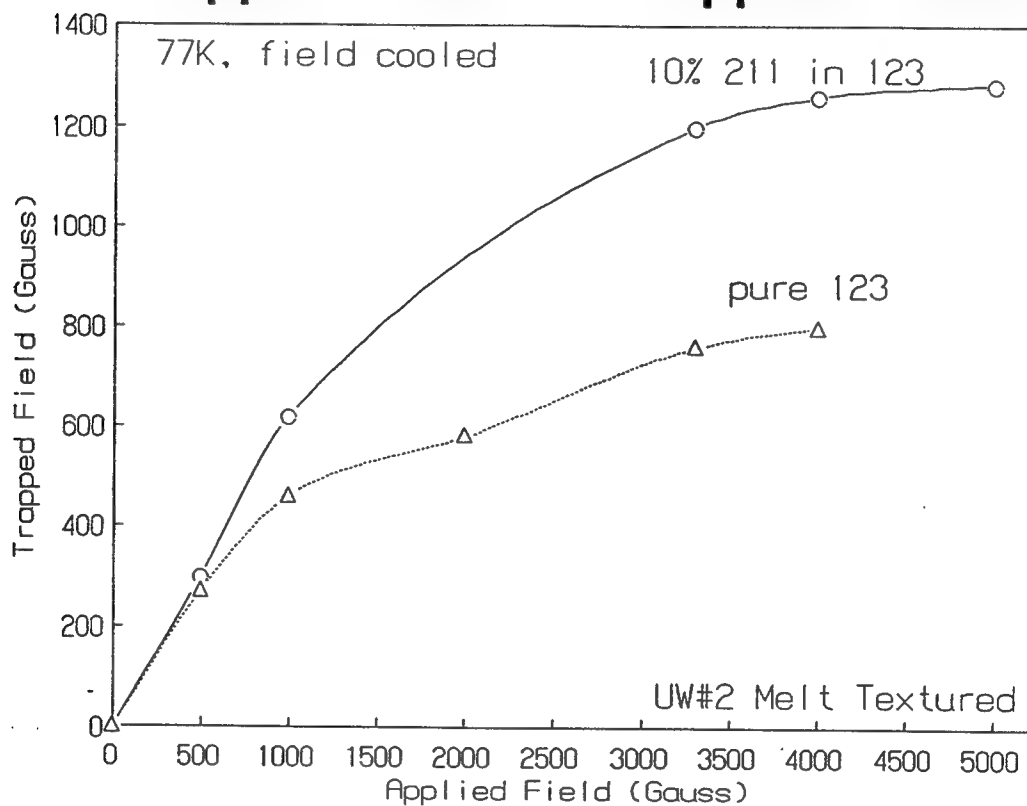


Figure 47. Trapped-flux vs applied field for melt-textured $\text{YBa}_2\text{Cu}_3\text{O}_{7-x}$ with 10 at. % of Y_2BaCuO_5 phase added.

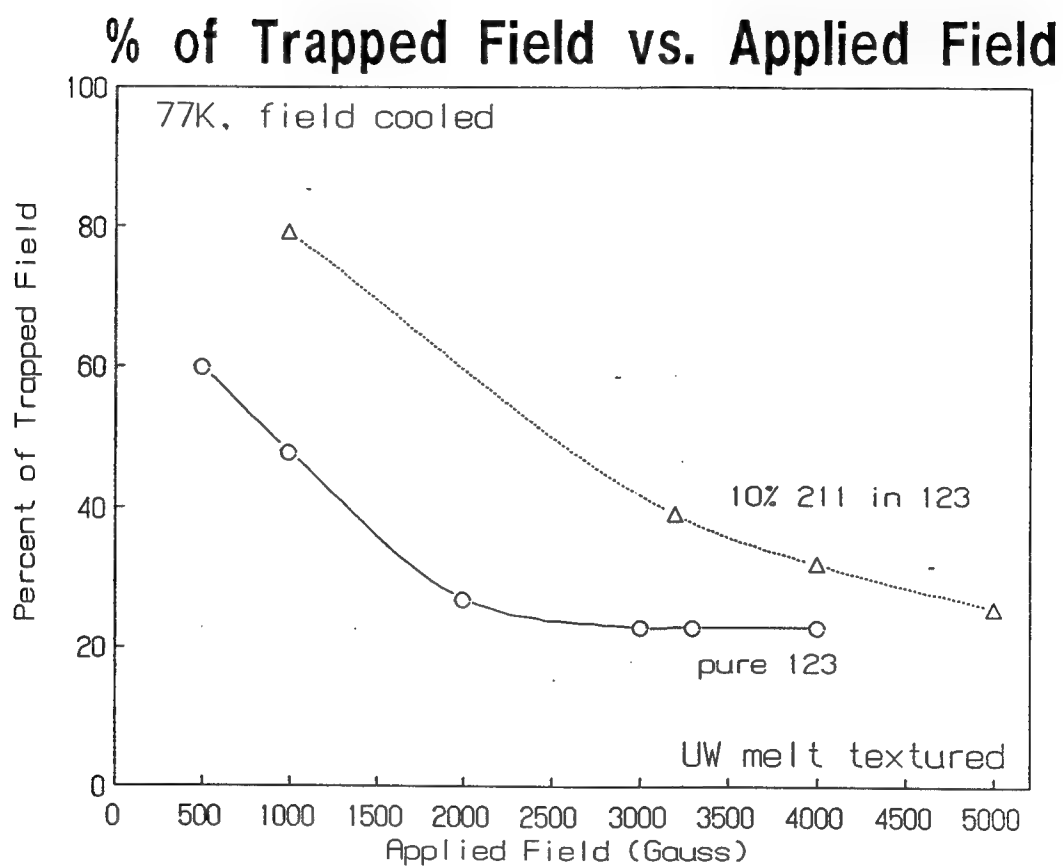


Figure 48. Percentage of trapped field vs. applied field for a melt-textured $\text{YBa}_2\text{Cu}_3\text{O}_{7-x}$ sample shown in Figure 47.

Trapped Flux Profile

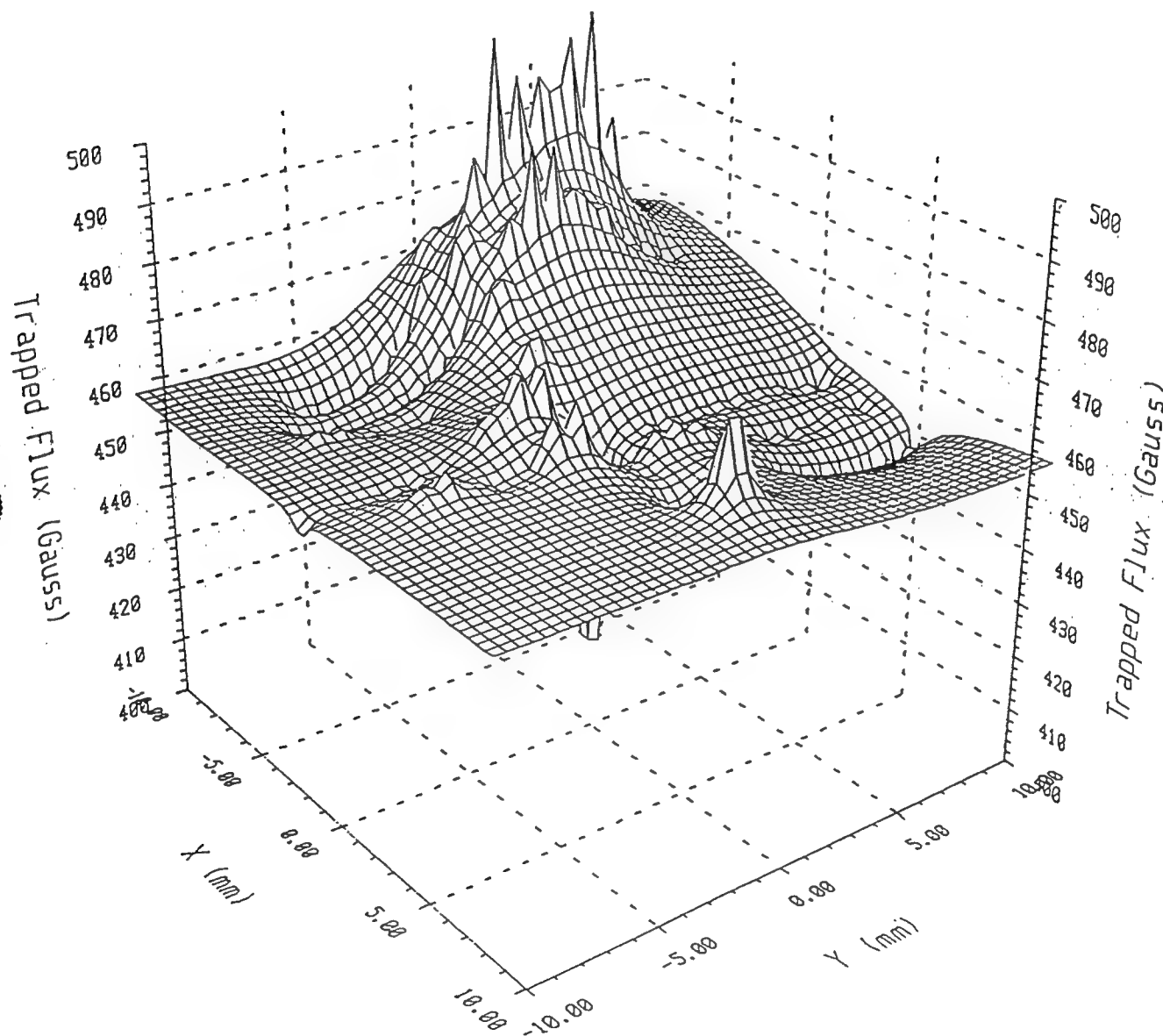


Figure 49. A flux profile map of a melt-textured $\text{YBa}_2\text{Cu}_3\text{O}_{7-x}$.

Flux Trapping vs. Distance

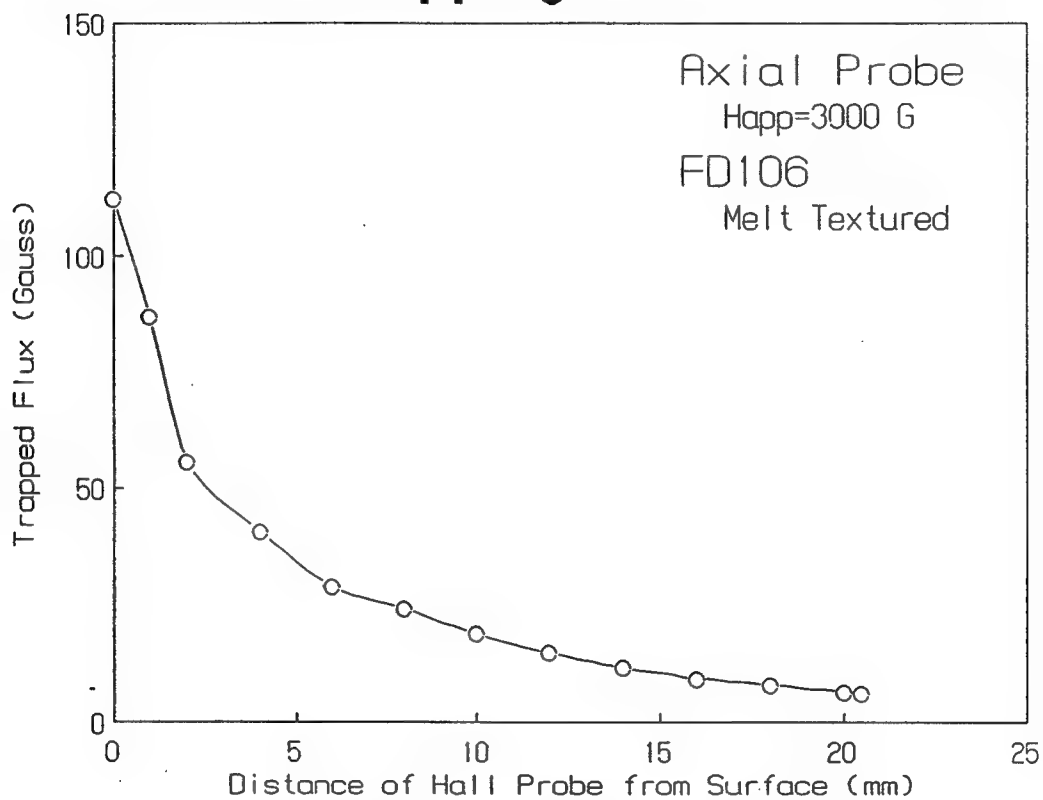


Figure 50. Flux-trapping vs. distance of the Hall probe from the sample surface for melt-textured $\text{YBa}_2\text{Cu}_3\text{O}_{7-x}$.

Mechanism of flux-trapping is being investigated as a function of resident time of the sample in applied magnetic field during field trapping. It was determined that the trapped field decreases with increased resident time in the field at relatively high fields (> 3000 Gauss) as presented in Figure 51. This is probably due to the flux creep problems associated with higher magnetic fields. The full understanding and implications of this observation, very important for our rivet gun application, are being investigated.

Quenching experiments of trapped flux were designed with respect to a superconducting rivet gun device. Some preliminary experimental results are presented in Figures 52-54. Initial quenching experiments were performed on a cylindrical sample to determine the presence of macroscopic circulating currents flowing around in a cylinder. As observed in Figure 52, where the trapped field profile was measured across the cylindrical sample, no significant circulating currents were detected as demonstrated by the changing sign of a trapped field. The lack of circulating currents are due to microstructural effects, where large 123 grains were poorly connected, hence limiting the transport current density. In the quenching experiments, the trapped field in a melt-textured sample was quenched thermally (Figure 53). The quenching speed was investigated as a function of heater power input with sample positioned on a heater coil (Figure 54). The quenching occurred rather rapidly (in less than a second) but it is yet unclear if the quenching occurred due to a temperature increase from the heater or an increase in electrical current carried by the sample by transferring the current from the heater into the superconductor. In this quenching experiment, the trapped flux dropped from about 250 Gauss to 150 Gauss in less than a second (Figure 53). This partial quench may be due to a single grain being quenched in the sample located closer to the heater, yet retaining some flux trapped in another grain further away from the heater.

A new EG&G Vibrating Sample Magnetometer (VSM), Model 155, was installed in Superconductivity Characterization Laboratory during the second quarter. The VSM allows for the magnetic characterization of magnetic moments as small as 5×10^{-5} emu in magnetic fields ranging from zero to 2 Tesla using a conventional, water cooled, Walker model-12H electromagnet. The 2 Tesla electromagnet is also used for the flux-trapping experiments.

The flux-trapping experimental setup is shown in Figure 55, where a superconducting sample is either zero field or field cooled in an electromagnet or a superconducting magnet. The superconducting sample, contained in a ceramic microform for cryogenic cooling, is then placed on a micrometer stage and a flux profile is generated with a cryogenic Hall probe attached to F.W. Bell 9900 Gaussmeter.

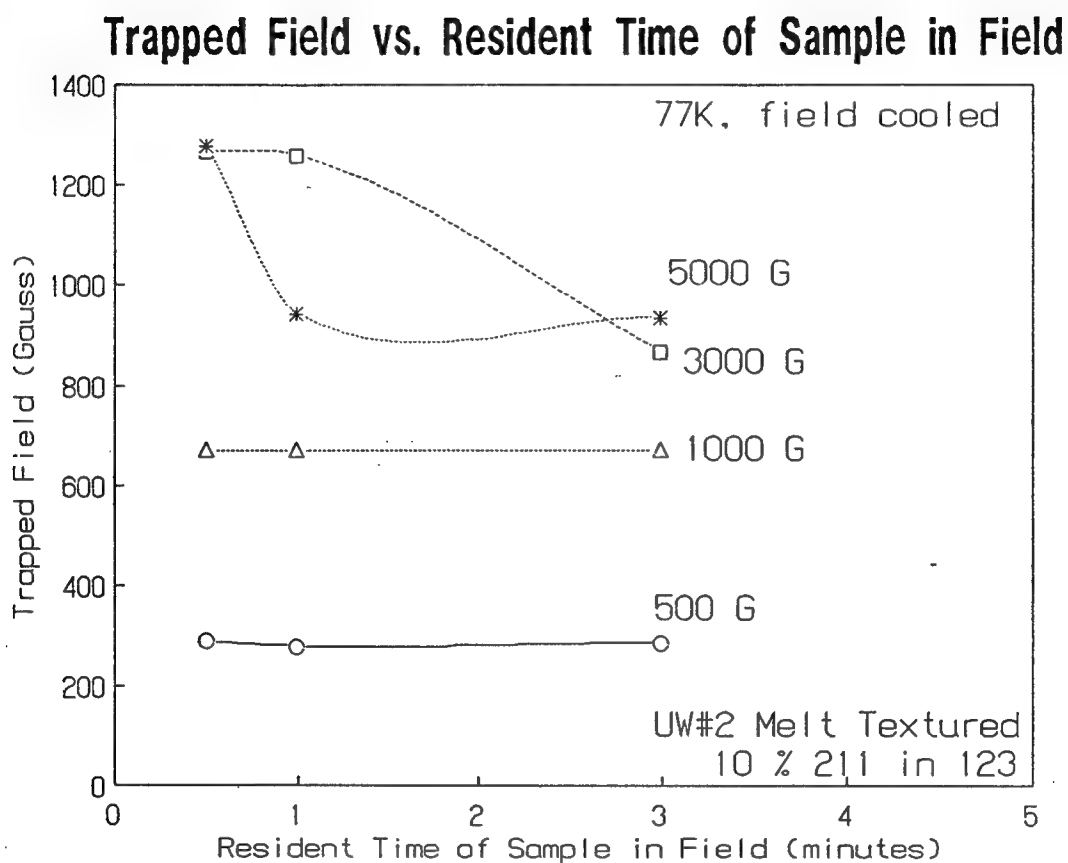


Figure 51. Trapped field vs. resident time of melt-textured 123 sample in a magnetic field during field cooling.

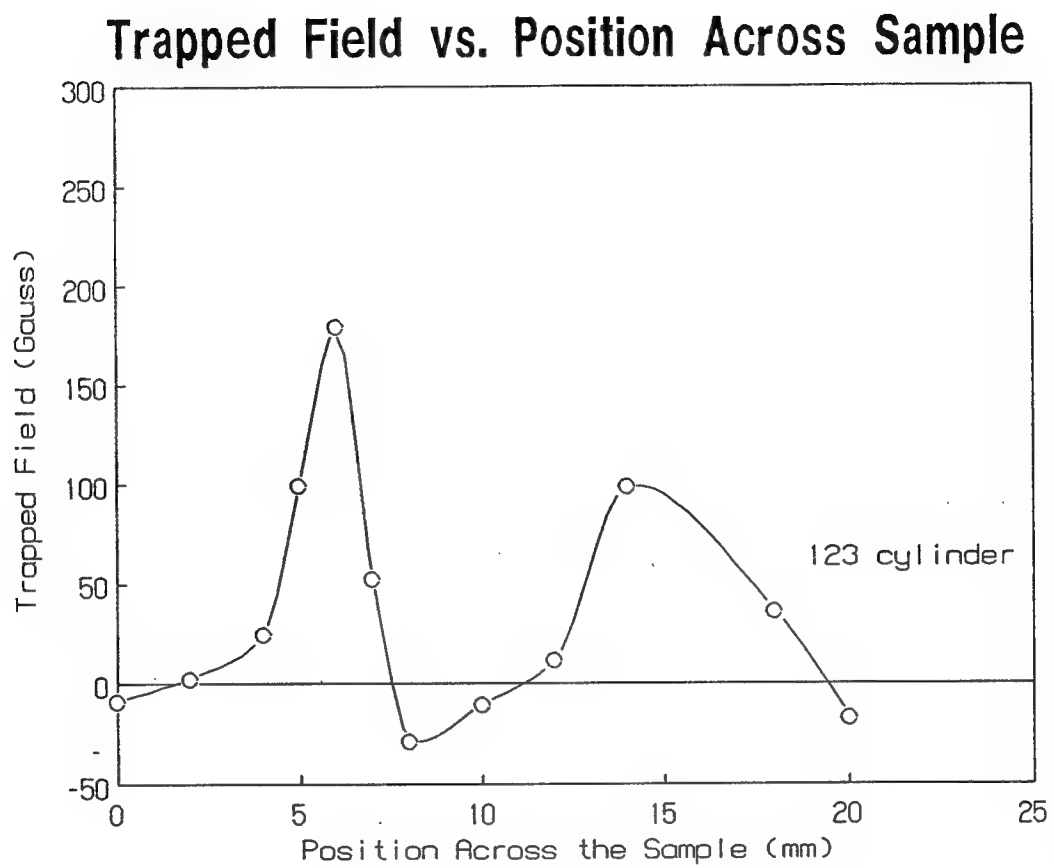


Figure 52. Trapped field vs. position across a cylindrical, melt-textured $\text{YBa}_2\text{Cu}_3\text{O}_{7-x}$ sample.

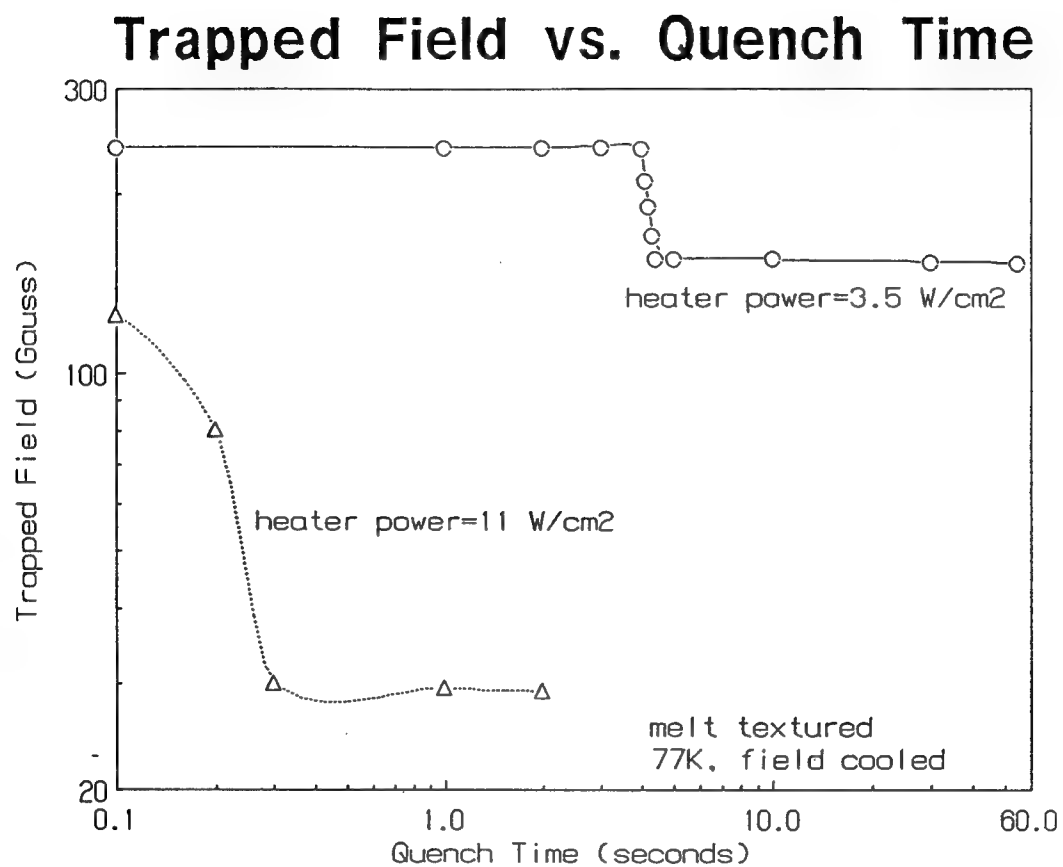


Figure 53. Trapped field vs. quench time for a melt-textured $\text{YBa}_2\text{Cu}_3\text{O}_{7-x}$ sample.

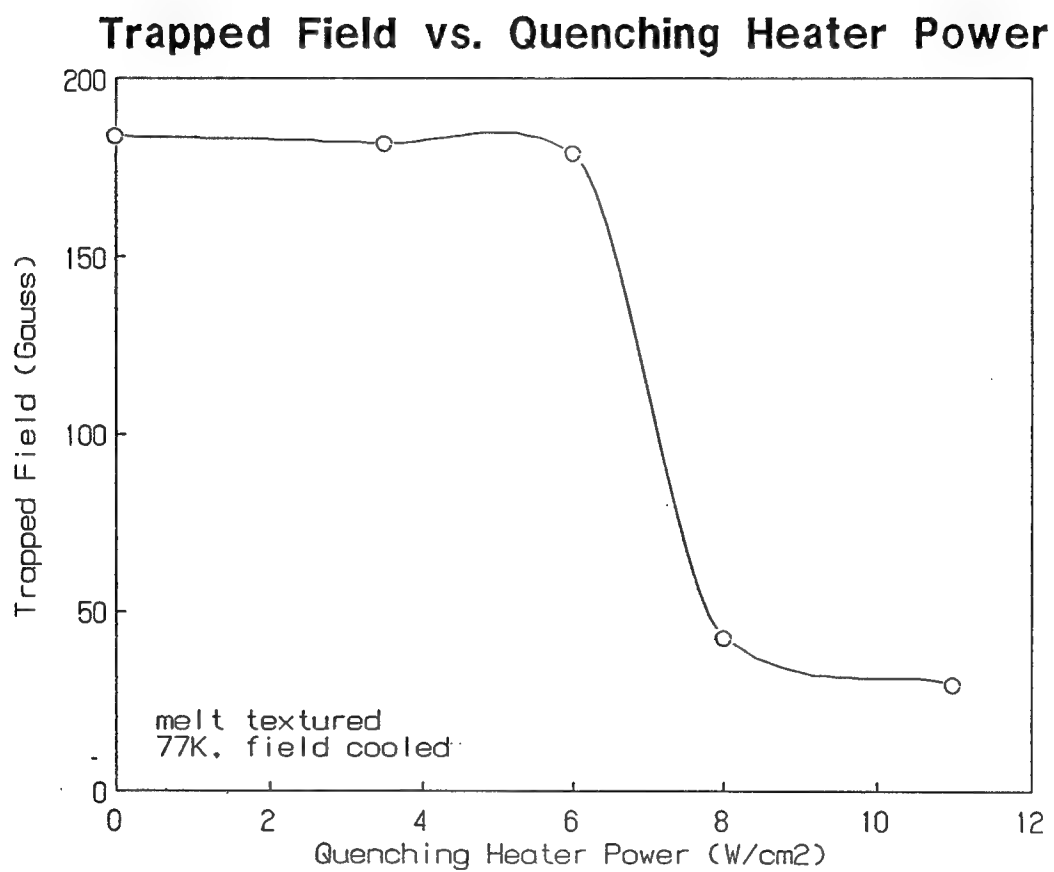


Figure 54. Trapped field vs. quenching heater input power for a melt-textured $\text{YBa}_2\text{Cu}_3\text{O}_{7-x}$ sample.

FLUX TRAPPING EXPERIMENTAL SETUP

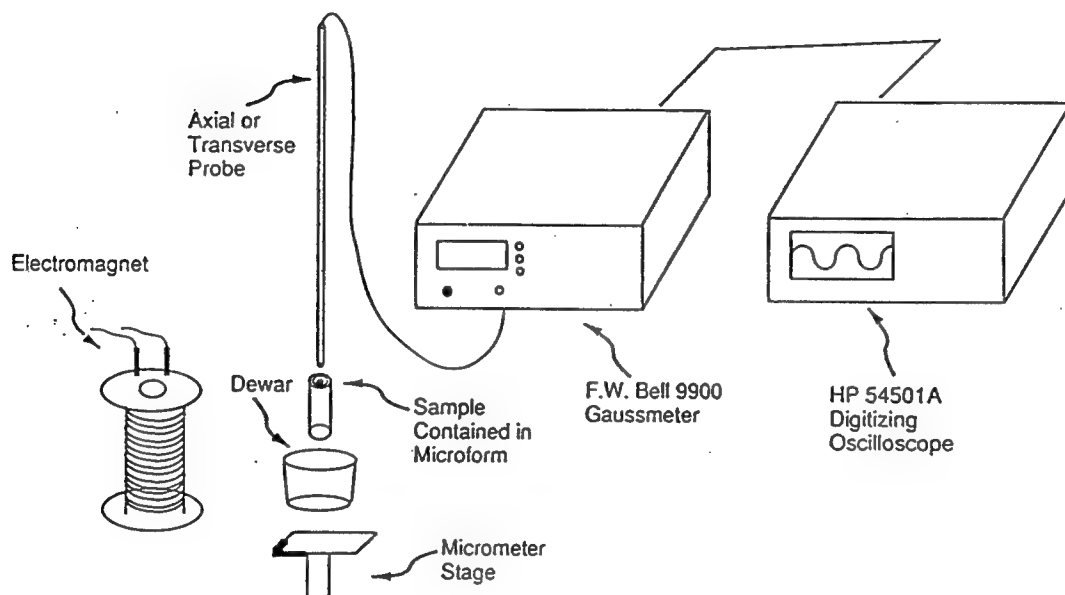


Figure 55. Experimental setup for flux-trapping experiments.

The superconducting properties related to the experimental design issues for Boeing's devices were evaluated by performing flux-trapping experiments. Flux-trapping measurements were carried out on the melt-textured samples as a function of applied field. Fields of up to 1800 Gauss (with applied field of 5000 Gauss) were trapped in the melt-textured samples (5 mm thick x 30 mm long x 8 mm wide) containing additional 211 phase (up to 20 at % 211, Figure 56). We investigated the effects of (a) initial powder state (quenched vs. non-quenched), (b) pure vs. 211 doped powder, and (c) oxygenation time, on the magnitude of trapped field.

(a) Effect of Initial Powder State (quenched vs. non-quenched)

Figure 57, shows the result of flux-trapping experiments for two samples. The higher flux-trapping capability was exhibited by the sample prepared using quenched powder. As mentioned earlier, we believe the quenching step leads to the formation of nanometer size particles in the 123 grains, which may serve as flux-pinning sites. This hypothesis is based on our TEM analysis.

(b) Effect of Excess 211

The main purpose for the addition of excess 211 was to enhance the flux-trapping values by altering the concentration of nano-size particles within the 123 grains. In Figure 58, we display the flux-trapping results for two samples. One of these samples was prepared using 123 quenched powder and the second sample was prepared using 123 + 20% 211 quenched powder. These results indicate that the presence of excess 211 nearly doubled the magnitude of trapped flux. We believe, that the presence of excess 211 provides two advantages; (i) increases the concentration of pinning centers (Figure 59) and (ii) enhances compositional uniformity across the sample, which in turn leads to the formation of samples with more uniform properties. In Figure 60, 3-D flux profiles are shown for pure and 211 doped 123 samples, demonstrating the increased homogeneity of trapped flux with increased 211 content. A systematic study is in progress to determine the effect of incorporation of various amounts of excess 211 on the superconducting properties.

(c) Effect of Oxygenation Time

Figure 61 shows the flux-trapping capabilities for a 20% 211 doped 123 sample oxygenated at low temperatures (400-600°C) for 3, 6, and 9 days, respectively. As evident from these results, the magnitude of trapped flux has increased with increased oxygenation time. This may be explained by very low diffusion rates in very dense melt-textured samples. The role of 211 in oxygen diffusion may be evident from Figure 62, where trapped field is shown as a function of annealing time in oxygen for pure 123 and 211 doped 123 samples. The flux-trapping capability for the pure 123 does not change with extended oxygenation time since the samples are not 100% dense,

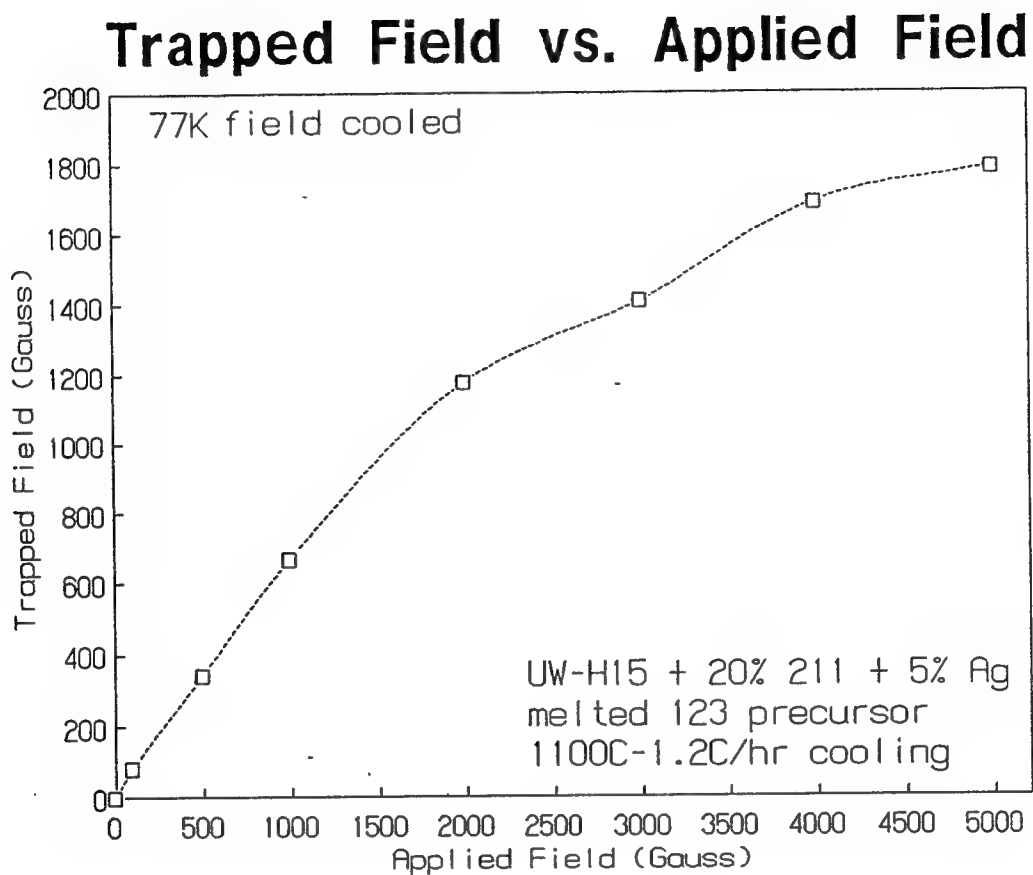


Figure 56. Trapped-flux vs. applied field for melt-textured $\text{YBa}_2\text{Cu}_3\text{O}_{7-x}$ with 20% 211 and 5% Ag.

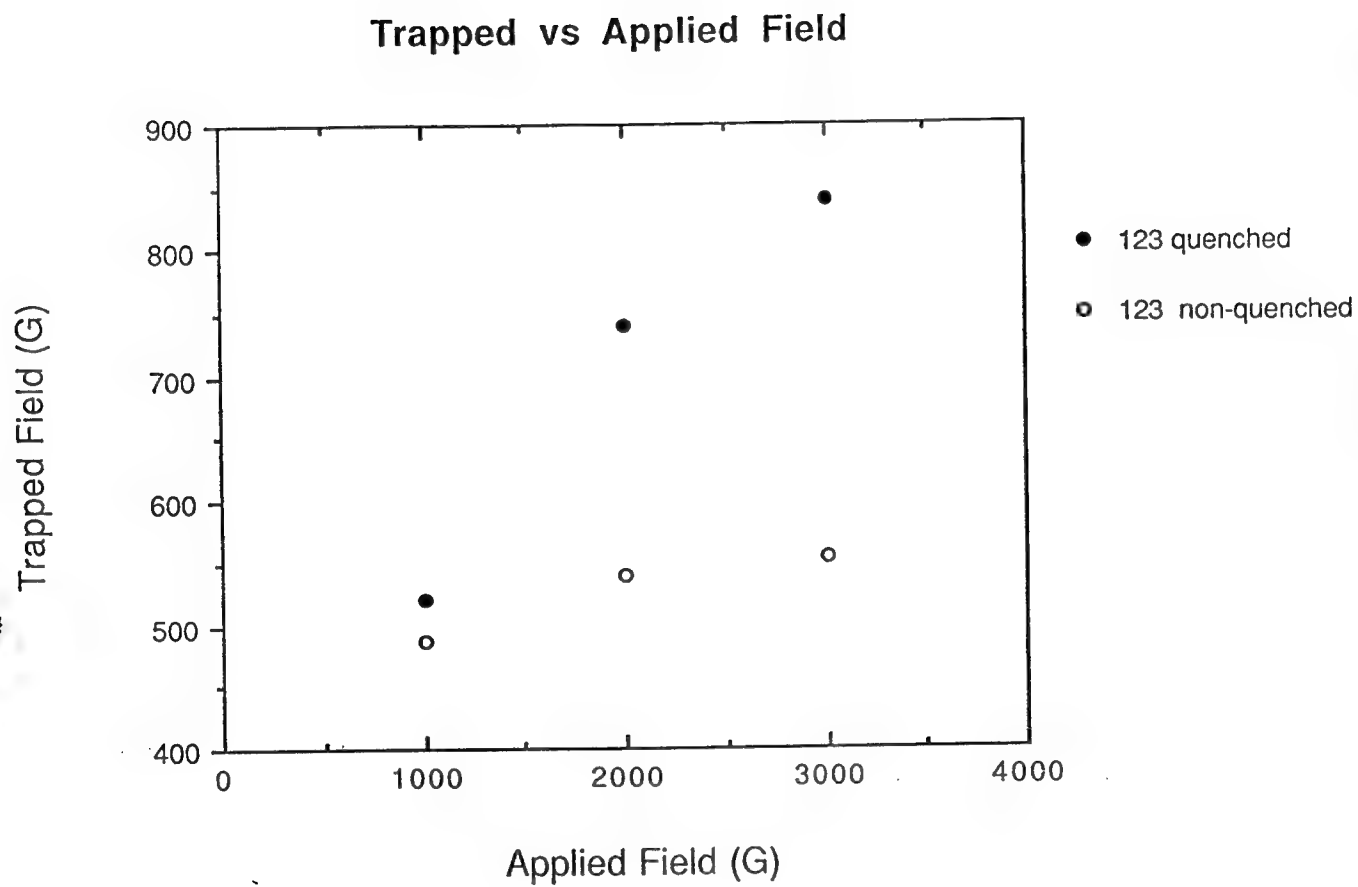


Figure 57. Comparison of flux-trapping data for samples prepared using quenched and non-quenched 123 powder.

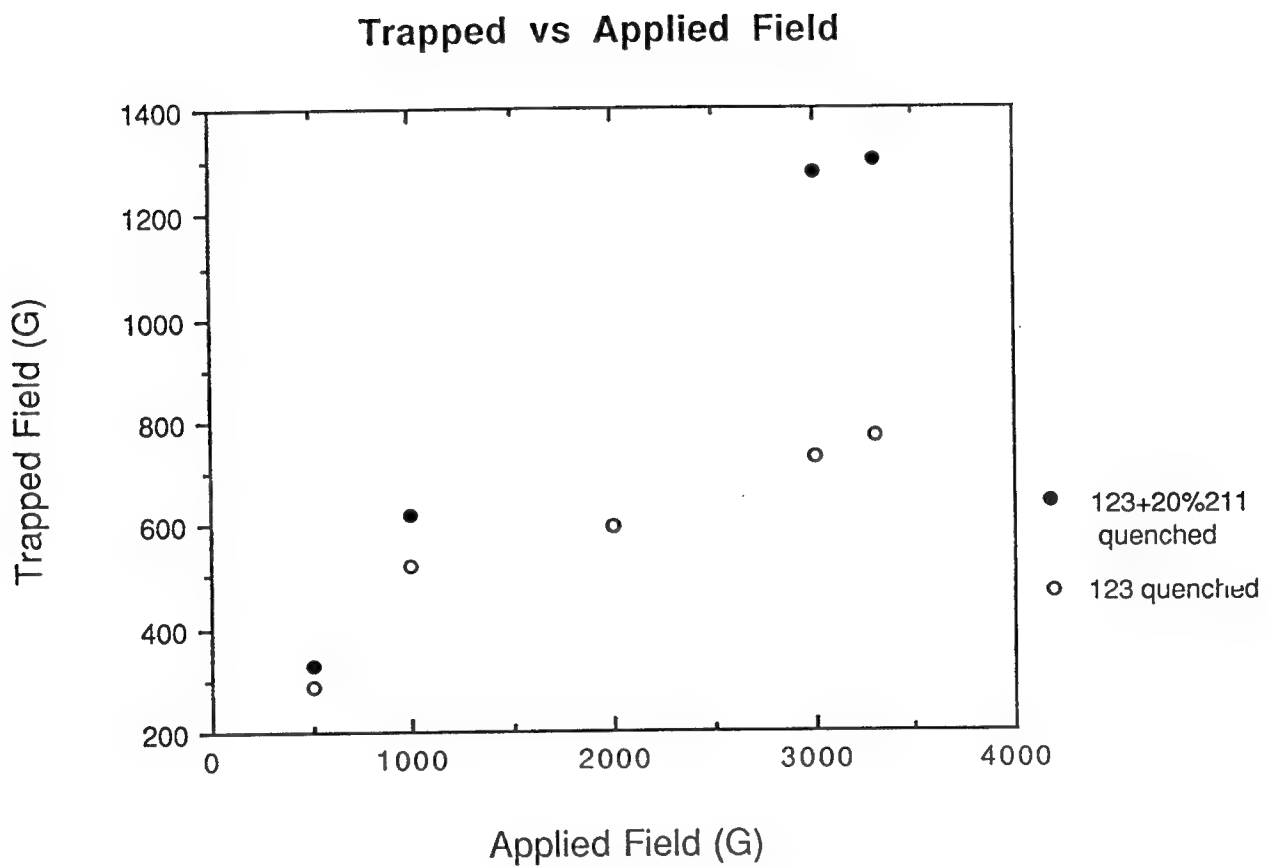


Figure 58. Comparison of flux-trapping data for samples prepared using quenched 123 and 123 + 20% 211 powder.

Trapped Field vs. Applied Field

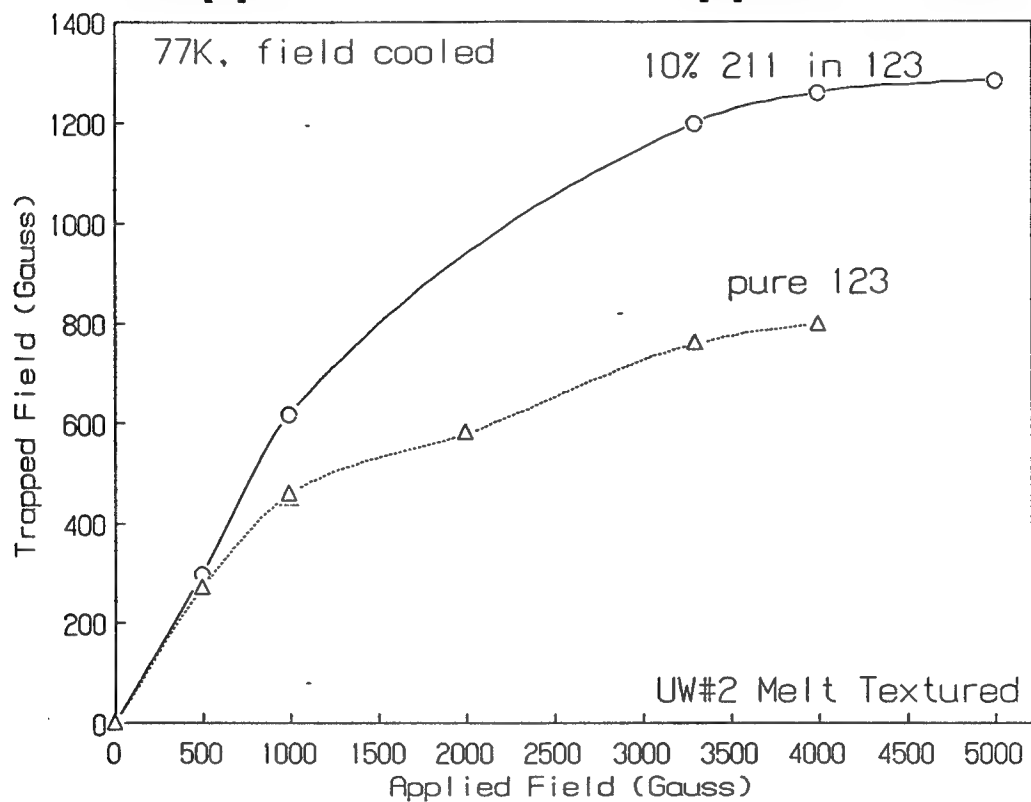
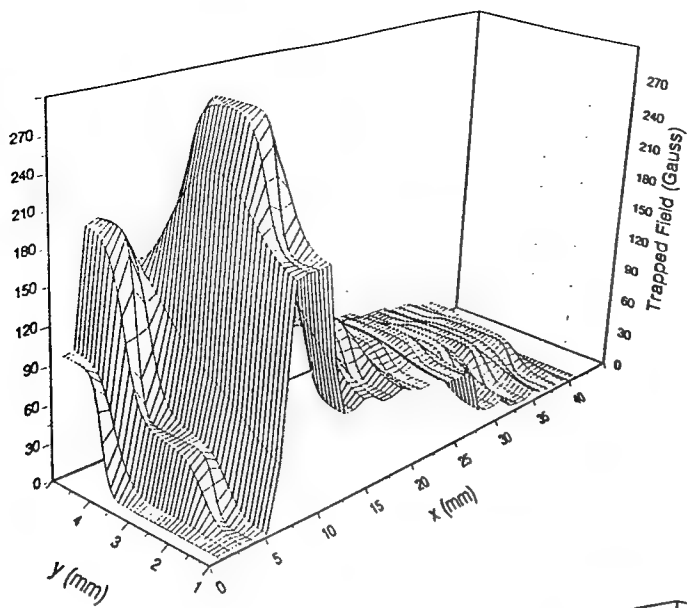


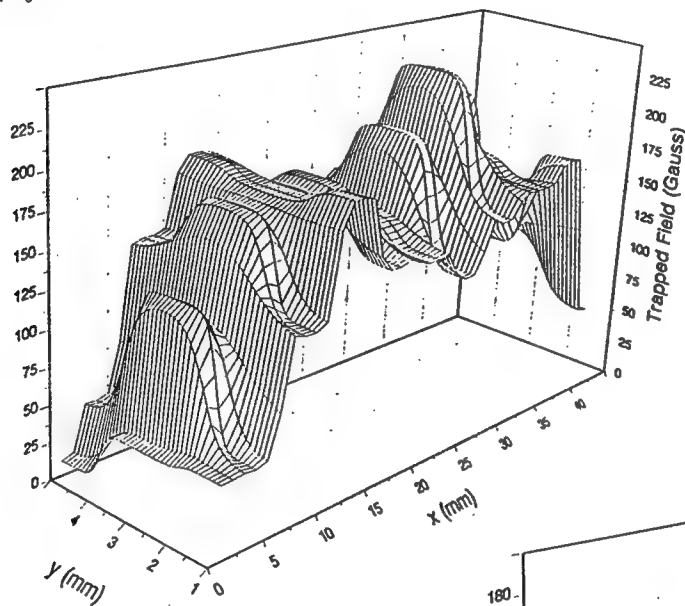
Figure 59. Trapped-flux vs. applied field for melt-textured $\text{YBa}_2\text{Cu}_3\text{O}_{7-x}$ and 123 + 10% 211.

Trapped Field (Gauss)



Melt Textured 123
950/12 air non-melted
1100C-1000C/100C/hr air
1000C-900C/1C/hr air
Applied Field = 1000 Gauss
77K, field cooled

Trapped Field (Gauss)



Melt Textured 123 + 50% 211
950/12 air, non-melted
1100C-1000C/100C/hr air
1000C-900C/1C/hr air
Applied Field = 1000 Gauss
77K, field cooled

Trapped Field (Gauss)

Melt Textured 123 + 10% 211
950/12 air, non-melted
1100C-1000C/100C/hr air
1000C-900C/1C/hr air
Applied Field = 1000 Gauss
77K, field cooled

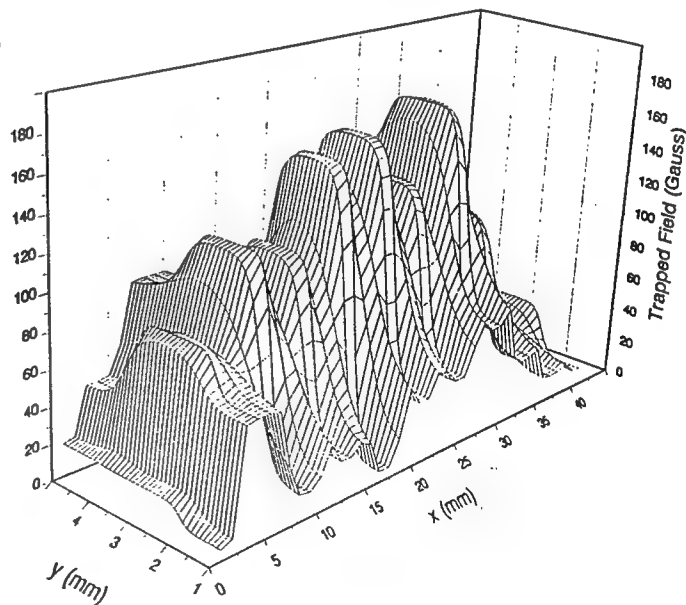


Figure 60. Flux profile maps of melt-textured $\text{YBa}_2\text{Cu}_3\text{O}_{7-x}$ with 10 and 50% 211 phase.

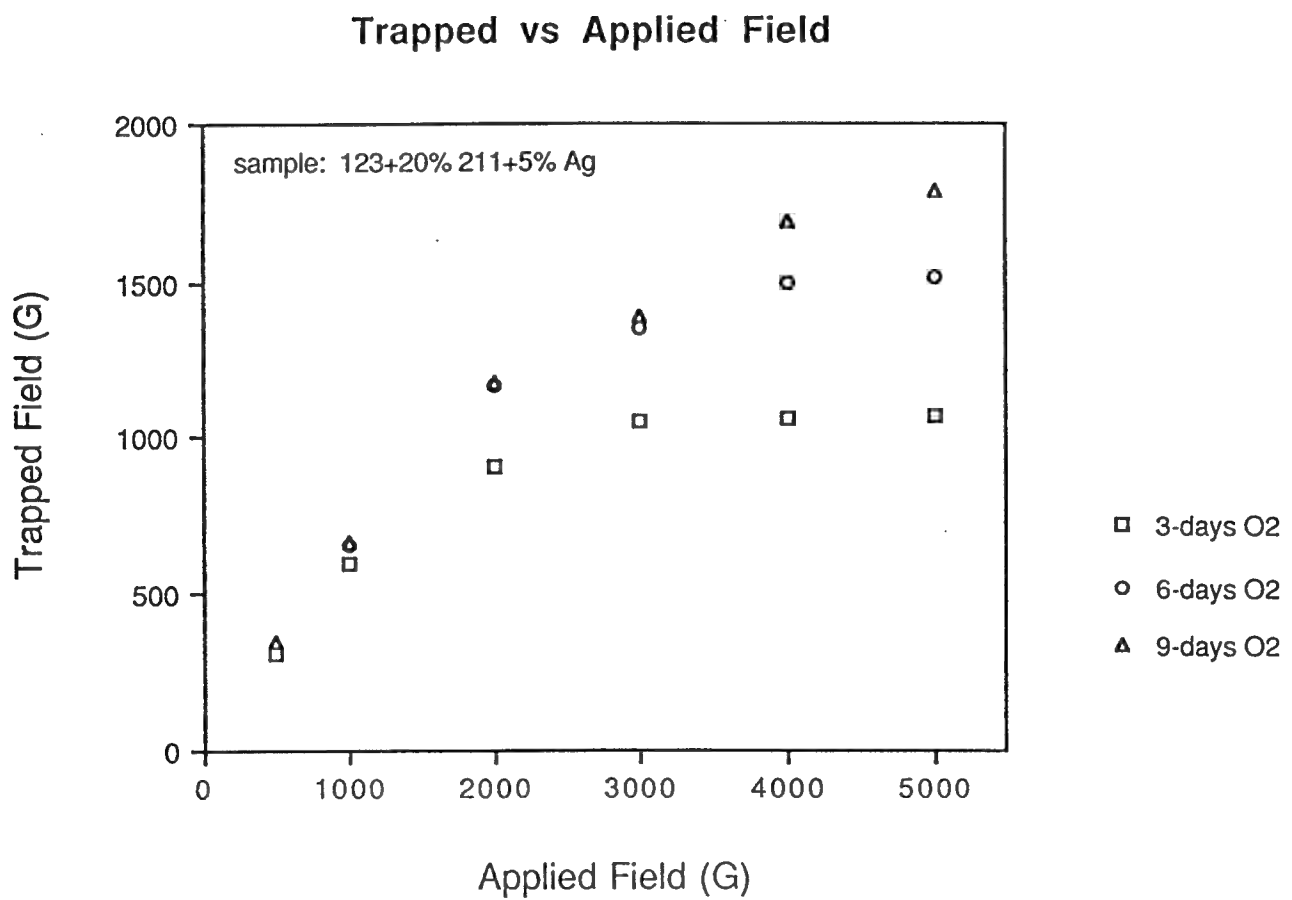


Figure 61. Flux-trapping data as a function of oxygenation time.

Trapped Field vs. Annealing Time

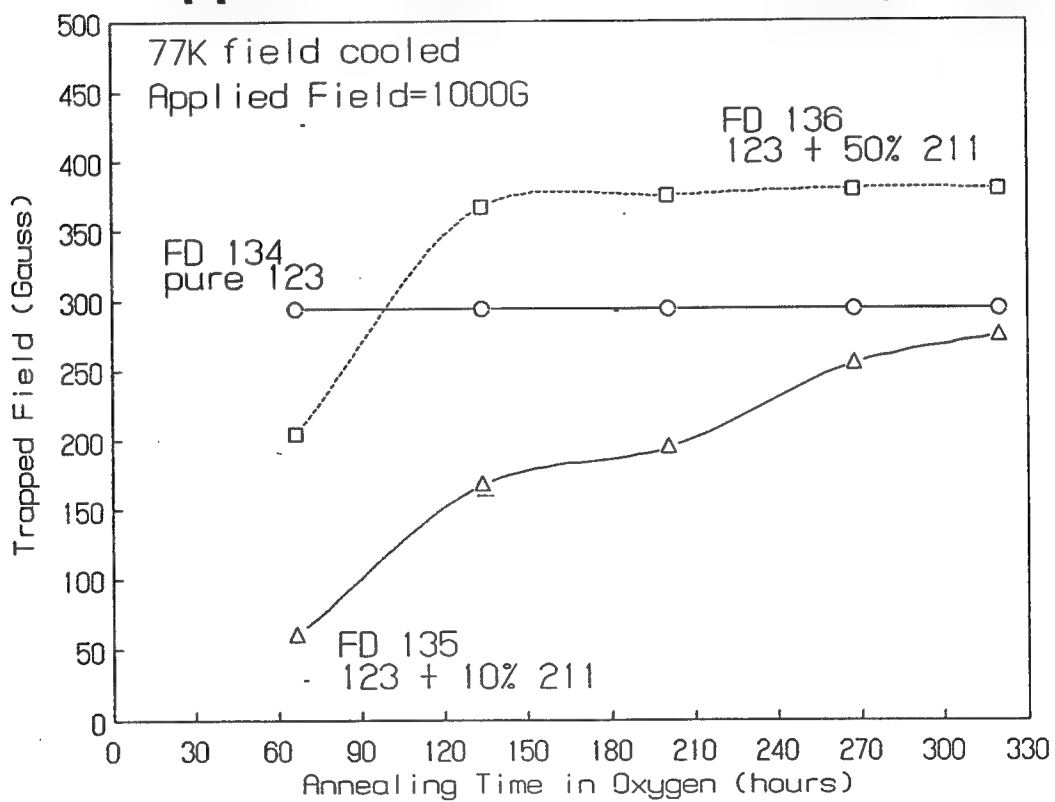


Figure 62. Trapped field vs. annealing time of pure melt-textured $\text{YBa}_2\text{Cu}_3\text{O}_{7-x}$ with 10% and 50% 211 additions.

hence oxygen diffusion is not the limiting factor during oxygenation. In the case of 10% 211 doped 123, we can see from Figure 62, that the flux-trapping properties are improving with prolonged oxygen annealing. The 50% 211 doped 123 sample saturates with oxygen at much shorter annealing time, possibly due to enhanced diffusion rates facilitated by microscopically dispersed 211 phase.

Several geometrical (thickness, grain orientation, grain size, trapped field as a function of distance from the sample surface) factors affecting the flux trapping abilities of the melt-textured samples were also investigated.

B. Quenching Experiments

Quenching experiments of trapped flux were designed with respect to a superconducting dent puller and a rivet gun device. Initial quenching experiments were performed on a rectangular 123 sample, with 2 holes drilled in the sample, to determine the presence of macroscopic circulating currents flowing in a cylinder. The quenching experiments were conducted in the 123 sample with a Ni-Cr heater coil embedded in the superconductor (Figure 63). The DC heater power density was 200 W/cm^2 per heater. A trapped field of 600 Gauss, was quenched thermally (Figure 64) in about 0.5 second. Thermodynamic calculations, described in the next section, suggest, that the high heat capacity and low thermal conductivity of the 123 might be the limiting factors in DC thermal quenching. AC and rf methods are presently being investigated as alternative heating/quenching methods.

The electromagnetic devices require quenching times on the order of milliseconds. This can be achieved in a superconductor by inducing a flux-jump. From the calculations described in the next section, it is evident that the easiest way to produce a flux-jump is by lowering the heat capacity of the 123 sample. This may be achieved by introducing voids throughout the 123 sample (air has very low heat capacity), thus effectively lowering the heat capacity of 123 and making it more susceptible to flux-jumps with smaller temperature perturbations.

New operational design of the dent puller and proof tester was developed. The alternative design employs a very fast shutter to block the magnetic field from a superconducting magnet, thereby the magnetic energy derived from a collapsing magnetic field is obtained. This design obviates the need for "quenching" the superconducting magnet altogether.

It utilizes a very high permeability ($M\mu$ metal or supermalloy) and very high saturation limit so as to block the major portion of the enclosed magnetic field when the shutter is in the closed position. The shutter permits rapid collapse of a magnetic field through a conductor. The energy released from a collapsing field ($E = B^2/2\mu$)

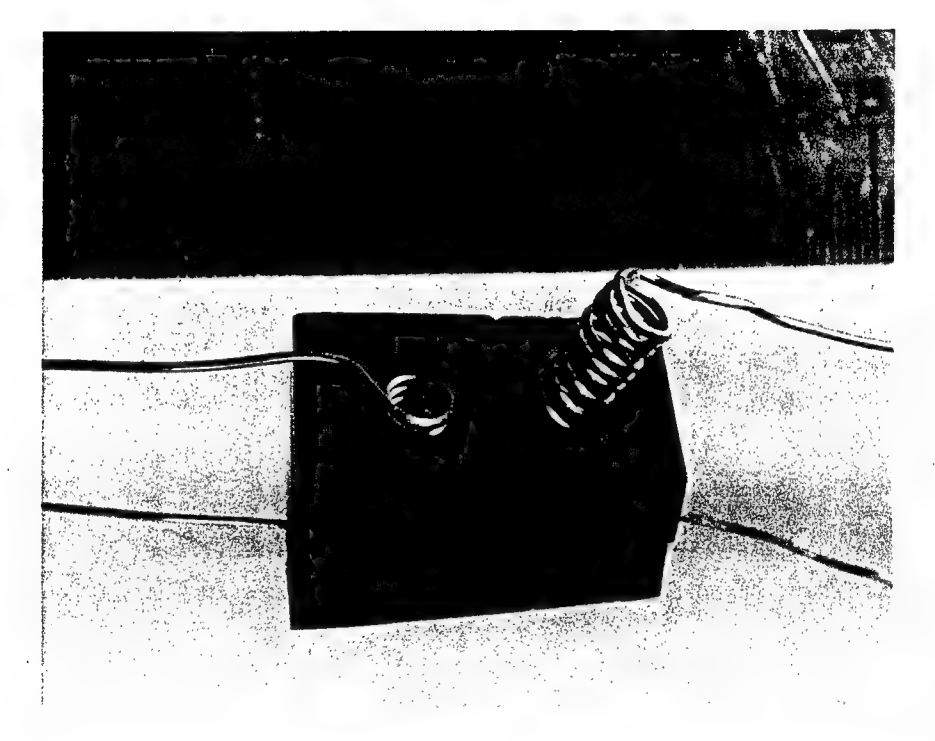


Figure 63. 123 sample configuration for magnetic field quenching experiments.

hp stopped

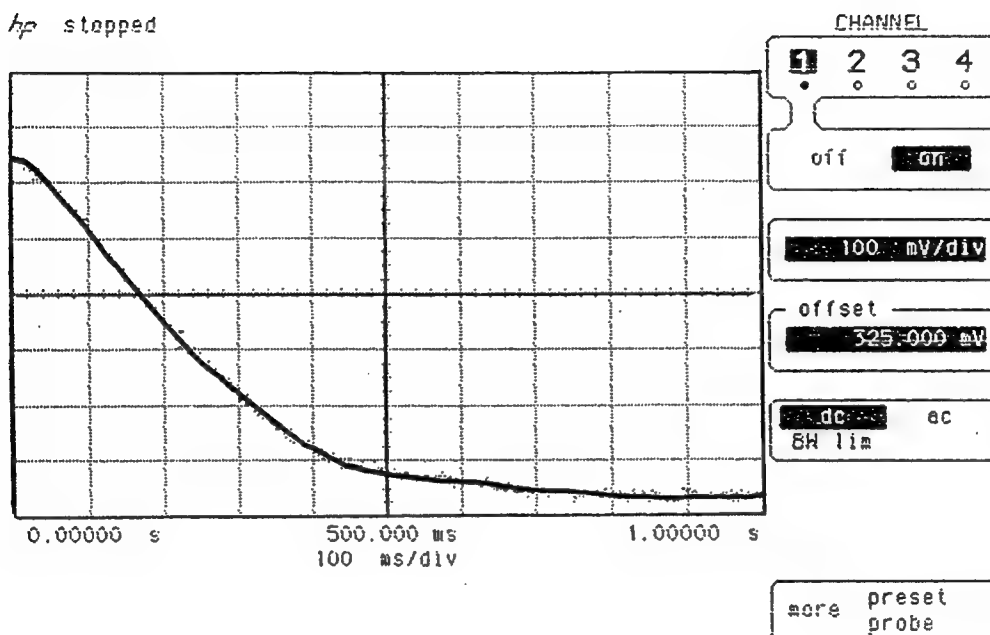


Figure 64. Oscilloscope output of trapped field vs. quenching time for the sample shown in Figure 63.

is translated into mechanical work, used in such devices as the electromagnetic dent puller, the electromagnetic proof tester (for metal/composite bond strength measurements) or other electromagnetic devices (Invention Disclosure Filed).

The basic operation depends on a shutter (or shield) of an appropriate thickness and appropriate alloy composition (depending on the magnetic field to be shielded).

A number of configurations (Figures 65-68) of the magnetic shutter are possible.

The preliminary experiments employing different configurations of the magnetic shutter show so far the fastest collapse of the magnetic field on the order of 1-5 milliseconds. This was achieved with a high permeability metal shutter attached to a metal spring actuator (Figure 69).

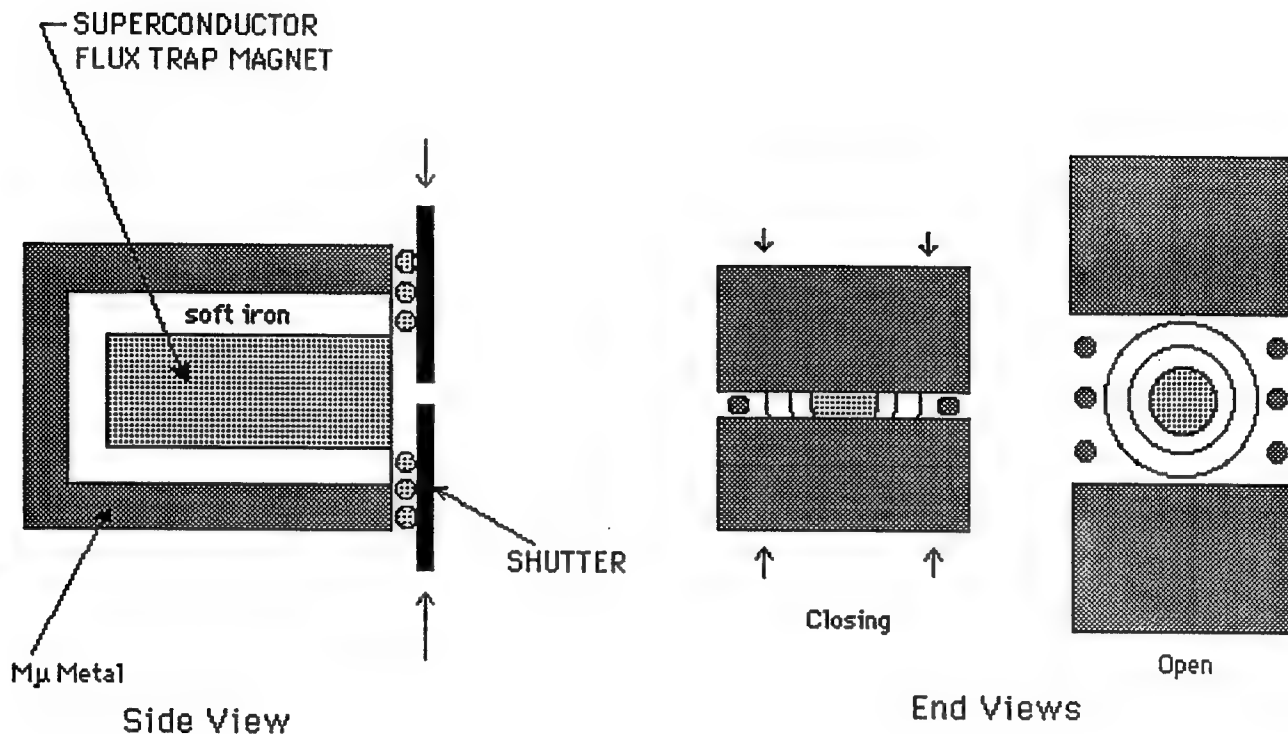
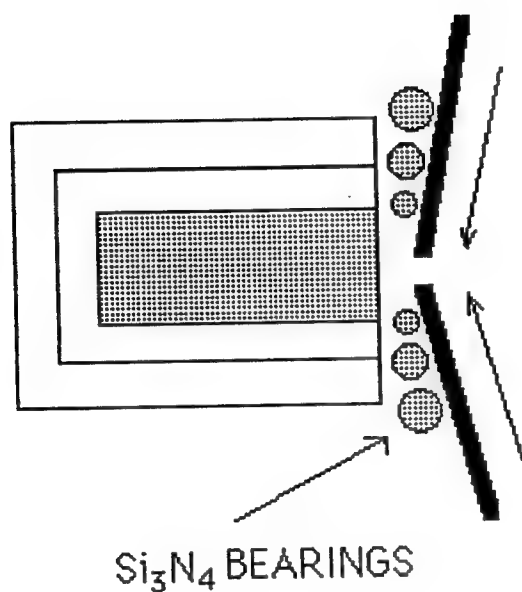


Figure 65. The basic configuration of the shutter. It depicts a superconducting flux-trap magnet surrounded by a soft iron for a magnetic flux return pathway. The $M\mu$ metal on outside is used for external shielding of the magnetic field. The closing shutter permits rapid collapse of a magnetic field through a conductor. The energy released from a collapsing field ($E = B^2/2\mu$) is translated into mechanical work, used in such devices as the electromagnetic dent puller.



note: Roller bearings of
silicon nitride so as to be
unaffected by magnetic
field.

Figure 66. Magnetic shield for the shutter itself can ride on roller bearings on a slight slope so as to use the energy of the magnetic field to assist in the closure of the shutter.

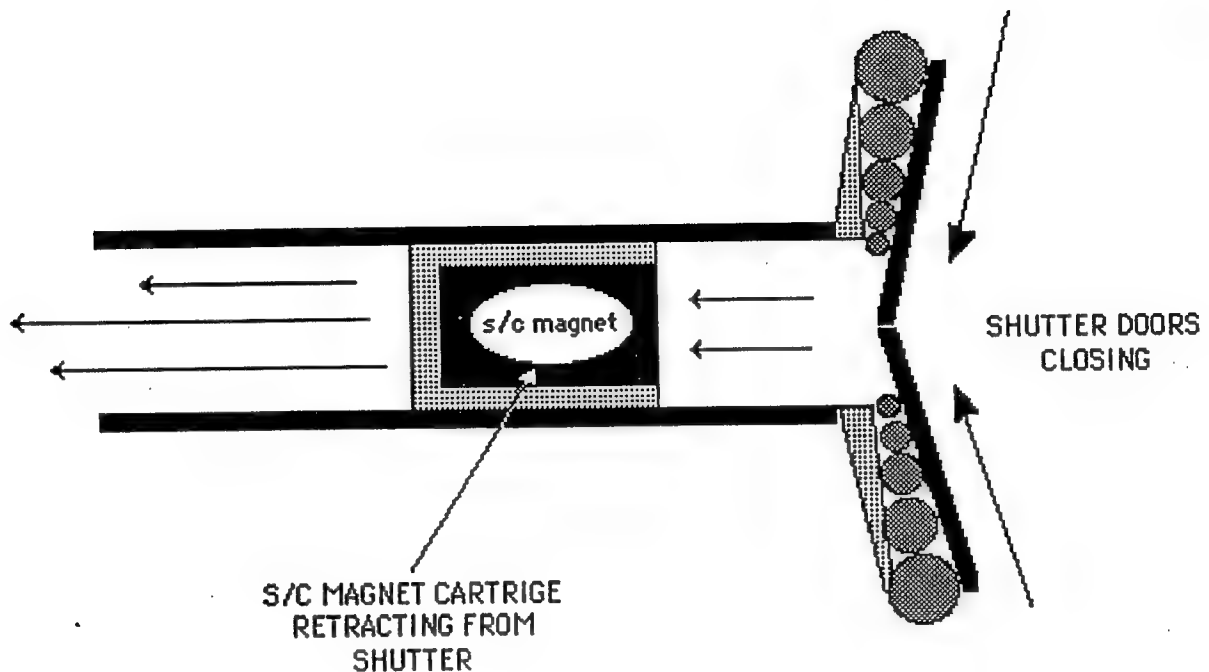


Figure 67. This shows a possible shutter lamination configuration to achieve best shielding and closure characteristics. The shutter can be (1) hydraulically closed, (2) pneumatically closed, (3) spring closed (as in a crossbow), or (4) even explosively closed.

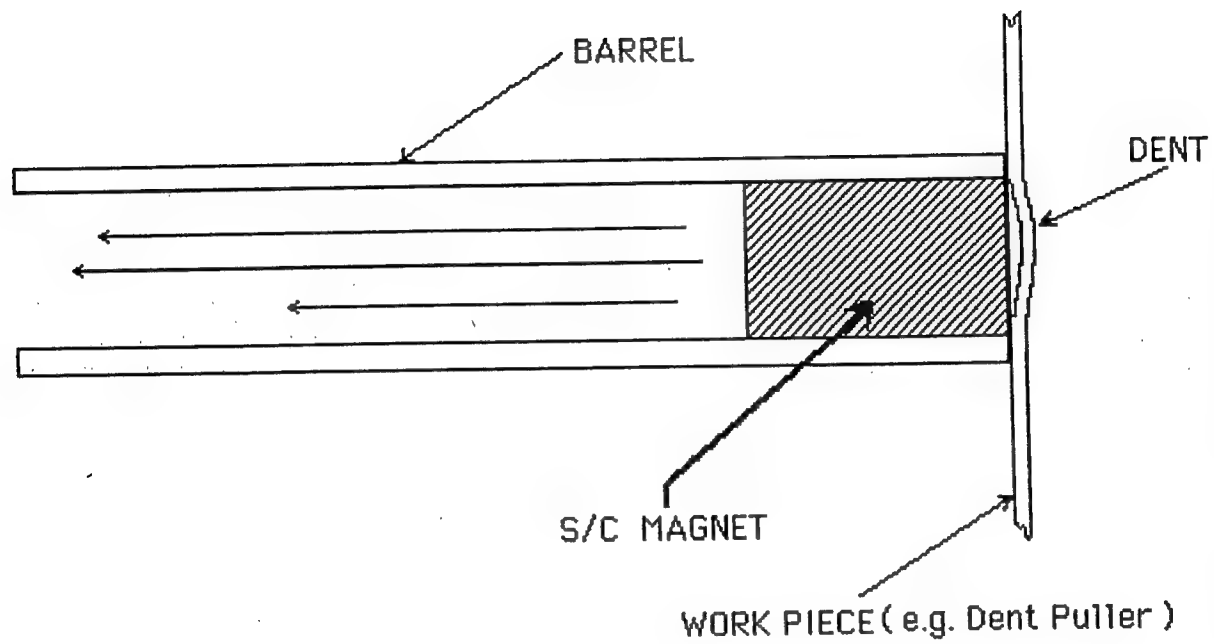


Figure 68. This illustrates another embodiment of the design which obviates the need of the shutter altogether. It totally relies on the rapid retraction of the superconducting magnet assembly from the work surface.

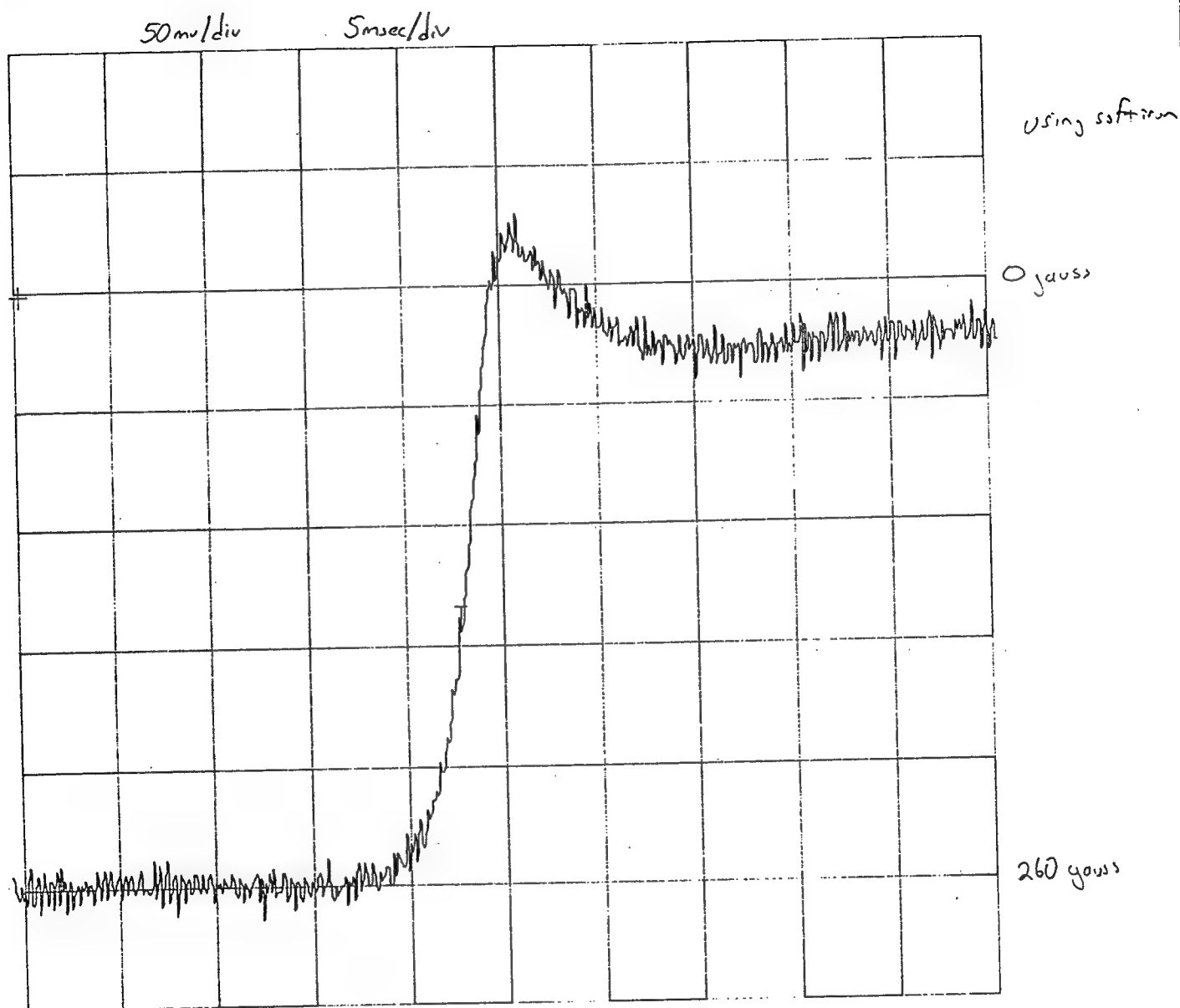


Figure 69. Collapse of a magnetic field from a closed magnetic shutter operated by a spring actuator.

DEVICE REQUIREMENTS AND DESIGNS

A. Operational Principles and Designs

The concept of obtaining mechanical work from the collapsing field in a high temperature superconducting "permanent" magnet is being evaluated. A light, compact, low voltage, electromechanical rivet gun would be of considerable interest to the aerospace industry. Such a device should be able to deliver a peak force of about 90 kNt (20,000 lb) in 1 msec (Figure 70).

We examined various schemes to repetitively flux pump, i.e. magnetically charge, hollow cylindrical shapes and then discharge them in the required time frame. We also considered the possibility of combining the charge and discharge methods and what engineering data will have to be collected and what materials properties will have to be attained, in order to build such a device.

Design Concepts for a Superconducting Rivet Gun

We first discuss various concepts of utilizing the unique properties of high temperature superconductors and their ability to be switched from the superconducting to the normal state to perform mechanical work. We then apply these ideas to the conceptual designs of an electromechanical rivet gun and a dent puller to be used in the aerospace industry.

A. Background Information

1. Superconductivity - Relevant Parameters

Before attempting to apply superconductors in any device, it may be worthwhile to review some of the properties that control their unique behavior. This brief survey covers both classical Type II superconductors, in general, and the high temperature superconductors (HTS) in particular.

Flux Penetration

From the fact that the resistivity, ρ , is zero in a superconductor, it follows that any change in magnetic field, B , must also be zero. Conversely, when the field changes in a bulk superconductor, its resistivity cannot be rigorously zero, and there will be some energy dissipation. When the field is increased on a superconducting specimen that has first been cooled in zero field (ZFC), we will usually see some flux exclusion, up to the limits of superconductivity, as defined by the temperature dependent upper critical field, H_{c2} .

SUPERCONDUCTING RIVET GUN

PROPERTY	DESIGN CRITERIA	DESIGN REQUIREMENT
Energy of Deformation Required	Force/displacement for 5/16" diameter 7050 rivet	120 Joules
Energy Density in 3 Tesla Field	$\frac{B_T^2}{4\mu_0} \left(\frac{\text{Joules}}{\text{m}^3} \right)$	1.8 (MJ/m ³)
Superconductor Size	Disk 10 cm diameter x 2 cm thick $B_r = 1/2 B_T$	85 % efficiency
Critical Current Density at 3 Tesla	$J_c = \frac{B_{Tc}}{\mu_0 r} \left(\frac{\text{A}}{\text{m}^2} \right)$	$4.8 \times 10^3 \text{ (A/cm}^2\text{)}$
Strength of Material	Hoop stress, solid disk $B_M = 4B_T; \frac{B^2}{2\mu_0} \left(\frac{\text{N}}{\text{m}^2} \right)$	832 psi tension
Temperature Rise/Quench	$\Delta T = \frac{\Delta Q(\text{J})}{C \text{ (J/kgK)} m \text{ (kg)}}$	1.8 K

Figure 70. Design requirements for a superconducting rivet gun.

By contrast, the theoretically important flux expulsion, $B=0$, or Meissner property only operates to the very low limits designated as the lower critical field, H_{c1} . The relative amount of flux expulsion observed in a field or Meissner property only operates to the very low limits designated as the lower critical field, H_{c1} . The relative amount of flux expulsion observed in a field-cooled (FC) sample is sometimes used to estimate the amount of superconductor present, but this can give very misleading results. As long as we stay below H_{c1} , flux penetration is limited to the London penetration depth (λ), and the process is reversible and loss-free. However, except for gyroscopes and rf cavities, few bulk superconducting devices operate below H_{c1} .

Limits and Flux Pinning

Every superconducting material has its related temperature and field limits, designated as T_c and H_{c2} . These are intrinsic or thermodynamic limits (except that their composition-dependent variability in HTS materials raises still unanswered questions). On the other hand, the magnitude of the critical current density is not an intrinsic property, in spite of the fact that the critical properties are often displayed in a 3-dimensional "phase-diagram", Figure 71.

Critical currents in Type II materials are pictured as being controlled by flux pinning sites, such as dislocations and other imperfections. These sites resist flux motion in the presence of the $\mathbf{J} \times \mathbf{B}$ Lorentz force. When motion occurs, it is thermally activated, hence the temperature variation in J_c . The concentration and distribution of pinning sites can be varied over wide ranges, so as to vary current densities. For HTS, oxygen deficiencies may also act as pinning sites.

Steepness and Width of Transition

The transition from the superconducting to the normal state as a function of current (or current density) is never a step function, but rather has a finite width, which, among other factors, depends on the uniformity of the material. The development of the fully normal resistivity, P_n , in this flux-flow region may cover a current range of 1 to 10%, Figure 72. The onset region is often described by a single-exponent power law fit, which is then useful as a measure of the uniformity and quality of the conductor. Experimental limitations on measuring small onset voltages contribute to the uncertainty in accurately locating the surface of the "cage" in Figure 72.

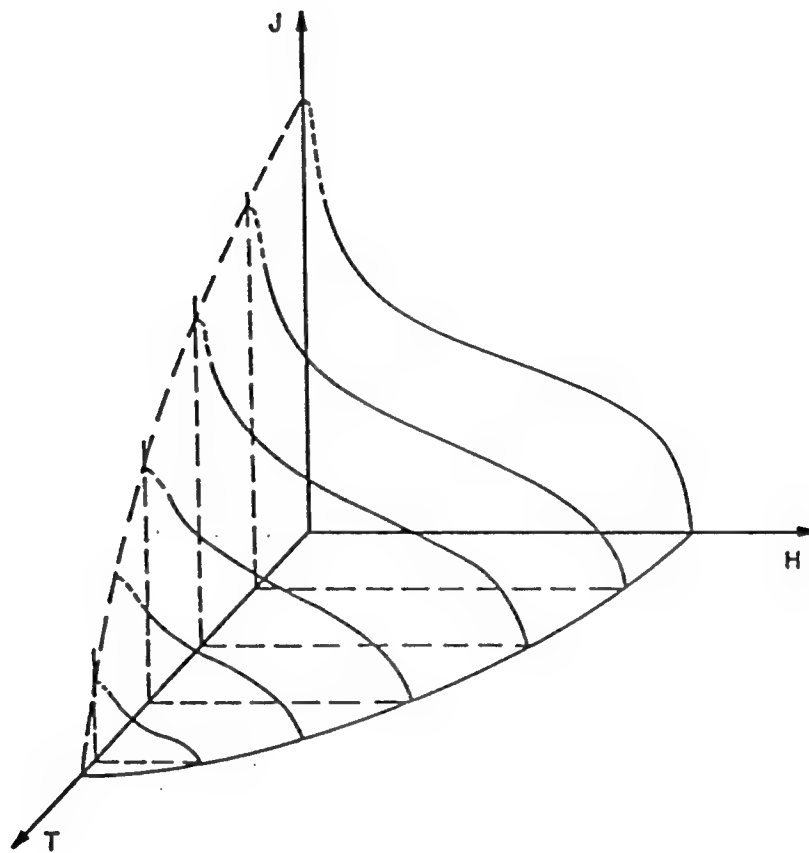


Figure 71. Phase Diagram for Type II Superconductors.

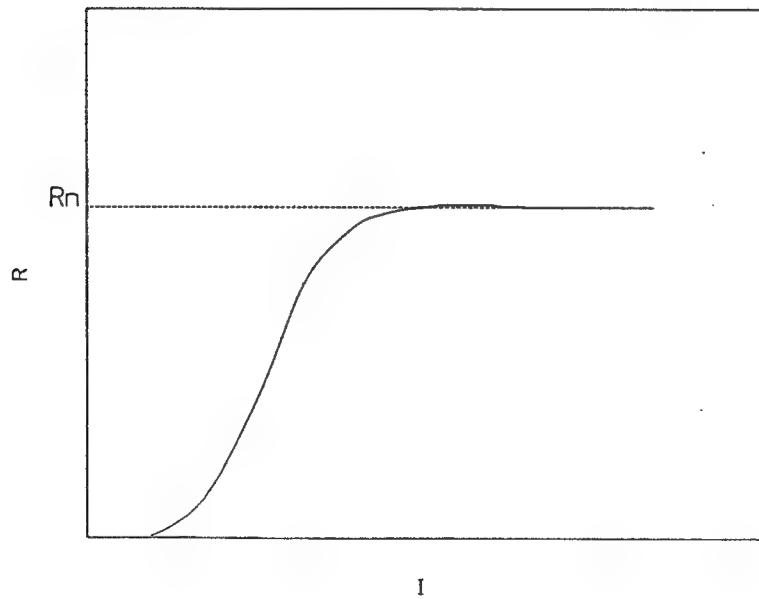
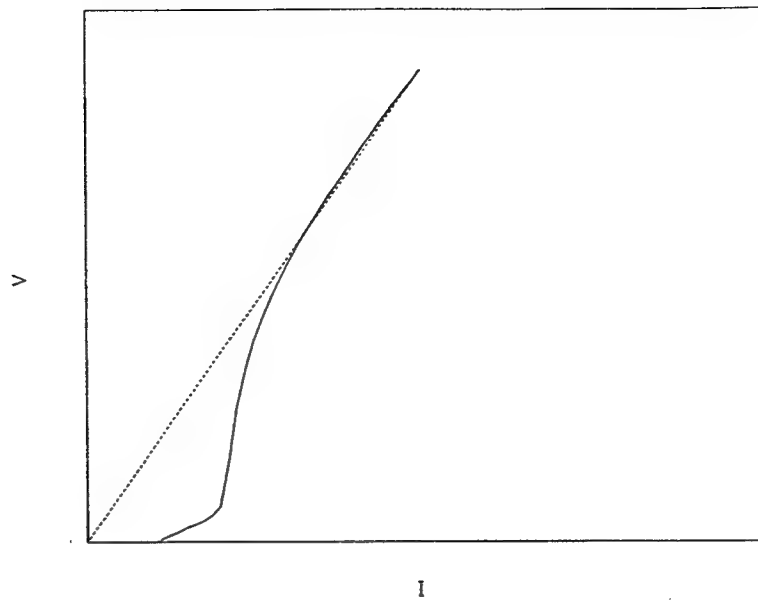


Figure 72. Voltage and Resistance Transitions.

Induction Processes at DC

In all electrical conductors, field transients induce what are usually called eddy currents, except that with zero resistivity they will persist indefinitely. In other words, in superconductors AC induction processes will persist down to DC. The magnetic energy density associated with induced persistent currents becomes an important consideration in properly utilizing high-field superconductors.

2. Flux Shielding and Trapping

Hollow bulk shapes with, preferably, cylindrical symmetry can be used to either shield or trap magnetic fields. The interpretation of such trapping experiments, Figure 73, led to the Kim-Anderson flux creep model, which predicts a field decay that is logarithmic, rather than exponential in time. This adds additional vagueness to the location and reality of the cage in Figure 71.

Bean - London Critical State Model

The details of the isothermal flux penetration into superconductors beyond the Meissner region, i.e. above H_{c1} , are described by the Bean-London critical state model, which postulates that whenever flux moves in and out of a bulk superconductor, the induced currents are at their critical value. The currents are zero in regions where no flux has penetrated, and their direction reverses when the applied field is made to decrease. This flux motion is hysteretic and B loss-free, so that thermal (heating) effects can arise. It is also important to remember the limitations of the model, in light of the previously mentioned vagueness and time dependence associated with the measurement of critical currents. Nor does the model easily describe field-cooled trapping processes, where frozen-in current densities can become less than critical by simply lowering the temperature.

HTS Advantages - Enhanced Stability

There are at least two advantages in using high temperature superconductors for various applications. The first is the potential of cheaper and simpler cryogenic operations, such as using a polystyrene foam cup to hold liquid nitrogen, while placing a permanent magnet at ambient temperature in close proximity below it. The second advantage lies in the tremendously enhanced thermal stability inherent in using superconductors at temperatures such as 77 K, where specific heats are so much larger than they are at 4 K. For our purposes, this changing stability is best expressed by the magnitude of the field difference (across a semi-infinite slab) that can just produce a flux jump, as calculated from the adiabatic stability theory, Figure 74. It remains to be shown whether the descending right-hand portion of Figure 74 can be verified experimentally in HTS.

Flux Trapping (with Flux Jumps)

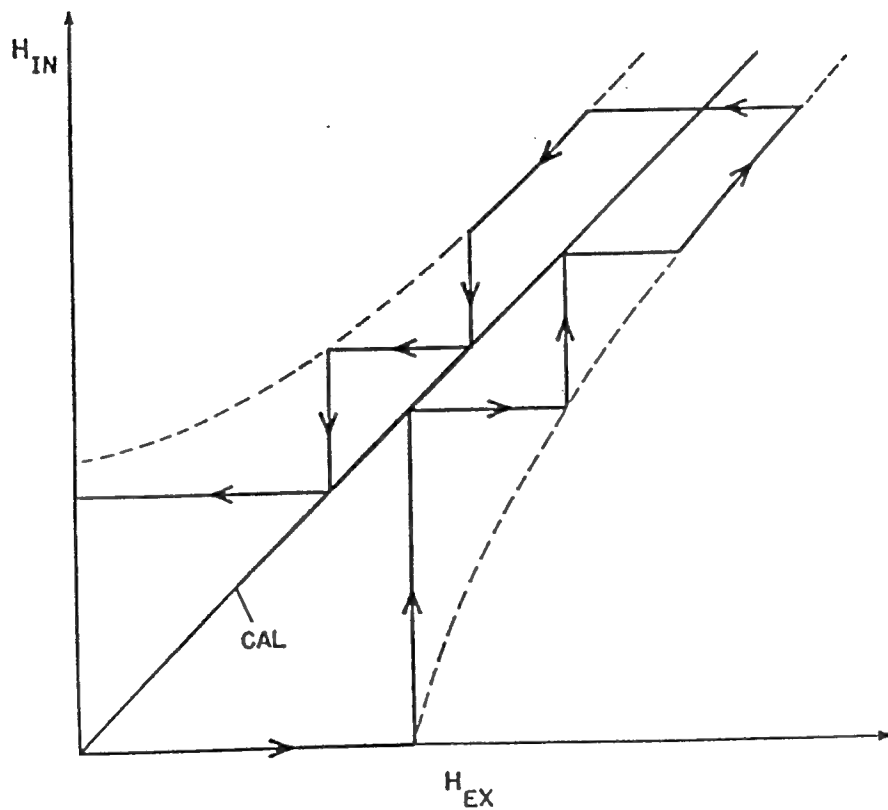


Figure 73. Flux Trapping Observations with Flux Jump and Flux Creep Regions.

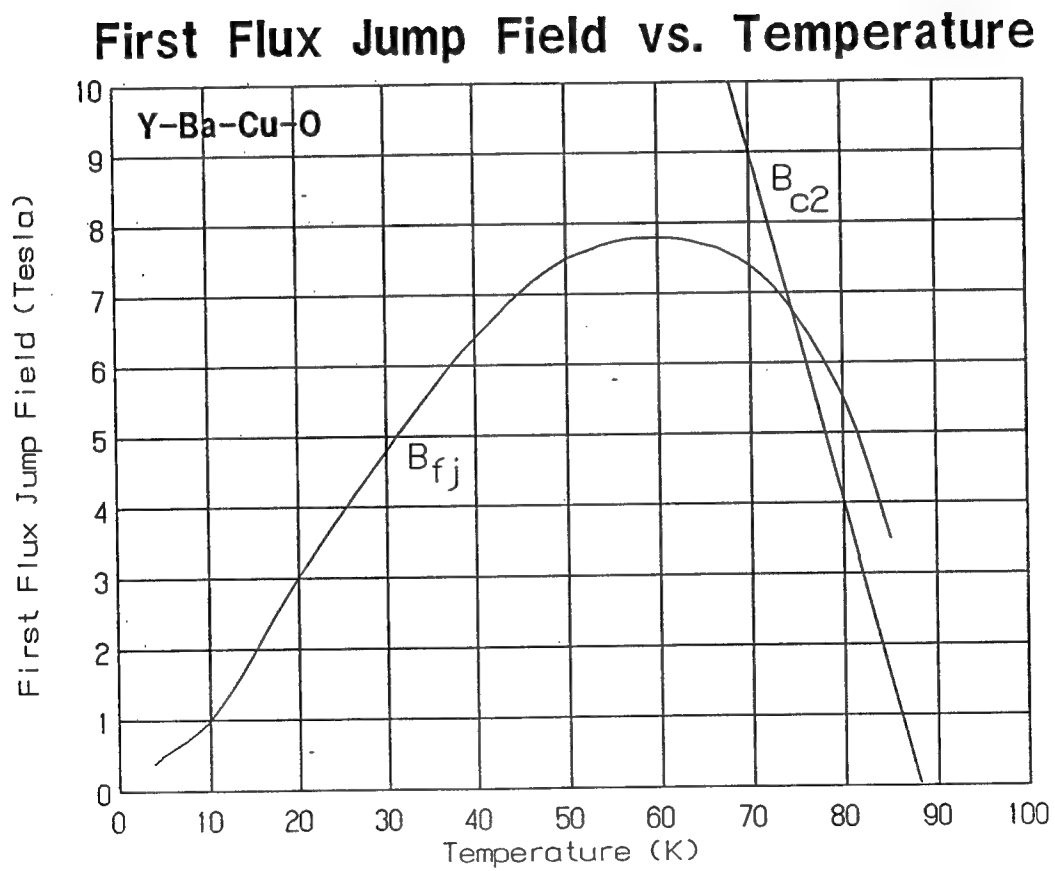


Figure 74. Flux Jump Limits as a Function of Temperature.

HTS Complications - Anisotropy

At present, there are at least two problems with using bulk high temperature superconductors. The first, which will hopefully disappear through continuing research and development efforts, is the weak link phenomenon, generally defined as limited current transfer across grain boundaries.

The second complication, and one that can never disappear, arises from the inherent anisotropy of the materials. Its effects can only become more pronounced as we reduce the weak link problem by better texturing.

A third problem may be the limited or complete lack of pinning. That has been observed for certain compositions, such as BiSCCO, for temperatures as much as 40% below T_c . It can also be seen for specific crystallographic directions in well textured materials.

3. Flux Pumping

Flux pumping, or the enhancement of trapped fields, follows quite naturally from the trapping concept. The simplest device is a single-shot flux displacer and goes back to the 1930's. To make the process repetitive requires switches or valves in a configuration or circuit that is topologically described as "multiply connected". The flux can be provided either by moving a permanent magnet in and out of the circuit, by powering a stationary electromagnet on and off, or by reversing its field. The switching process is usually thermal, but can also be magnetic.

Flux pumps can be divided into three classes:

a) Mechanical pumps, invented by Elleman and Hildebrandt at JPL, Figure 75a. They were originally developed with monolithic shapes and a moving flux displacer. However, the concept can also be applied to potted superconducting coils and the displacer could be replaced by an internal coil (Figure 75b), which would transform the device into an electrical type of pump. It should be pointed out that it is not easy to physically separate the thermal switching regions from the adjacent trapping regions in a bulk geometry.

b) Electrical or switching (rectifier) pumps, invented by Laquer at LASL (LANL), Figure 76. These work with coils only, but have no moving parts. The switching regions are easily separated from the coil region and can also be made from a different, more easily switched conductor.

c) Flux flow types, as invented by Volger and Admiraal at Philips (Eindhoven) and by Wipf, while at Westinghouse. They work with coils only and might, at first glance, appear to be singly

MONOLITHIC FLUX PUMP

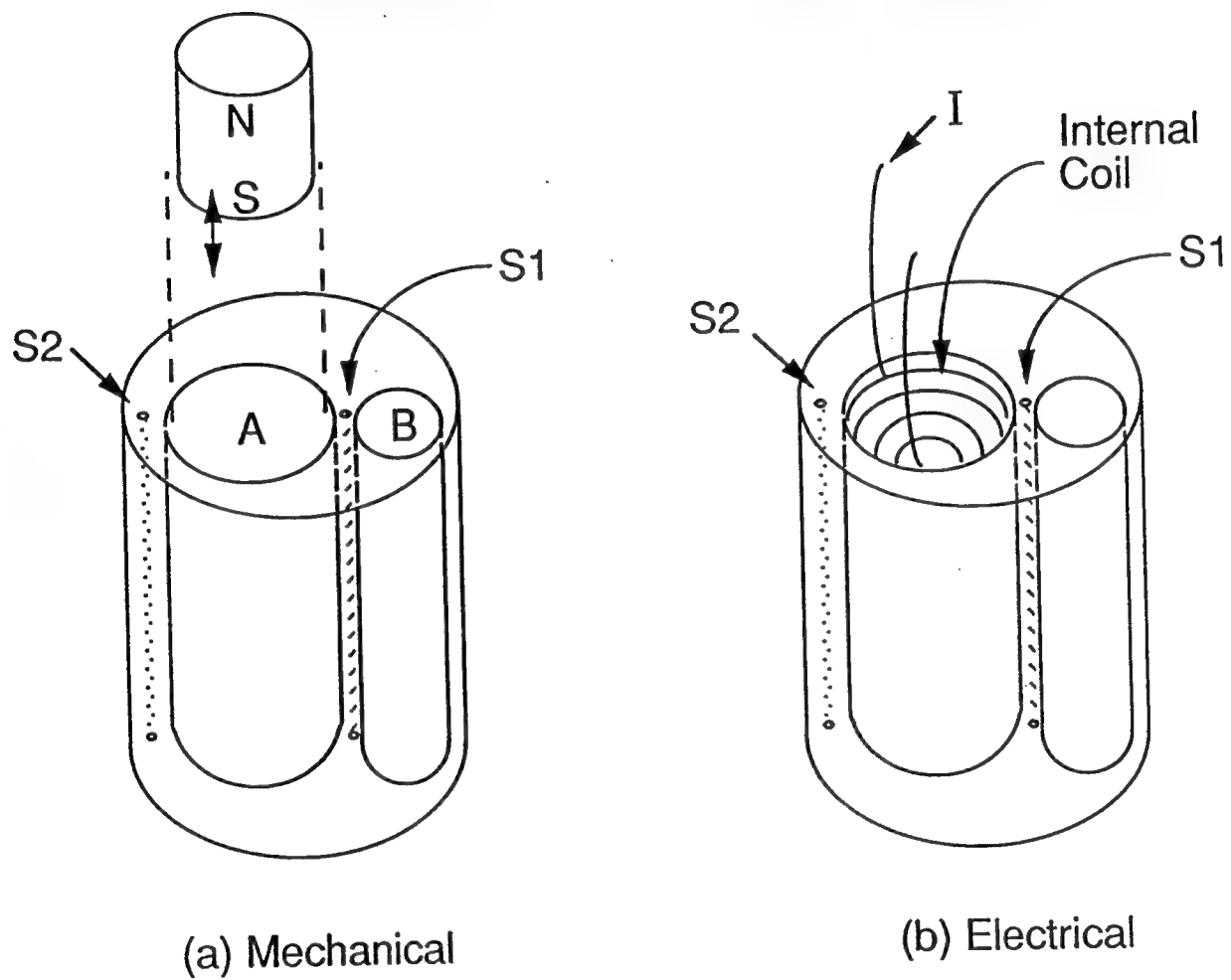


Figure 75. Monolithic Flux Pump: (a) Mechanical, (b) Electrical, the heater switches S1 and S2 are located in longitudinal holes.

SCHEMATIC DIAGRAM OF ELECTRICAL FLUX PUMPING METHOD

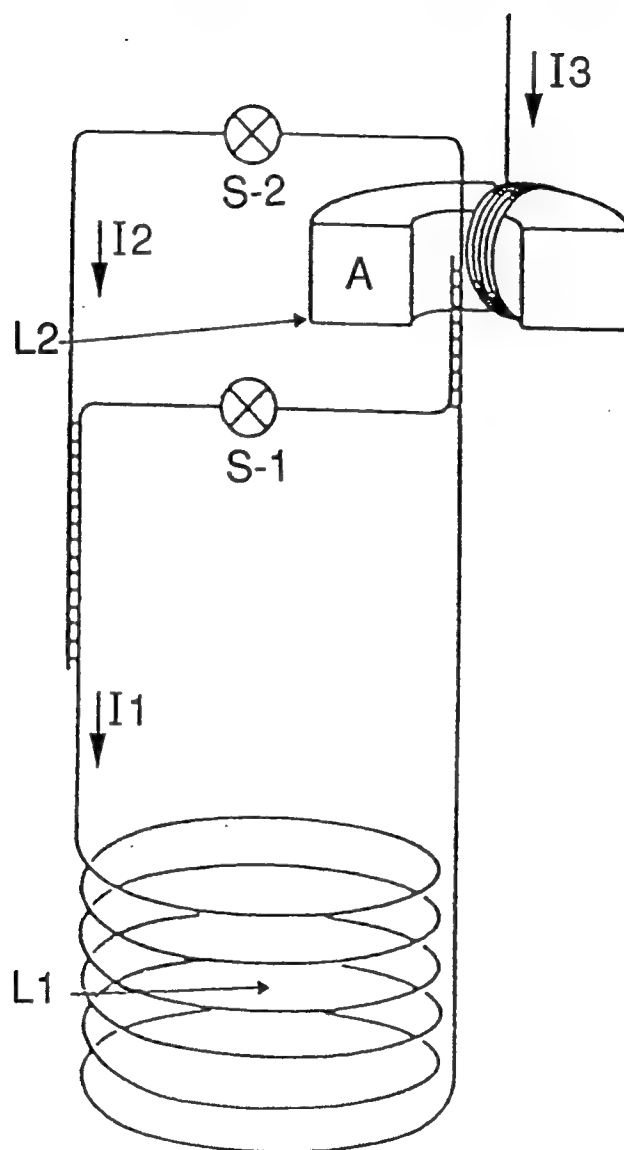


Figure 76. Wound Conductor Flux Pump (Rectifier Type).

connected. Actually, they become multiply-connected by forcing a flux spot through a wide barrier region. The source of flux may be either a rotating or reciprocating permanent magnet or electromagnet, or it may be a set of coils powered sequentially from a three-phase (or multi-phase) source.

Steps in Flux Pumping

The principles of operating the flux pumps of Figure 75 and Figure 76 are identical, in spite of their apparent differences in geometry.

Repetitive pumping requires a 4-step cycle:

Step 1: Open switch S-2 and introduce flux into the "A" region. As mentioned, this can be done by inserting a permanent magnet (Figure 75a), or by powering-up a fixed-in-place electromagnet, such as the simple coil in Figure 75b, or by putting current into the primary winding of a toroidal "Variac" TM transformer core (Figure 76).

Step 2: Close switch S-2 to trap, i.e. keep the flux invariant, while a supercurrent is generated around "A" and through S-2 and S-1 (inductance L2), by removing the source of flux introduced in step 1. This is done by removing the permanent magnet or turning off the current in the electromagnet or transformer primary winding.

Step 3: Open switch S-1 and force additional flux into the "B" (Figure 75) or coil (Figure 76) region (inductance L1) by pushing a bulk superconducting flux displacer into "A", or by applying current in the reverse direction in the fixed electromagnet or in the transformer primary.

Step 4: Close S-1 to trap the flux in "B" or L1.

Step 5: Open S-2 and repeat the cycle from step 1.

Actually the phasing of the switch opening and flux reversal operations may be timed so that the openings take place at zero current conditions for greatest energy efficiency, or at maximum current for easiest switching. The energy stored in the pumped field comes entirely from the mechanical or electrical work done in steps 2 and 3.

4. Switching Processes

The change in resistivity associated with the transition from the superconducting to the normal state, and vice versa, appears to be a ready-made phenomenon to be exploited in all sorts of electrical and electromechanical devices. To evaluate these concepts, we have to remember that all switching processes involve some kind of energy transfer, and that speed and efficiency will be determined

by the circuit inductances. Indeed, for the best energy transfer, the L/R time constant should be as short as possible. However, as was pointed out earlier, the transition has a finite width. This means that we must not only reach the fully normal state, but also maintain it for the duration of the energy transfer. The switch must "latch" in the fully normal, maximum resistance position.

As sketched in Figure 77, latching requires maintaining and possibly increasing the combined switching parameters of field, current density, and temperature, while the current density and field are decreasing due to the energy transfer. If this is not done, energy transfer may be incomplete and the system may actually hang or oscillate in a partially switched condition. The surest way of maintaining the "open" state of the switch is to raise its temperature above T_c . This is also the slowest and least energy efficient, since it entails providing and subsequently removing the enthalpy difference between operating and critical temperatures, and since it may be limited by heat transfer and thermal conductivity. (A detailed analysis has to consider the magnetic and thermal diffusivities in the system.)

There is also a theorem which states that the mass, volume and materials cost of a normal-going-superconducting switch are proportional to its peak power handling capacity and inversely proportional to its normal state resistivity and to the square of its operating current density. It is clear that for efficiency, as well as for ease of switching, superconducting switches should be operated as close to their critical current densities as possible.

1. Energy Storage - Power Conditioning

The fact that magnetic fields represent stored energy, means that flux-trapped or flux-pumped superconducting magnets have potential utility not only as alternatives to conventional permanent magnets or electromagnets, but also as sources of pulse power.

The primary differences between conventional permanent magnets and their superconducting equivalents, once fully developed, are:

- a) their hoped for higher fields and energy densities, and
- b) their ability to be discharged or switched off on demand, which opens the way to devices with power conditioning potential.

Energy storage and power conditioning devices typically employ a slow, low power charge, followed by a fast, high power discharge. Applications vary in power level, and in timing and recovery requirements, which then define the pulse repetition rate, or "rep-rate". Most applications of superconducting energy storage, studied up to now, have been purely electrical, with pulse power output to replace capacitor banks, or with longer term energy delivery into an electric utility system.

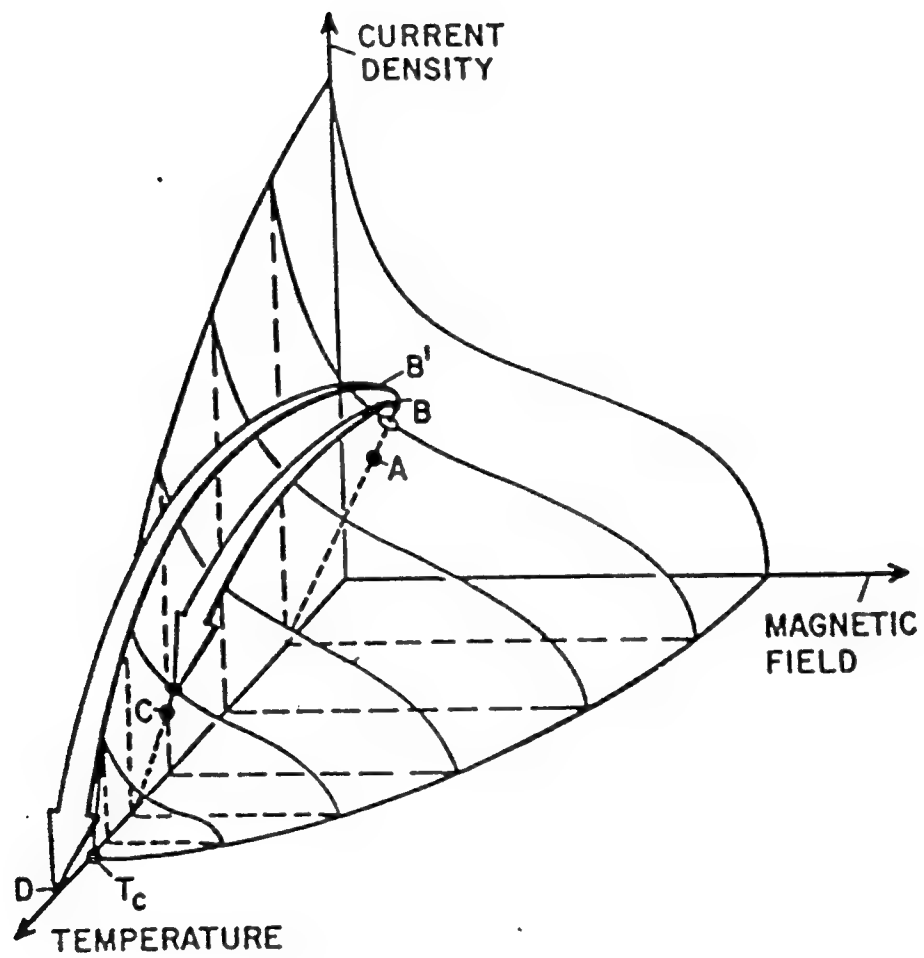


Figure 77. Dynamics of switching and latching.

It is also possible, however, to have a quickly changing magnetic field do mechanical work. The well known freshman physics demonstration of an aluminum ring thrown into the air by a current discharge through a solenoid exemplifies this concept. The $J \times B$ driving forces demonstrated here result from the interaction between the radial magnetic field and the circumferential currents induced in the aluminum ring.

2. Rivet Gun - General Requirements

The electromagnetic driver, described above, can form the basis of a rivet gun with potential uses in the aerospace industry. It can also be turned around to act as a dent puller, when the field is switched off quickly. Currently, the only drawback in using such devices seems to be in the dangerously high voltages needed to make them work. The question is, how to use the much safer energy pulse from a switched superconducting persistent current magnet to do the mechanical work. The general specifications for a rivet gun are given in Table I. The fields and currents needed for a dent puller are about half of these numbers, so that a dent puller (or foil adhesion tester) would be easier to develop.

Table I. The Rivet Gun Specifications.

Force 10 tonnes (20,000 lb)

Pulse Length 1 msec

Free Travel 10 mm

$J_c \sim 20,000 \text{ A/cm}^2$ at 2T (over the device diameter)

High Normal Resistivity - for Speed and Efficiency

Mechanical Strength

Complete Switching - Requires Thermal Latching

10-20 sec Rep-Rate (allows time for thermal recovery)

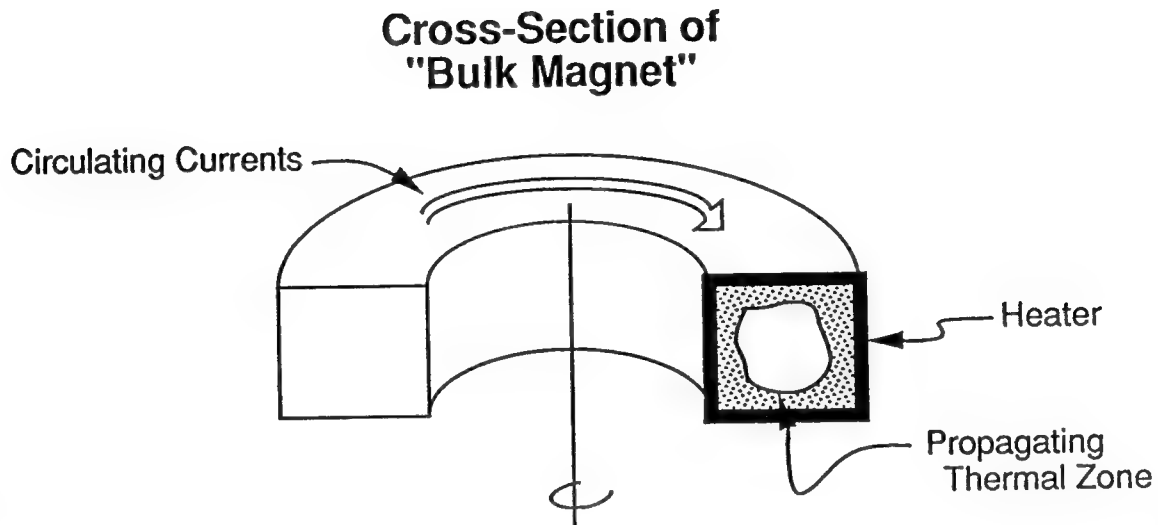
3. Conceptual Designs with Separated Functions

Simple Trapping

As a start we consider a simple ring or tube with a short heated switching section, Figure 78, to be operated as follows:

a) charge by insertion or juxtaposition of a conventional permanent magnet with the switch open, or with the tube above T_c ,

THERMAL SWITCHING MECHANISM



Conditions for Rapid Switching are Suitable

L/R

- single turn coil, low L
- large normal state ρ
- requires steep slope to I - V curve

Controlled Thermal Zone

- low k
- high C_p

Figure 78. Thermal switching mechanism in a flux-trap cylindrical magnet.

b) withdraw the permanent magnet with the switch closed, which does the work of putting the energy into the field, and

c) discharge the trapped flux by opening, i.e. heating the switch.

The main problem in applying this concept to a rivet gun is in doing enough work on the driver plate. Not only must we have a large enough radial field component, but it also must change or decay quickly enough to induce the currents to produce the force. Unfortunately, the better a conductor the driver ring, the slower the field decay and its exit through the ring. This is quite different from the physics demonstration discussed earlier, where the rising field and its penetration into the driver are opposed by the induced currents.

There is also the question of how to scale-up the device to the required force levels. Conceivably, one might shape the field so as to enhance the radial field component by providing a high-permeability or superconducting flux return path. The dent puller application, on the other hand, does not need a separate driver and can work directly on the skin of the aircraft.

Numerical Estimates for Switching Process

Without setting up a full finite element model of the switching process and of the force development, we can make rough estimates for the energy required to heat the switching section in Figure 78, the power to do it in 10 ms, and the limitations imposed by thermal conductivity. We also discuss how one might estimate the maximum force that can be produced.

The volumetric specific heat of YBCO is about half that of copper, or $10^6 \text{ J/m}^3\text{.K}$ at 80 K ($1 \text{ J/cm}^3\text{.K}$). To completely heat 1 cm^3 from 77 to 92 K, then takes 15 J. To do this in 10 ms would require delivering 1.5 kW. On the other hand, a mere 10 or 20% of this energy might be enough to raise the temperature by 1.5 or 3 K and thereby trigger the collapse of the field, so that the balance of the energy needed for latching will come from the field. In a sense this amounts to forcing a flux jump, and the only question is to show experimentally whether this can be done with 123 material at temperatures corresponding to the right-hand portion of Figure 74.

The thermal conductivity of YBCO is about 0.5 W/m.K (5 mW/cm.K). To drive 300 W across a 1 cm cube would require a (not very practical) ΔT of 60,000 K. Clearly, energy from the collapsing field would be the preferred source. However, we should also consider AC and rf heating methods that can deliver energy directly into the interior of the bulk superconductor, once it is in the normal state, so that we would not be limited by the low thermal conductivity.

As a very simplified limit for the force that can be generated with the dent puller, one could calculate the axial compressive body force in the ends of a 1 T solenoid and make the questionable assumption that the current density in the superconductor is transferred into the skin. To do this analysis correctly requires a knowledge of the decay time constants of the magnet and of the skin material, as well as their separation. The force on the skin would be proportional to its thickness.

Flux Pumping

As discussed earlier, the amount of stored energy can be increased with the JPL flux pump, Figure 75a. Our options are to alternate inserting a permanent magnet and a superconducting flux displacer into the larger hole, or we can periodically reverse the direction of the permanent magnet, instead of using the passive flux displacer. The modified procedure of Figure 75b would use a small, stationary cryogenic electromagnet in the larger hole. This would avoid mechanical motion, but would greatly increase the number of pumping cycles.

Discharge Methods

The use of the same heater elements, shown in Figure 75 and Figure 78, to control the trapping or pumping, as well as the discharge would be the preferred way of operating these devices, since it avoids adding additional components.

4. A Simpler Alternative.

The following concept for a rivet gun builds on the earlier considerations and appears to present a somewhat simpler alternative. It consists of a superconducting driver plate or disk of thickness, t , inner radius r_1 and outer radius r_2 , which is pushed against a conventional permanent magnet, Figure 79a. As the disk approaches the magnet, superconducting "image" currents will be induced in it, Figure 79b and the repulsive force between the disk and the magnet increases, Figure 79c. Up to this point, there is an elastic restoring force, analogous to the force exerted in a superconducting bearing. The disk is shaped, so that the critical state will be reached simultaneously throughout its cross-section, Figure 79d. Once it has been completely filled up to its critical current densities, no additional force can be generated and any further push should make it "crash" forward.

The advantage of this scheme is that the driver disk will be designed to reach the critical state throughout its entire cross-section and then switch automatically, uniformly and simultaneously. However, we do not as yet know whether and how well the device will "latch" by itself, and whether it will have to draw on the momentum from its forward motion to complete the

SUPERCONDUCTING DISK- PERMANENT MAGNET RIVET GUN

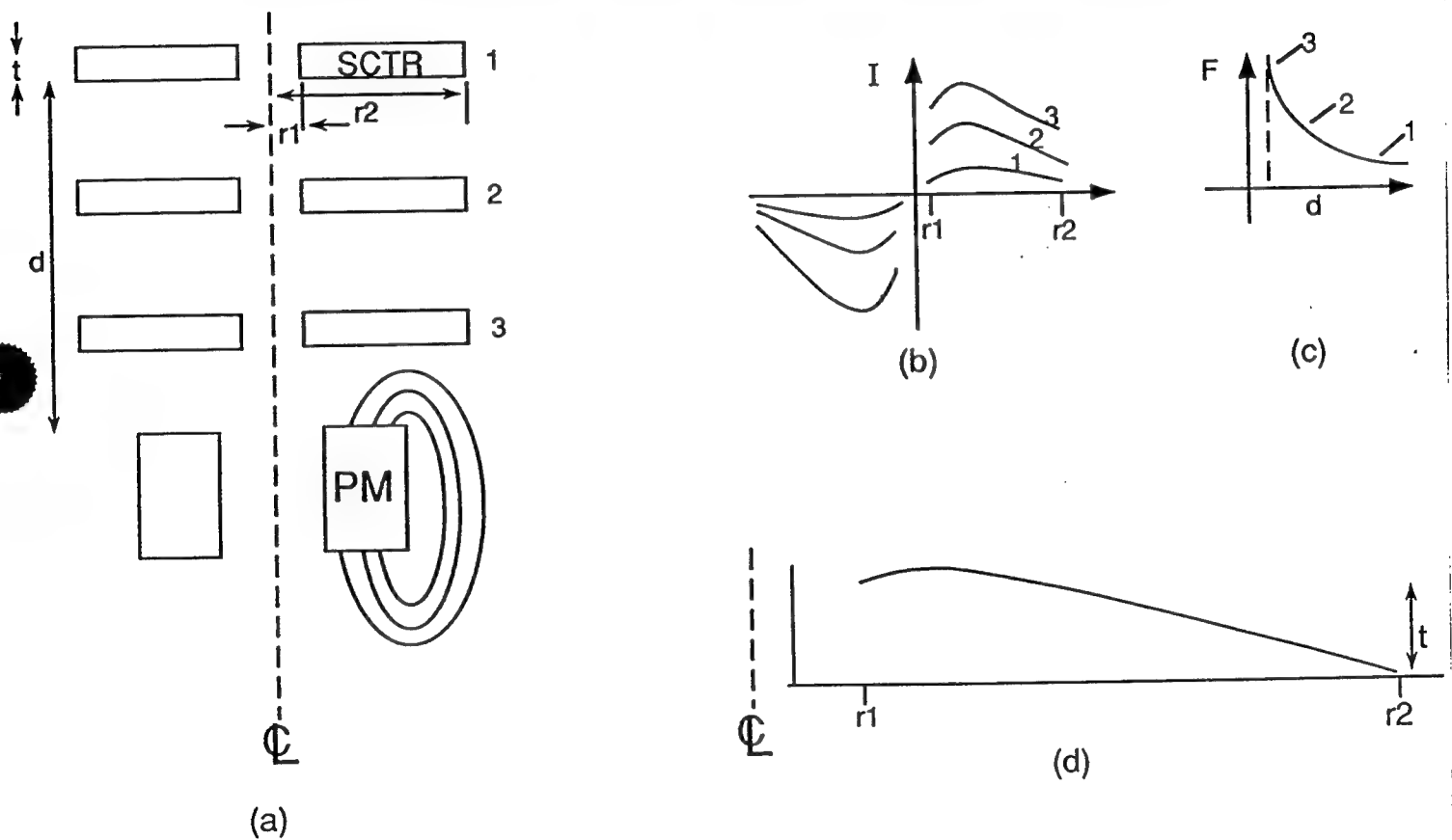


Figure 79. Superconducting Disk - Permanent Magnet Rivet Gun.

stroke. We suspect that the details of the force vs. distance curve, once the driver starts to accelerate, will be a function of how fast it has been approaching.

To repeat the process, all trapped flux will have to be removed by heating the driver or letting it warm to above its critical temperature. (Similar to Automatic Center Punch)

Design Concept for a Superconducting Device

The concept of obtaining mechanical work from the collapsing field in a high temperature superconducting "permanent" magnet was evaluated (Figure 80).

A schematic flow diagram for a superconducting device (dent puller, proof-tester, or rivet gun) is shown in Figure 81. The device operational principles include: 1) trapping, 2) flux pumping, and 3) quenching. Figure 82 shows a schematic diagram of trapping, where magnetic flux (from a permanent magnet) is introduced into a superconducting sample above its transition temperature while the thermal switch is open, hence no macroscopic superconducting currents are flowing in the sample. Thermal switch is then closed to keep flux invariant and screening currents are established upon removal of permanent magnet. Figures 83-84 show a schematic diagrams for trapping in solid disks and cylinders, respectively. Figures 85-86 show a schematic diagram of flux pumping, where the flux is displaced inside a toroid with a superconducting plunger. Screening currents are thus build to operational levels. Figure 87 shows a schematic diagram of a quenching process, where screening currents are quenched thermally (Figure 88), by flux-jumping (Figures 89-91, or by a weak link collision (Figure 92).

How an EM Superconducting Device Will Operate

Device Operational Flow

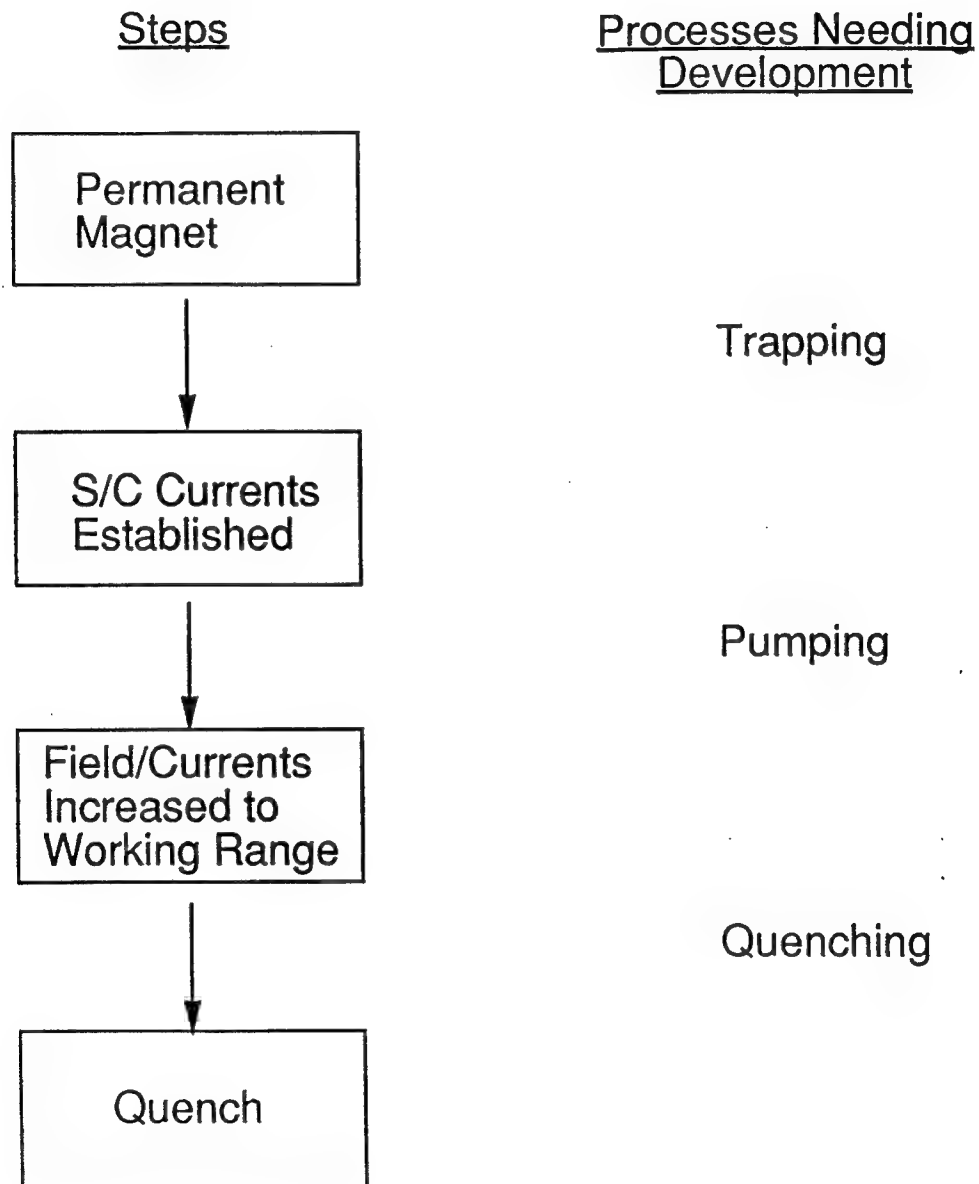


Figure 80.

SCHEMATIC FLOW FOR EM SUPERCONDUCTING DEVICE

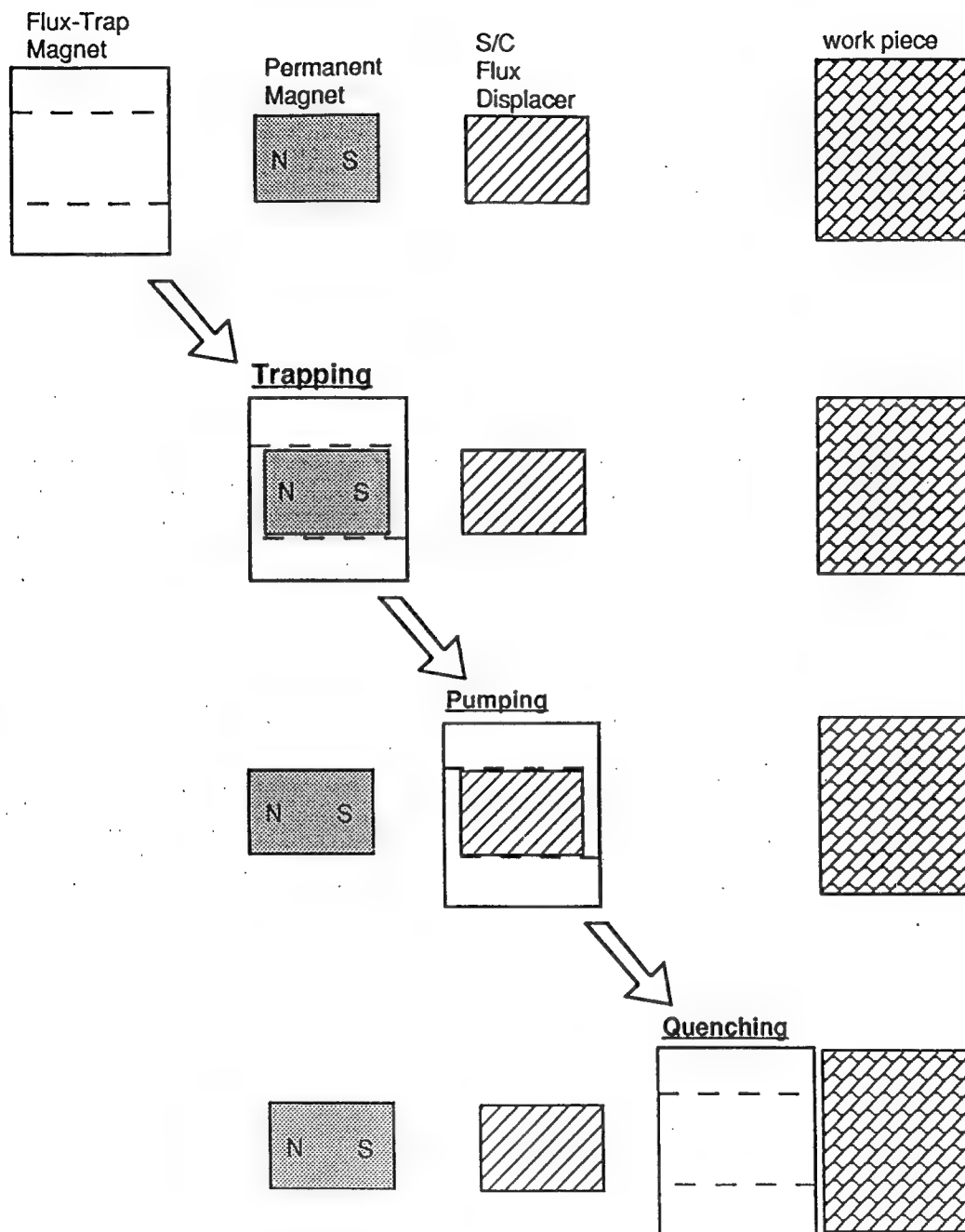
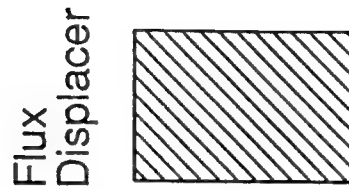
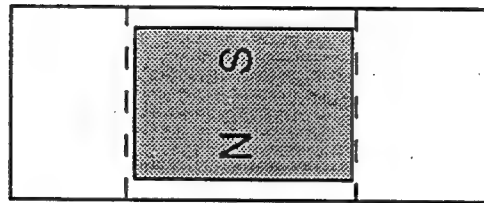
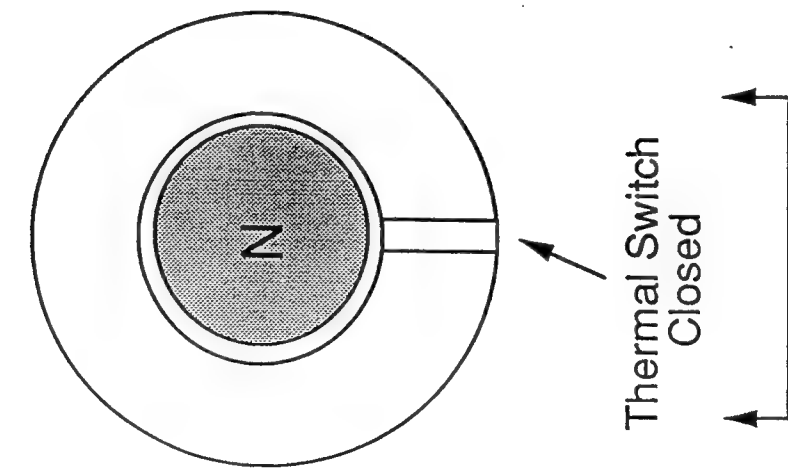


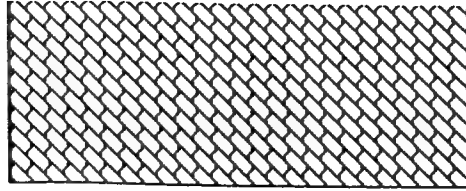
Figure 81.

OPERATIONAL PRINCIPLES

TRAPPING



work piece



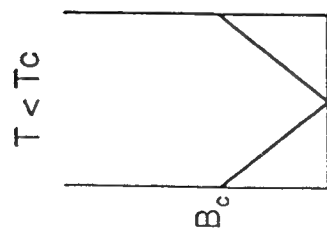
- Flux introduced
- Switch closed to keep flux invariant
- Screening currents established by removing permanent magnet

Figure 82.

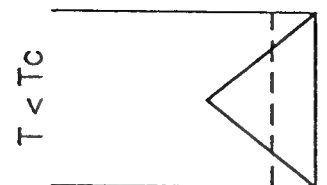
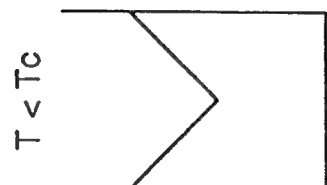
DEVICE OPERATIONAL FLOW: TRAPPING IN SOLID DISKS

PROGRAM GOAL: Convert Field From Best Permanent Magnets to Supercurrents

PROCESS 1

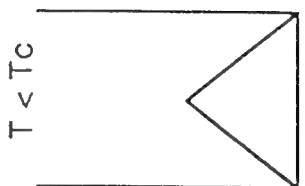
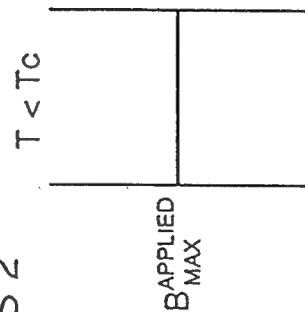


$$H_{\text{MAX}}^{\text{APPLIED}} = 2H_c$$



$$B_{\text{TRAP}} = \frac{1}{4} H_{\text{MAX}}^{\text{APPLIED}} = \frac{1}{2} H_c = 1000 \text{ Gauss}$$

PROCESS 2



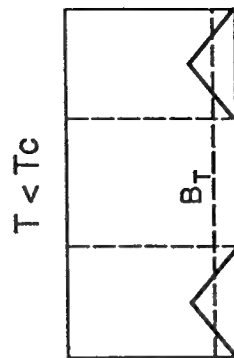
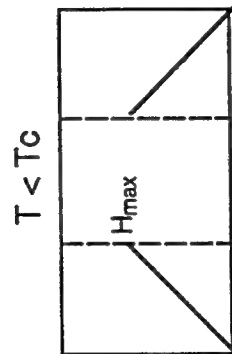
$$B_{\text{TRAP}} = \frac{1}{2} H_{\text{MAX}}^{\text{APPLIED}} = 2000 \text{ Gauss}$$

Figure 83.

DEVICE OPERATIONAL FLOW: TRAPPING IN CYLINDERS

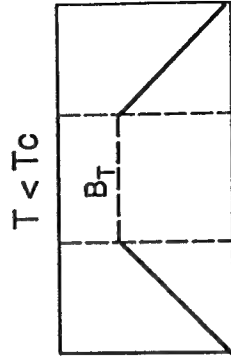
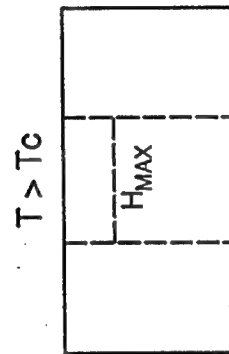
Program Goal: Convert Field From Best Permanent Magnets
to Superconducting Currents

PROCESS 1



$B_{TRAP} = 1/4 H_{MAX} = 1000$ Gauss

✓ PROCESS 2



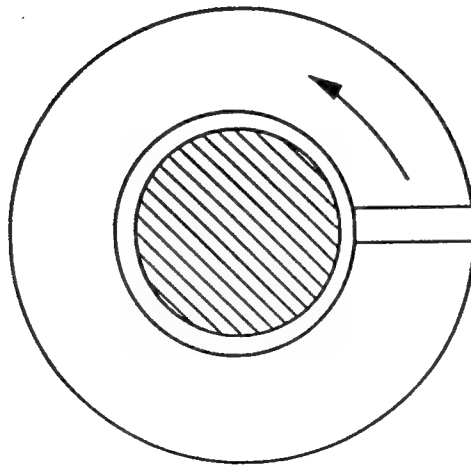
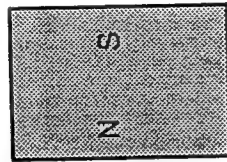
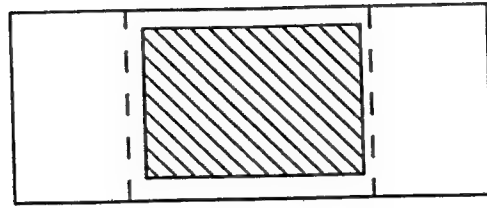
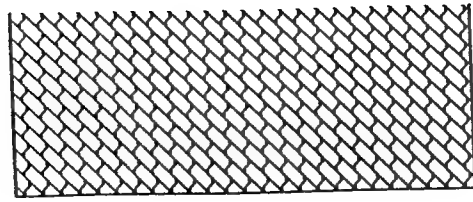
$B_{TRAP} = H_{MAX} = 4000$ Gauss

Figure 84.

OPERATIONAL PRINCIPLES

FLUX PUMPING

work piece



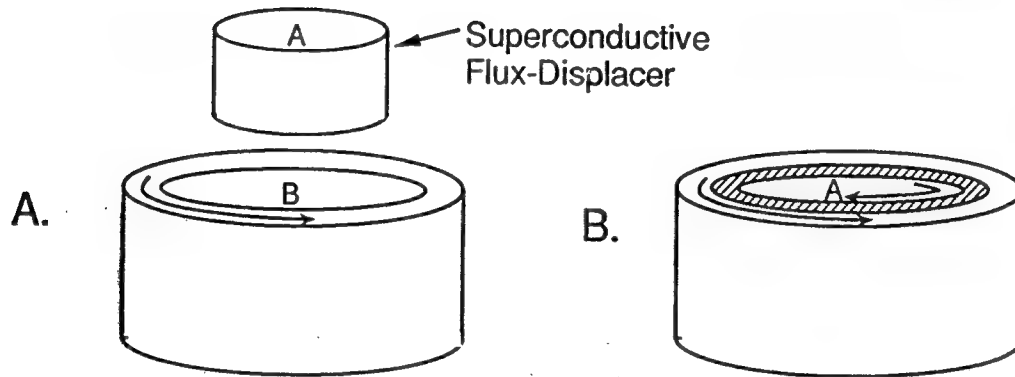
Thermal Switch
Closed



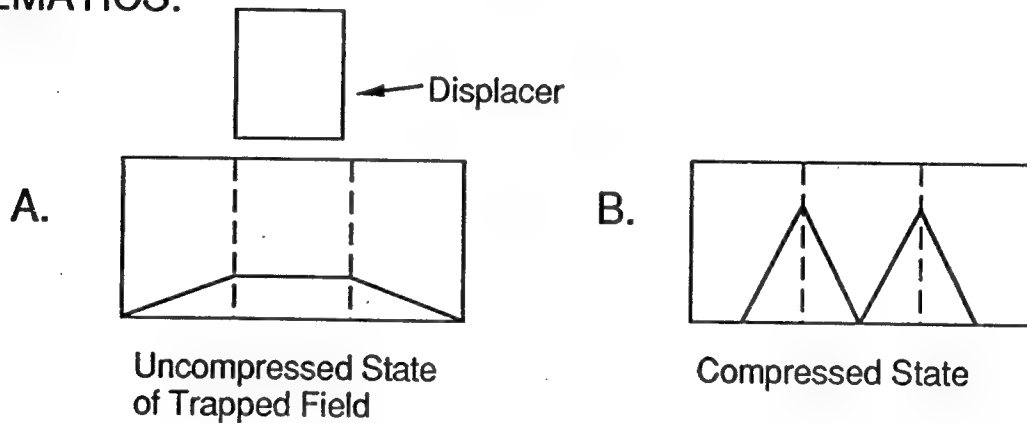
- Flux displaced inside toroid
- Currents and fields build to operational level

Figure 85.

Mechanical Monolithic Flux Pump



SCHEMATICS:



$$\text{Pumping Capacity} = \frac{\text{Area B}}{2(\text{Area B} - \text{Area A})}$$

0.4 to 1 T If $A_{\text{radius}} = 2 \text{ cm} \rightarrow \text{Gap} = 0.11 \text{ cm}$

Figure 86.

OPERATIONAL PRINCIPLES

QUENCHING

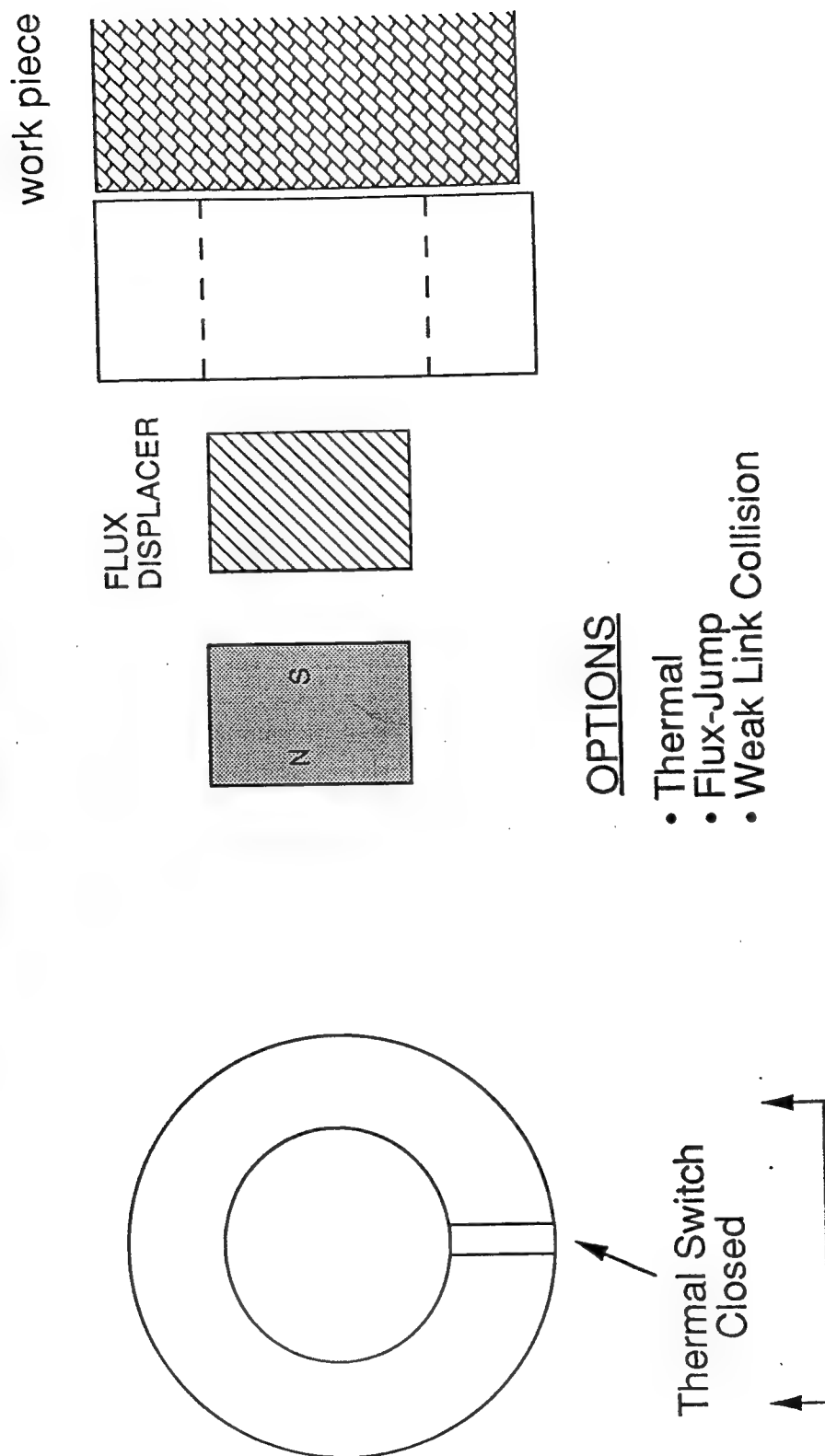
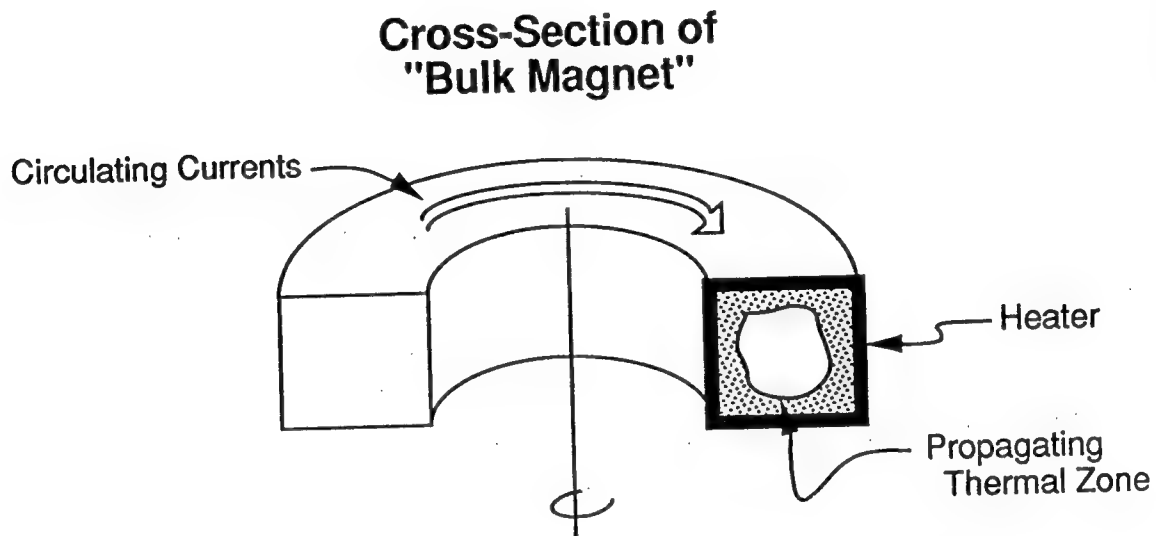


Figure 87.

QUENCHING PROCESS

DC THERMAL SWITCHING MECHANISM



Conditions for Rapid Switching are Suitable

L/R

- single turn coil, low L
- large normal state ρ
- requires steep slope to I-V curve

Controlled Thermal Zone

- low k
- high C_p

Figure 88.

QUENCHING PROCESS

FLUX - JUMPING

PROBLEM

High specific heat at 77K makes superconducting currents very stable against flux jumps

SOLUTION

Operate close to T_c to minimize required temperature rise

HEAT BALANCE FOR DEVICE

Effective Specific
Heat of Device = Specific Heat of Superconductor - Flux Flow
Dissipation

$$\gamma C_e = \gamma C - \frac{\mu_0 J_c^2 a^2}{3(T_c - T_0)}$$

Figure 89.

QUENCHING PROCESS

First Flux Jump Field vs. Temperature

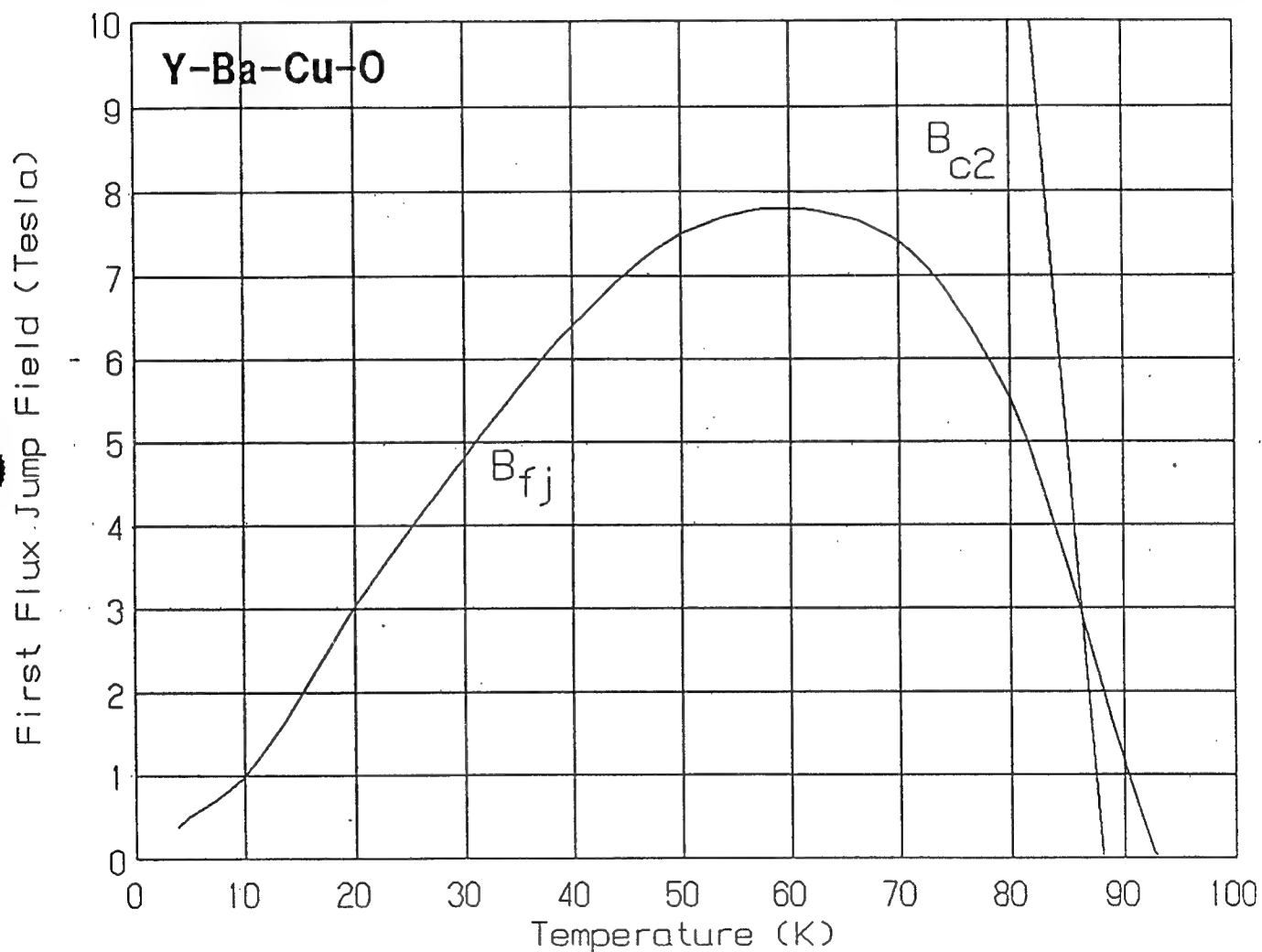


Figure 90.

QUENCHING PROCESS

Adiabatic Stability Limits for Generic HTSC

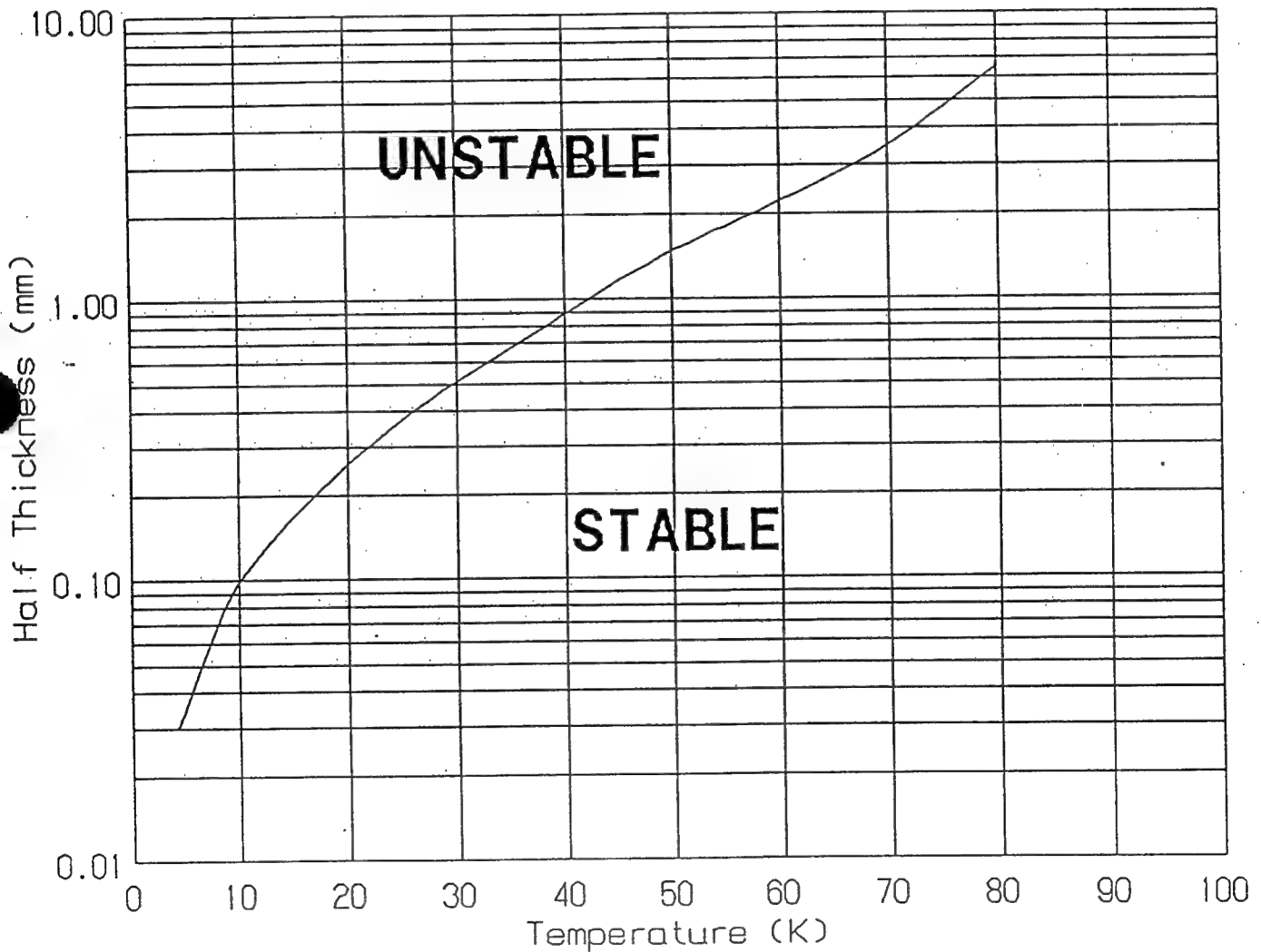
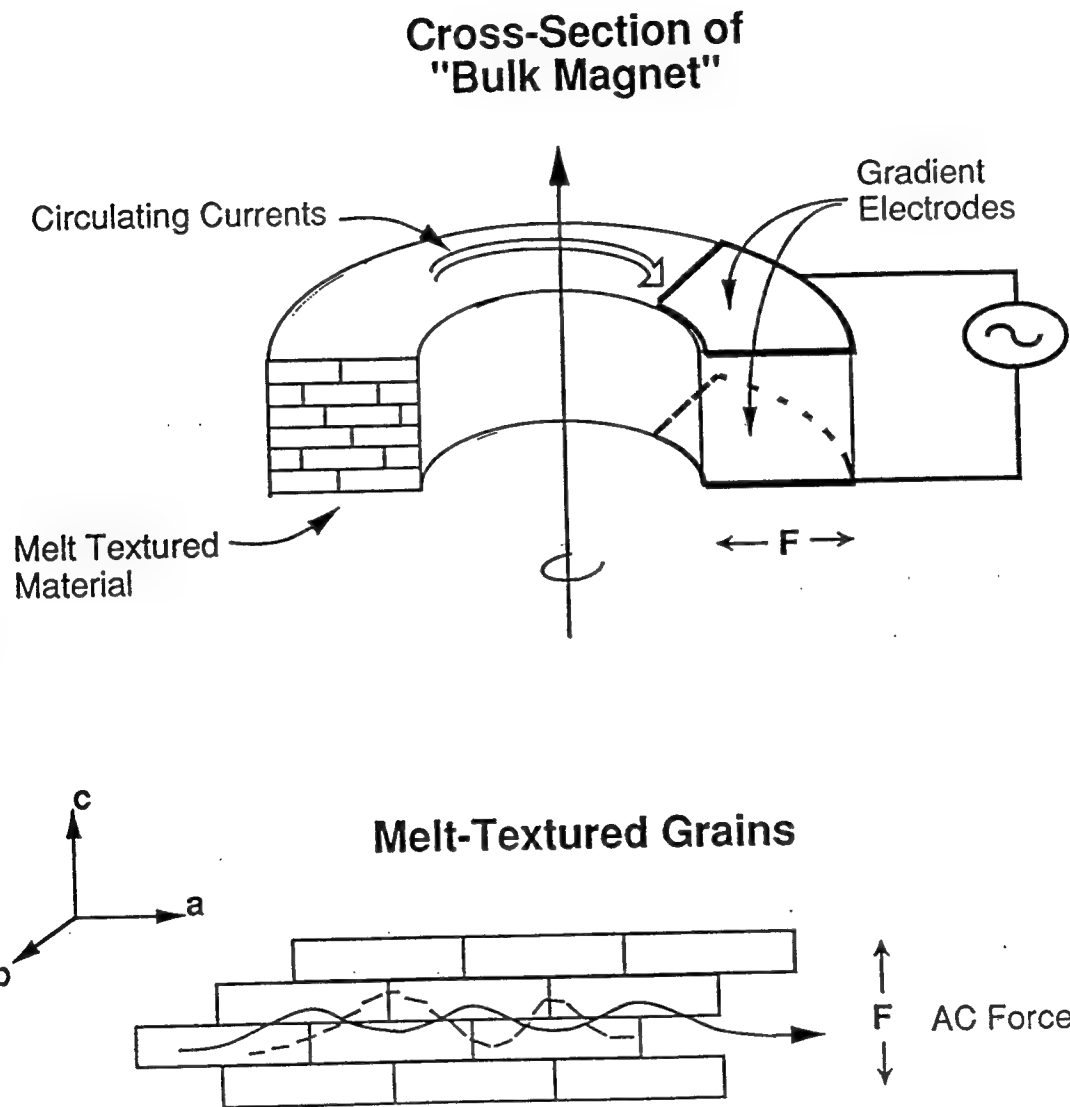


Figure 91.

QUENCHING PROCESS

Weak-Link Collision Quench



Patent Disclosure

Figure 92.

B. Applications

Early Technology Insertion

Among the potential applications we have been exploring for the early technology insertion of 123 ceramic superconductors is an electromagnetic dent puller. Two major areas of use of the dent puller identified are in airplane manufacture and proof-testing of adhesively bonded aerosurface skin structures. The dent puller has a potential to significantly improve cost and productivity in manufacturing of military and commercial airplanes.

In the proof-testing application, the dent puller is the only method which can reliably assess aluminum bonded skin strengths (Figure 93); ultrasonic inspection is not able to determine the difference between weakly bonded and securely bonded structures. Significant amounts of bonded composites are currently used on military airplanes with increasing use predicted for commercial airplanes. Proof-testing with an electromagnetic device (which utilizes rapidly collapsing magnetic fields) is the only reliable method being used at the present time. These conventional electromagnetic systems are very large, not easily transportable (1000 pounds for the capacitor unit), and very dangerous (495 Volts and 30,000 Amperes) in operation. They require large cables connecting the capacitors and the hand-held unit, making the accessibility of the dent puller very impractical or sometimes impossible. In our proposed high temperature superconducting system, the capacitors are replaced by magnetic energy stored in flux-trapped magnets. Advantages accrued with the superconducting system include safety, portability, simple operation under hazardous and remote conditions, and improved productivity and reproducibility. Early studies show that field strengths of only 1 Tesla would be required in a working superconducting device. Trapped fields of this magnitude are predicted in 123 material before the end of 1991.

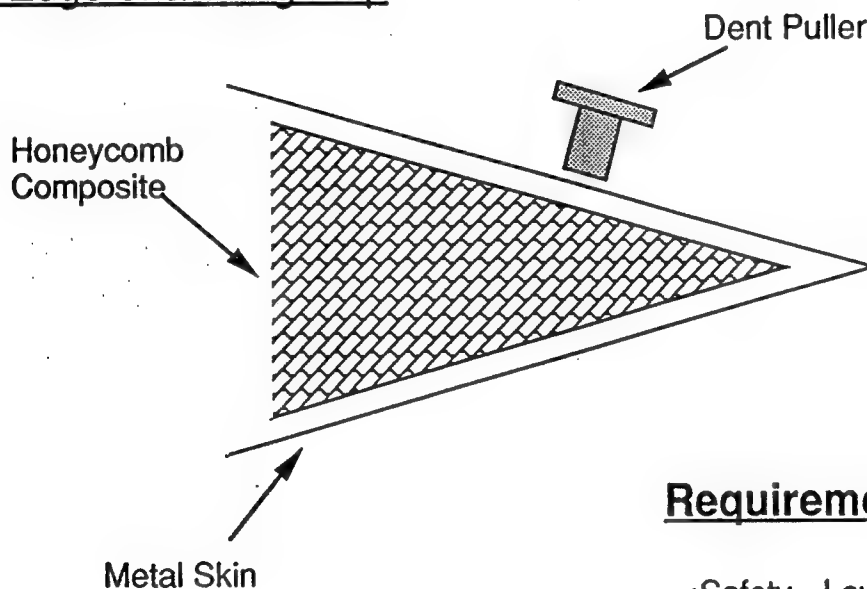
Wide spread use and significant cost savings are forecasted. For example, it costs about \$25K to proof-test a leading edge of a wing flap on an F-18 airplane. This test is currently being researched at the Boeing Company. With the availability of the superconducting dent puller, the test can be performed in-service, thus significantly reducing the cost and time of the test. The U.S. Air Force and Navy are very interested in the possibility of testing airplanes in active service (Figure 94).

In the manufacture of commercial and military airplanes, dent pullers are used for removing inadvertent damage during manufacture. Very significant time and cost savings could be realized with the availability of safe, portable dent pullers. The airline industry will also benefit tremendously in terms of cost and time savings in repairing airplanes dented in service (Figure 95).

OPERATIONAL PRINCIPLES

Proof-Testing of Adhesively Bonded Composite Skins on Military Aircraft

Trailing Edge of a Wing Flap



Requirements:

- Safety - Low Voltage
- Portability
- Field of 0.5-1.5 Tesla Needed
- Low Cost

Figure 93.

Potential Military Payoffs of a Superconducting Dent Puller

- The only reliable technique available to proof-test adhesively bonded composite skins on military aircraft (the ultrasonic technique is not reliable)
- Dent Repair on Military Aircraft
 - During manufacturing
 - In service
- Possible repair or proof-testing of aircraft in service:
 - Combat situations
 - Aircraft carriers
 - Remote locations

Figure 94.

Examples of Potential Cost Savings for Airlines By Using a Dent Puller

Grounding Costs:

Example: Boeing 747

\$8000 / hr

This is inconvenience time

Actual cost is much higher if passengers have to be accommodated in hotels or on other flights

Repair Costs:

Repair of dented leading edge of horizontal stabilizer on a 737-500 in service required:

- Removal
- Repair
- Reinstallation

Total Cost: Approx. \$10,000 in labor costs only plus the cost of the airplane being out of service

Figure 95.

It costs between \$10K and \$25K to remove a dent from an airframe in service. If it could be repaired on location, the cost would be minimized. McDonnell Douglas Corp. saves approximately \$50-60K a week by repairing dents in airframe panels using a dent puller instead of traditional techniques. These savings would be significantly higher with the availability of a portable dent puller (Figure 96).

Finally, a device based on bulk HTS material has the added benefit of enabling superconductivity to find a place both on the manufacturing floor, and in the field performing real time inspections and repairs of airplane structures. The potential application of the superconducting electromagnetic type device is certainly not limited only to the aerospace industry but conceivably may be utilized across the wide spectrum of manufacturing industry. Experience gained under these conditions in their use would undoubtedly lead to other exciting and revolutionary opportunities for high temperature superconductors.

Technology Insertion Plan

A Technology Insertion Plan for a Superconducting Dent Puller, Proof Tester, Clamp, and a Rivet Gun was developed (Figure 97). Payoffs and benefits of these superconducting electromagnetic devices were identified. Potential customers and markets for the superconducting devices were identified (U.S. Military, Airplane Manufacturers, and Airlines). Among the potential customers initially contacted were the Air Force, Navy, Boeing, McDonnell Douglas, United, American, Northwest, Delta, and Continental Airlines. Industrial involvement in the Technology Insertion Plan was outlined.

Dent Puller Operation

The basic concept employed in an electromagnetic dent puller, originally developed at Boeing (Figures 98-99), involves producing a high negative magnetic field gradient across the facesheet of a structure. The interior field is then rapidly collapsed back toward the flux concentrator, by selectively canceling the exterior field and thus producing the outward force on the facesheet of the structure (Figure 100). By varying the magnetic field level within the structure, the pulling force on the facesheet can be regulated and precisely controlled.

When subjected to a pulsed magnetic field, the basic phenomena occurring in a metal sheet is the diffusion of that magnetic field into and through that sheet. Specific pulse frequencies are required to first allow the magnetic field to readily penetrate the metal sheet (push); and to then enable the same sheet to shield or prevent the rapidly collapsing field from easily diffusing back through the sheet (effective pull). The tension force is achieved

Examples of Potential Cost Savings for Airplane Manufacturers By Using a Dent Puller

Boeing:

Approx. \$250,000 saved in a month on repaired production parts

McDonnell Douglas:

Approx. \$1.25 M saved in the last quarter of 1990 in repairing rejected production parts (cost of parts only)

McDonnell Douglas:

Replacing "Bondo" filler on C-5 airplanes during overhaul costs approx. \$25,000

Figure 96.

TECHNOLOGY INSERTION PLAN

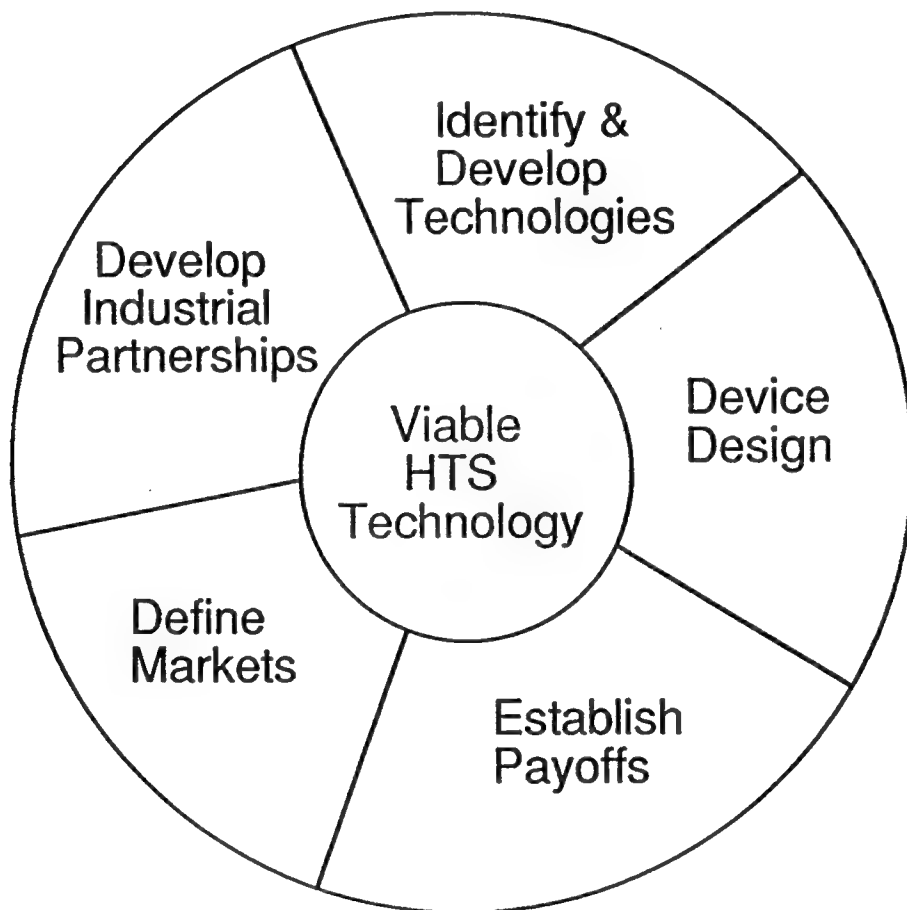


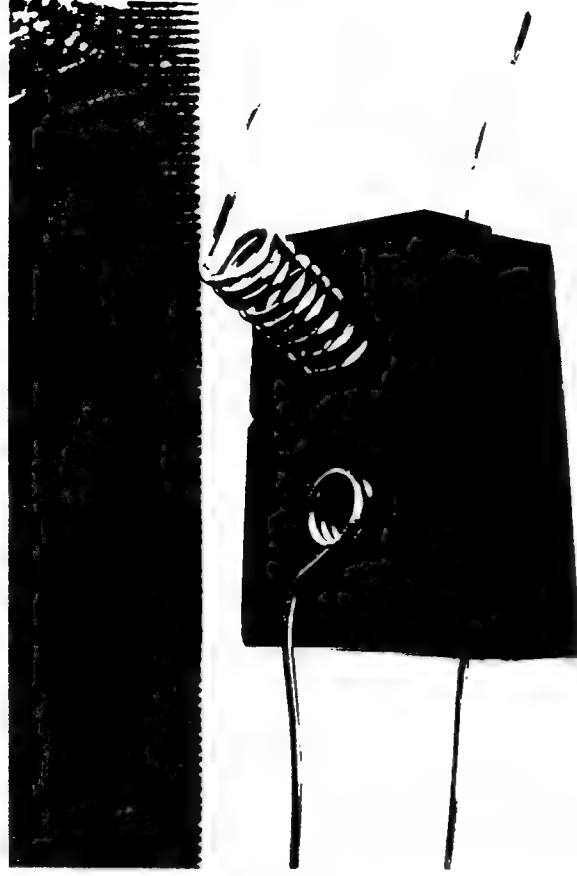
Figure 97.

High-Temperature Superconductors

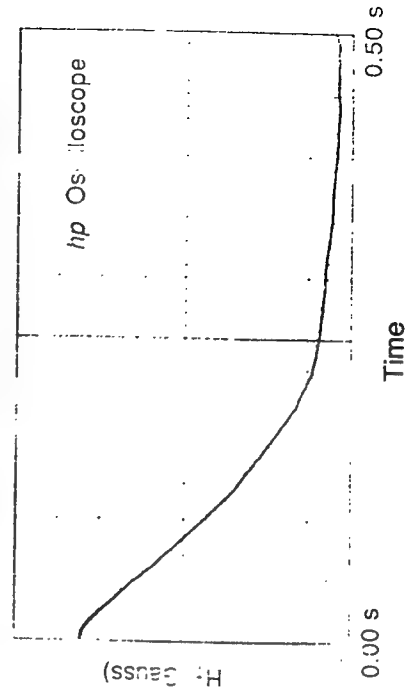
EXISTING TECHNOLOGY



TECHNOLOGY DEVELOPMENT



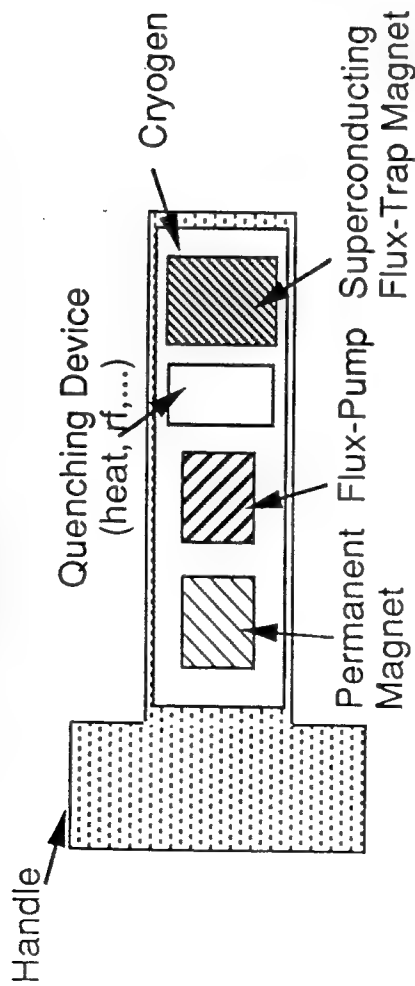
Trapped Field vs. Quenching Time



High-Temperature Superconductors

SUPERCONDUCTING DENT PULLER

QUENCHING OF MAGNETIC FIELD



OPERATION OF A DENT PULLER

1. Apply magnetic field gradient to a dented part - negative magnetic field produced across the facesheet of a part
2. Collapse the magnetic field by cancelling the applied field - outward force produced on the facesheet - dent pulled
3. By varying the magnetic field level within the structure - pulling force on the facesheet can be regulated and controlled

ELECTROMAGNETIC DENT PULLER IN OPERATION



OPERATIONAL PRINCIPLES

Electromagnetic Dent Pulling Operating Sequence

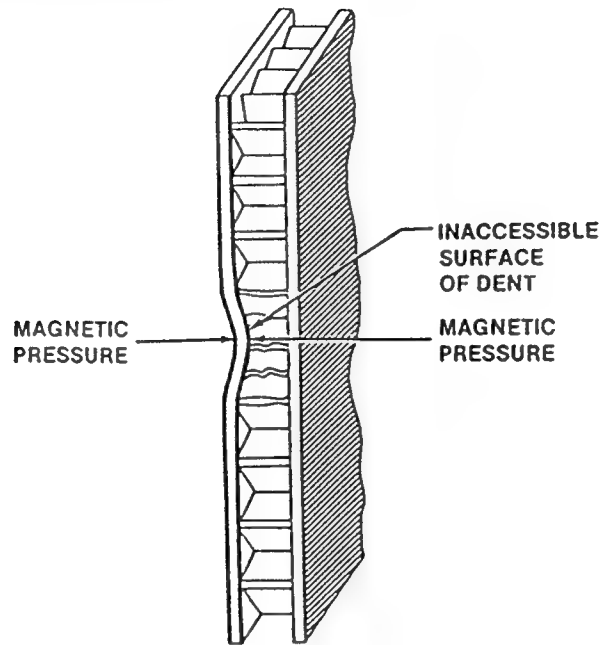


FIGURE 1. PRINCIPLE OF MAGNETIC TENSION

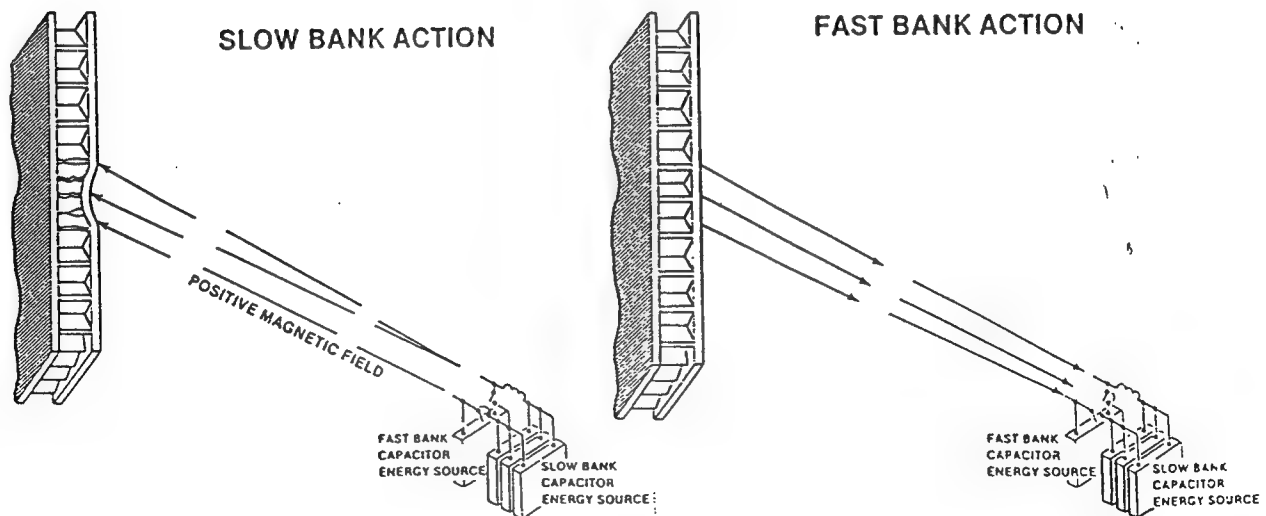


FIGURE 2. SLOW BANK ACTION

FIGURE 3. FAST BANK ACTION

Figure 100.

by first establishing a magnetic field on both sides of the metal sheet with a field generating coil on the outside of the metal sheet. The coil is kept energized until the low frequency field has completely penetrated. If the magnetic field at the outside is then rapidly reduced to zero, the magnetic pressure on the inside will push toward the outside resulting in the effective pulling force (Figure 101).

Dents in airplane structures are presently being repaired by potting with a "Bondo" filler. This conventional dent repair includes surface cleaning and preparation, filling with potting compound, curing, sanding, priming, and painting. When a dent cannot be repaired by a "Bondo" filler, the dented part has to be completely replaced. The advantages of a dent repair by a dent puller are:

- structurally superior repairs to either potted or unrepaired dents
- portable unit (hand-held)
- safe operation (low voltage)
- permanent repairs
- low cost
- shorter repair times (no need to remove parts to access a dent)
- superior cosmetic appearance of the repaired area
- repair possible without access to the back of the dent
- improved inspectability of the repaired area
- honeycomb repairs possible
- no additional weight added to the aircraft
- reproducibility
- repairs of painted surfaces possible

Superconducting Clamp

Among the latest potential applications for early technology insertion in manufacture of military and commercial airplanes is a superconducting clamp based on flux-trap magnets (Figure 102). Permanent magnets are used widely and in diverse applications such as in attracting and holding ferromagnetic objects and in clamping non-magnetic objects and assemblies during manufacturing. Currently, permanent magnets are frequently the only feasible way of holding objects in confined areas during manufacturing. In addition to permanent magnets, larger electromagnetic clamps and chucks are being used extensively throughout the manufacturing industry. Superconducting clamps will allow for the diversity that the electromagnetic clamp provides with the safety and ease of use of a permanent magnet. Figure 103 shows a comparison of several operational factors for superconducting vs. electromagnetic and permanent magnet clamps.

OPERATIONAL PRINCIPLES

Output Current Waveform for an Electromagnetic Dent Puller and Proof Tester

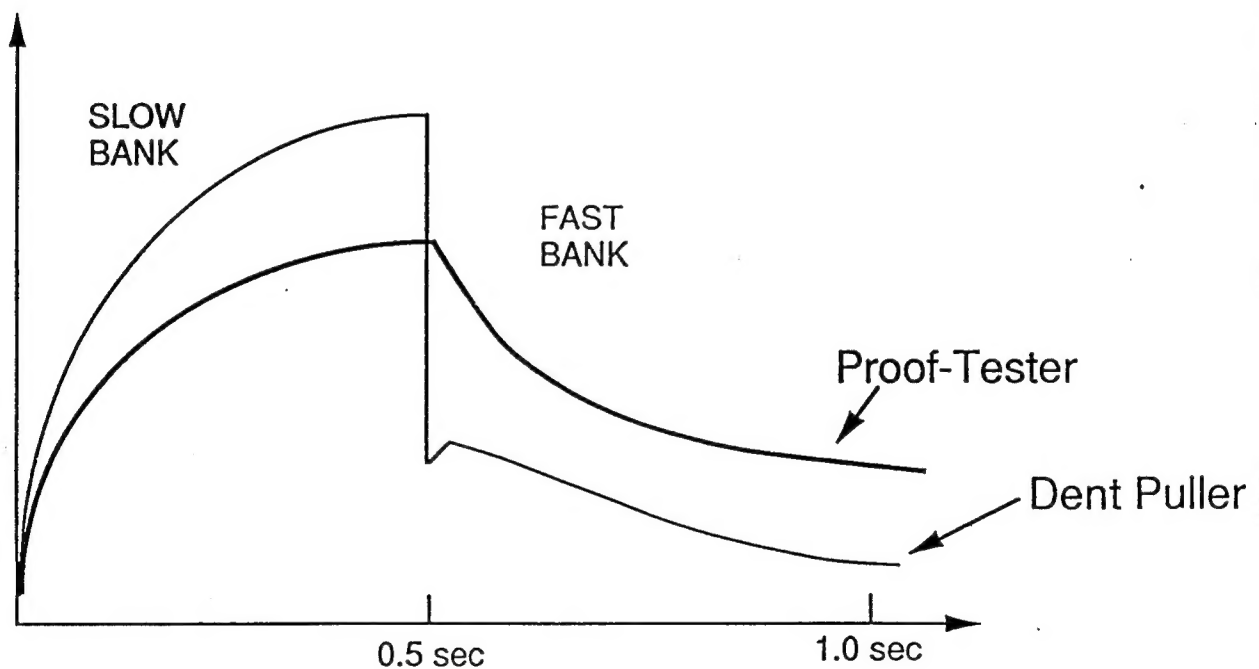
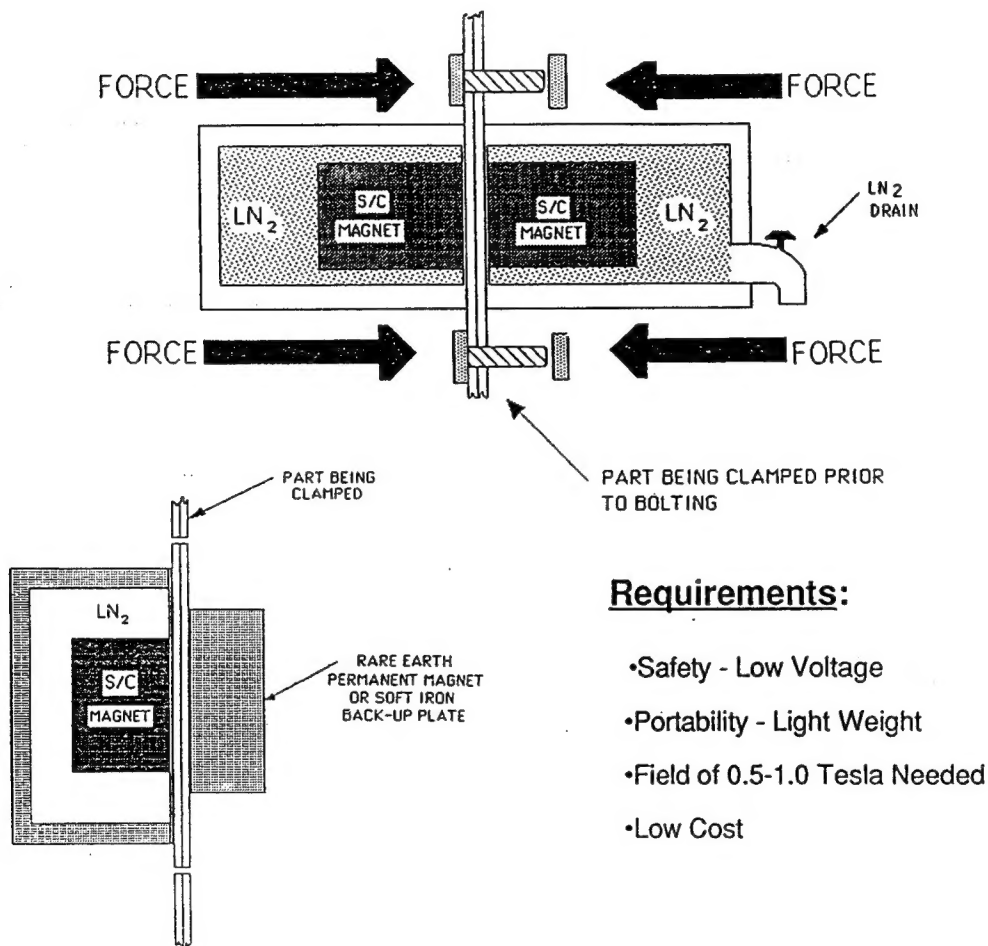


Figure 101.

SUPERCONDUCTING CLAMP



Requirements:

- Safety - Low Voltage
- Portability - Light Weight
- Field of 0.5-1.0 Tesla Needed
- Low Cost

Figure 102.

Comparison of Superconducting vs. Electromagnetic and Permanent Magnet Clamp

	Permanent Magnet	Electromagnetic	Superconducting
Safety	Relatively Safe	Very Dangerous High Amps; High Voltage	Very Safe
Size	Small	Large, Bulky Very Heavy	Small Lightweight
Portability	No Attached Air Hoses	No Attached Power Cables	Yes
Capital Cost	Approx. \$2K	Approx. \$20-100K	Unknown
Operational Cost	Small	Very Large Due to Large Resistance Losses in Cu Wires	Minimal - No Losses Cryogen Cost
Clamping Force	Very Low Force Required to Remove Clamp	Large	Extremely Large
Reproducibility	Poor Damage to Surrounding Areas	Good	Good
Miscellaneous	Magnetic Field Cannot be Turned Off - Accidental Attachement to Other Parts	Heat Build-Up Due to Resistance in Cu Coil	Magnetic Field Can be Turned Off

Figure 103.